ROYAL HOLLOWAY UNIVERSITY OF LONDON

A DISSERTATION SUBMITTED TO THE UNIVERSITY OF LONDON FOR THE DEGREE OF DOCTOR OF PHILOSOPHY

Spin Ice: a Wonderful World

Author:
Gabriele SALA

Supervisors:
Prof. Jon P. GOFF
Dr. Claudio CASTELNOVO
Advisor:
Prof. Matthias ESCHRIG
Moderator:
Dr. Nikolas KAUER

July 10, 2014

Declaration of Authorship

I, Gabriele Sala, hereby declare that this thesis and the work presented in it is entirely my own. Where I have consulted the work of others, this is always clearly stated.

Signed:

Date:

Memento Audere Semper,
quoniam Audentes Fortuna Iuvat.

Abstract

Among the huge variety of compounds that Nature offers us, two crystals exhibit extraordinary features at low temperatures: $Dy_2Ti_2O_7$ and $Ho_2Ti_2O_7$. Their properties, modelled on the basis of water ice, have earned them the name of Spin Ice crystals. The competition between the crystal electric field and the ferromagnetic interactions in their pyrochlore lattice, results in a geometrically frustrated system whose topological defects share properties similar to Dirac's magnetic monopoles. Modelling the dynamics of these defects, as well as studying their physical properties, is a challenging problem.

The analysis of the internal field distribution showed that there is considerable local structure between high and low fields, mainly due to the symmetry of the pyrochlore lattice. However, the presence of monopoles alters this equilibrium and breaks the symmetry of the system.

We studied two kinds of structural defects: oxygen vacancies and non magnetic Yttrium impurities. In the former case the diffuse neutron scattering analysis at low temperatures showed that the rare earth ions move away from the oxygen vacancy, due to Coulomb repulsion. The presence of neighbouring oxygen vacancies affects the crystal electric field of the rare earth; the single ion anisotropy changes from easy axis to easy plane, the magnitude of the magnetic moments is suppressed and, therefore, the magnetisation of the compound is reduced.

Moreover AC susceptibility measurements showed that vacancies can slow down the long-time monopole dynamics at sub-Kelvin temperatures, trapping the monopole.

Doping the crystal with non magnetic Yttrium impurities leaves the lattice unchanged, since the atomic radii of the Dy and Y are similar. The magnetisation of the system decreases linearly with the doping level, but the ice rules are still preserved at low temperatures. Non magnetic impurities are likely to affect the correlations between spins, as a result the internal field distribution at low and high temperatures for high doping levels look very similar.

Acknowledgements

This thesis is dedicated to all people that helped me in every single aspect of my private life, my work and my character during the past 28 years of my life.

I would like to thank my supervisors J. P. Goff and C. Castelnovo for the help they gave me during the past three years of my PhD. All the members of my big family, in particular: my mother L. Maggioni and my father W. Sala for giving me everything, including the great opportunity to study abroad, my uncle I. Maggioni and especially my granny C. Vimercati for the love and advices I received since I was born. Moreover, I would also like to thank my uncle M. Sighinolfi, my aunt L. Giovani (la nina) and A. Zanforlin (Ale Zanfo) for the strong support and help they gave me when I was living in Ferrara.

A special thanks goes also to M. J. Gutmann (ISIS) who taught me everything about neutron scattering, X-ray experiments and data analysis. The major part of this work was possible thanks to the excellent crystals growth by D. Prabhakaran (Oxford), who I thank for the useful lessons on the magnetometer too.

I would like to thank all my previous teachers and professors, in particular: R. Zara, M. A. Molteni, M. Beretta, A. Tentorio, G. Pesaresi, M. Fabbri, R. Zivieri, F. Nizzoli, G. Bottoni and F. F. Alonso. Without their teachings and their advices, I would not have been here today.

A giant thanks goes to the Casadei family, my "second family", in particular to M. Casadei and N. Poggi for the love they gave me since I was a child, and to my nephews N. Casadei and D. Casadei. I want also to thank the Cernari family, M. Cernari and A. Ferrario, for their support and their kindness during the bad period of my life.

I have to thank all my best friends L. Citterio, M. Cernari (Cerny), R. Rubini ("il bieko uno"), R. Manini (Ricky), M. Caggio (Jhonny "the king" Cage), B. Galvani (la Trix), B. Motta (Benny), S. Cernari (Saretta), J. Gazzoli (J), T. Konstantinidou and M. Casadei (Mirkone) for believing in my skills, and in my dreams.

Finally, I thank my friends D. G. Porter (Dan) and D. J. Voneshen (Dave) for helping me with X-ray measurements and board games, and my friends L. Sumner, P. Sahafi, K. E. Porsch, H. van der Vliet, E. Balkind (Cobra), N. Wennerdal (Nic), T. Willis, E. Cemal, T. Giles, J. Poulten and D. Bowman for the craziest party nights ever.

I hope one day to be able to repay all of you for what you have done for me. "All for one, one for all."

Contents

List of Figures

List of Tables

Chapter 1

Review of spin ice physics

Contents

Spin ice crystals represent an interesting system where the fractionalisation and the topological order marry the idea of the existence of magnetic monopoles.

Fractionalisation (Ref. [1]) is the phenomenon where the quantum numbers of the low lying excitations of a many body system, are non integer multiples of those of the constituents. Fractionally charged and fractional statistics excitations in quantum Hall phases (Refs. [2],[3]), are an example of this phenomenon in condensed matter physics.

The term topological order (Ref. [4]) has its roots in studies on spin liquids, and lattice gauge theories (Refs. [5],[6]). This term describes ordering characterised by the emergence of a gauge field, as opposed to the emergence of a local order parameter field in broken symmetry phases. Again we can find an example of these topologically ordered phases in quantum Hall systems (Refs. [7],[8]).

The idea of magnetic monopoles is centred around the seminal work of P.A. Dirac (Ref. [9]); he was interested in the constraint placed on the existence of magnetic monopoles in quantum mechanics. These particles have not been found in experiments, but they have been invoked in theories of Particle Physics beyond the Standard model. The current belief is that monopoles probably exist, but they are extremely rare and massive.

1.1 Spin ice crystals $Dy_2Ti_2O_7$ and $Ho_2Ti_2O_7$

Spin ice crystals such as $Dy_2Ti_2O_7$ and $Ho_2Ti_2O_7$ (Refs. [10]-[13]) can be described by a corner sharing network of tetrahedra forming a pyrochlore lattice, where the rare earth ions carry localised magnetic moments $\mu \approx 10\mu_B$ (see Fig. 1.1). These sites are at the same time the midpoints of the bonds of a diamond lattice (black line), defined by the centres of the tetrahedra (green spheres). The Ising axes are the local $\langle 111 \rangle$ directions, which point along the respective diamond lattice bonds. By contrast the nearest neighbour magnetic ions of the pyrochlore lattice are along the $\langle 110 \rangle$ directions.

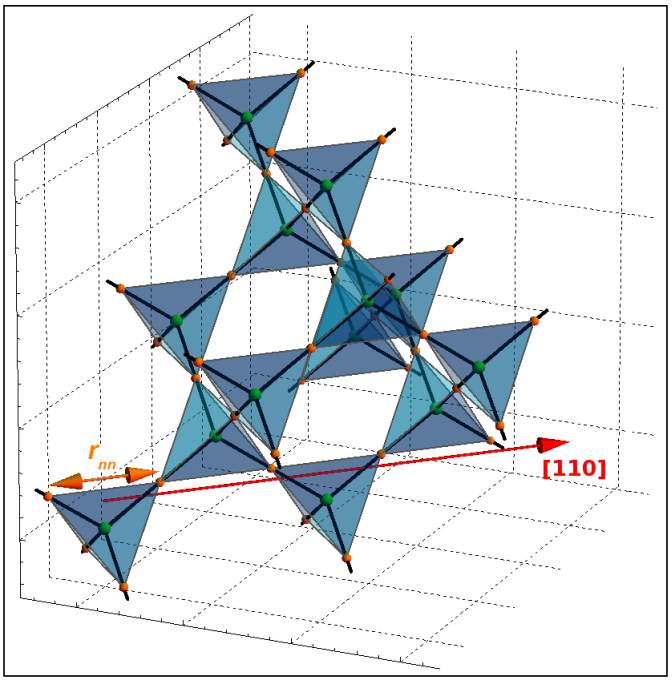

Figure 1.1: *Pyrochlore lattice in spin ice crystals $Dy_2Ti_2O_7$ and $Ho_2Ti_2O_7$.* – Magnetic moments in spin ice reside on the sites of the pyrochlore lattice (orange spheres), which consists of corner sharing tetrahedra. These sites are at the same time the midpoints of the bonds of the diamond lattice (black line), defined by the centres of the tetrahedra (green spheres). The Ising axes are the local $\langle 111 \rangle$ directions, which point along the respective diamond lattice bonds. The nearest neighbour magnetic ions of the pyrochlore lattice ($r_{nn} = 3.54$ Å) are along the $\langle 110 \rangle$ directions.

The pairwise interaction is made up of both exchange and dipolar terms, thus the Hamiltonian that describes the system is:

$$H = -J_{ex} \sum_{<ij>} \mathbf{S}_i \cdot \mathbf{S}_j + D \sum_{i<j} \left[\frac{\mathbf{S}_i \cdot \mathbf{S}_j}{|\mathbf{r}_{ij}|^3} - \frac{3(\mathbf{S}_i \cdot \mathbf{r}_{ij})(\mathbf{S}_j \cdot \mathbf{r}_{ij})}{|\mathbf{r}_{ij}|^5} \right] \qquad (1.1)$$

where J_{ex} is the nearest neighbour exchange constant, D is the dipolar constant, $\mathbf{r}_{ij}$ is the vector that connects two spins in the system and $\mathbf{S}_i$ is a spin of unit length.

Notice that the Hamiltonian in Eq. 1.1 reproduces the experimental data with a remarkable agreement, however it has been speculated in Ref. [13] that this model is only a basis for studying spin ice compounds since, e.g., it is insufficient to describe the polarised magnetic diffuse scattering of $Dy_2Ti_2O_7$. A better approximation including second and third nearest neighbour correlations has been proposed by Yavors'kii et al. who extrapolated the new exchange and dipolar constants from the experimental data sets (see Ref. [14] for details). Notwithstanding this remarkable job we chose a traditional approach to describe spin ice systems using Eq. 1.1 since this is the most common one. The low number of parameters in the model Hamiltonian and the fact that both the exchange and dipolar constants truncated at first nearest neighbours are well known, helped us to write and benchmark a MC algorithm to model all our measurements. However, we note that if the model is extended to include interactions with magnetic impurities, next nearest neighbour exchange should, in principle, be considered on as equal footing.

The energy scale of the system is around 1 K. The coupling constants are: $J_{ex} = 3.72$ K for $Dy_2Ti_2O_7$ and 1.56 K for $Ho_2Ti_2O_7$, while the dipolar term can be explicitly calculated in the following way [15]:

$$D = \frac{\mu_0}{4\pi k_B} \frac{\mu^2}{r_{nn}^3} \approx 1.41 \text{ K} \tag{1.2}$$

where μ_0 is the vacuum permeability, k_B is the Boltzmann's constant and $r_{nn} = 3.54$ Å is the distance between two nearest neighbour spins in the pyrochlore lattice (see Fig. 1.1).

These energy scales are 100 times smaller than the crystal field terms (Ref. [15]) that force the spins to point along the axis joining the centres of two adjoining tetrahedra. As a result the moments behave as Ising spins along the local $\langle 111 \rangle$ directions. Remarkably, within this Ising description the long range dipolar interactions are almost perfectly screened at low temperatures (Refs. [13]-[17]), with the result that the low energy properties are almost identical to those of an effective geometrically frustrated nearest neighbour model with ferromagnetic interactions (Ref. [18]). Notice that a geometrically frustrated system is one in which the geometry of the lattice precludes the simultaneous minimisation of all interactions. This leads to highly degenerate ground states with a non-zero residual entropy.

In order to illustrate this statement we can imagine having two 2D antiferromagnets; the first one on a square lattice, the second one on a triangular lattice as depicted in Fig. 1.2. In the first case each spin can be anti aligned with all its neighbours, but in the second case such a configuration is impossible. Three neighbouring spins cannot be pairwise anti aligned with each other and, therefore, the system is geometrically frustrated.

In a tetrahedron with collinear spins and antiferromagnetic interactions, things get even worse. If we look at Fig. 1.2(c) we can see that there are six nearest neighbour interactions, four of them are antiparallel and thus favourable, but the

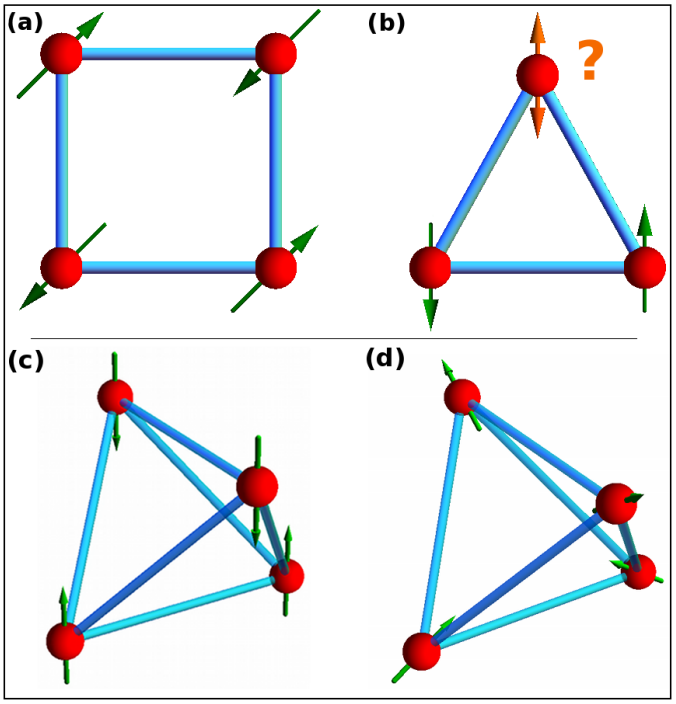

Figure 1.2: *An example of geometrical frustration.* – The antiferromagnetic interaction between spins can be satisfied on a square lattice **(a)** since all the spins can be anti aligned with each others. Such a configuration is impossible on a triangular lattice **(b)** since the third spin (orange arrow) cannot be pairwise anti aligned with the others. Therefore the system is geometrically frustrated. In 3D things get even worse. **(c)** In a tetrahedron with collinear spins and anti ferromagnetic interactions, we have 4 favourable interactions and 2 non favourable. **(d)** In a tetrahedron with non collinear easy axis spins, geometrical frustration arises if there is a ferromagnetic interaction. In this case spins are forced to point 2in-2out from the tetrahedron in order to minimise the energy.

other two are unfavourable. Therefore it is not possible to anti align all the spins with each other. Notice that geometrical frustration is also possible if spins are arranged in a non collinear way, like in spin ice. Lets consider a tetrahedron like in Fig. 1.2(d), with a spin on each vertex that is pointing along the easy axis (directly towards or away from the centre of the tetrahedron).

In this system, geometrical frustration arises if there is a ferromagnetic interaction between neighbours, and the only possible arrangement to minimise this interaction is having two spins pointing towards the centre of the tetrahedron and two spins pointing away from it. The ferromagnetic interaction means that, if a spin points in, it wants its neighbours to point out. This situation cannot be realised for all of the spins. The best compromise is to have two spins pointing in and two pointing out.

The first characteristic of spin ice, as reported by Harris et al. (Ref. [10]) is that, despite a ferromagnetic Curie-Weiss temperature $\approx$ 2 K, this compound fails to develop long ranged spin order down to a temperature four times lower. The crystal does not order even when cooled further, but instead it falls out of the equilibrium. The second characteristic, discovered by Ramirez et al. (Ref. [19]) via calorimetry, is that spins do not fully lose their entropy down to the lowest temperatures. Spin ices samples exhibit a macroscopic entropy per spin which is essentially equal to the macroscopic entropy per hydrogen exhibited by water ice.

Notice that these observations are coupled: the first implies the existence of the frustration, and the second quantifies it and explains the absence of any phase transition since the system fails to reach a particularly favourable ordered state.

Given the previous characteristics, the spin ice model is indeed equivalent to Pauling's model for proton disorder in water ice (Refs. [20], [21]), which estimates a ground state entropy per spin of $(1/2)\log(3/2)$ in excellent agreement with the experimental data. The extensive set of spin ice states satisfy the Bernal-Fowler ice rules (Ref. [22]), that are a 3D analogue of the 6 vertex model with topological constraints consisting of two spins pointing into and two out of each tetrahedron (familiarly called 2in-2out), as shown in Fig. 1.3(a).

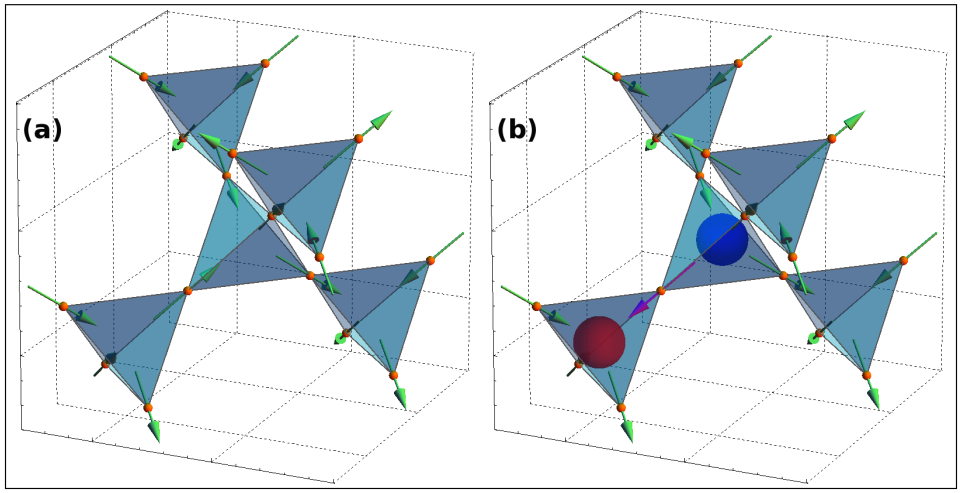

Figure 1.3: *Spin ice configurations in the Unit Cell.* – **(a)** The ground state of the system satisfies the Bernal-Fowler ice rules with 2 spins pointing into and 2 out of each tetrahedron (green arrows). **(b)** flipping one spin (magenta arrow) breaks the constraint and it creates a pair of topological defects.

Flipping one of the spins breaks the constraint leaving neighbouring tetrahedra with 3in-1out and with 3out-1in as shown in Fig. 1.3(b), which constitutes a pair of topological defects (shown in the figure with a blue and a red sphere). Within the nearest neighbour model, the creation of the defect pair costs $4J_{eff}$ with $J_{eff} = (5D - J_{ex})/3 = 1.11$ K, while further spin flips can move the defects at zero additional energy cost. This means that it does not cost anymore energy to flip

other spins beyond the Coulomb energy, and at that point monopoles behave like a deconfined Coulomb phase. The nature and properties of these topological defects are similar to Dirac's theory of magnetic monopoles (Ref. [9]) which we will revise in the following chapter.

The theory of spin ice magnetic monopoles (Ref. [23]), inspired by Nagle's work on the "unit model" description of water ice (Ref. [24]), can be summarised as follows.

First of all we can replace the dipole interaction in Eq. 1.1, with the interaction energy of "dumbbells" consisting of equal and opposite magnetic charges that live at the ends of the diamond bonds (see Fig. 1.4). The two charges will be assigned in order to represent the two orientations of the original dipole assuming the real strength of the dipole moment of the spin. This constraint fixes the value of the charge at $Q = \pm\mu/a_d$, where $a_d = \sqrt{3/2}r_{nn}$ is the diamond lattice bond length.

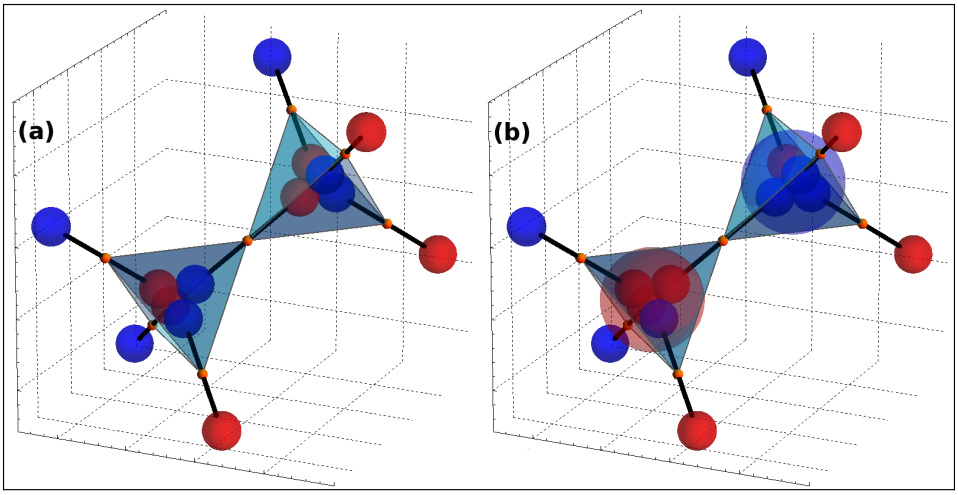

Figure 1.4: *The "dumbbell" model in spin ice.* – **(a)** The ground state of the system can be visualised by replacing the magnetic interaction with "dumbbells" consisting of equal and opposite opposite magnetic charges. **(b)** Flipping one of the "dumbbells" creates an imbalance in the charge of the two adjacent tetrahedra, which leads to the manifestation of topological defects similar to magnetic monopoles (highlighted with the bigger red and blue spheres).

Now, the energy of a configuration of dipoles can be calculated as the pairwise interaction energy of magnetic charges, given by the following Hamiltonian:

$$H = \frac{\mu_0}{4\pi} \sum_{\alpha<\beta} \frac{Q_\alpha Q_\beta}{r_{\alpha\beta}} + \frac{1}{2}\nu_0 \sum_\alpha Q_\alpha^2 \tag{1.3}$$

where Q_α is the total magnetic charge at site α in the diamond lattice and $r_{\alpha\beta}$ is the distance between the two sites.

Notice that the finite "self-energy" term $\nu_0/2$ is required in order to reproduce the net nearest neighbour interaction. In particular:

$$\nu_0 \left(\frac{\mu}{a_d}\right)^2 = \frac{J_{ex}}{3} + \frac{4}{3}\left(1+\sqrt{\frac{2}{3}}\right) D \tag{1.4}$$

Within this model the ground state of the system is minimised if each diamond lattice site is net neutral, i.e. $Q_\alpha = 0$, but this is possible only if the ice rules are respected. The most elementary excitation involves an inversion of the dumbbell, in order to generate a net dipole moment of 2μ. Notice that the inverted dumbbell corresponds to two adjacent sites with net magnetic charge of $Q_\alpha = \pm 2\mu/a_d = \pm q_m \approx 4.6\mu_B/\text{Å}$, i.e. a nearest neighbour monopole - anti-monopole pair.

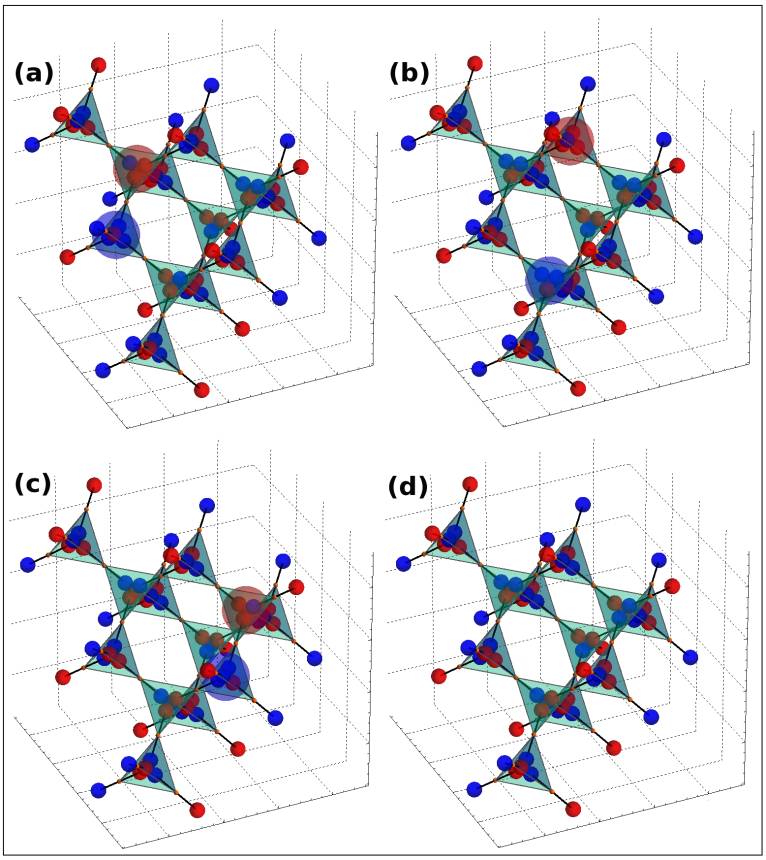

Figure 1.5: *Closed loops created by magnetic monopoles.* – **(a)** A couple of topological defects (big red and blue spheres) is created by flipping a "dumbbell". **(b),(c)** Flipping other "dumbbells" moves the defects to adjacent tetrahedra. **(d)** The last "dumbbell" flips and annihilates the two defects, restoring the ground state of the system. Notice that the cost of the first flip is $4J_{eff}$, while further flips are at zero energy cost (i.e. they are deconfined).

In this model two monopoles can be separated from one another without further violations of local neutrality by flipping a chain of adjacent "dumbbells" (see Fig. 1.5), and they are going to experience a magnetic Coulombic interaction equal to:

$$F_{nn} = \frac{\mu_0}{4\pi}\frac{q_m^2}{r} \approx 97.4\ 10^{-15}\ \mathrm{N} \tag{1.5}$$

Notice that it takes only a finite energy cost to separate the monopoles to infinity (i.e. they are deconfined).

In general it is well known that a string of dipoles arranged head to tail realises a monopole - anti monopole pair at its ends. However, in order to have deconfined monopoles, it is essential that the cost of creating such a string of dipoles remain bounded as its length grows, i.e. the relevant string tension should vanish.

What is remarkable about spin ice is that the system allows for the deconfinement of these effective magnetic charges so that they occur in the bulk of the material on all scales, rather than just at the surfaces within a coarse grained description. A 2D equivalent system may exist in artificial spin ice, constituting a nanoscale array of magnets (see Ref. [25]).

1.2 Difference from Dirac's monopoles in quantum mechanics

As we said in the previous section one of the most important features of spin ice crystals is that they exhibit topological defects, arising from the excitation of the lattice, with properties similar to Dirac's magnetic monopoles.

Standard electromagnetic theory does allow for such excitations (see Ref. [26]), which correspond to divergences in the magnetic field $\mathbf{H}$, or in the magnetic moment $\mathbf{M}$, rather than in the magnetic induction $\mathbf{B}$. Under these considerations Gauss' theorem is still valid since:

$$\nabla \cdot \mathbf{B} = \nabla \cdot (\mathbf{H} + \mathbf{M}) = 0 \tag{1.6}$$

On all length scales above the atomic scale, a 3in-1out defect appears to be a local sink in the magnetic moment and therefore as a source of field lines in $\mathbf{H}$. It can lower its energy by moving in the direction of an external field and therefore it carries a positive magnetic charge (see Ref. [27]).

We want to stress the fact that these topological defects are not exactly the same particles predicted by Dirac, and the term monopole is used here only to identify a phenomenon that has similar characteristics. In order to better understand this fact we first revise Dirac's theory in quantum mechanics, deriving the main property of his magnetic monopoles.

As it is well known there is a strong symmetry between electrical and magnetic fields, however a magnetic charge (called in this case magnetic monopole) analogous to the electric one is absent in Maxwell's equations. A priori this is very

surprising, and one can test this assumption with a simple experiment. If we take a common bar magnet and we try to separate its north and south pole it turns out that, no matter how many times we break the magnet, it is impossible to divide the two poles one from the other. This is a property of the magnetic field that, unlike the electric one, has closed force lines.

In nature the source of magnetic fields can be either a moving electric charge or a static magnetic dipole, but never a static magnetic charge. This fact is mathematically expressed in Gauss' theorem which states that:

$$\nabla \cdot \vec{B} = 0 \tag{1.7}$$

which means that the magnetic field is solenoidal.

By contrast Maxwell's equation for the electric field states that:

$$\nabla \cdot \vec{E} = 4\pi\rho \tag{1.8}$$

where ρ is the charge density.

We start our discussion supposing that there is a point-like magnetic monopole sitting at the origin of our reference system with strength e_M, in perfect analogy with a point-like electron (see Ref. [28]). In this case the static magnetic field should be:

$$\vec{B} = \frac{e_M}{r^2}\hat{r} \tag{1.9}$$

Since this field has spherical symmetry, it is easier to use spherical coordinates to study the problem.

At a first sight we may derive the above expression for the magnetic field using the following vector potential:

$$\vec{A} = \frac{e_M(1-\cos\theta)}{r\sin\theta}\hat{\phi} \tag{1.10}$$

In fact

$$\nabla \times \vec{A} = \frac{e_M}{r^2}\hat{r} = \vec{B} \tag{1.11}$$

However, this kind of vector potential is not well defined in all space, in particular along negative $\hat{z}$, since it has a singularity at $\theta = \pi$:

$$\lim_{\theta\to 0} \frac{e_M(1-\cos\theta)}{r\sin\theta}\hat{\phi} = \lim_{\theta\to 0} \frac{e_M\sin\theta}{r\cos\theta}\hat{\phi} = 0 \tag{1.12}$$

$$\lim_{\theta\to \pi} \frac{e_M(1-\cos\theta)}{r\sin\theta}\hat{\phi} = \frac{-2e_M}{0} \tag{1.13}$$

In order to solve the problem we can use a mathematical trick to construct the following pair of potentials:

$$\vec{A}_I = \frac{e_M(1-\cos\theta)}{r\sin\theta}\hat{\phi} \quad \theta < \pi - \epsilon \tag{1.14}$$

$$\vec{A}_{II} = -\frac{e_M(1+\cos\theta)}{r\sin\theta}\hat{\phi} \quad \theta > \epsilon \tag{1.15}$$

At this point we have to consider what happens in the overlap region $\epsilon < \theta < \pi - \epsilon$. Since the two potentials lead to the same form of magnetic field, they must be related to each other by a gauge transformation Λ. In order to find this expression we first note that:

$$\vec{A}_I - \vec{A}_{II} = -\frac{2e_M}{r\sin\theta}\hat{\phi} \tag{1.16}$$

Therefore the correct expression for Λ is:

$$\Lambda = -2e_m\phi \tag{1.17}$$

In fact:

$$\nabla\Lambda = \frac{\partial\Lambda}{\partial r}\hat{r} + \frac{1}{r}\frac{\partial\Lambda}{\partial\theta}\hat{\theta} + \frac{1}{r\sin\theta}\frac{\partial\Lambda}{\partial\phi}\hat{\phi} = -\frac{2e_M}{r\sin\theta}\hat{\phi} \tag{1.18}$$

Finally we can study the effect of the magnetic field in Eq. 1.9 applied on a particle with charge e. In the overlap region of the two potentials, the two wave functions of the charge particle are related to each other in the following way:

$$\psi_{II} = \exp\left[-\imath\frac{2ee_M}{\hbar c}\phi\right]\psi_I \tag{1.19}$$

where $\hbar = h/2\pi$ and c is the speed of light.

The two wave functions must be single valued since, once we chose a particular gauge, the expansion of the eigenvalues in term of the eigenvectors must be unique. Thus, if we examine their behaviour on the equatorial plane ($\theta = \pi/2$) and we increase the angle $0 \leq \phi \leq 2\pi$, both ψ_{II} and ψ_I must return to their original values and this is possible only if:

$$\frac{2ee_M}{\hbar c} = N \Rightarrow e_M = \frac{\hbar c}{2|e|}N \tag{1.20}$$

where N is an integer. This formula states that if a magnetic monopole exists, its charge must be quantised and the equality can also be used to explain why electric charges are quantised in the same way.

Notice that the "dumbbell model" developed in Ref. [23] does not make any reference to Dirac's quantisation condition (Eq. 1.20). Within this model the magnitude of a spin ice monopole should be:

$$q_m = \frac{2\mu}{a_d} = \frac{\mu}{\mu_B}\alpha\frac{\lambda_C}{\pi a_d}e_M \approx \frac{e_M}{8000} \tag{1.21}$$

where λ_C is the Compton wavelength for an electron, and $\alpha = 1/137$. Moreover we can always tune continuously the charge of a spin ice monopole by applying pressure to the crystal, since this changes the ratio of μ/a_d.

In conclusion we can not talk about magnetic monopoles in spin ice in the sense of Dirac because these topological defects are not sources of $\vec{B}$, but sources of $\vec{H}$. The term is used here as an analogy, in order to represent a phenomenon which manifests a magnetic field equal to the one expressed in Eq. 1.9.

1.3 Thermodynamic properties of spin ice crystals

One of the most interesting properties of frustrated systems is that their ground state is many fold degenerate. For this reason the study of the energy fluctuations (e.g. the heat capacity) becomes very important in order to understand how the system behaves at low temperatures. This is an interesting region for spin ice crystals.

The heat capacity is an extensive property of matter, meaning that it is proportional to the size of the system. In general it is the sum of three different contributions: phonons, magnetism, and the movement of electrons. In this thesis we will neglect the latter contribution which is much smaller compared to the others.

We first study how the magnetism of rare earth ions affects the energy fluctuations of the system, due to the high magnetic moment carried by the spin. Therefore, in order to suppress the phonon contribution, we measured our crystals in a range of temperatures between $0.6 \leq T \leq 12$ K.

1.3.1 The Debye Hückel model of the Heat Capacity

We begin our study of the heat capacity by revising what has been done in Ref.[29].

The model dipolar Hamiltonian that describes spin ice crystals is given in Eq. 1.1. At low temperatures the system is populated by a finite density of magnetic monopoles and the total monopole density (ρ_{nn}) is equal to:

$$\rho_{nn} = \frac{2\mathrm{exp}(-\Delta/\mathrm{T})}{1 + 2\mathrm{exp}(-\Delta/\mathrm{T})} \tag{1.22}$$

where Δ is the energy cost of an isolated monopole (assumed in the following to be measured in Kelvin). The subscript nn denotes that the long range dipolar interactions can be neglected and the nearest neighbour approximation is applied.

Taking advantage of the analogy between spin ice defects and a two-component Coulomb liquid (with no external field), it is possible to use the Debye approximation to estimate the magneto static contribution to the free energy (in degrees Kelvin per spin):

$$\frac{F_{el}}{N_s k_B} = -\frac{NT}{4N_s \pi \rho_V a_d^3}\left[\frac{(a_d\kappa)^2}{2} - (a_d\kappa) + \ln(1 + a_d\kappa)\right]$$

$$\kappa = \sqrt{\frac{\mu_0 q_m^2 \rho_V}{k_B T}} \tag{1.23}$$

where N_s is the number of spins, $\rho_V = N/V$ is volume density of monopoles and a_d is the distance between the centres of two neighbouring tetrahedra.

It is convenient to express the dimensionless quantity $a_d\kappa$ in terms of the Coulomb energy between two neighbouring monopoles $E_{nn} = \mu_0 q_m^2/(4\pi a_d k_B) \approx 3.06$ K:

$$a_d\kappa = \sqrt{4\pi \frac{E_{nn}}{T} \rho_V a_d^3} \tag{1.24}$$

Combining Eqs. 1.22 and 1.23 we obtain a mean field free energy of an ensemble of N monopoles on a lattice, with long range Coulomb interactions:

$$\frac{F_{el}}{N_s k_B} = \frac{\rho}{2}\Delta + \frac{T\rho}{2}\ln\left(\frac{\rho/2}{1-\rho}\right) + \frac{T}{2}\ln(1-\rho) - \frac{T}{3\sqrt{3}\pi}\left\{\frac{\alpha^2(T)\rho}{2} - \alpha(T)\sqrt{\rho} + \ln[1+\alpha(T)\sqrt{\rho}]\right\} \tag{1.25}$$

with

$$\alpha(T) = \sqrt{\frac{3\sqrt{3}\pi E_{nn}}{2T}} \tag{1.26}$$

Notice that this reduces to the non interacting limit if $E_{nn} = 0$

Minimising with respect to the defect density ρ, one obtains a self consistent set of equations that can be used to determine $\rho(T)$ (see Ref. [29]). Finally the heat capacity of the system in the DH approximation is:

$$C_v = -N_A k_B T \frac{\partial^2}{\partial T^2}\left(\frac{F_{el}}{N_s k_B}\right) \tag{1.27}$$

Another useful approximation to obtain the spin ice free energy and thus the heat capacity is to use a truncated cluster expansion. We can consider only one tetrahedron and compute the free energy by direct summation over all the 2^4 states. At this level all the interactions are only due to the nearest-neighbour ions, and in terms of their effective short range coupling ($J_{eff} = 1.11$ K) the partition function of the system is:

$$Z = 6 + 8e^{-2J_{eff}/T} + 2e^{-8J_{eff}/T} \tag{1.28}$$

Notice that in Eq. 1.28 we scaled the energy reference to that of the ground state of the system.

From this, the partition function for the entire system and the free energy per spin are:

$$Z = 2^{N_s}\left[\frac{6 + 8e^{-2J_{eff}/T} + 2e^{-8J_{eff}/T}}{16}\right]^{N_t} \tag{1.29}$$

$$\frac{F}{N_s k_B} = -\frac{T}{N_s}\ln Z \tag{1.30}$$

where N_s is again the number of spins and $N_t = N_s/2$ is the number of tetrahedra. Notice that the choice of $J_{eff} = 1.11$ K yields a very poor agreement with the experimental data, therefore instead of truncating the dipolar contribution to $5D/3$, one can use the "dumbbell model" decomposition to derive a value of $J_{eff} = 1.45$ K.

In Monte Carlo (MC) simulations the heat capacity can be obtained by the usual fluctuation-dissipation route, measuring the average energy $\langle\epsilon\rangle$ and its fluctuations, so:

$$C_v = \frac{R}{N_s T^2}[\langle\epsilon^2\rangle - \langle\epsilon\rangle^2] \tag{1.31}$$

These approximations provide an excellent description of the low temperatures physics of spin ice, and the equations can be used to study heat capacity measurements. In particular we found that Eq. 1.31 is a powerful instrument to test if the energy of the system is minimised in the correct way during the Monte Carlo simulation. In fact the comparison between the experimental data and the MC simulation using Eq. 1.31, provides a direct bench mark that both the simulation and the model are able to describe the energy fluctuations of the system in the correct way.

1.4 The Pyrochlore lattice

Most physical and chemical properties of materials are closely related to the positions of the ions in the lattice. The stress tensor, conductivity, magnetism are just a few examples, and since in spin ice the frustration is in part due to the Crystal Electric Field (CEF) environment set up by the ions surrounding the rare earth, the study of its lattice becomes much more important in order to better understand the physics of the system.

The general formula of the oxide pyrochlores can be written as $\mathrm{A_2B_2O_6O'}$ with four crystallographic non equivalent kinds of atom. Usually A cation is trivalent and it belongs to the rare earth group (e.g. $\mathrm{Dy^{3+}}, \mathrm{Ho^{3+}}, \mathrm{Tb^{3+}}, \mathrm{Er^{3+}}, \mathrm{Yb^{3+}}$) or to the transition metal group (e.g. $\mathrm{Y^{3+}}$), while the B cation is a tetravalent transition metal (e.g. $\mathrm{Ti^{4+}}$) ion that can form a strong bond with oxygen.

This structure shows several different physical properties spanning electronic insulators (e.g. $\mathrm{La_2Zr_2O_7}$ [30]), ionic conductors (e.g. $\mathrm{Gd_{1.9}Ca_{0.1}Ti_2O_{6.9}}$ [31]), metallic conductors (e.g. $\mathrm{Bi_2Ru_2O_{7-\delta}}$ [32]), mixed ionic and electronic conductors, spin ice systems ($\mathrm{Dy_2Ti_2O_7}$, $\mathrm{Ho_2Ti_2O_7}$ [11]), spin glass systems (e.g. $\mathrm{Y_2Mo_2O_7}$ [33]), Haldane chain systems (e.g. $\mathrm{Tl_2Ru_2O_7}$ [34]) and superconducting materials (e.g. $\mathrm{Cd_2Re_2O_7}$ [35]).

The space group of the ideal pyrochlore lattice is $Fd\bar{3}m$ (227) containing eight molecules per unit cell (Z=8). The structure is composed of two types of cation coordination polyhedron (see Ref. [36]): the A cations (usually 1 Å ionic radius) are eight coordinated within scalenohedra (distorted cubes along the diagonal) that contain six equally spaced anions (usually oxygen) at a slightly shorter distance from the central cation. The smaller B cations ($\sim$ 0.6 Å ionic radius) are six coordinated and they are located within trigonal anti prisms with all the six anions equidistant. These structures are shown in Fig. 1.6 where we highlighted the scalenohedra and the trigonal anti prisms in orange and yellow respectively.

Notice that it is common to refer to the six-fold and eight-fold coordination structures as octahedral and cubic coordination polyhedra respectively. However, from a crystallographic point of view, this is not exactly correct because the space group has D_{3d} symmetry. Therefore the conditions for the existence of perfect octahedra and cubic coordination polyhedra can not be simultaneously satisfied.

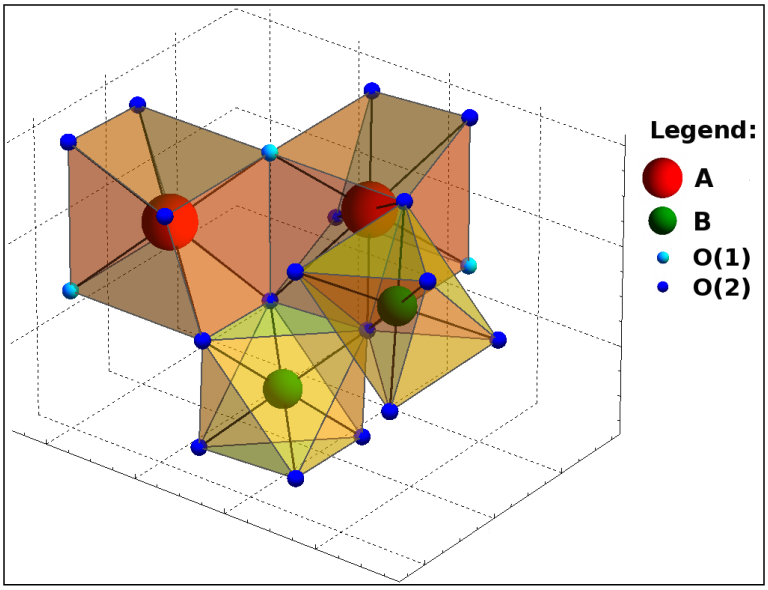

Figure 1.6: *Environment surrounding A and B cations in the pyrochlore lattice.* – The A cations (red) are eight coordinated, and located at the centre of scalenohedra (orange). Within this structure, the two oxygen ions along the longest diagonal (cyan) are commonly called O(1), while the other six ones O(2) (blue). B cations (green) are six coordinated and located at the centre of trigonal anti prisms (yellow) at the same distance from the O(2) anions.

Since there are four inequivalent atom sites, there can be four different choices for the origin of the system. One of the most useful is summarised in Tab. 1.1.

Notice that we wrote only the crystallographic coordinates of the main ions, since the other ones can be found by translation using the following set of vectors: $(0,0,0)$; $(0,1/2,1/2)$; $(1/2,0,1/2)$; $(1/2,1/2,0)$ that identify the directions of the bonds of the pyrochlore lattice.

As one can see from Tab. 1.1, inside the unit cell of $Dy_2Ti_2O_7$ there are 16 Ti ions and 16 Dy ions both arranged in regular tetrahedra. Likewise for $Ho_2Ti_2O_7$ and $Y_2Ti_2O_7$. It is useful to make a distinction among the 56 oxygen anions in the following way: the first group contains 8 oxygen ions located at the centres of the rare earth tetrahedra (commonly called O(1) site) while the second group contains 48 oxygen ions (commonly called O(2) site). As we showed in Fig. 1.6 the O(2) anions form trigonal anti prism cages around Ti cations, filling the interstitial regions between Ti and the rare earth. The value of the parameter x can be determined

Ion	Location	Site	Coordinates
$16A$	$16d$	D_{3d}	$(1/2,1/2,1/2);(1/2,1/4,1/4);$ $(1/4,1/2,1/4);(1/4,1/4,1/2)$
$16B$	$16c$	D_{3d}	$(0,0,0);(0,1/4,1/4);$ $(1/4,0,1/4);(1/4,1/4,0)$
$48O(2)$	$48f$	C_{2v}	$(x,1/8,1/8);(\bar{x},7/8,7/8);$ $(1/4-x,1/8,1/8);(3/4+x,7/8,7/8);$ $(1/8,x,1/8);(7/8,\bar{x},7/8)$ $(1/8,1/4-x,1/8);(7/8,3/4+x,7/8);$ $(1/8,1/8,x);(7/8,7/8,\bar{x});$ $(1/8,1/8,1/4-x);(7/8,7/8,3/4+x);$
$8O(1)$	$8b$	T_d	$(3/8,3/8,3/8);(5/8,5/8,5/8)$

Table 1.1: *Common crystallographic coordinates of the pyrochlore lattice.*

using X-ray or neutrons.

Figure 1.7 shows the cubic unit cell of $Dy_2Ti_2O_7$ following the crystallographic notation of Tab. 1.1, and using a length of the unit cell equal to $2\sqrt{2}r_{nn} \approx 10$ Å. We highlighted the two interpenetrating pyrochlore structures of Dy^{3+} and Ti^{4+} in red and green respectively. Notice that the colour scheme of Fig. 1.7 will be used from now on to indicate a particular type of ion in the lattice. According to this convention Dy^{3+} is red, Ti^{4+} is green, O(1) is cyan and O(2) is blue.

Although many pyrochlore compositions crystallise in the cubic structure, there are a few cases containing deviations from cubic symmetry. In particular we can have tetragonal, rhombohedral and triclinic distortions.

The position of the O(2) anions are subject to a displacement parameter x. Even though never realised experimentally, its limiting values should be $0.3125 \leq x \leq 0.375$ (Ref. [36]). For the lower limit the B ion has a perfect octahedral coordination while the A ion is eight coordinated in a form of a distorted hexagon, whose plane is perpendicular to the O(1)-A-O(1) bond. For the upper limit the A cation would be situated in a regular cubic 8-fold coordination (again no D_{3d} symmetry) whereas the B ion is at the centre of a highly distorted octahedron. The A-O(1) bond length is always less than A-O(2), but it becomes equal to it when $x = 0.375$. The stability of the ideal stoichiometric structure is mainly due to the smaller atomic radius of the B cation.

In this thesis we are also interested in what happens when we have a defect structure, that can be created by removing the O(1) from the main lattice. In this case the general unit formula becomes $A_2B_2O_{7-\delta}$ with $0 < \delta \leq 1$. Notice that in the extreme case of $\delta = 1$, the formula becomes $A_2B_2O_6 = ABO_3$ and the system undergoes to a structural phase transition from cubic to orthorhombic. In this case ions are arranged on a perovskite lattice whose characteristics will be described in

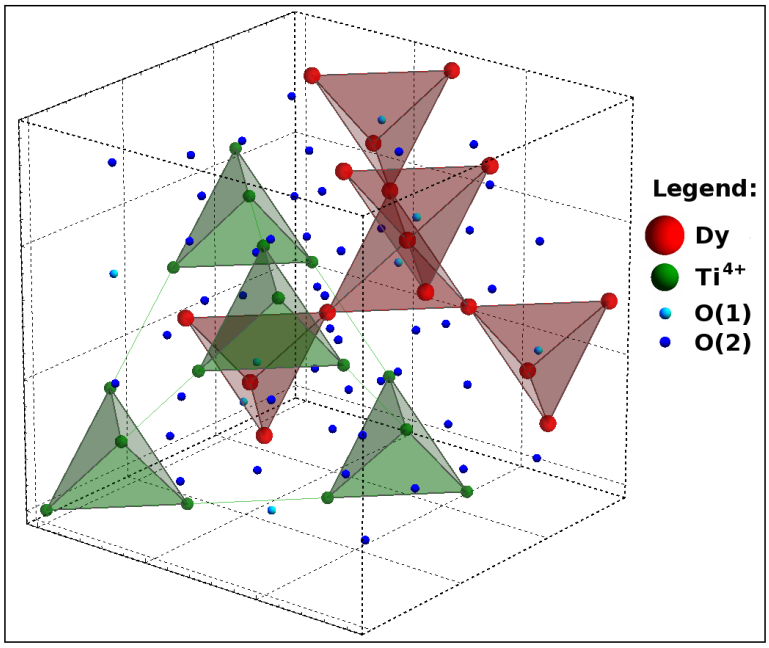

Figure 1.7: *Cubic unit cell of $Dy_2Ti_2O_7$.* – The colour scheme of this figure will be used from now on to indicate a particular type of ion in the lattice. According to this convention Dy^{3+} is red, Ti^{4+} is green, O(1) is cyan and O(2) is blue. We highlighted the two interpenetrating pyrochlore structures of Dy^{3+} and Ti^{4+} in red and green respectively. The length of the unit cell is equal to $2\sqrt{2}r_{nn} \approx 10$ Å.

the following section.

It is very interesting to try to understand for which value of δ we have this structural phase transition, that is mainly due to the fact that the pyrochlore configuration is not able to dilute the Coulomb repulsion between A cations left unshielded from the O(1) vacancy. One of the possible ways to study this phenomena consists of the application of the percolation theory to the defect system. However, this challenging study goes beyond the scope of this thesis.

Notice that in the case of $Dy_{2-x}Y_xTi_2O_7$ crystals, the cubic lattice is always preserved even at very high doping levels. In these systems Y^{3+} ions substitute Dy^{3+} in the pyrochlore lattice, lowering the number of magnetic ions in the tetrahedra. The valence states of both Y and Dy ions are the same and the ionic radii are similar, thus the overall structure remains the same.

We also stress the fact that the nature of the crystal and its quality, depends strongly on the growth condition. This process is not trivial, and it requires a high degree of accuracy in the preparation of the powders and in the selection of the temperature and gas atmosphere in the growth chamber. As we shall show, small deviations from the ideal system can determine new interesting properties or even catastrophic events during experiments. Notice that defects can sometimes

be eliminated, for example annealing in oxygen can potentially remove oxygen vacancies.

1.4.1 Comparison with the Perovskite lattice

The perovskite structure has the general formula ABO_3 where A and B are cations that can assume a variety of oxidation states and O is an anion (usually oxygen). Traditionally the lattice consists of small B cations within regular oxygen octahedra, and lager A cations which are 12-fold coordinated by the anions (see Ref. [37]).

The ideal perovskite is cubic, but many materials exhibit the orthorhombic $Pnma$ or $Pbnm$ distorted structure at room temperature (RT). A further distortion is also possible resulting in a rhombohedral structure with space group $R\bar{3}c$ or in the formation of an hexagonal $P6_3cm$ structure. In the latter case lattice distortions are so great that A cations are now 7-coordinate, and B cations are 5-coordinate. As a result they are not strictly considered as perovskite structures but as an intermediate between the perovskite and the bixbyite or garnet structures.

We show in Fig. 1.8 the orthorhombic unit cell of $DyTiO_3$.

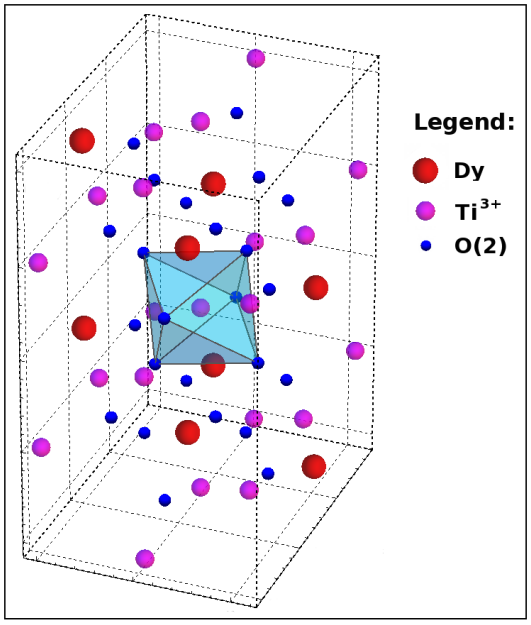

Figure 1.8: *Perovskite unit cell of* $DyTiO_3$. – The orthorhombic perovskite cell of $DyTiO_3$ shows that the pyrochlore lattice of Dy^{3+} is broken down. oxygen ions are rearranged in new structures to dilute the Coulomb repulsion of the cations, in particular the trigonal anti prisms become regular octahedra while the scalenohedra disappear. This structure is highlighted in cyan. Notice that this system contains only Ti^{3+} whose colour reference will be magenta from now on.

As one can see the pyrochlore lattice of Dy^{3+} is broken down, and oxygen ions are rearranged in new structures to dilute the Coulomb repulsion of the cations. In particular we highlighted in cyan the trigonal anti prism that becomes a regular octahedron in the new system, while the scalenohedron disappears. Notice that this system contains only Ti^{3+}, whose colour reference will be magenta from now on.

Similarly to the pyrochlore lattice, it is the ionic radii of the B cations that determines the stability of these structures. In principle any deviation from the ideal cubic perovskite can be computed using the following formula:

$$R_A + R_O = t\sqrt{2}(R_B + R_O) \tag{1.32}$$

where R_i are the ionic radii of the ions and t is a parameter known as the tolerance factor, that is use to estimate the degree of distortion of the system.

Hines et al. (see Ref. [38]) suggested that a cubic perovskite should have $0.9 < t < 1.0$, while an orthorhombic one $0.75 < t < 0.9$. If the value drops below 0.75 the compound has been seen to adopt an hexagonal ilmenite structure (e.g. $FeTiO_3$ [39]).

1.4.2 Main symmetries inside the pyrochlore lattice

Figure 1.7 shows that the pyrochlore lattice has a high degree of symmetry. It is possible to choose the origin of the system coinciding with the centre of a rare earth tetrahedron, in order to write the position of the magnetic ions easily. In this case the origin corresponds to the crystallographic O(1) site, whose symmetry is the same as an FCC lattice. Figure 1.9 shows the main symmetry sites of the pyrochlore lattice that can be used in calculations and simulations.

As one can see O(1) sites (green spheres) create a network identical to an FCC cubic lattice, since they are located on the vertices and at the centre of the faces of the cube. However there is another high symmetric site in the unit cell, which corresponds to the centre of the Ti tetrahedra (yellow spheres). These positions create another FCC lattice, that is interconnected with the previous one. Moreover these sites are "special" because they identify the centres of the super tetrahedra of the rare earth, that can be created uniting 4 rare earth tetrahedra (see Fig. 1.9 orange pyramid). These positions are at the same time equidistant from the spins and the furthest away from them, moreover they play an important role in the analysis of the internal fields of spin ice crystals (see Sec. 4.1).

Notice that these symmetries are a consequence of the fact that both Dy and Ti ions are arranged on two co-penetrating pyrochlore structures (see Fig. 1.7). For practical reasons we will show the results of our MC calculations only in one quarter of the pyrochlore unit cell, therefore we highlighted the main symmetry sites inside it in the right panel of Fig. 1.9 (see cyan prism).

Finally, it is common to express the length of the unit cell using the average distance between two nearest neighbour spins (r_{nn}), in this way $a = 2\sqrt{2}r_{nn} \approx 10.1$ Å.

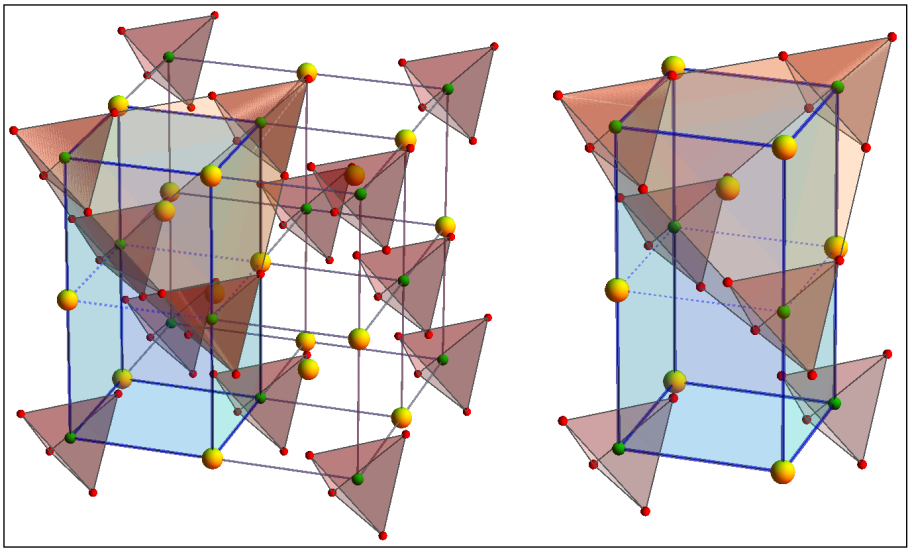

Figure 1.9: *Symmetry sites inside the pyrochlore unit cell.* – O(1) sites (green spheres) and the centres of Ti tetrahedra (yellow spheres) create a network of two interconnected FCC lattices. The latter site is also the centre of the rare earth super tetrahedra (orange pyramid), a position that is at the same time equidistant from the spins and the furthest away from them. We highlighted the main symmetry sites in one quarter of the unit cell of the pyrochlore lattice (cyan prism) in the right panel.

Chapter 2

Theory of magnetism in spin ice

Contents

Another interesting aspect of spin ice crystals, is the fact that the rare earth ions are carrying the strongest magnetic moment one can find in nature. This is of the order of $\approx 10\mu_B$ per ion and, due to the Crystal Electric Field (CEF), they behave like Ising spins.

This chapter is dedicated to the revision of the main theories of magnetism (in classical and quantum mechanics), and on the analysis of the CEF environment of Dy^{3+} and Ho^{3+} from first principles.

2.1 The Crystal Electric Field

As we said in the previous sections the Crystal Electric Field (CEF) plays an important role in spin ice crystals, since it gives rise to the frustration. However its calculation is rather non trivial.

Generally speaking the CEF calculation is used in Condensed Matter Physics and Chemistry to study complex many body systems. This technique requires a detailed knowledge of three tools: point groups, tesseral harmonics and quantum mechanical angular momentum operators. The formalism developed in this chapter is entirely taken from the work done by M. T. Hutchings (Ref. [40]).

2.1.1 The Point Charge Model (PCM)

The first step in the CEF calculation is to find the correct positions of the ions inside the lattice using, for example, X-ray or neutron scattering techniques. From the positions of the ions one obtains the space group of the crystal, and all the relevant bond distances between the magnetic ion and its closest neighbours.

Since the Coulomb potential has spherical symmetry, the second step is to write the Hamiltonian using a linear combination of tesseral harmonics. The coefficients in front of the expansion can be calculated from first principles and then they can be tuned in order to best fit the experimental data.

Notice that as an approximation we assume a Point Charge Model (PCM), i.e. we do not consider the overlap between the orbitals of the atoms. This approach tends to work well for rare earth compounds with localised moments, but is more problematic for transition metals (see Ref. [41] for details).

Once the Hamiltonian is written, we have to transform the linear combination of tesseral harmonics into Stevens Operators. These operators contain all the information regarding the angular momentum of the atoms thus, with an appropriate choice of the basis, our Hamiltonian becomes a linear combination of L^2, S^2, J^2, J_z (suitable for 4f shells) or L_z, S_z, S^2, L^2 (for atoms with 3d shells).

Finally, diagonalising the above Hamiltonian, one can find all the eigenvalues and eigenvectors of the system. Notice that, in principle, the ground state of a system could be degenerate (if there is no external field applied), and this is related to both the particular symmetry of the lattice and to the value of the total angular momentum J (see 2.1.4).

2.1.2 The Crystal Field Spin Ice Hamiltonian

We focus our attention on the scalenohedron, surrounding the rare earth ion. The origin of our reference system is chosen on a Dy (Ho) ion with the $\hat{z}$ axis along the O(1)-O(1) bond (that is the highest symmetry rotational axis) and the $\hat{y}$ axis along one of the C_2 axes of the system. The above convention is called Prather's convention and it ensures to have the minimum number of CEF parameters in the expansion.

Using spherical coordinates we can calculate the position of the eight oxygen ions in the scalenohedron as follows:

$$
\begin{aligned}
r &= \sqrt{x^2 + y^2 + z^2} \\
\theta &= \arccos\left(\frac{z}{r}\right) \\
\phi &= \arcsin\left(\frac{y}{\sqrt{x^2 + y^2}}\right)
\end{aligned}
\tag{2.1}
$$

On the basis of a simple PCM, the determination of the perturbing Hamiltonian is primarily the evaluation of the electrostatic potential of the magnetic ion

$V(r,\theta,\phi)$, due to the surrounding point charges. Following Ref. [40] we have:

$$V(r,\theta,\phi) = \frac{1}{4\pi\epsilon_0}\sum_j \frac{q_j}{|R_j - r|} \tag{2.2}$$

where q_j is the charge at the jth neighbouring ion, at distance R_j from the origin.

If the magnetic ion has charge q_i, then the perturbing crystalline potential energy U will be:

$$U = \sum_i q_i V_i = \frac{1}{4\pi\epsilon_0}\sum_i\sum_j \frac{q_i q_j}{|R_j - r_i|} \tag{2.3}$$

We are normally concerned with the summation over the electrons in unfilled shells, since the CEF affects closed shells only in a high order of perturbation. This is also true for ions in an s state, and throughout this discussion we shall omit such ions.

The first method to calculate the crystalline potential U has been discussed by Griffith [42] and Prather [43] and it is based on the spherical harmonics addition theorem. In this case the potential can be re-written as:

$$V(r,\theta,\phi) = \frac{1}{4\pi\epsilon_0}\sum_j \frac{q_j}{|R_j - r|} = \frac{1}{4\pi\epsilon_0}\sum_j q_j \sum_n \frac{r^n}{R_j^{(n+1)}}\frac{4\pi}{2n+1} \sum_{m=-n}^{n} (-1)^m Y_n^{-m}(\theta_j,\phi_j) Y_n^m(\theta,\phi) \tag{2.4}$$

Therefore

$$V(r,\theta,\phi) = \frac{1}{4\pi\epsilon_0}\sum_n \sum_{m=-n}^{n} r^n \gamma'_{nm} Y_n^m(\theta,\phi) \tag{2.5}$$

where for k charges

$$\gamma'_{nm} = \sum_{j=1}^{k} \frac{q_j}{R_j^{(n+1)}}\frac{4\pi}{2n+1}(-1)^m Y_n^{-m}(\theta_j,\phi_j) \tag{2.6}$$

Here q_j is the charge of the ligand (i.e. of the anions), R_j is the position of the ligand and $Y_n^{\pm m}(\theta_j,\phi_j)$ is the spherical harmonic.

The second method is very useful if we want to write the Hamiltonian using Stevens Operators, in this case the potential is expanded as:

$$V(x,y,z) = \frac{q_j}{4\pi\epsilon_0}\sum_{n=0}^{\infty}\frac{r^n}{R_j^{(n+1)}}\left[\sum_m \frac{4\pi}{(2n+1)} Z_{nm}(x_j,y_j,z_j) Z_{nm}(x,y,z)\right] \tag{2.7}$$

Therefore:

$$V(x,y,z) = \frac{1}{4\pi\epsilon_0}\sum_n^{\infty}\sum_m r^n \gamma_{nm} Z_{nm}(x,y,z) \tag{2.8}$$

where for k charges

$$\gamma_{nm} = \sum_{j=1}^{k} \frac{q_j}{R_j^{(n+1)}} \frac{4\pi}{2n+1} Z_{nm}(x_j, y_j, z_j) \tag{2.9}$$

Here q_j is again the charge of the ligand, R_j is the position of the ligand and $Z_{nm}(x_j, y_j, z_j)$ is the tesseral harmonic.

As one can see there is a clear correspondence between the two methods. In fact by definition:

$$Z_{n0} = Y_n^0 \tag{2.10}$$

$$Z_{nm}^c = \frac{1}{\sqrt{2}}[Y_n^{-m} + (-1)^m Y_n^m] \tag{2.11}$$

$$Z_{nm}^s = \frac{\imath}{\sqrt{2}}[Y_n^{-m} - (-1)^m Y_n^m] \tag{2.12}$$

The superscripts c and s stand for cosine and sine, and they represent the real and imaginary part of the spherical harmonics.

Notice that the coefficients of the expansion can be real or imaginary if one uses spherical harmonics, but they are always real using tesseral harmonics. It is also important to write the Hamiltonian in such a way that it commutes with the parity operator Π; this condition follows from the property of the angular momentum since $[J, \Pi] = 0$. Therefore one has to consider only the terms in cosine in the expansion of the tesseral harmonics.

For some systems, with a very low space group symmetry, this could be impossible since the number of parameters in the expansion could not approximate the potential in the correct way. In this case we have to use also the term in sine, and it is highly recommended to use only the second method to calculate U.

Equation 2.9 gives the coefficients of the linear combination of the tesseral harmonics. Notice that for every space group only a few terms in the expansion are non zero (see Ref. [44]), and these terms coincide with the number of Stevens Operators we have to use in order to write the Hamiltonian. Many books report the correct form of the Hamiltonian for every single space group, thus at the end of the calculation one can always double check if the number of the terms is correct. Of course another cross check is to use the spherical harmonics expansion; the result must contain exactly the same number of terms. In our calculations we checked that the two methods agreed.

The symmetry point group of the scalenohedron is D_{3d}, therefore only the terms Z_{20}, Z_{40}, Z_{43}, Z_{60}, Z_{63} and Z_{66} are required to write the Hamiltonian.

Finally we can use the so called Stevens' Operators Equivalence Method to evaluate the matrix elements of the crystalline potential specified by one particular value of the total angular momentum J. This method states that if $f(x, y, z)$ is a Cartesian function of given degree, then to find the operator equivalent to such a term one replaces x, y, z with J_x, J_y, J_z respectively, always remembering the commutation rules of the quantum operators. This is done by replacing products

of x, y, z by an expression consisting of all the possible different combinations of J_x, J_y, J_z, divided by the total number of combinations. Notice that although it is conventional to use J or L in the equivalent operator method, when evaluating the matrix elements all factors of $\hbar$ are dropped.

Since we are studying the ground state of a rare earth system, S^2, L^2, J^2, J_z are good quantum numbers and the Crystal Field Hamiltonian can now be written as:

$$H_{CEF} = const. \sum_{nm} \left[\frac{e^2}{4\pi\epsilon_0} \gamma_{nm} \langle r^n \rangle \theta_n \right] O_n^m = \sum_{nm} \underbrace{[A_n^m \langle r^n \rangle \theta_n]}_{B_{nm}} O_n^m = \sum_{nm} B_{nm} O_n^m \tag{2.13}$$

where γ_{nm} is the same factor as in Eq. 2.9, e is the electron charge, ϵ_0 is the vacuum permittivity, $\langle r^n \rangle$ is the expectation value of the radial part of the wave function, θ_n is a numerical factor that depends on the rare earth ion, $const.$ is also a numerical factor to normalise the tesseral harmonics (it is the coefficient in front of the tesseral harmonics) and O_n^m are Stevens Operators.

The terms $A_n^m \langle r^n \rangle$ are commonly called CEF parameters, and they are difficult to calculate from first principles for two reasons:

1. We do not know the exact expression of the radial part of the wave function.
2. We have to keep in mind that this is a PCM, so the approximation needs to be revised in order to take care of the overlap between the orbitals.

We can finally write the Crystal Field Spin Ice Hamiltonian in this way:

$$H_{CEF} = B_{20}O_2^0 + B_{40}O_4^0 + B_{43}O_4^3 + B_{60}O_6^0 + B_{63}O_6^3 + B_{66}O_6^6 \tag{2.14}$$

2.1.3 Crystal Field parameters from first principles

We present here a general method for the calculation of the CEF parameters for every type of lattice.

In Eq. 2.13, θ_n are called the Stevens factors and they depend on the particular ion we want to study. In the Stevens method they are denoted as $\theta_2 = \alpha_J, \theta_4 = \beta_J$, $\theta_6 = \gamma_J$ and they can be calculated according to the following formula:

$$\theta_n = 2^n (2l+1)(2J+1) \sqrt{\frac{(2J-n)!}{(2J+n+1)!}} (-1)^{S+L+J+1} \underbrace{\begin{pmatrix} l & n & l \\ 0 & 0 & 0 \end{pmatrix}}_{3-j} \underbrace{\begin{pmatrix} J & n & J \\ L & S & L \end{pmatrix}}_{6-j} \tag{2.15}$$

where we used the $3-$j and $6-$j symbols.

As one can see these coefficients depend on the ion of interest through J, L, S, l and n; moreover only some terms are non zero due to the properties of the $3-$j and $6-$j symbols. In particular only the terms with even n survive in the calculation, while all the odd terms are perfectly zero.

The expectation value of r^n can be computed using an approximate hydrogenous radial wave function:

$$R_{nl}(r) = N\sqrt{\left(\frac{2Z}{a_0 n}\right)^3 \frac{(n-l-1)!}{2n((n+l)!)^3}} e^{Zr/a_0 n} \left(\frac{2Zr}{na_0}\right)^l L_{n-l-1}^{2l+1}\left(\frac{2Zr}{a_0 n}\right) \quad (2.16)$$

where N is the normalising coefficient, a_0 is the Bohr radius, Z is the charge of the ion and L_n^l is the Laguerre Polynomial.

The expectation values are then:

$$\langle r^n \rangle = \int_0^\infty |R_{nl}(r)|^2 r^{2+n} dr \quad (2.17)$$

Since we do not know the exact form of the radial wave function, the previous formula is only an approximation, but it gives very good results for $\langle r^2 \rangle$ and $\langle r^4 \rangle$ within a 12% of error from the values tabulated in many papers using Hartree-Fock or Dirac-Fock method. The expectation value of $\langle r^6 \rangle$ is very difficult to find with Eq. 2.16, because it depends strongly on relativistic correction. For this reason we suggest to use the values tabulated in the papers or to calculate this coefficient using an expansion of the wave function as in Ref. [45]. In this second case the radial part of the wave function for the Dy atom is:

$$P_{4f}(r) = \sum_{i=1}^{4} C_i r^4 e^{-Z_i r} =$$
$$2480.4 r^4 e^{-13.46r} + 448.84 r^4 e^{-7.53r} + 55.97 r^4 e^{-5.02r} + 2.35 r^4 e^{-2.76r} \quad (2.18)$$

Now using Eq. 2.17 we can find the expectation value of $\langle r^6 \rangle$ with an error of 20% respect to the tabulated values.

2.1.4 Kramers' Theorem

We present here the mathematical formalism to prove Kramers' theorem taken from Ref. [46]. This theorem is of fundamental importance in order to study systems with J half integer (e.g. $Dy_2Ti_2O_7$), since it has non trivial consequences on the spectrum of the system and on its magnetic properties. Those phenomena are closely related to the time reversal operator.

The existence of the degeneracy in the energy states of a quantum system, when this degeneracy is not an accidental consequence of the numerical values of its parameters, is closely related to the symmetries of the system under some operator A. In this case $[H, A] = 0$, and they can be diagonalised simultaneously.

Now if we assume that H is the Hamiltonian of a generic system, A the symmetry operator and ψ an eigenfunction of H corresponding to an energy E, then from the Schrödinger equation we have:

$$H\psi = E\psi \quad \Rightarrow \quad AH\psi = (AHA^{-1})A\psi = E(A\psi) \tag{2.19}$$

where we have inserted the factor $A^{-1}A$ equal to the unity operator. Now if H is invariant under A, that is if $AHA^{-1} = H$ and $AH = HA$, it follows from the previous equation that $A\psi$ is an eigenfunction of H corresponding to the energy E.

Nevertheless this argument does not prove that the invariance of the Hamiltonian under the operation A necessarily implies degeneracy of the energy levels, because it is possible that $A\psi$ is a function not essentially different from ψ, that is $A\psi$ may be a constant multiple of ψ. Thus only if ψ and $A\psi$ are linearly independent, it follows that E is degenerate.

Kramers' theorem, which says that the energy states of a system with an odd number of electrons are at least doubly degenerate, is an assertion of the existence of degeneracy under rather general conditions and one can expect a correlated symmetry property. Wigner has shown that this corresponding symmetry property is the invariance under time reversal (see Ref. [47]). In the absence of velocity dependent interactions and, in particular, in the absence of magnetic fields, a general Hamiltonian $H(q, p)$ is equal to $H(q, -p)$. Therefore we can say that it is invariant under time reversal. If we want to prove this theorem we have to find an operator K which has the following property:

$$KH(\mathbf{r}, \mathbf{p}, \mathbf{s})K^{-1} = H(\mathbf{r}, -\mathbf{p}, -\mathbf{s}) = H'$$

$$KH\psi = (KHK^{-1})K\psi = H'(K\psi) = E(K\psi) \quad \Rightarrow \quad \psi' = K\psi \tag{2.20}$$

For example if we assume that the Hamiltonian H is purely subjected to electric fields, it will be invariant under the time reversal operator.

Lets consider the one electron case. The operator K can be written as $K = \imath\sigma_y C$, where σ_y is one of the Pauli matrix and C is defined by the relation $C\phi(r) = \phi^*(r)$ (basically C replaces a function by its complex conjugate and $C^{-1} = C$). In order to prove that this operator has the desired property of Eq. 2.20 we can notice that:

$$CHC^{-1} = H^* \quad \text{and} \quad (CHC^{-1})\phi = (CH)\phi^* = (H^*)\phi \tag{2.21}$$

Now a general Hamiltonian can always be written using Pauli matrices in this way:

$$H(\mathbf{r}, \mathbf{p}, \mathbf{s}) = H_0(\mathbf{r}, \mathbf{p})\mathbb{I} + H_x(\mathbf{r}, \mathbf{p})\sigma_x + H_y(\mathbf{r}, \mathbf{p})\sigma_y + H_z(\mathbf{r}, \mathbf{p})\sigma_z \tag{2.22}$$

Therefore

$$CHC^{-1} = H_0(\mathbf{r}, -\mathbf{p})\mathbb{I} + H_x(\mathbf{r}, -\mathbf{p})\sigma_x - H_y(\mathbf{r}, -\mathbf{p})\sigma_y + H_z(\mathbf{r}, -\mathbf{p})\sigma_z$$

$$(\imath\sigma_y)CHC^{-1}(\imath\sigma_y)^{-1} = H_0(\mathbf{r},-\mathbf{p})\mathbb{I} - H_x(\mathbf{r},-\mathbf{p})\sigma_x - H_y(\mathbf{r},-\mathbf{p})\sigma_y \\ -H_z(\mathbf{r},-\mathbf{p})\sigma_z = H(\mathbf{r},-\mathbf{p},-\mathbf{s}) = H' \quad (2.23)$$

As we can see the operator K satisfies the required condition and if we now turn to the n electron system, where $K = \imath^n\sigma_{y1}.....\sigma_{yn}C$, we can see that each factor σ_{yj} reverses the sign of the corresponding σ_{xj} and σ_{zj} in the Hamiltonian.

Finally to complete the proof of Kramers' theorem we must show that ψ and ψ' are linearly independent for odd electron systems. We notice that:

$$K^2 = \imath^{2n}\mathbb{I} = (-1)^n\mathbb{I} \quad (2.24)$$

For even electron systems K^2 is the unity operator, for odd electron systems it is the negative of the unit operator. Now if we assume that ψ' and ψ are linearly dependent:

$$\psi' = K\psi = a\psi \quad (2.25)$$

where a is a complex number. Therefore

$$K^2\psi = K\psi' = Ka\psi = a^*K\psi = |a|^2\psi \quad \Rightarrow \quad |a|^2 = (-1)^n \quad (2.26)$$

This can be true only if n is even. Hence for odd n, ψ' and ψ are necessarily linearly independent and the energy states are degenerate.

Another important theorem closely related to Kramers' theorem, that has significant consequences in the theory of paramagnetic susceptibilities is the following: "The expectation value of the magnetic moment is zero in any non degenerate state".

In general the paramagnetic susceptibility of a system as given by the Langevin Debye formula is the sum of two terms: the first one is proportional to the sum of the squares of the diagonal matrix elements (expectation values in pure states) of the magnetic moment operator (J_x, J_y, J_z) and it varies with temperature as T^{-1}, the second term is essentially independent of the temperature but it depends on the non diagonal terms of the magnetic moment operator. Thus at low temperatures for a system with even electrons (like Ho), the paramagnetic susceptibility will approach a constant proportional to the second term mentioned above while for an odd electron system the susceptibility will be inversely proportional to the temperature as it goes to zero.

2.2 Analysis of the Crystal Field of $Dy_2Ti_2O_7$ and $Ho_2Ti_2O_7$

Now we show a qualitative analysis of the CEF of $Dy_2Ti_2O_7$ and $Ho_2Ti_2O_7$ based on the theory developed in the previous sections and assuming a PCM. We first analyse the scalenohedron of the pyrochlore lattice assuming a value of the parameter x that has been obtained refining the X-ray and neutron scattering data. Then we will try to make predictions on the CEF spectrum tuning the value of x in such a

way that the O(2) can move simultaneously towards the fixed O(1) ions, following the directions of the three crystallographic axes. This idea is shown in Fig. 2.1, green arrows indicate the directions of the O(2) displacements.

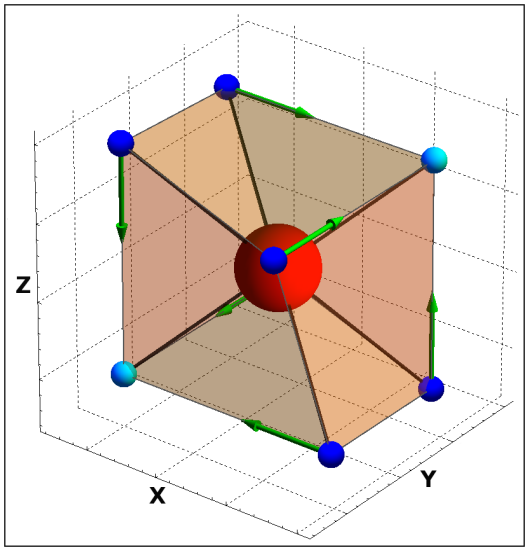

Figure 2.1: *Directions of the displacements of the O(2) ions.* – We can imagine to distort the environment surrounding the rare earth by moving the O(2) (blue spheres) parallel to the three crystallographic directions (green arrows). In this way we can change the 8-fold coordination polyhedron from a scalenohedron to a perfect cube.

As we said in Sec. 1.4.2, the symmetry space group of the pyrochlore lattice is D_{3d}. Therefore, following Prather's convention, we rotated the reference system of the scalenohedron in order to have the highest degree rotational axis C_3 along $\hat{z}$ and one of the three C_2 axes along $\hat{y}$. Notice that the C_3 axis coincides with the $[111]$ direction as shown in Fig. 2.2.

As one can see the two O(1) are now located along $\hat{z}$ while the six O(2) live in two planes perpendicular to the easy axis. In principle one can also choose another convention for the reference system, in this case he will end up with a higher number of CEF parameters in the Hamiltonian but with exactly the same eigenvalues, since they are independent from the choice of the bases. In our calculation we checked that those two methods agreed perfectly and we show the spectrum of $Dy_2Ti_2O_7$ and $Ho_2Ti_2O_7$ in Tab. 2.1.

The ground state of Dy^{3+} is a Kramers' doublet as one must expect since $J = 15/2$. In this case the hexagonal symmetry of the D_{3d} group gives a total of 8 doublets for Dy^{3+} and a mixture of 5 singlets and 6 doublets for Ho^{3+}. This division is in perfect agreement with the scheme proposed in Ref. [44], however the PCM is not able to capture the correct sequence of high energy levels of the Ho^{3+}. In fact comparison with the experimental data of Ref. [48] shows that the

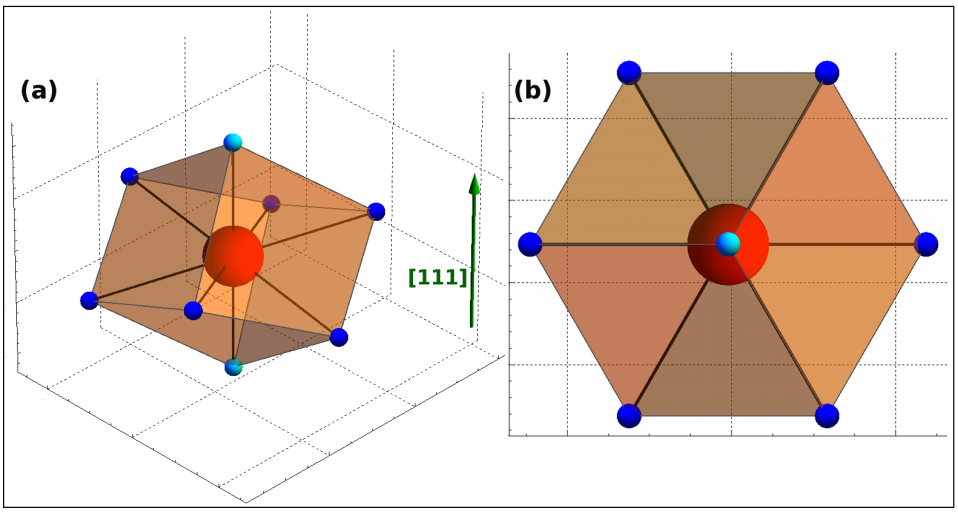

Figure 2.2: *Prather's convention for the D_{3d} symmetry system.* – **(a)** The highest degree rotational axis C_3, which coincides with the $[111]$ direction, has been rotated along $\hat{z}$ and one of the three C_2 axes along $\hat{y}$. This choice guarantees to have the lowest number of CEF parameters in the Hamiltonian. **(b)** Top view of the scalenohedron showing the positions of the O(2) ions arranged in a regular hexagon. Notice that the prospective is misleading, since the O(2) are not located in the same plane but they are alternating in two different planes perpendicular to the easy axis.

seventh and the eighth excited state should be a singlet and a doublet respectively. This discrepancy is mainly due to the B_6^n coefficients of the expansion, since the expectation value of r^6 is very difficult to calculate from first principles.

Notice that there is a huge gap between the ground state and the first excited state in both the systems, this characteristic is in perfect agreement with the experimental evidence of Ref. [48].

We can now imagine to distort the scalenohedron in order to obtain a perfect cube with all the oxygen ions at the same distance from the rare earth ion. According to Tab. 1.1 this is possible only if $x = 0.375$, and in this case the point group of the system changes from D_{3d} to O_h which is centro-symmetric. This ideal environment, shown in Fig. 2.3, has a higher degree of symmetry. Therefore the number of CEF parameters in the Hamiltonian is now reduced to only five terms:

$$H_{CEF} = B_{40}O_4^0 + B_{43}O_4^3 + B_{60}O_6^0 + B_{63}O_6^3 + B_{66}O_6^6 \tag{2.27}$$

This Hamiltonian does not respect Prather's convention, in fact we left the C_3 axis ($[111]$ direction) along $\hat{z}$ and not the C_4 of the cube. This choice is motivated by the fact that we want an exact comparison with the common scalenohedron environment, therefore it is very useful to check what happens to the easy axis when the environment gets distorted.

Dy^{3+} **Level**	**Energy (meV)**	Ho^{3+} **Level**	**Energy (meV)**
GS	$0.0 \quad (d)$	GS	$0.0 \quad (d)$
1	$43.177 \quad (d)$	1	$30.239 \quad (s)$
2	$58.00 \quad (d)$	2	$30.701 \quad (d)$
3	$62.896 \quad (d)$	3	$32.372 \quad (d)$
4	$65.431 \quad (d)$	4	$33.142 \quad (s)$
5	$80.942 \quad (d)$	5	$40.159 \quad (d)$
6	$85.264 \quad (d)$	6	$46.045 \quad (s)$
7	$86.106 \quad (d)$	7	$48.129 \quad (d)$
		8	$51.084 \quad (s)$
		9	$51.139 \quad (d)$
		10	$52.182 \quad (s)$

Table 2.1: *Crystal Field levels calculated for the scalenohedron environment.*

Table 2.2 shows the spectrum of the ideal cubic system for $Dy_2Ti_2O_7$ and $Ho_2Ti_2O_7$ crystals.

Dy^{3+} **Level**	**Energy (meV)**	Ho^{3+} **Level**	**Energy (meV)**
GS	$0.0 \quad (q)$	GS	$0.0 \quad (t)$
1	$13.392 \quad (q)$	1	$1.139 \quad (d)$
2	$14.273 \quad (d)$	2	$3.872 \quad (t)$
3	$59.768 \quad (d)$	3	$38.053 \quad (t)$
4	$61.851 \quad (q)$	4	$41.512 \quad (d)$
		5	$44.756 \quad (t)$
		6	$48.673 \quad (s)$

Table 2.2: *Crystal Field levels calculated for the ideal cubic environment.*

Within this environment the ground state of Dy^{3+} collapses to a quartet, while the one of Ho^{3+} is a triplet. Those results are due to the symmetry of the environment and they are in perfect agreement with Ref. [44]. The energy of the levels is lower compared to the previous case but a huge gap is still present between the second and the third excited state.

Finally we would like to study the magnetism of these two environments and, for the sake of illustration, we applied an external field $B = 1$ tesla along $\hat{z}$ (i.e. along the easy axis). In this case we can write the Hamiltonian of the system as follows:

$$H = H_{CEF} - g_J \mu_B \vec{J} \cdot \vec{B}(r, \theta, \phi) \tag{2.28}$$

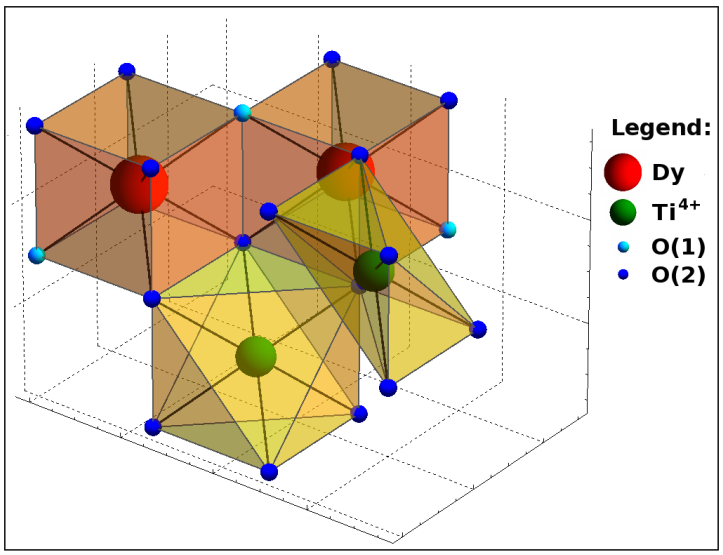

Figure 2.3: *Ideal cubic environment in the pyrochlore lattice.* – According to Tab. 1.1 when $x = 0.375$, the rare earth is at the centre of a perfect cube with all oxygen ions at the same distance. In this case the symmetry of the point group changes from D_{3d} to O_h which is centro-symmetric, and it has a higher symmetry.

The external field is able to lift the degeneracy of the ground state (Zeeman effect); Tabs. 2.3, 2.4 show the new spectrum of the system for the common scalenohedron and for the ideal cubic environment respectively.

As we can see the degeneracy of the levels is completely lifted, and if we calculate the mean value of the magnetisation on the ground state ($\langle 0|M|0\rangle$) we obtain that $M_{Dy} = 9.977\mu_B$ and $M_{Ho} = 9.996\mu_B$, in excellent agreement with the theoretical values.

The Zeeman effect removes the degeneracy even in the ideal cubic environment however, if we calculate $\langle 0|M|0\rangle$, we obtain that $M_{Dy} = 7.074\mu_B$ and $M_{Ho} = 6.527\mu_B$. Therefore we can conclude that the magnetisation of the sample is greatly affected by the environment surrounding the magnetic ion and, in order to fully understand this statement, we can analyse the behaviour of the magnetisation in these two systems calculating the expectation values of $\langle 0|M_x|0\rangle$, $\langle 0|M_y|0\rangle$ and $\langle 0|M_z|0\rangle$ for different directions of B. Figure 2.4 shows the shape of the anisotropy of the magnetisation calculated within the scalenohedron (a) or the ideal cubic environment (b).

Many values of the magnetisation are shown simultaneously for applied fields uniformly distributed on the unit sphere. The results suggest that the magnetisation in the scalenohedron environment has an Ising $[111]$ anisotropy (as we must expect), since the spheres are always located along $\hat{z}$. The highest strength of the magnetic moment is $\approx 10\mu_B$ for both Dy and Ho in perfect agreement with the theory. By contrast, the ideal cubic set up shows that the magnetisation has

Dy^{3+} **Level**	**Energy (meV)**	Ho^{3+} **Level**	**Energy (meV)**
GS	$0.0 \quad (s)$	GS	$0.0 \quad (s)$
1	$1.155 \quad (s)$	1	$1.157 \quad (s)$
2	$43.263 \quad (s)$	2	$30.810 \quad (s)$
3	$44.246 \quad (s)$	3	$31.175 \quad (s)$
4	$58.538 \quad (s)$	4	$31.362 \quad (s)$
5	$58.62 \quad (s)$	5	$32.882 \quad (s)$
6	$63.342 \quad (s)$	6	$33.034 \quad (s)$
7	$63.603 \quad (s)$	7	$33.724 \quad (s)$
8	$65.691 \quad (s)$	8	$40.277 \quad (s)$
9	$66.324 \quad (s)$	9	$41.199 \quad (s)$
10	$81.278 \quad (s)$	10	$46.624 \quad (s)$
11	$81.751 \quad (s)$	11	$48.516 \quad (s)$
12	$85.634 \quad (s)$	12	$48.899 \quad (s)$
13	$86.061 \quad (s)$	13	$51.411 \quad (s)$
14	$86.358 \quad (s)$	14	$51.533 \quad (s)$
15	$87.009 \quad (s)$	15	$52.028 \quad (s)$
		16	$52.892 \quad (s)$

Table 2.3: *Crystal Field levels calculated for the scalenohedron environment with an external field of* 1 *tesla applied along* $\hat{z}$.

a Heisenberg behaviour with a calculated average strength of $\approx 7\mu_B$ for Dy and $\approx 6.5\mu_B$ for Ho.

Once again we must note that the symmetry of the environment is of fundamental importance for the physical properties of the system. Even with these naive PCM calculations we were able to show that different structures around the magnetic ion change completely the energy levels, and the nature of the compounds in a non trivial way. This can have dramatic consequences in the experiments, as we will see in the next chapters.

2.3 Classic and quantum mechanics theories on magnetism

In this section we derive and analyse the differences in the classical Langevin equation for the Ising, Heisenberg, soft spin and easy plane model. Then we compare these results with the Brillouin function that describes the magnetism in quantum mechanics. Figure 2.5 shows the reference system we chose to develop our calculations.

Dy^{3+} **Level**	**Energy (meV)**	Ho^{3+} **Level**	**Energy (meV)**
GS	$0.0 \quad (s)$	GS	$0.0 \quad (s)$
1	$0.299 \quad (s)$	1	$0.329 \quad (s)$
2	$0.508 \quad (s)$	2	$0.556 \quad (s)$
3	$0.807 \quad (s)$	3	$1.505 \quad (s)$
4	$13.513 \quad (s)$	4	$1.529 \quad (s)$
5	$13.629 \quad (s)$	5	$3.941 \quad (s)$
6	$13.844 \quad (s)$	6	$4.219 \quad (s)$
7	$14.090 \quad (s)$	7	$4.518 \quad (s)$
8	$14.547 \quad (s)$	8	$38.059 \quad (s)$
9	$14.941 \quad (s)$	9	$38.388 \quad (s)$
10	$59.952 \quad (s)$	10	$38.710 \quad (s)$
11	$60.325 \quad (s)$	11	$41.8306 \quad (s)$
12	$61.920 \quad (s)$	12	$41.8309 \quad (s)$
13	$62.107 \quad (s)$	13	$45.068 \quad (s)$
14	$62.479 \quad (s)$	14	$45.086 \quad (s)$
15	$62.595 \quad (s)$	15	$45.159 \quad (s)$
		16	$49.043 \quad (s)$

Table 2.4: *Crystal Field levels calculated for the ideal cubic environment with an external field of* 1 *tesla applied along* $\hat{z}$.

2.3.1 Langevin theory for the Ising model

We start with the calculation of the Langevin equation for a system with an Ising axis. We can imagine to have a system as depicted in Fig. 2.5, where we put an external field along $\hat{z}$ and we suppose that the system has an easy axis. In this case a general magnetic moment can be written as $\vec{\mu} = \sigma\mu\hat{e}_\mu$, where σ is a discrete variable that can take only the values ± 1, and the external field is $\vec{H} = H\hat{z}$. Following Langevin's approach, the energy of this system and the magnetisation along $\hat{z}$ can be calculated as:

$$E = -\vec{\mu} \cdot \vec{H} = -\sigma\mu H(\hat{e}_\mu \cdot \hat{z}) \tag{2.29}$$

$$M_z = \frac{N}{V}\mu\langle\sigma\rangle(\hat{e}_\mu \cdot \hat{z}) \tag{2.30}$$

where N is the number of the spins in the system and V is the volume.

The thermodynamic average $\langle\sigma\rangle$ is given by:

$$\begin{aligned}\langle\sigma\rangle = \frac{\sum_{\sigma=\pm1} \sigma \mathrm{e}^{\beta\sigma\mu\mathrm{H}(\hat{\mathrm{e}}_\mu\cdot\hat{\mathrm{z}})}}{\sum_{\sigma=\pm1} \mathrm{e}^{\beta\sigma\mu\mathrm{H}(\hat{\mathrm{e}}_\mu\cdot\hat{\mathrm{z}})}} &= \frac{\mathrm{e}^{\beta\mu\mathrm{H}(\hat{\mathrm{e}}_\mu\cdot\hat{\mathrm{z}})} - \mathrm{e}^{-\beta\mu\mathrm{H}(\hat{\mathrm{e}}_\mu\cdot\hat{\mathrm{z}})}}{\mathrm{e}^{-\beta\mu\mathrm{H}(\hat{\mathrm{e}}_\mu\cdot\hat{\mathrm{z}})} + \mathrm{e}^{\beta\mu\mathrm{H}(\hat{\mathrm{e}}_\mu\cdot\hat{\mathrm{z}})}} \\ &= \tanh[\beta\mu H(\hat{e}_\mu \cdot \hat{z})]\end{aligned} \tag{2.31}$$

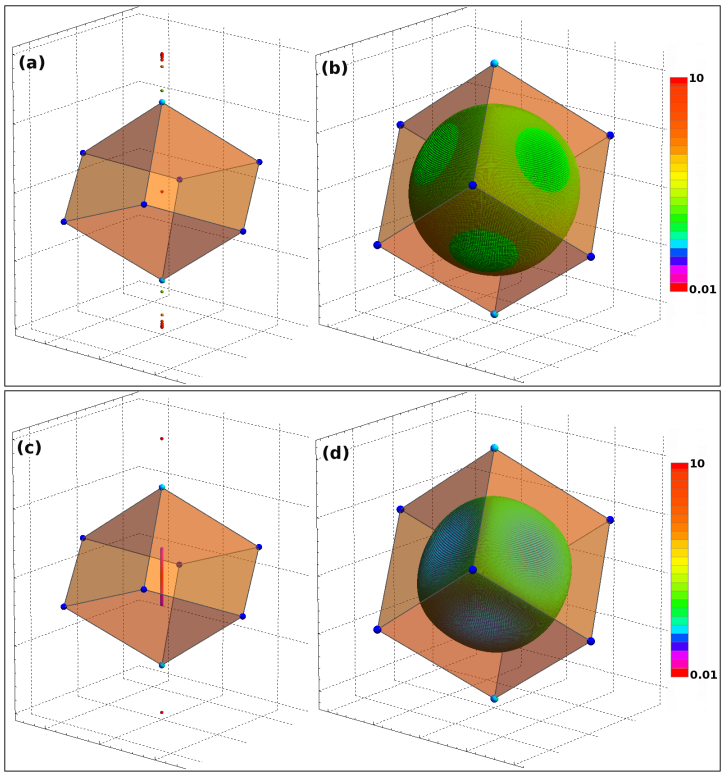

Figure 2.4: *The shape of the anisotropy of the magnetisation for* Dy^{3+} *(top) and* Ho^{3+} *(bottom).* – Many values of the magnetisation are shown simultaneously for applied fields uniformly distributed on the unit sphere. **(a),(c)** Within the scalenohedron environment the magnetisation has a clear Ising anisotropy along the $[111]$ direction, the highest strength is $\approx 10\mu_B$. **(b),(d)** The spherical shape suggests a Heisenberg behaviour of the magnetisation in the ideal cubic set up with a calculated moment of $\approx 7\mu_B$ for Dy and $\approx 6.5\mu_B$ for Ho (see Sec. 2.2). The colour bar indicates the magnitude of the magnetic moment in units of Bohr magnetons.

where $\beta = 1/(k_B T)$.

Finally the Langevin equation for an Ising spin system is:

$$M_z = \frac{N}{V}\mu(\hat{e}_\mu \cdot \hat{z}) \tanh[\beta\mu H(\hat{e}_\mu \cdot \hat{z})] \tag{2.32}$$

Within a single tetrahedron of the pyrochlore lattice, the magnetic moments of the four spins can be written as (see Fig. 2.5):

$$\vec{\mu}_1 = \mu\hat{e}_1 = \frac{\mu}{\sqrt{3}}\begin{pmatrix} 1 \\ 1 \\ 1 \end{pmatrix} \quad \vec{\mu}_2 = \mu\hat{e}_2 = \frac{\mu}{\sqrt{3}}\begin{pmatrix} 1 \\ -1 \\ -1 \end{pmatrix}$$

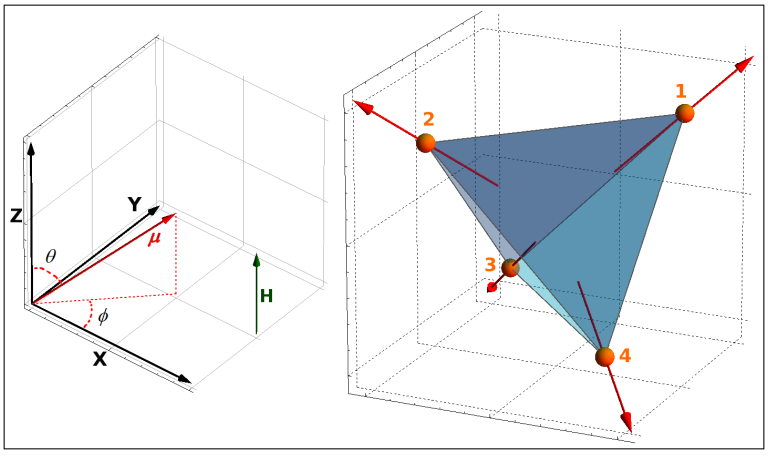

Figure 2.5: *Reference system used to derive the Langevin paramagnetic equations.* – Due to the spherical symmetry of the problem, we used spherical coordinate to describe the direction of the magnetic moments of the spins. The external field $\vec{H}$ will be apply along $\hat{z}$ for simplicity.

$$\vec{\mu}_3 = \mu\hat{e}_3 = \frac{\mu}{\sqrt{3}}\begin{pmatrix} -1 \\ 1 \\ -1 \end{pmatrix} \quad \vec{\mu}_4 = \mu\hat{e}_4 = \frac{\mu}{\sqrt{3}}\begin{pmatrix} -1 \\ -1 \\ 1 \end{pmatrix}$$

Therefore using Eq. 2.32 and applying an external field along [100], the component of the magnetisation along the axis can be calculated as:

$$M = \sum_{i=1}^{N_s} m_i = \sum_{i=1}^{N_s} \frac{\mu}{V} e_{x_i} \tanh(\beta\mu H e_{x_i}) = \sum_{i=1}^{N_s/2} \frac{\mu}{V\sqrt{3}} \tanh(\beta\mu H/\sqrt{3}) + \sum_{i=1}^{N_s/2} -\frac{\mu}{V\sqrt{3}} \tanh(-\beta\mu H/\sqrt{3}) = \frac{N_s\mu}{V\sqrt{3}} \tanh(\beta\mu H/\sqrt{3}) \quad (2.33)$$

where N_s is the number of spins in the crystal. Now by analogy, if we apply the external field along [110]:

$$M = \sum_{i=1}^{N_s/4} \frac{2\mu}{V\sqrt{6}} \tanh(2\beta\mu H/\sqrt{6}) + \sum_{i=1}^{N_s/4} -\frac{2\mu}{V\sqrt{6}} \tanh(-2\beta\mu H/\sqrt{6}) = \frac{N_s\mu}{V\sqrt{6}} \tanh(2\beta\mu H/\sqrt{6}) \quad (2.34)$$

Finally if the the external field is along [111]:

$$M = \sum_{i=1}^{N_s/4} \frac{\mu}{V} \tanh(\beta\mu H) + \sum_{i=1}^{3N_s/4} -\frac{\mu}{3V} \tanh(-\beta\mu H/3) = \frac{N_s}{4V}\mu[\tanh(\beta\mu H) + \tanh(\beta\mu H/3)] \quad (2.35)$$

The limit of Eq. 2.35 for very high fields is $M_{sat} \propto \mu/2$.

Notice that the previous cases refer to crystal systems, thus in order to conclude this analysis we would like to calculate the magnetisation of a powder sample too. In this case the scalar product between the magnetic moment of the spins and the external field is proportional to $\cos\theta_i$, since spins are pointing in random directions and our only assumption is that there is an easy axis. We can calculate the expectation value of the cosine restricting the integration on the first half quadrant since, for an Ising system, the second half is equal to the first half with a reverse sign. For simplicity we apply the external field along $[001]$:

$$M = \sum_{i=1}^{N_s} m_i = \sum_{i=1}^{N_s} \mu \cos\theta_i \tanh(\beta\mu H \cos\theta_i) \tag{2.36}$$

Now we can call $\beta\mu H = a$ and the expectation value of the cosine can be calculated as:

$$\langle\cos\theta\rangle = \frac{\int_0^{2\pi} d\phi \int_0^{\pi/2} \cos\theta \tanh(a\cos\theta)\sin\theta d\theta}{\int_0^{2\pi} d\phi \int_0^{\pi/2} \sin\theta d\theta} = \int_0^1 a\tanh(ax)dx = \frac{12a^2 - \pi^2 + 24a\ln(1+e^{-2a}) - 12Li_2(-e^{-2a})}{24a^2} = G(a) \tag{2.37}$$

where $Li_n(z)$ is the poly-logarithm function. Finally the magnetisation of a powder Ising sample is:

$$M = \frac{N_s}{V}\mu G(\beta\mu H) \tag{2.38}$$

Figure 2.6 shows the comparison of the different Langevin equations derived for an Ising system.

2.3.2 Langevin theory for the Heisenberg model

Now we consider the same system in Fig. 2.5 but for a Heisenberg spin, and we only suppose to apply the external field along $\hat{z}$ for simplicity. In this case the energy and the magnetisation along $\hat{z}$ are:

$$E = -\vec{\mu}\cdot\vec{H} = -\mu H\cos\theta \tag{2.39}$$

$$M = \frac{N}{V}\mu\langle\cos\theta\rangle \tag{2.40}$$

We have to evaluate $\langle\cos\theta\rangle$ that represents the average over all the possible directions of the spin with respect to the external magnetic field:

$$\langle\cos\theta\rangle = \frac{\int_0^{2\pi} d\phi \int_0^{\pi} d\theta \sin\theta\cos\theta e^{\beta\mu H\cos\theta}}{\int_0^{2\pi} d\phi \int_0^{\pi} d\theta \sin\theta e^{\beta\mu H\cos\theta}} = \frac{\int_{-1}^{1} te^{ta}dt}{\int_{-1}^{1} e^{ta}dt} = \frac{f'(a)}{f(a)} =$$

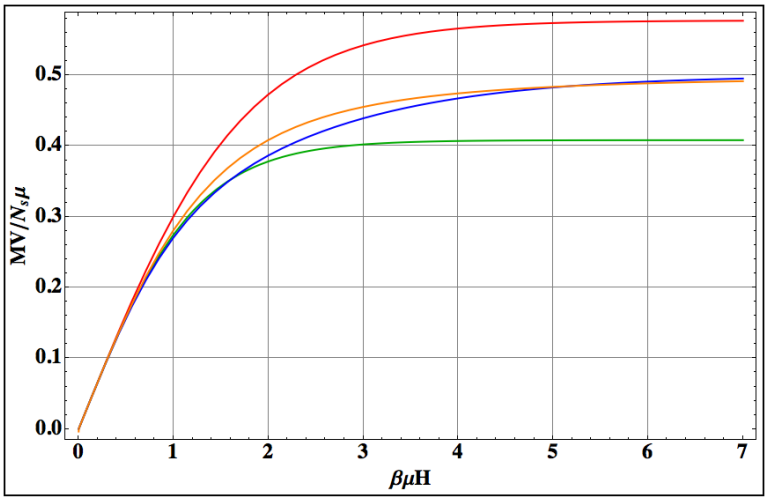

Figure 2.6: *Comparison of the different Langevin equations derived for an Ising system.* – Qualitative behaviour of the magnetisation applying an external field along: [100] (red line), [110] (green line), and [111] (blue line) directions. The magnetisation for a powder sample is shown with the orange line.

$$\frac{d}{da}\ln f(a) = \frac{\mathrm{e}^{\mathrm{a}} + \mathrm{e}^{-\mathrm{a}}}{\mathrm{e}^{\mathrm{a}} - \mathrm{e}^{-\mathrm{a}}} - \frac{1}{a} = \coth a - \frac{1}{a} = L(a) \tag{2.41}$$

where we made the substitution $a = \beta\mu H$ and $t = \cos\theta$. The function $L(a)$ is called the Langevin function, and the magnetisation for the Heisenberg system is:

$$M = \frac{N}{V}\mu L(a) \tag{2.42}$$

where N is the number of spins in the system and V is the volume. Taking the limit for very high fields we obtain that $M_{sat} \propto \mu$. Figure 2.7 shows the behaviour of $L(a)$ for different values of μ.

2.3.3 Langevin theory for the Soft Spin model

The third method we can use to fit the experimental data is based on the theory of soft easy axis spins. In this case we can write the magnetic moment of each spin as $\vec{\mu} = \eta\mu\hat{z}$ where the parameter $\eta \in (-1, 1)$, and the external field as $\vec{H} = H\hat{z}$. The Hamiltonian of this system is:

$$H = -\vec{\mu}\cdot\vec{H} + D|\vec{\mu}|^2 = -\mu H\eta + D\mu^2\eta^2 \tag{2.43}$$

where D is a parameter that couples to the magnitude of the spin. Notice that: $D > 0$ favours $\eta = 0$, while $D < 0$ favours $\eta = \pm 1$ and we obtain an Ising-like spin. If $D = 0$ the model is equivalent to a Heisenberg paramagnet.

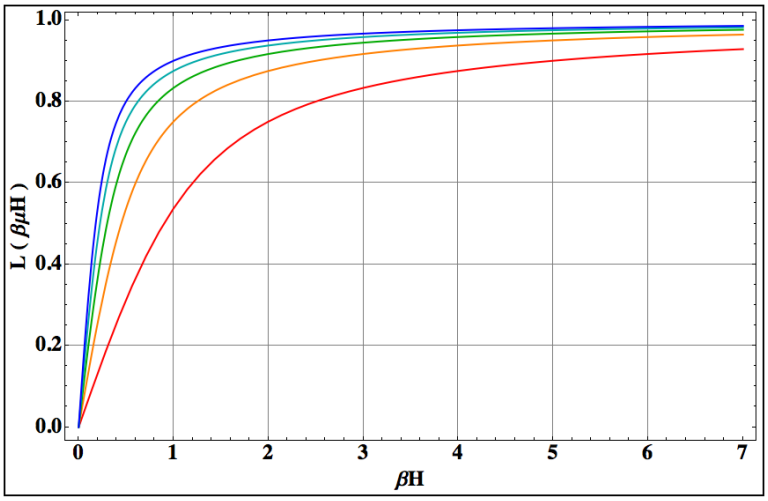

Figure 2.7: *The behaviour of the Langevin function for different values of μ.* – Comparison of the different classical Langevin function for: $\mu = 3/2$ (red line), $\mu = 5/2$ (orange line), $\mu = 7/2$ (green line), $\mu = 11/2$ (cyan line) and $\mu = 15/2$ (blue line).

We can calculate the magnetisation as follow:

$$M = \frac{N}{V}\mu\langle\eta\rangle \tag{2.44}$$

where

$$\langle\eta\rangle = \frac{\int_{-1}^{1} \eta \mathrm{e}^{\beta\mu\mathrm{H}\eta - \mathrm{D}\beta\mu^2\eta^2}\mathrm{d}\eta}{\int_{-1}^{1} \mathrm{e}^{\beta\mu\mathrm{H}\eta - \mathrm{D}\beta\mu^2\eta^2}\mathrm{d}\eta} = \frac{d}{dA}\ln\left[\int_{-1}^{1}(e^{A\eta - B\eta^2}d\eta)\right]$$

For convenience, we introduced the variables $A = \beta\mu H$ and $B = D\beta\mu^2$ to simplify the expression.

2.3.4 Langevin theory for the Easy Plane model

In the last method we calculate the Langevin equation for an easy plane system. We follow a general approach to calculate the magnetisation, supposing that the spin is rotating in the xy plane (where we took $\hat{z}$ parallel to the $[111]$ direction) and we apply the external field in a random direction. With these assumptions the components of the magnetic moment and of the field can be written as:

$$\vec{\mu} = \mu(\cos\eta, \sin\eta, 0) \qquad \vec{H} = H(\sin\theta, 0, \cos\theta) \tag{2.45}$$

Notice that one can always choose the reference system in order to have $\phi = 0$, in this way $\hat{x}$ lies precisely on the top of the projection of the field onto the plane.

This choice imposes no restriction on the direction of the field, but it simplifies considerably the calculations. The energy of this system is:

$$E = -\vec{\mu} \cdot \vec{H} = -\mu H \cos\eta \sin\theta \tag{2.46}$$

Again we can calculate the magnetisation along the field direction as:

$$M = \frac{N}{V} \mu \sin\theta \langle \cos\eta \rangle \tag{2.47}$$

where

$$\langle \cos\eta \rangle = \frac{\int_0^{2\pi} d\eta \cos\eta \mathrm{e}^{\beta\mu \mathrm{H}(\sin\theta \cos\eta)}}{\int_0^{2\pi} d\eta \mathrm{e}^{\beta\mu \mathrm{H}(\mathrm{h_x} \cos\eta)}} = \frac{I_1(\sin\theta \beta\mu \mathrm{H})}{I_0(\sin\theta \beta\mu \mathrm{H})} \tag{2.48}$$

here $I_n(z)$ is the modified Bessel function of the first kind.

Now we want to calculate the magnetisation of a crystal with an external field along the $[111]$ direction. Following the previous convention for the reference system, one possibility is to write the direction of the magnetic moments in order to have $\hat{x}$ aligned with the projection of the $[111]$ field onto their respective easy planes:

$$\begin{aligned}
\vec{\mu}_1 &= \mu \left[\frac{\sin\omega_1}{\sqrt{2}} \begin{pmatrix} 1 \\ -1 \\ 0 \end{pmatrix} + \frac{\cos\omega_1}{\sqrt{6}} \begin{pmatrix} 1 \\ 1 \\ -2 \end{pmatrix} \right] \\
\vec{\mu}_2 &= \mu \left[\frac{\sin\omega_2}{\sqrt{2}} \begin{pmatrix} 0 \\ -1 \\ 1 \end{pmatrix} + \frac{\cos\omega_2}{\sqrt{6}} \begin{pmatrix} 2 \\ 1 \\ 1 \end{pmatrix} \right] \\
\vec{\mu}_3 &= \mu \left[\frac{\sin\omega_3}{\sqrt{2}} \begin{pmatrix} -1 \\ 0 \\ 1 \end{pmatrix} + \frac{\cos\omega_3}{\sqrt{6}} \begin{pmatrix} 1 \\ 2 \\ 1 \end{pmatrix} \right] \\
\vec{\mu}_4 &= \mu \left[\frac{\sin\omega_4}{\sqrt{2}} \begin{pmatrix} -1 \\ 1 \\ 0 \end{pmatrix} + \frac{\cos\omega_4}{\sqrt{6}} \begin{pmatrix} 1 \\ 1 \\ 2 \end{pmatrix} \right]
\end{aligned}$$

where μ is the value of the magnetic moment of the ions and ω is the rotating angle in the (111) plane. Applying an external field $\vec{H} = H(1,1,1)/\sqrt{3}$, the energy of this system becomes:

$$\begin{aligned}
E_i = -\vec{\mu}_i \cdot \vec{H} = \begin{cases} E_1 = -\vec{\mu}_1 \cdot \vec{H} = 0 \\ E_2 = -\vec{\mu}_2 \cdot \vec{H} = -\frac{4\mu H \cos\omega_2}{3\sqrt{2}} \\ E_3 = -\vec{\mu}_3 \cdot \vec{H} = -\frac{4\mu H \cos\omega_3}{3\sqrt{2}} \\ E_4 = -\vec{\mu}_4 \cdot \vec{H} = -\frac{4\mu H \cos\omega_4}{3\sqrt{2}} \end{cases} \\
\Rightarrow E_{tot} = -\frac{2\sqrt{2}\mu H}{3} (\cos\omega_2 + \cos\omega_3 + \cos\omega_4)
\end{aligned} \tag{2.49}$$

Notice that it is possible to compute each spin contribution separately, and then sum all of them with a factor of $1/4$ to account for the fact that each of them represents $1/4$ of the total number of spin. The expectation value of the cosine can be calculated as:

$$\langle \cos \omega_2 \rangle = \frac{\int_0^{2\pi} \frac{2\sqrt{2}}{3} \cos \omega_2 \mathrm{e}^{-\beta \mathrm{E_{tot}}} \mathrm{d}\omega_2}{\int_0^{2\pi} \mathrm{e}^{-\beta \mathrm{E_{tot}}} \mathrm{d}\omega_2} = \frac{2\sqrt{2}}{3} \frac{I_1(2\sqrt{2}\beta\mu \mathrm{H}/3)}{I_0(2\sqrt{2}\beta\mu \mathrm{H}/3)} \tag{2.50}$$

Finally the magnetisation of the system is:

$$M = \frac{3N_s}{4V} \langle \cos \omega_2 \rangle = \frac{N_s}{V\sqrt{2}} \frac{I_1(2\sqrt{2}\beta\mu \mathrm{H}/3)}{I_0(2\sqrt{2}\beta\mu \mathrm{H}/3)} \tag{2.51}$$

where $I_n(z)$ is again the modified Bessel function of the first kind. Taking the limit for very high fields we obtain that $M_{sat} \propto \mu/\sqrt{2}$.

2.3.5 The Brillouin Function in quantum mechanics

A complete analysis of the magnetism must treat this theory in quantum mechanics too.

The Brillouin function is the analogue of the paramagnetic Langevin function in quantum mechanics, and it depends only on the knowledge of the total angular momentum of the magnetic ion. This property makes this approach very useful when we do not know a priori the behaviour of the spin with an external field applied.

In general we can express the magnetic moment of an atom in this way:

$$\vec{\mu} = g_J \mu_B \vec{J} \tag{2.52}$$

where g_J is the Landé g factor, $\vec{J} = \vec{L} + \vec{S}$ is the total angular momentum operator and we are assuming a field applied along $\hat{z}$.

The ground state of a system has a total angular momentum J that can be found using Hund's rules. In this case since both Dy^{3+} and Ho^{3+} have shells more than a half filled $J = L + S$ ($15/2$ and 8 respectively). By contrast if we are studying Ti^{3+} $J = |L - S| = 3/2$ since there is only one electron in the $3d$ shell. Notice that this assumption is correct if the energy difference between the first excited state J' and the ground state J satisfies the relation:

$$E_{J'} - E_J \gg k_B T \tag{2.53}$$

where k_B is the Boltzmann constant and T is the temperature of the system.

If the above condition is satisfied, then we can neglect the influence of excited states. According to quantum mechanics the ground state is $2J+1$ fold degenerate, but if we apply an external field we can always lift this degeneracy and split it in a number of levels equal to the number of values assumed by the quantum number $m_J = -J, -J+1, ..., J-1, J$. This effect is called the Zeeman effect, and m_J

is the quantum number of the total angular momentum. Therefore it is associated with the projection of the total angular momentum operator along the direction of the field.

In order to derive the Brillouin function we have to take care of the fact that the energy is quantised. First of all we can express Helmholtz energy in this way:

$$F = -k_B T \ln Z \tag{2.54}$$

where Z is the partition function of the system:

$$Z = \sum_{m_J=-J}^{J} \exp^{-\beta E_J} \tag{2.55}$$

with

$$E_J = g_J \mu_B H m_J \tag{2.56}$$

In this way we can rewrite Eq. 2.54 like:

$$F = -k_B T \ln \left[\sum_{m_J=-J}^{J} \exp^{-\beta g_J \mu_B H m_J} \right] \tag{2.57}$$

If we now divide the above expression by $k_B T$ and we take the exponential of the result, we find a useful definition of the free energy of the system expressed using a convergent geometric series:

$$\exp^{-\beta F} = \sum_{m_J=-J}^{J} \exp^{-\beta g_J \mu_B H m_J} \tag{2.58}$$

We can call the argument of the series $q = \exp^{-\beta g_J \mu_B H} < 1$ then, using the sum rule of the geometric series with a finite number of terms, we obtain that:

$$\sum_{m_J=-J}^{J} q^{m_J} = \frac{q^{-J} - q^{J+1}}{1-q} \tag{2.59}$$

Therefore:

$$\exp^{-\beta F} = \frac{q^{-J} - q^{J+1}}{1-q} = \frac{q^{-(J+1/2)} - q^{J+1/2}}{q^{-1/2} - q^{1/2}} \tag{2.60}$$

Finally we can substitute q back in the above equation:

$$\exp^{-\beta F} = \frac{\exp^{\beta g_J \mu_B H (J+1/2)} - \exp^{-\beta g_J \mu_B H (J+1/2)}}{\exp^{\beta g_J \mu_B H/2} - \exp^{-\beta g_J \mu_B H/2}} \tag{2.61}$$

The Helmholtz energy can be calculated applying the logarithm to Eq. 2.61:

$$F = -\frac{1}{\beta} \ln \left[\frac{\exp^{f(H)+g(H)} - \exp^{-f(H)-g(H)}}{\exp^{g(H)} - \exp^{-g(H)}} \right] \tag{2.62}$$

where we assumed $f(H) = \beta g_J \mu_B H J$ and $g(H) = \beta g_J \mu_B H/2$.

Now, for a number N of non interacting ions, the magnetisation is only the derivative respect to the field of the free energy at constant temperature:

$$M = \frac{N}{V} g_J \mu_B J \underbrace{\left[\left(\frac{2J+1}{2J} \right) \coth \left(\frac{2J+1}{2J} x \right) - \frac{1}{2J} \coth \left(\frac{1}{2J} x \right) \right]}_{B_J(x)} \tag{2.63}$$

where $B_J(x)$ is the Brillouin function and $x = \beta g_J \mu_B J H$.

Notice that the behaviour of the Brillouin function is similar to the classical Langevin one, as one can see from Fig. 2.8. Both functions have a crescent-shaped, monotonic behaviour and they vary between 0 and 1. However, since the Brillouin function has been derived using quantum mechanics, we will have different curves depending on the value of the total angular momentum J. By contrast, in the classical case the difference in the curves of the Langevin function depends only on the spin model we are studying, since there is no dependence on J.

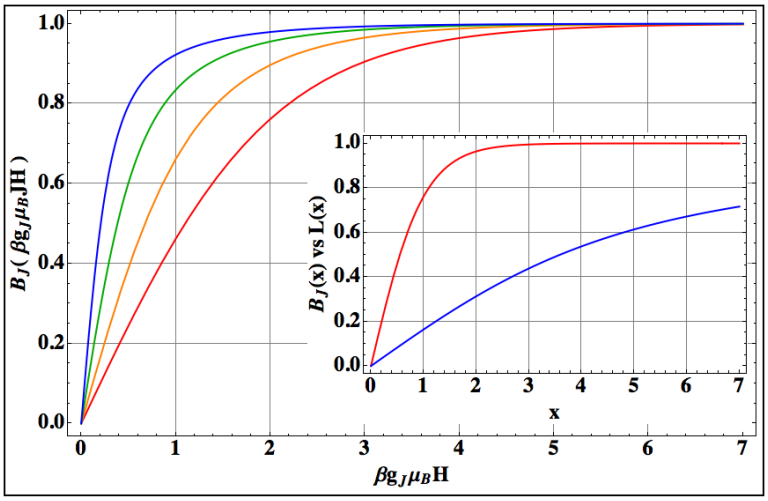

Figure 2.8: *Comparison of the different Brillouin functions for different J at fixed $g_J = 1$.* – Qualitative behaviour of the Brillouin function for $J = 1/2$ (red line), $J = 5/2$ (orange line), $J = 11/2$ (green line) and $J = 15/2$ (blue line). The inset shows the comparison between $B_J(x)$ (red line) and $L(x)$ (blue line) for $\mu = 1/2$ and $g_J = 2$.

2.4 The Ewald Summation Technique

The Ewald summation technique (see Ref. [49]) is a suitable method to treat long range interactions without truncating the series expansion and losing contributions from terms at long range.

As it is known from the literature the series expansion of a long range potential can only be conditionally convergent. Moreover calculations are very time consuming when the system is composed of a big supercell. The Ewald method splits the summation in two parts: one in real space and one in reciprocal space in order to improve the speed of the computation, and to ensure the convergence of the series with an high degree of precision (see Ref. [50] for further details).

In this section we show how it is possible to use the Ewald method to calculate the dipolar interaction in Eq. 1.1 and the magnetic field in 3D systems. This formula will be used in the analysis of the internal fields in spin ice crystals treated in Sec. 4.1.

2.4.1 The Ewald method applied to 3D systems

The Hamiltonian of a system of N particles for Monte Carlo (MC) and molecular-dynamic simulations, under periodic boundary is (Ref. [51]):

$$H = \frac{1}{2}\sum_{n}{}' \left[\sum_{i=1}^{N}\sum_{j=1}^{N} \phi(\vec{r}_{ij} + \mathcal{L}\vec{n}, \Omega_i, \Omega_j) \right] \tag{2.64}$$

Here $\vec{r}_{ij} = \vec{r}_j - \vec{r}_j$ and Ω_i, Ω_j are Euler angles of the two particles, $\mathcal{L}$ is the length of the cubic simulation sample that contains N particles and, in order to reduce the error during the calculation of the potential, this quantity multiplies a shift vector $\vec{n} = (n_x, n_y, n_z)$ that allows to calculate the potential from a point in the main reference system to another point in the adjacent one. The prime over the summation means that when $i = j$ the term $n = 0$ has to be omitted, because we do not need to calculate the potential when two points are superimposed.

The charge-charge interaction corresponds to:

$$\phi(\vec{r}_{ij})_{c.c} = q_i q_j \frac{1}{\mid \vec{r}_{ij} \mid} \tag{2.65}$$

while the dipole-dipole interaction corresponds to:

$$\phi(\vec{r}_{ij})_{d.d} = -(\mu_i \cdot \nabla)(\mu_j \cdot \nabla)\frac{1}{\mid \vec{r}_{ij} \mid} \tag{2.66}$$

It should be noted that, in this case, the operator gradient is the derivative respect to $\vec{r}_{ij}$.

Now, if we evaluate the Hamiltonian in Eq. 2.64 using the charge-charge interaction, we can find that H has the form of:

$$H = \sum_{1 \le i < j \le N} \frac{1}{\mathcal{L}} q_i q_j \Psi\left(\frac{\vec{r}_{ij}}{\mathcal{L}}\right) + \frac{\xi}{2\mathcal{L}}\sum_{i=1}^{N} q_i^2 + \frac{2\pi}{3\mathcal{L}^3}\left|\sum_{i=1}^{N} q_i r_i\right|^2 \tag{2.67}$$

where the Ewald potential Ψ is:

$$\Psi(\vec{x}) = \sum_n \frac{\mathrm{erfc}(\alpha \mid \vec{x} + \vec{n} \mid)}{\mid \vec{x} + \vec{n} \mid} + \frac{1}{\pi} \sum_{n \neq 0} \frac{1}{\mid \vec{n} \mid^2} e^{2\pi\imath \vec{n}\cdot\vec{x} - \pi^2 \frac{|\vec{n}|^2}{\alpha^2}} \tag{2.68}$$

Here we chose $(\vec{x} = \vec{r}_{ij}/\mathcal{L})$.

The second term in the Hamiltonian represents the chemical potential and it is independent of the position of the charges, while the third term is the square of the total dipole moment of the system. The term erfc(z) represents the complementary error function:

$$\mathrm{erfc(z)} = 1 - \mathrm{erf(z)} = \frac{2}{\sqrt{\pi}} \int_z^\infty e^{-t^2} dt = \frac{e^{-z^2}}{z\sqrt{\pi}} \sum_{n=0}^{\infty} (-1)^n \frac{(2n-1)!!}{(2z^2)^n} \tag{2.69}$$

For the analysis in Sec. 4.1, we need to find the expression of the magnetic field calculated with the Ewald summation technique, in order to check the behaviour of the curve in the medium regime of strength field values. First of all we need to set some conditions, in order to simplify the calculation:

1. We consider the case where there is only one spin at the centre of the unit cell.

2. The spin is pointing along $\hat{z}$, thus $\vec{\mu} = \mu\,(0, 0, 1)$.

3. With the previous choice of coordinate system, B is the vector field due to the dipole μ_j computed at site r_i. Therefore the dipole μ_j is not only pointing along $\hat{z}$, but it is also at the origin of the coordinate system, and we can write $\vec{r}_{ij} = \vec{r_i} - \vec{r_j} = \vec{r_i}$.

Under these assumptions, we can calculate the magnetic field using the Ewald summation technique observing that the dipole-dipole interaction can be rewritten as:

$$\phi(\vec{r}_{ij})_{d.d} = -\frac{1}{q_i q_j} (\mu_i \cdot \nabla)(\mu_j \cdot \nabla) \phi(\vec{r}_{ij})_{c.c} \tag{2.70}$$

and the Hamiltonian can be rewritten explicity as a summation over i, j as:

$$H = \sum_{ij} \frac{1}{\mathcal{L}} q_i q_j \Psi\left(\frac{\vec{r}_{ij}}{\mathcal{L}}\right) - \frac{1}{\mathcal{L}} q_i^2 \Psi(0) + \frac{2\pi}{3\mathcal{L}^3} q_i q_j \vec{r}_i \cdot \vec{r}_j + const. \tag{2.71}$$

where the term $const.$ takes care of all the terms regarding the chemical potential.

Now, from the dipole-dipole interaction, we obtain the following Hamiltonian:

$$H = \sum_{ij} -\frac{1}{q_i q_j} (\mu_i \cdot \nabla)(\mu_j \cdot \nabla) \left[\frac{1}{\mathcal{L}} q_i q_j \Psi\left(\frac{\vec{r}_{ij}}{\mathcal{L}}\right) - \frac{1}{\mathcal{L}} q_i^2 \Psi(0) + ...\right] \tag{2.72}$$

$$H = -\frac{1}{2} \sum_{i \neq j} \frac{1}{\mathcal{L}} (\mu_i \cdot \nabla)(\mu_j \cdot \nabla) \Psi\left(\frac{\vec{r}_{ij}}{\mathcal{L}}\right) - \frac{1}{2} \sum_{i=j} ..... \tag{2.73}$$

where we put $1/2$ to avoid the double counting, and we split the two summations because we only need the terms where $i \neq j$.

This equation can be compared with the classical Hamiltonian:

$$H = -\frac{1}{2}\sum_{i \neq j} \vec{\mu_j} \cdot \vec{B}_i(r_{ij}) + \sum_i v_i \tag{2.74}$$

Again the term $\sum_i v_i$ takes care of the terms where $i = j$, but we do not need them.

We can therefore identify:

$$H = -\vec{\mu_j} \cdot \vec{B}_i(r_{ij}) = -\frac{1}{\mathcal{L}}(\vec{\mu_j} \cdot \nabla)(\vec{\mu_i} \cdot \nabla)\Psi\left(\frac{\vec{r}_{ij}}{L}\right) \tag{2.75}$$

Thus

$$\vec{B}_i(r_{ij}) = \frac{1}{\mathcal{L}}\nabla\left[\vec{\mu_i} \cdot \nabla\Psi\left(\frac{\vec{r}_{ij}}{\mathcal{L}}\right)\right] \tag{2.76}$$

Note that the gradients are taken with respect to $\vec{r}_{ij}$.

Expressing B in S.I. units and re-writing the gradients with respect to $\vec{x} = \vec{r}_{ij}/L = (x,\ y,\ z)$ we obtain:

$$\vec{B}_i(\vec{r}_{ij}) = \frac{\mu_0\mu}{4\pi}\frac{1}{\mathcal{L}^3}\nabla_x\left[\hat{\mu}_i \cdot \nabla_x\Psi(\vec{x})\right] \tag{2.77}$$

This equation is consistent even from the dimensional point of view; in fact in S.I. units we can check that:

$$[T] = \frac{[T]^2[m]^3}{[J]}\frac{[J]}{[T]}\frac{1}{[m]^3} \tag{2.78}$$

Now the potential Ψ can be rewritten in this way:

$$\Psi(\vec{x}) = \sum_n \frac{\mathrm{erfc}(\alpha \mid \vec{x} + \vec{n} \mid)}{\mid \vec{x} + \vec{n} \mid} + \frac{1}{\pi}\sum_{n \neq 0}\frac{1}{\mid \vec{n} \mid^2}e^{2\pi\imath\vec{n}\cdot\vec{x} - \pi^2\frac{|\vec{n}|^2}{\alpha^2}} \tag{2.79}$$

Therefore the only problem is to calculate the gradient of the wave function. Obviously we have to calculate only the derivative along $\hat{z}$ (thanks to the second assumption); so first of all we split the wave function in two parts:

$$A_1 = \frac{\partial}{\partial z}\sum_n \frac{\mathrm{erfc}(\alpha \mid \vec{x} + \vec{n} \mid)}{\mid \vec{x} + \vec{n} \mid} \tag{2.80}$$

$$A_2 = \frac{\partial}{\partial z}\frac{1}{\pi}\sum_{n \neq 0}\frac{1}{\mid \vec{n} \mid^2}e^{2\pi\imath\vec{n}\cdot\vec{x} - \pi^2\frac{|\vec{n}|^2}{\alpha^2}} \tag{2.81}$$

The first one can be rewritten as:

$$A_1 = \frac{\partial}{\partial z}\sum_{n_x,n_y,n_z=-\infty}^{\infty} \frac{\mathrm{erfc}(\alpha\sqrt{(\mathrm{x}+\mathrm{n_x})^2 + (\mathrm{y}+\mathrm{n_y})^2 + (\mathrm{z}+\mathrm{n_z})^2})}{\sqrt{(x+n_x)^2 + (y+n_y)^2 + (z+n_z)^2}} \tag{2.82}$$

and, using the third assumption above, the derivative is:

$$A_1 = \sum_{n_x,n_y,n_z=-\infty}^{\infty} -\frac{2\alpha(n_z+z)e^{-\alpha^2[(n_x+x)^2+(n_y+y)^2+(n_z+z)^2]}}{\sqrt{\pi}[(n_x+x)^2+(n_y+y)^2+(n_z+z)^2]} - \frac{(n_z+z)\mathrm{erfc}[\alpha\sqrt{(\mathrm{n_x+x})^2+(\mathrm{n_y+y})^2+(\mathrm{n_z+z})^2}]}{[(n_x+x)^2+(n_y+y)^2+(n_z+z)^2]^{3/2}} \tag{2.83}$$

The second one can be written as:

$$A_2 = \frac{\partial}{\partial z}\frac{1}{\pi}\sum_{n_x,n_y,n_z=-\infty,\neq 0}^{\infty}\frac{1}{n_x^2+n_y^2+n_z^2}e^{2\pi\imath[n_x x+n_y y+n_z z]-\pi^2\frac{n_x^2+n_y^2+n_z^2}{\alpha^2}} \tag{2.84}$$

and, using again the third assumption, the derivative is:

$$\sum_{n_x,n_y,n_z=-\infty,\neq 0}^{\infty}\frac{2\pi\imath n_z e^{2\pi\imath[n_x x+n_y y+n_z z]-\pi^2\frac{n_x^2+n_y^2+n_z^2}{\alpha^2}}}{\pi(n_x^2+n_y^2+n_z^2)} \tag{2.85}$$

Or better:

$$A_2 = \sum_{n_x,n_y=-\infty}^{\infty} e^{2\pi\imath[n_x x+n_y y]}\sum_{n_z=-\infty,\neq 0}^{\infty} 2\imath n_z e^{2\pi\imath n_z z}\underbrace{\frac{e^{-\pi^2\frac{n_x^2+n_y^2+n_z^2}{\alpha^2}}}{(n_x^2+n_y^2+n_z^2)}}_{f(n^2)} \tag{2.86}$$

It is convenient to re-sum the second term as:

$$\sum_{n_z=-\infty,\neq 0}^{\infty} 2n_z\imath f(n^2)e^{2\pi\imath n_z z} = \sum_{n_z=-\infty}^{-1} 2n_z\imath f(n^2)e^{2\pi\imath n_z z} + \sum_{n_z=+1}^{\infty} 2n_z\imath f(n^2)e^{2\pi\imath n_z z} = \sum_{n_z=+1}^{\infty} -2n_z\imath f(n^2)e^{-2\pi\imath n_z z} + \sum_{n_z=+1}^{\infty} 2n_z\imath f(n^2)e^{2\pi\imath n_z z} = \sum_{n_z=+1}^{\infty} 2n_z\imath[e^{2\pi\imath n_z z}-e^{-2\pi\imath n_z z}]f(n^2) \tag{2.87}$$

And using Euler's formula:

$$\sum_{n_z=+1}^{\infty} 2n_z\imath f(n^2)2\imath\sin(2\pi n_z z) = \sum_{n_z=+1}^{\infty} -4f(n^2)n_z\sin(2\pi n_z z) \tag{2.88}$$

Similarly for n_x and n_y:

$$\sum_{n_x=-\infty}^{\infty} f(n^2)e^{2\pi\imath n_x} = \sum_{n_x=-\infty}^{-1} f(n^2)e^{2\pi\imath n_x} + [f(n^2)e^{2\pi\imath n_x}]_{n_x=0} + \sum_{n_x=+1}^{\infty} f(n^2)e^{2\pi\imath n_x} \tag{2.89}$$

The central term is equal to $f(0, n_y, n_z)$. For the other two, we can use the same trick as before and Euler's formula to obtain:

$$\sum_{n_x=-\infty}^{\infty} f(n^2)e^{2\pi\imath n_x} = f(0, n_y, n_z) + \sum_{n_x=+1}^{\infty} 2f(n^2)\cos(2\pi n_x) \tag{2.90}$$

Likewise for n_y. We can thus write Eq. 2.84 without any explicit imaginary units:

$$\begin{aligned} A_2 = -\Bigg(& \sum_{n_z=+1}^{\infty} 4n_z \sin(2\pi n_z z) f(0,0,n_z) \quad + \\ & \sum_{n_x,n_z=+1}^{\infty} 8n_z \sin(2\pi n_z z) f(n_x,0,n_z)\cos(2\pi n_x x) \quad + \\ & \sum_{n_y,n_z=+1}^{\infty} 8n_z \sin(2\pi n_z z)\cos(2\pi n_y y) f(0,n_y,n_z) \quad + \\ & \sum_{n_x,n_y,n_z=+1}^{\infty} 16n_z \sin(2\pi n_z z)\cos(2\pi n_y y) f(n^2)\cos(2\pi n_x x) \Bigg) \end{aligned} \tag{2.91}$$

The scalar product between $\vec{\mu_i}$ and the gradient gives only the component on the $\hat{z}$ direction (because of the assumption made before). Now to find the component of the magnetic field we only have to calculate the second gradient deriving again respect to x, y, z and obtaining for the first part:

$$\begin{aligned} B_{x1} = \sum_{n_x,n_y,n_z=-\infty}^{\infty} & + \frac{6(n_x+x)(n_z+z)\alpha e^{-[(n_x+x)^2+(n_y+y)^2+(n_z+z)^2]\alpha^2}}{\sqrt{\pi}[(n_x+x)^2+(n_y+y)^2+(n_z+z)^2]^2} \quad + \\ & \frac{4\alpha^3(n_x+x)(n_z+z)e^{-[(n_x+x)^2+(n_y+y)^2+(n_z+z)^2]\alpha^2}}{\sqrt{\pi}[(n_x+x)^2+(n_y+y)^2+(n_z+z)^2]} \quad + \\ & \frac{3(n_x+x)(n_z+z)\mathrm{erfc}[\sqrt{(\mathrm{n_x+x})^2+(\mathrm{n_y+y})^2+(\mathrm{n_z+z})^2}\alpha]}{[(n_x+x)^2+(n_j+y)^2+(n_z+z)^2]^{5/2}}\hat{x} \end{aligned} \tag{2.92}$$

$$\begin{aligned} B_{y1} = \sum_{n_x,n_y,n_z=-\infty}^{\infty} & + \frac{6(n_y+y)(n_z+z)\alpha e^{-[(n_x+x)^2+(n_y+y)^2+(n_z+z)^2]\alpha^2}}{\sqrt{\pi}[(n_x+x)^2+(n_y+y)^2+(n_z+z)^2]^2} \quad + \\ & \frac{4\alpha^3(n_y+y)(n_y+z)e^{-[(n_x+x)^2+(n_y+y)^2+(n_z+z)^2]\alpha^2}}{\sqrt{\pi}[(n_x+x)^2+(n_y+y)^2+(n_z+z)^2]} \quad + \\ & \frac{3(n_y+y)(n_z+z)\mathrm{erfc}[\sqrt{(\mathrm{n_x+x})^2+(\mathrm{n_y+y})^2+(\mathrm{n_z+z})^2}\alpha]}{[(n_x+x)^2+(n_j+y)^2+(n_z+z)^2]^{5/2}}\hat{y} \end{aligned} \tag{2.93}$$

$$B_{z1} = \sum_{n_x,n_y,n_z=-\infty}^{\infty} - \frac{2\alpha e^{-[(n_x+x)^2+(n_y+y)^2+(n_z+z)^2]\alpha^2}}{\sqrt{\pi}[(n_x+x)^2+(n_y+y)^2+(n_z+z)^2]} \quad +$$

$$\frac{6(n_z+z)^2\alpha e^{-[(n_x+x)^2+(n_y+y)^2+(n_z+z)^2]\alpha^2}}{\sqrt{\pi}[(n_x+x)^2+(n_y+y)^2+(n_z+z)^2]^2} \quad +$$
$$\frac{4(n_z+z)^2\alpha^3 e^{-[(n_x+x)^2+(n_y+y)^2+(n_z+z)^2]\alpha^2}}{\sqrt{\pi}[(n_x+x)^2+(n_y+y)^2+(n_z+z)^2]} \quad -$$
$$\frac{\mathrm{erfc}[\alpha\sqrt{(\mathrm{n_x}+\mathrm{x})^2+(\mathrm{n_y}+\mathrm{y})^2+(\mathrm{n_z}+\mathrm{z})^2}]}{[(n_x+x)^2+(n_j+y)^2+(n_z+z)^2]^{3/2}} \quad +$$
$$\frac{3(n_z+z)^2\mathrm{erfc}[\alpha\sqrt{(\mathrm{n_x}+\mathrm{x})^2+(\mathrm{n_y}+\mathrm{y})^2+(\mathrm{n_z}+\mathrm{z})^2}]}{[(n_x+x)^2+(n_j+y)^2+(n_z+z)^2]^{5/2}}\hat{z} \tag{2.94}$$

and for the second part:

$$B_{x2} = \sum_{n_x,n_z=+1}^{\infty} \frac{16\pi n_x n_z e^{-\frac{\pi^2(n_x^2+n_z^2)}{\alpha^2}}}{n_x^2+n_z^2}\sin(2\pi n_x x)\sin(2\pi n_z z) \quad +$$
$$\sum_{n_x,n_y,n_z=+1}^{\infty} \frac{32\pi n_x n_z e^{-\frac{\pi^2(n_x^2+n_y^2+n_z^2)}{\alpha^2}}}{n_x^2+n_y^2+n_z^2}\sin(2\pi n_x x)\cos(2\pi n_y y)\sin(2\pi n_z z)\hat{x} \tag{2.95}$$

$$B_{y2} = \sum_{n_y,n_z=+1}^{\infty} \frac{16\pi n_y n_z e^{-\frac{\pi^2(n_y^2+n_z^2)}{\alpha^2}}}{n_y^2+n_z^2}\sin(2\pi n_y y)\sin(2\pi n_z z) \quad +$$
$$\sum_{n_x,n_y,n_z=+1}^{\infty} \frac{32\pi n_y n_z e^{-\frac{\pi^2(n_x^2+n_y^2+n_z^2)}{\alpha^2}}}{n_x^2+n_y^2+n_z^2}\cos(2\pi n_x x)\sin(2\pi n_y y)\sin(2\pi n_z z)\hat{y} \tag{2.96}$$

$$B_{z2} = -\left(\sum_{n_z=+1}^{\infty} 8\pi\cos(2\pi n_z z)e^{-\frac{\pi^2 n_z^2}{\alpha^2}} \quad +\right.$$
$$\sum_{n_x,n_y,n_z=+1}^{\infty} \frac{32\pi n_z^2 e^{-\frac{\pi^2(n_x^2+n_y^2+n_z^2)}{\alpha^2}}}{n_x^2+n_y^2+n_z^2}\cos(2\pi n_x x)\cos(2\pi n_y y)\cos(2\pi n_z z) \quad +$$
$$\sum_{n_x,n_z=+1}^{\infty} \frac{16\pi n_z^2 e^{-\frac{\pi^2(n_x^2+n_z^2)}{\alpha^2}}}{n_x^2+n_z^2}\cos(2\pi n_x x)\cos(2\pi n_z z) \quad +$$
$$\left.\sum_{n_y,n_z=+1}^{\infty} \frac{16\pi n_z^2 e^{-\frac{\pi^2(n_y^2+n_z^2)}{\alpha^2}}}{n_y^2+n_z^2}\cos(2\pi n_y y)\cos(2\pi n_z z)\right)\hat{z} \tag{2.97}$$

Finally the magnetic field is:

$$\|\vec{B}\| = \frac{\mu_0\mu}{4\pi}\frac{1}{\mathcal{L}^3}\sqrt{(B_{x1}+B_{x2})^2+(B_{y1}+B_{y2})^2+(B_{z1}+B_{z2})^2} \tag{2.98}$$

where

$$\begin{cases} x = (r_i^x - r_j^x)/\mathcal{L} = r_i^x/\mathcal{L} \\ y = (r_i^y - r_j^y)/\mathcal{L} = r_i^y/\mathcal{L} \\ z = (r_i^z - r_j^z)/\mathcal{L} = r_i^z/\mathcal{L} \end{cases} \tag{2.99}$$

and $\mathcal{L}$ is the dimensional size of the total simulation cell (i.e. $\mathcal{L} = 2\sqrt{2}Lr_{nn}$).

We show in App. A.1 the three components of the field for a spin with μ along $(1,1,1)/\sqrt{3}$.

2.5 Monte Carlo simulations in spin ice

Spin ice crystals form a formidable test bench for theorists who, taking advantage of the symmetries of the system and using statistical mechanics, can write a program to calculate thermodynamic quantities such as heat capacity, magnetisation and susceptibility or, focusing on a specific plane, make predictions on the neutron scattering cross section (see Sec. 3.1). Notice that all the previous quantities can be calculated only when the system is at equilibrium, however one can also perform a calculation out of the equilibrium in order to study the dynamics of the monopoles. One of the best review that explains in great details how to calculate the previous quantities for both $Dy_2Ti_2O_7$ and $Ho_2Ti_2O_7$, can be found in Ref. [50].

In this section we explain the basics of Monte Carlo (MC) simulation (Ref. [52]), and we show some useful tricks to improve the computational speed of the calculation exploiting the symmetry of the pyrochlore lattice.

2.5.1 What is a Monte Carlo simulation ?

Monte Carlo methods are a broad class of computational algorithms that rely on repeated random sampling to obtain numerical results. Typically one runs simulations many times in order to obtain the distribution of an unknown probabilistic entity. The name comes from the resemblance of the technique used for playing and recording your results in a real gambling casino. In physics-related problems, Monte Carlo methods are quite useful for simulating systems with many coupled degrees of freedom (fluids, disordered materials, strongly coupled solids), or cellular structures (Potts model).

Lets assume that a system at a given temperature (i.e at equilibrium) and whose Hamiltonian is known, follows Boltzmann statistics. The mean value of some macroscopic variable A can be computed over all the phase space (PS) using the Boltzmann distribution as follows:

$$\langle A \rangle = \int_{PS} A(\vec{r}) \frac{\exp^{\beta E(\vec{r})}}{Z} d\vec{r} \tag{2.100}$$

where $E(\vec{r})$ is the energy of the system for a given state $\vec{r} = (\vec{q}, \vec{p})$ and Z is the partition function. One possible approach to solve this multivariable integral is to

exactly enumerate all possible configurations of the system, and calculate averages at will. Therefore, the estimate under MC integration of the above integral is:

$$\langle A \rangle \simeq \frac{1}{N} \sum_{i=1}^{N} A(\vec{r}) \frac{\exp^{\beta E(\vec{r})}}{Z} \tag{2.101}$$

where $\vec{r}_i$ are uniformly obtained from all of PS and N is the number of sampling points.

This is actually done in exactly solvable systems and in simulations of samples with few particles. However in realistic systems even an exact enumeration can be difficult to implement, and the Monte Carlo integration is generally employed since the error grows as $1/\sqrt{N}$, independently of the dimension of the integral.

Now, as it is well known, there are some zones of the PS that are generally more important to the mean value of the variable A than others. In particular, those that have the value of $\exp^{-\beta E(\vec{r}_i)}$ sufficiently high compared to the rest of the energy spectrum are the most relevant for the integral. If $p(\vec{r})$ is a distribution that chooses states that are known to be more relevant to the integral, the mean value of A can be rewritten as:

$$\langle A \rangle = \int_{PS} p^{-1}(\vec{r}) \frac{A(\vec{r})}{Z p^{-1}(\vec{r})} \exp^{-\beta E(\vec{r})} d\vec{r} =$$

$$\int_{PS} \frac{p^{-1}(\vec{r}) A^*(\vec{r})}{Z} \exp^{-\beta E(\vec{r})} d\vec{r} \tag{2.102}$$

where $A^*(\vec{r})$ are the sampled values taking into account the importance probability $p(\vec{r})$. This integral can be estimated as:

$$\langle A \rangle \simeq \frac{1}{N} \sum_{i=1}^{N} p^{-1}(\vec{r}_i) \frac{A^*(\vec{r}_i)}{Z} \exp^{-\beta E(\vec{r}_i)} \tag{2.103}$$

where $\vec{r}_i$ are now randomly generated using the $p(\vec{r})$ distribution. Since most of the times it is not easy to find a way to generate those states with a given distribution, the Metropolis algorithm must be used.

It is known from the literature that the most likely states are those that maximise the Boltzmann distribution, also called the canonical distribution. Let

$$p(\vec{r}) = \frac{\exp^{-\beta E(\vec{r})}}{Z} \tag{2.104}$$

Substituting Eq. 2.104 in the previous sum:

$$\langle A \rangle \simeq \frac{1}{N} \sum_{i=1}^{N} A^*(\vec{r}_i). \tag{2.105}$$

Therefore the procedure to obtain a mean value of a given variable, using the Metropolis algorithm, with the canonical distribution, is to use the Metropolis algorithm to generate states given by the distribution $p(\vec{r})$ and perform means over $A^*(\vec{r})$.

Notice that when performing a given measure, i.e. a realisation of $\vec{r}_i$, one must ensure that the new realisation is not correlated with the previous state of the system, otherwise the states are not being "randomly" generated. This statement is relevant in systems with high energy gaps, where the time needed to decorrelate the state can tend to infinity.

A careful reader should have noticed that, in order to perform a MC simulation, we need at least four different tools: the Hamiltonian of the system (Eq. 1.1) a random generator code that gives us an ensemble of many uncorrelated configurations in PS (Marsaglia code Ref. [53] is one of the best for this aim), and a MC algorithm coupled with a Metropolis condition that performs the calculation of the variable we are looking for.

In spin ice systems our ensemble of configurations is given by the different directions of the Ising spins and the MC algorithm is a periodical update of the configuration using a "single spin flip" method, that calculates the energy difference between the two configurations before and after the "single spin flip". Finally the Metropolis condition accepts of rejects the update according to the Boltzmann distribution for that particular value of T. With only these ingredients we are able to study spin ice systems with a high degree of accuracy and then we can also compare the simulation results with the experimental data, that are the final bench mark of the calculation.

Once the main program has been written, one can always spend a little bit of time trying to improve the speed of the calculation. Notice that this advice is not a waste of time since some calculations can be very time consuming, especially when we are dealing with very large simulation systems. In this case the optimisation of the code is crucial in order to achieve a robust result in the simulation.

For this reason we suggest here a couple of tricks exploiting the symmetry of the pyrochlore lattice, that can be very useful to study spin ice systems:

1. Commonly we can set the origin of the reference system at the centre of the rare earth tetrahedron. This choice allows us to write the position of the four rare earth spins in a very simple way since they are located at the same distance from the centre along the local $\langle 111 \rangle$ directions. Moreover we can focus our attention only on the main sub lattice of the pyrochlore lattice (see Fig. 2.9 red tetrahedra), since the other centres (green spheres) will be a translation of the first one along the bonds of the pyrochlore lattice $(1/2, 1/2, 0)$; $(1/2, 0, 1/2)$ and $(0, 1/2, 1/2)$ written in the appropriate units.

2. We can scale the length of the system using as common unit the distance between two neighbouring rare earth ions ($r_{nn} = 1$), in this way all the other distances are quantised in unit of $2\sqrt{2}$ (see Sec. 1.4.2).

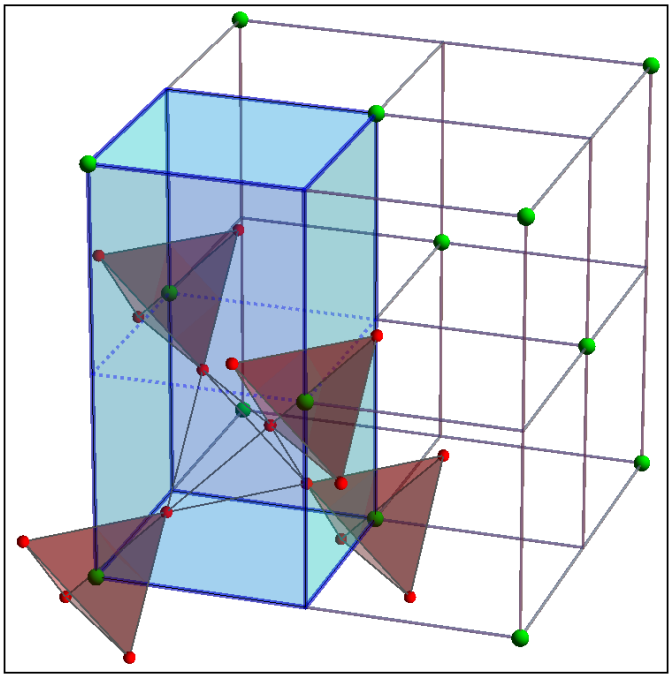

Figure 2.9: *Unit cell used in MC simulation.* – A common choice for the reference system consists of having the origin at the centre of the rare earth tetrahedron (green spheres). This method allows us to write the position of the magnetic ions in an easy way since they are located at the same distance from the centre along the local $\langle 111 \rangle$ directions. Moreover we can focus our attention only on the main sub lattice of the pyrochlore lattice (red tetrahedra), since the other centres will be a translation of the first one along the bonds of the pyrochlore lattice. A quarter of the unit cell of the lattice is highlighted in cyan.

3. The main problem in Eq. 1.1 is the calculation of the dipolar energy, that becomes time consuming for very large systems ($\mathcal{L} \geq 8$). We have already seen how to treat long range interactions using the Ewald technique in the previous section, however another hint is to simplify the formula in the following way:

$$E_{dip} = D \sum_{i<j} \left[\frac{\mathbf{S}_i \cdot \mathbf{S}_j}{|\mathbf{r}_{ij}|^3} - \frac{3(\mathbf{S}_i \cdot \mathbf{r}_{ij})(\mathbf{S}_j \cdot \mathbf{r}_{ij})}{|\mathbf{r}_{ij}|^5} \right] = \underbrace{D \sum_{i<j} \left[\frac{\hat{e}_i \cdot \hat{e}_j}{|\hat{r}_{ij}|^3} - \frac{3(\hat{e}_i \cdot \hat{r}_{ij})(\hat{e}_j \cdot \hat{r}_{ij})}{|\hat{r}_{ij}|^3} \right]}_{D_{ij}} \sigma_i \sigma_j \tag{2.106}$$

where $\hat{e}_i$ are the unit vectors of the spin written in Fig. 2.5, $\hat{r}_{ij}$ are the bond unit vectors of the pyrochlore lattice and $\sigma_i = \pm 1$ is a discrete variable used

to indicate that the spin is pointing in or out of the tetrahedron. Notice that according to the common definition of $\hat{e}_i$, a plus sign means spin out and vice versa for minus. The user can use this formula to compute the matrix elements D_{ij} with the Ewald technique, save them in an external file and read them only when it is necessary.

4. The last bottleneck in our program is the "single spin flip" update of the MC. In this case the choice is dictated by the physics of the system, but one can always use a "cluster spin flip" update that increases the speed of the simulation and avoids local minima.

Chapter 3

Experimental techniques

Contents

Following the spirt of Galileo's and Newton's science, every single theoretical result must be benchmarked with an experiment.

The beauty of spin ice crystals is that they can be easily characterised by means of several techniques, e.g. neutron scattering, μSR, NMR, SQUID and PPMS.

For our specific analysis we used the following instruments:

1. Unpolarised neutron scattering at the SXD facility to study the features of the structural diffuse scattering arising from the defect structure of the lattice.

2. Polarised neutron scattering at the DNS facility to study the magnetism of the sample measuring the spin flip (SF) and non spin flip (NSF) channels.

3. 7 tesla SQUID magnetometer at the Clarendon Laboratory in Oxford to measure the difference in the magnetisation of the samples.

3.1 General aspects of neutron scattering

The neutron is a subatomic hadron particle that has no net electric charge and a mass slightly larger than that of a proton ≈ 1 GeV. With the exception of hydrogen-1, it is present in the nucleus of every single atom, and it dilutes the Coulomb repulsion of the protons. Neutrons bind with protons and one another via the nuclear force; the effective number of neutrons in the nucleus is called the neutron number and it reveals the specific isotope of that atom.

While bound neutrons in nuclei can be stable, free neutrons are unstable and they undergo a beta decay with a mean lifetime of 881.5 ± 1.5s. Free neutrons can be produced in nuclear fission and fusion, while for experiment there are dedicated neutron sources like research reactors (e.g. DNS in Munich) and spallation sources (e.g. SXD in ISIS). The wavelengths of thermal neutrons make them suitable as probes for the determination of both the chemical and magnetic structures of the compounds.

Here we outline the relevant theory of neutron scattering following Ref. [54]. We first derive the expression of the potential due to the magnetic interaction between a neutron and an unpaired electron. The operator which corresponds to the magnetic dipole moment of the neutron is:

$$\hat{\mu}_n = -\gamma \frac{e\hbar}{2m_p} \hat{\sigma} \tag{3.1}$$

where m_p is the mass of the proton, e its charge, $\gamma = 1.913$ and $\hat{\sigma} = \{\sigma_x, \sigma_y, \sigma_z\}$ is the Pauli spin operator for the neutron.

The corresponding operator of the magnetic dipole moment of the electron is:

$$\hat{\mu}_e = -2 \frac{e\hbar}{2m_e} \hat{s} \tag{3.2}$$

where m_e is the mass of the electron and e its charge. Here $\hat{s}$ represents the spin angular momentum operator in unit of $\hbar$, thus the eigenvalues of its components are $\pm 1/2$. Notice that, although $\hat{\sigma}$ and $\hat{s}$ both relate to particles of spin $1/2$, their definition differ by a factor of 2 due to relativistic corrections.

If we consider an electron with momentum $\hat{p}$, the magnetic field due to its magnetic dipole moment at a general point $\vec{R}$ is:

$$\vec{B}_D = \nabla \times \vec{A} \quad \text{with} \quad \vec{A} = \frac{\mu_0}{4\pi} \frac{\hat{\mu}_e \times \hat{R}}{|\vec{R}|^2} \tag{3.3}$$

where $\hat{R}$ is a unit vector in the direction of $\vec{R}$ and μ_0 is the vacuum permeability.

The magnetic field due to the momentum of the electron can be calculated using the Biot-Savart law as:

$$\vec{B}_I = \frac{\mu_0}{4\pi} I \frac{\vec{dl} \times \hat{R}}{|\vec{R}|^2} \tag{3.4}$$

where $I\vec{dl} = -2\mu_B \hat{p}/\hbar$.

Therefore the total magnetic field is:

$$\vec{B} = \vec{B}_D + \vec{B}_I = \frac{\mu_0}{4\pi} \left[\nabla \times \left(\frac{\hat{\mu}_e \times \hat{R}}{|\vec{R}|^2} \right) - \frac{2\mu_B}{\hbar} \frac{\hat{p} \times \hat{R}}{|\vec{R}|^2} \right] \tag{3.5}$$

The potential of a neutron with dipole moment $\hat{\mu}_n$ in this field is:

$$V = -\hat{\mu}_n \cdot \hat{B} = -\frac{\mu_0}{4\pi}\gamma\mu_B \left(\frac{e\hbar}{m_p}\right)\hat{\sigma}\cdot\left[\nabla\times\left(\frac{\hat{s}\times\hat{R}}{|\vec{R}|^2}\right) + \frac{1}{\hbar}\frac{\hat{p}\times\hat{R}}{|\vec{R}|^2}\right] \tag{3.6}$$

In general the cross section for a process in which the system changes from an initial state λ to a final state λ', and the neutron changes from an initial state $(\vec{k},\sigma)$ to a final state $(\vec{k}',\sigma')$ is:

$$\left(\frac{d^2\sigma}{d\Omega dE'}\right)_{\sigma\lambda\to\sigma'\lambda'} = \frac{k'}{k}\left(\frac{m}{2\pi\hbar^2}\right)^2 |\langle\hat{k}'\sigma'\lambda'|V_m|\hat{k}\sigma\lambda\rangle|^2\delta(E_\lambda - E_{\lambda'} + \hbar\omega) \tag{3.7}$$

where V_m is the potential between the neutron and all the electrons in the scattering system.

The evaluation of $\langle\hat{k}'|V_m|\hat{k}\rangle$ is written in many books (see e.g. Ref. [54]), and it can be demonstrated that the final result is:

$$\left(\frac{d^2\sigma}{d\Omega dE'}\right)_{\sigma\lambda\to\sigma'\lambda'} = \frac{k'}{k}(\gamma r_0)^2|\langle\sigma'\lambda'|\hat{\sigma}\cdot\vec{Q}_\perp|\sigma\lambda\rangle|^2\delta(E_\lambda - E_{\lambda'} + \hbar\omega) \tag{3.8}$$

where r_0 is the classical radius of the electron and $\vec{Q}_\perp$ is the vector projection of $\vec{Q}$ (the Fourier transform of the magnetisation) on to the plane perpendicular to $\hat{k}$. In particular, the geometrical relation between $\vec{Q}$ and $\vec{Q}_\perp$ is:

$$\vec{Q}_\perp = \vec{Q} - (\vec{Q}\cdot\hat{k})\hat{k} \tag{3.9}$$

Therefore we can write:

$$\begin{aligned}\vec{Q}_\perp^\dagger\cdot\vec{Q}_\perp = [\vec{Q}^\dagger - (\vec{Q}^\dagger\cdot\hat{k})\hat{k}]\cdot[\vec{Q} - (\vec{Q}\cdot\hat{k})\hat{k}] = \vec{Q}^\dagger\cdot\vec{Q} + \\ -\vec{Q}^\dagger\cdot(\vec{Q}\cdot\hat{k})\hat{k} - \vec{Q}\cdot(\vec{Q}^\dagger\cdot\hat{k})\hat{k} + (\vec{Q}^\dagger\cdot\hat{k})\hat{k}\cdot(\vec{Q}\cdot\hat{k})\hat{k} = \\ \vec{Q}^\dagger\cdot\vec{Q} - (\vec{Q}^\dagger\cdot\hat{k})(\vec{Q}\cdot\hat{k}) = \sum_{\alpha,\beta}(\delta_{\alpha\beta} - \hat{k}_\alpha\hat{k}_\beta)Q_\alpha^\dagger Q_\beta\end{aligned} \tag{3.10}$$

where $\alpha,\beta = x,y,z$ and $\delta_{\alpha\beta}$ is the Kronecker delta.

Notice that the cross section in Eq. 3.8 must be summed over the final states (σ',λ') and averaged over the initial states (σ,λ), thus:

$$\begin{aligned}\frac{d^2\sigma}{d\Omega dE'} = \frac{k'}{k}(\gamma r_0)^2\sum_{\alpha,\beta}(\delta_{\alpha\beta} - \hat{k}_\alpha\hat{k}_\beta) \\ \sum_{\lambda,\lambda'}p_\lambda\langle\lambda|Q_\alpha^\dagger|\lambda'\rangle\langle\lambda'|Q_\beta|\lambda\rangle\delta(E_\lambda - E_{\lambda'} + \hbar\omega)\end{aligned} \tag{3.11}$$

where p_λ is the probability that the neutron is initially in the state λ.

3.1.1 Elastic Cross Section for Single Crystals

For a Bravais crystal with localised electrons, the elastic cross section (i.e. when $\hbar\omega = 0$) is obtained from Eq. 3.11 by replacing the matrix elements with their limiting values as $t \to \infty$. Therefore the general formula for unpolarised neutrons is:

$$\left(\frac{d\sigma}{d\Omega}\right)_{el} = const. \left[\frac{1}{2} g_J F(\vec{k})\right]^2 \sum_{\alpha,\beta} (\delta_{\alpha\beta} - \hat{k}_\alpha \hat{k}_\beta) \sum_{\vec{l}} \exp^{\imath \vec{k}\cdot\vec{l}} \langle S_0^\alpha \rangle \langle S_{\vec{l}}^\beta \rangle \quad (3.12)$$

where $const. = (\gamma r_0)^2 N \exp^{-2W}$. Here $r_0 = \mu_0 e^2 / 4\pi m_e \sim 2.82\ fm$, N is the number of cells in the system, $g_J = g_S + g_L$ is the Landé g factor, $F(\vec{k})$ is the magnetic form factor to the ion and W is the Debye-Waller factor.

Equation 3.12 is the most general expression of the cross section, but we can try to simplify it exploiting the symmetries of the pyrochlore lattice. We have already seen in Sec. 1.4.2 that the O(1) are located on the sites of an FCC lattice (see Fig. 3.1), thus we can choose the origin of our reference system at this point and then we can find the coordinates of the rare earth ions.

The common basis for the FCC lattice is:

$$\hat{a}_1 = \frac{1}{\sqrt{2}}(0,1,1) \quad \hat{a}_2 = \frac{1}{\sqrt{2}}(1,0,1) \quad \hat{a}_3 = \frac{1}{\sqrt{2}}(1,1,0) \quad (3.13)$$

The length of the $Dy_2Ti_2O_7$ unit cell is $a = 2\sqrt{2} r_{nn}$ with $r_{nn} \approx 3.54$ Å, but it is common to define $r_{nn} = 1$ so the distance between two oxygens in the system becomes $\tilde{a} = 2$ in these units. Therefore a vector in the FCC lattice can be written as:

$$\vec{l} = n\frac{\tilde{a}}{\sqrt{2}}(0,1,1) + m\frac{\tilde{a}}{\sqrt{2}}(1,0,1) + p\frac{\tilde{a}}{\sqrt{2}}(1,1,0) \quad (3.14)$$

If we now want to express all the positions of the rare earth ions in the system using the length of the unit cell as a common unit, the previous vector becomes:

$$\vec{l} = \vec{t} + \vec{\Delta} = \frac{a}{2} n(\hat{j} + \hat{k}) + \frac{a}{2} m(\hat{k} + \hat{i}) + \frac{a}{2} p(\hat{i} + \hat{j}) + \vec{\Delta} \quad a = 2\sqrt{2} \quad (3.15)$$

Where $\vec{t}$ represents the displacements of the oxygens in the system and $\vec{\Delta}$ is the displacement of the rare earth ions from the centre of the tetrahedron. With this basis a general vector in the reciprocal space can be written as:

$$\vec{k} = \frac{2\pi}{a} k_1(\hat{j} + \hat{k} - \hat{i}) + \frac{2\pi}{a} k_2(\hat{k} + \hat{i} - \hat{j}) + \frac{2\pi}{a} k_3(\hat{i} + \hat{j} - \hat{k}) = \frac{2\pi}{a}(k_x, k_y, k_z) \quad (3.16)$$

Here $\hat{i} = (1,0,0)$ $\hat{j} = (0,1,0)$ and $\hat{k} = (0,0,1)$ are the three fundamental unit vectors, and if we evaluate the dot product between $\vec{t}$ and $\vec{k}$ we obtain:

$$\vec{k} \cdot \vec{t} = 2\pi(k_1 n + k_2 m + k_3 p) \quad (3.17)$$

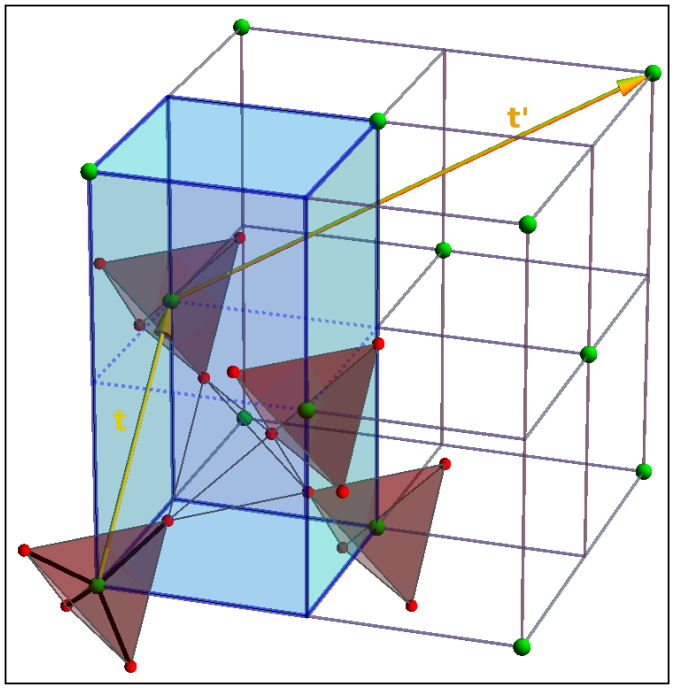

Figure 3.1: *Unit cell used for neutron scattering MC simulations.* – The origin of the reference system is commonly chosen on an O(1) site, in this way the four rare earth ions are located at the same distance (Δ) along the local $\langle 111 \rangle$ directions (black bar). Within this reference all the other tetrahedra can be reached with a translation t of the origin along the primitive vectors of the FCC lattice (yellow arrows).

Finally the elastic cross section of the pyrochlore lattice can be written as:

$$\left.\frac{\partial\sigma}{\partial\Omega}\right|_{el} = const. \left[\frac{1}{2} g_J F(\vec{k})\right]^2 \sum_{\alpha,\beta=x,y,z} \left[\left(\delta_{\alpha,\beta} - \frac{k_\alpha k_\beta}{|\vec{k}|^2}\right) \sum_{t,t'=-\infty}^{+\infty} \sum_{\Delta,\Delta'=1}^{4} e^{\imath\vec{k}\cdot[(\vec{t}+\vec{\Delta})-(\vec{t'}+\vec{\Delta'})]} S^{\alpha}_{t,\Delta} S^{\beta}_{t',\Delta'}\right] \tag{3.18}$$

Using simple trigonometric formule we can calculate the displacements (Δ) of the four Dysprosium atoms from the centre of the tetrahedron: $\vec{\Delta}_1 = \frac{a}{8}(1,1,1)$, $\vec{\Delta}_2 = \frac{a}{8}(-1,-1,1)$, $\vec{\Delta}_3 = \frac{a}{8}(-1,1,-1)$ and $\vec{\Delta}_4 = \frac{a}{8}(1,-1,-1)$. Since the summation over Δ in Eq. 3.18 does not depend on t or t', we can take it out from the summation and then calculate it explicitly (see Tab. 3.1):

Therefore the phase factor becomes:

$$\sum_{\Delta,\Delta'=1}^{4} e^{\imath\vec{k}\cdot(\vec{\Delta}-\vec{\Delta'})} = 4 + 2\cos\left[2\pi\left(\frac{k_x}{4}+\frac{k_z}{4}\right)\right] + 2\cos\left[2\pi\left(\frac{k_x}{4}+\frac{k_y}{4}\right)\right]$$

$\Delta \| \Delta'$	$\frac{a}{8}(1,1,1)$	$\frac{a}{8}(-1,-1,1)$	$\frac{a}{8}(-1,1,-1)$	$\frac{a}{8}(1,-1,-1)$
$\frac{a}{8}(1,1,1)$	$(0,0,0)$	$\frac{a}{4}(1,1,0)$	$\frac{a}{4}(1,0,1)$	$\frac{a}{4}(0,1,1)$
$\frac{a}{8}(-1,-1,1)$	$\frac{a}{4}(-1,-1,0)$	$(0,0,0)$	$\frac{a}{4}(0,-1,1)$	$\frac{a}{4}(-1,0,1)$
$\frac{a}{8}(-1,1,-1)$	$\frac{a}{4}(-1,0-1)$	$\frac{a}{4}(0,1,-1)$	$(0,0,0)$	$\frac{a}{4}(-1,1,0)$
$\frac{a}{8}(1,-1,-1)$	$\frac{a}{4}(0,-1,-1)$	$\frac{a}{4}(1,0,-1)$	$\frac{a}{4}(1,-1,0)$	$(0,0,0)$

Table 3.1: *Phase factors of the magnetic ions in Eq. 3.18.*

$$+2\cos\left[2\pi\left(\frac{k_y}{4}+\frac{k_z}{4}\right)\right]+e^{\imath 2\pi\left(\frac{k_y}{4}-\frac{k_x}{4}\right)}+e^{\imath 2\pi\left(\frac{k_y}{4}-\frac{k_z}{4}\right)}+e^{\imath 2\pi\left(\frac{k_z}{4}-\frac{k_y}{4}\right)}$$
$$+e^{\imath 2\pi\left(\frac{k_z}{4}-\frac{k_x}{4}\right)}+e^{\imath 2\pi\left(\frac{k_x}{4}-\frac{k_y}{4}\right)}+e^{\imath 2\pi\left(\frac{k_x}{4}-\frac{k_z}{4}\right)} \quad (3.19)$$

Moreover we can also simplify the summation over t and t' in order to obtain the following expression:

$$\sum_{t,t'=-\infty}^{+\infty} e^{\imath\vec{k}\cdot(\vec{t}-\vec{t'})} = \sum_{n,m,p,n',m',p'=-\infty}^{+\infty} e^{\imath 2\pi[k_1(n-n')+k_2(m-m')+k_3(p-p')]} =$$

$$\sum_{n,m,p,n',m',p'=-\infty}^{+\infty} \cos\left\{2\pi[k_1(n-n')+k_2(m-m')+k_3(p-p')]\right\} \quad (3.20)$$

Finally the elastic magnetic cross section for a spin ice crystal is:

$$\left.\frac{\partial\sigma}{\partial\Omega}\right|_{el} = (\gamma r_0)^2 N\left[\frac{1}{2}g_J F(\vec{k})\right]^2 e^{-2W}\left(4+2\cos\left[\pi\left(\frac{k_x+k_z}{2}\right)\right]\right.$$
$$+2\cos\left[\pi\left(\frac{k_x+k_y}{2}\right)\right]+2\cos\left[\pi\left(\frac{k_y+k_z}{2}\right)\right]+e^{\imath\pi\left(\frac{k_y-k_x}{2}\right)}$$
$$\left.+e^{\imath\pi\left(\frac{k_y-k_z}{2}\right)}+e^{\imath\pi\left(\frac{k_z-k_y}{2}\right)}+e^{\imath\pi\left(\frac{k_z-k_x}{2}\right)}+e^{\imath\pi\left(\frac{k_x-k_y}{2}\right)}+e^{\imath\pi\left(\frac{k_x-k_z}{2}\right)}\right)$$
$$\sum_{\alpha,\beta=x,y,z}\left[\left(\delta_{\alpha,\beta}-\frac{k_\alpha k_\beta}{|\vec{k}|^2}\right)\sum_{n,m,p,n',m',p'=-\infty}^{+\infty} S^{\alpha}_{n,m,p,\Delta}S^{\beta}_{n',m',p',\Delta'}\right.$$
$$\left.\cos\left\{2\pi[k_1(n-n')+k_2(m-m')+k_3(p-p')]\right\}\right] \quad (3.21)$$

3.1.2 Polarisation Analysis

So far we have considered the scattering of the neutrons only from one momentum state to another one. However, experiments which determine the spin state as well as the momentum of the neutron can give further information on the sample.

The spin state of a neutron is defined relative to a direction known as the polarisation direction, and the scattered spin states of the particle are analysed along it. For simplicity we assume that this direction coincides with $\hat{z}$.

We can denote the spin states of the neutron in this way: up by (u) with eigenvalue $+1$ and down by (d) with eigenvalue -1. With these assumptions Eq. 3.8 gives rise to four different cross sections, known as spin state cross sections, which correspond to: $u \to u$, $d \to d$, $u \to d$ and $d \to u$. The first two processes do not involve any change in the spin direction, therefore they are called the Non Spin Flip (NSF) channels. The latter two are called the Spin Flip (SF) channels.

In order to calculate the four spin state cross-sections for the magnetic scattering in Eq. 3.8, we notice that:

$$\begin{aligned}
\langle u|\hat{\sigma}\cdot\vec{Q}_\perp|u\rangle &= Q_{\perp z}\\
\langle d|\hat{\sigma}\cdot\vec{Q}_\perp|d\rangle &= -Q_{\perp z}\\
\langle u|\hat{\sigma}\cdot\vec{Q}_\perp|d\rangle &= Q_{\perp x} - \imath Q_{\perp y}\\
\langle d|\hat{\sigma}\cdot\vec{Q}_\perp|u\rangle &= Q_{\perp x} + \imath Q_{\perp y}
\end{aligned} \tag{3.22}$$

For example we can verify the first of the above relations as follows:

$$\begin{gathered}
\langle u|\hat{\sigma}\cdot\vec{Q}_\perp|u\rangle = \langle u|(\sigma_x,\sigma_y,\sigma_z)\cdot(Q_{\perp x},Q_{\perp y},Q_{\perp z})|u\rangle = \\
\begin{pmatrix} 1 \\ 0 \end{pmatrix}\begin{pmatrix} Q_{\perp z} & Q_{\perp x} - \imath Q_{\perp y} \\ Q_{\perp x} + \imath Q_{\perp y} & -Q_{\perp z} \end{pmatrix}\begin{pmatrix} 1 \\ 0 \end{pmatrix} = Q_{\perp z}
\end{gathered} \tag{3.23}$$

The remaining three relations are obtained using the same procedure.

Therefore, once the polarisation direction is chosen, one can always find the components of $Q_\perp$ in order to calculate the NSF and SF channels. Notice that the sum of the two channels must give the non polarised cross section, and this can be a useful cross check at the end of the calculations. Moreover we can see that the NSF scattering is sensitive only to those components of the magnetisation parallel to the neutron spin, by contrast the SF scattering is sensitive only to those components perpendicular to it. Notice that if the polarisation is chosen parallel to the scattering vector, then the magnetisation in the direction of the polarisation will not be observed since the magnetic interaction vector is zero. In this case all magnetic scattering will be observed in the SF channel.

In spin ice experiments it is common to study the (hhl) plane, in this case the polarisation direction is along $[1,-1,0]/\sqrt{2}$, and we can express the four easy axis spins in the following way:

$$\hat{S}_1 = \tfrac{\sigma}{\sqrt{3}}\begin{pmatrix} 1 \\ 1 \\ 1 \end{pmatrix}\ \hat{S}_2 = \tfrac{\sigma}{\sqrt{3}}\begin{pmatrix} -1 \\ -1 \\ 1 \end{pmatrix}\ \hat{S}_3 = \tfrac{\sigma}{\sqrt{3}}\begin{pmatrix} -1 \\ 1 \\ -1 \end{pmatrix}\ \hat{S}_4 = \tfrac{\sigma}{\sqrt{3}}\begin{pmatrix} 1 \\ -1 \\ -1 \end{pmatrix}$$

where $\sigma = \pm 1$. Thus the three components of $S_\perp$ projected on the (hhl) plane are:

$$\hat{S}_{\perp,1} = \sigma\begin{pmatrix} \frac{2}{\sqrt{6}} \\ \frac{1}{\sqrt{3}} \\ 0 \end{pmatrix}\ \hat{S}_{\perp,2} = \sigma\begin{pmatrix} -\frac{2}{\sqrt{6}} \\ \frac{1}{\sqrt{3}} \\ 0 \end{pmatrix}$$

$$\hat{S}_{\perp,3} = \sigma \begin{pmatrix} 0 \\ -\frac{1}{\sqrt{3}} \\ -\frac{2}{\sqrt{6}} \end{pmatrix} \quad \hat{S}_{\perp,4} = \sigma \begin{pmatrix} 0 \\ -\frac{1}{\sqrt{3}} \\ \frac{2}{\sqrt{6}} \end{pmatrix}$$

Notice that only two spins contribute to the NSF channel in this plane, therefore we can rewrite Eq. 3.18 as follows:

$$\left.\frac{\partial\sigma}{\partial\Omega}\right|_{NSF} = const. \left[\frac{1}{2} g_J F(\vec{k})\right]^2 \sum_{t,t'=-\infty}^{+\infty} \sum_{\Delta,\Delta'=3}^{4} e^{i\vec{k}\cdot[(\vec{t}+\vec{\Delta})-(\vec{t'}+\vec{\Delta'})]} S^z_{\perp t,\Delta} S^z_{\perp t',\Delta'} \quad (3.24)$$

3.2 Characteristics of the SXD facility in ISIS

The Single Crystal Diffractometer (SXD) uses the time-of-flight Laue technique with an incident wavelengths ranging from $0.2 - 10$ Å to access large 3D volumes of reciprocal space in a single measurement (see Ref. [55]). This makes SXD especially powerful in applications involving surveys of reciprocal space such as phase transitions, incommensurate structures, and also in applications where sample orientation may be restricted due to its large shape. The eleven 64x64 pixel optically encoded ZnS scintillators provide an excellent resolution of reciprocal space with a very large Q range (see Fig. 3.2).

The structure determination programme reflects the strength of single crystal neutron diffraction in studies of non-bonded contacts, specifically those involving hydrogen atoms, thermal parameter analysis, and in the area of charge density studies where neutron diffraction data provide complementary information to high resolution X-ray studies. A recent innovation has resulted from exploitation of the flexible data collection method offered by the time-of-flight Laue technique, which allows data sets to be collected in relatively short periods of time. The ability to measure a structure at more than one temperature can have significant benefits, either to characterise thermal parameter behaviour (methyl group librations in paracetamol) or to study disorder (proton transfer in benzoic acid). The standard sample environment for measurements at room temperatures (RT) can be coupled with one of the following devices to explore different ranges of temperatures:

1. Liquid He Orange cryostat $(1.5 - 300)$ K.
2. Displex cooler $(12 - 300)$ K.
3. Furnace $(300 - 1200)$ K.
4. Cryostat with ^{3}He dilution insert $(0.3 - 300)$ K.
5. Top loading Closed Cycle Refrigerator (CCR) $(4 - 320)$ K.

The diffuse scattering caused by both dynamic and static effects can be studied, allowing short range order, defect structure and local orientational correlations to be probed. Applications of SXD also include:

1. Structure determination (including Hydrogen atom location).
2. Diffuse scattering (thermally induced disorder, disorder resulting from defect impurities, or the structure of short range magnetically ordered systems).
3. Phase transitions (including changes of symmetry, and superlattice reflections).
4. Incommensurate structures.
5. Fibre diffraction.

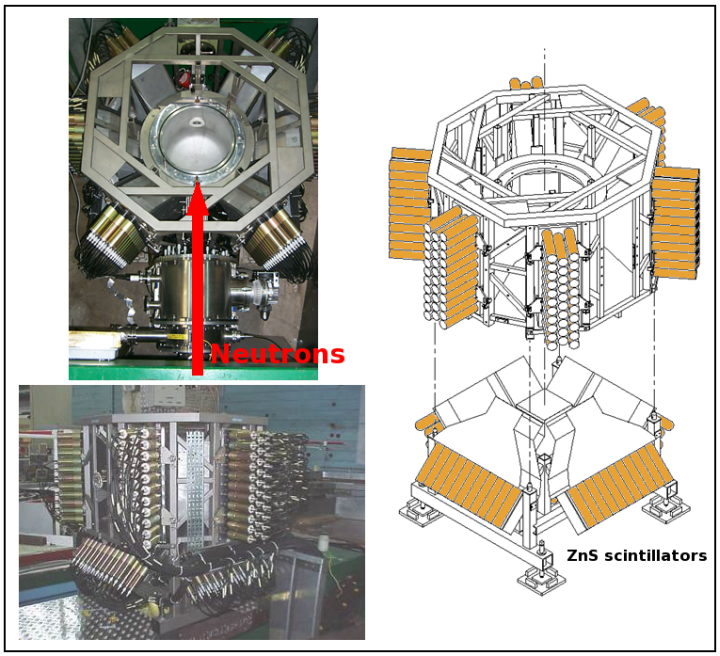

Figure 3.2: *The Single Crystal Diffractometer (SXD) at ISIS.* –

3.3 Characteristics of the DNS facility in Munich

The Diffuse Neutron Scattering spectrometer (DNS), visible in Fig. 3.3, is a versatile diffuse scattering cold neutron time-of-flight spectrometer with polarisation analysis (see Ref. [56]). It allows the unambiguous separation of nuclear coherent, spin incoherent and magnetic scattering contributions simultaneously over a large range of scattering vectors Q and energy transfers E. The wavelength of the monochromator ranges from $2.4 - 6$ Å, and it is possible to use both polarised and unpolarised neutrons for the analysis. In the former case 24 detection units with ^{3}He detector tubes provide a covered scattering angle in the horizontal plane ranging from $0 < 2\theta \leq 150$ degrees, in this case $Q_{max} = 4.84$ Å^{-1} with $E = 14.2$

meV or $Q_{max} = 1.93$ Å^{-1} with $E = 2.28$ meV. In the latter case 128 position sensitive ^{3}He tubes cover a total solid angle of 1.9 sr with a covered scattering angle in the horizontal plane ranging from $0 < 2\theta \leq 135$ degree.

The sample environment is excellent and it is very useful to study compounds at different temperatures. We can choose among these different types of cryostat:

1. Top loading CCR.
2. Closed cycle cold head.
3. Orange type cryostat.
4. Cryo furnace.
5. Dilution ^{3}He/^{4}He cryostat insert (down to $\sim$ 20 mK).
6. Cryomagnet (self-shielding, vertical field up to 5 tesla).

The main applications can be summarised as the follows:

1. Magnetic, lattice and polaronic correlations: geometrically frustrated magnets, strongly correlated electrons, emergent materials.
2. Single-crystal and powder time-of-flight spectroscopy: single-particle excitations, magnons and phonons.
3. Soft condensed matters: separation of coherent scattering from hydrogenous materials, polymer, liquids and glasses.

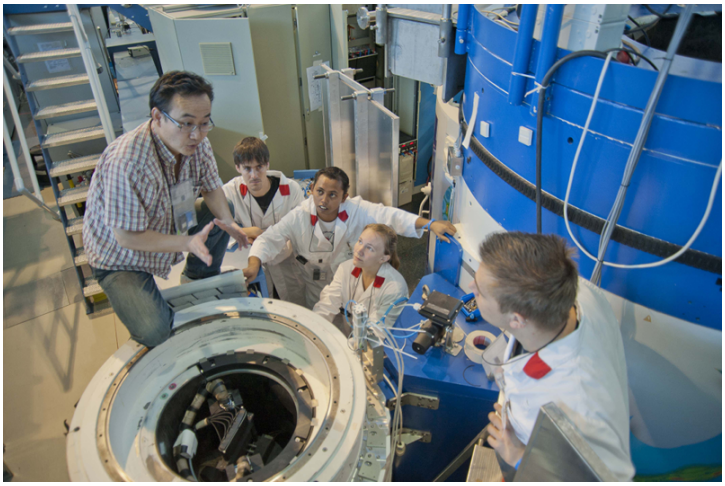

Figure 3.3: *The Diffuse Neutron Scattering spectrometer (DNS) in Munich. –*

3.4 7 tesla SQUID magnetometer

The Superconducting Quantum Interference Device (SQUID) consists of two superconducting magnets, separated by thin insulating layers to form two parallel Josephson junctions. We used it as a magnetometer in order to measure the magnetisation of our samples at $T = 2$ K.

In principle, two superconductors separated by a thin insulating layer, can experience the tunnelling effect of Cooper pairs of electrons through the junction. According to quantum mechanics, we can represent the Cooper pairs using wave functions similar to the free particle ones. In this way we can have two cases:

1. In the DC Josephson effect a current, proportional to the phase difference of the wave functions, can flow in the junction in the absence of a voltage.

2. In the AC Josephson effect a Josephson junction will oscillate with a characteristic frequency, which is proportional to the voltage across it.

Since frequencies can be measured with great accuracy, a Josephson junction has become the standard measure of voltage.

This device may be configured as a magnetometer to detect incredibly small magnetic fields ($\approx 10^{-14}$ tesla), small enough to be comparable to the magnetic fields in living organisms. For example they have been used to measure the magnetic fields in mouse brains to test whether there might be enough magnetism to attribute their navigational ability to an internal compass.

Figure 3.4: *The 7 tesla SQUID magnetometer at the Clarendon Laboratory in Oxford. –*

The great sensitivity of the magnetometer allows us to measure changes in the magnetic field associated with one quantum flux. One of the discoveries associated with Josephson junctions, was that flux is quantised in units of:

$$\Phi_0 = \frac{2\pi\hbar}{2e} \approx 2.0678\ 10^{-15}\ \text{tesla} * \text{m}^2 \tag{3.25}$$

If a constant biasing current is maintained in the magnetometer, the measured voltage oscillates with the changes in phase at the two junctions, which depends upon the change in the magnetic flux. Counting the oscillations allows us to evaluate the flux change which has occurred.

The user can measure both the magnetisation and the susceptibility of the system over a wide range of temperatures ($1.8 - 400$ K) with great accuracy, and the applied external magnetic field can go up to 7 tesla. Note that before starting the measurement, the sample is inserted into a white non magnetic straw closed at one end. This prevents the sample from falling in the chamber during the measurement and moving from the calibrated position when the system is oscillating.

Chapter 4

Internal Field Analysis

Contents

One of the most interesting features of spin ice is the study of the magnetic Coulomb field that emerges as the atomic dipoles fractionalise into magnetic monopoles. These topological defects have analogies in magnetic nano-arrays (Refs. [57]-[60]). Neutron scattering experiments, which provide magnetic fields correlations in reciprocal space, have produced some of the strongest evidence for the Gauge structure (Refs. [61],[62]) and "Dirac strings" (Ref. [63]) that emerge at low temperatures. However, a study on the magnetic fields on the lattice scale is still lacking.

The analysis of the internal fields of the crystal is very important to understand the field distribution generated from different spin configurations. In particular one could directly visualise the $1/r^2$ behaviour of the Coulomb field set up by a pair of monopoles in the system, and obtain useful information for the interpretation of NMR and μSR experiments.

In this chapter we show the main results of our MC simulations based on the theory developed in Sec. 2.5. These results are benchmarked with the experimental data obtained using NMR and μSR techniques (Refs. [64]-[66]).

4.1 Distribution of the internal Fields

The histograms of the internal field distribution $P(h)$, collected across a uniform cubic grid spanning the unit cell of a system with $\mathcal{L} = 4$, are shown in Fig. 4.1. The average has been calculated over 10^4 uncorrelated realisations of disorder.

In particular we show $P(h)$ for three specific cases of spin configurations: pure 2in-2out (i.e. the ground state) shown with a red line, configurations containing only two maximally separated monopoles, that are evaluated in the unit cell (blue line) or half the way between the pair (purple crosses), and completely random configurations of Ising spins with local $[111]$ easy axes (green line). Notice that the random configurations correspond to infinite temperature states of the system.

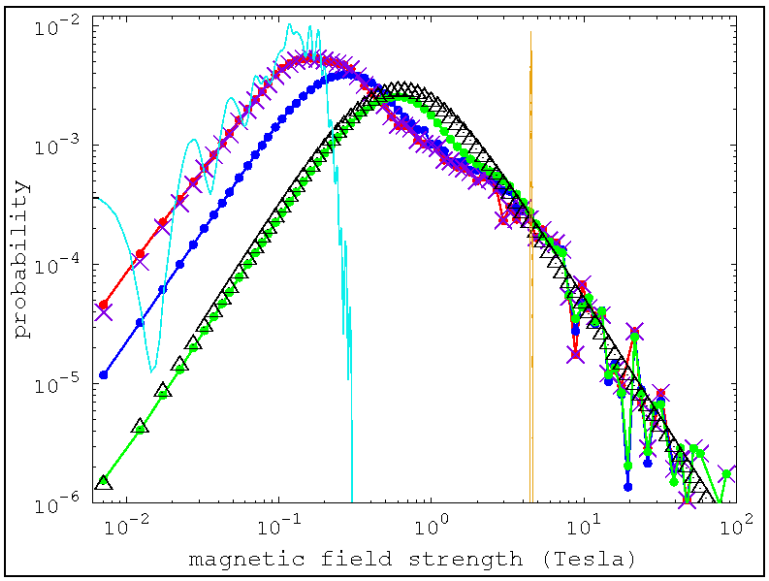

Figure 4.1: *Histogram of the internal field distribution for different spin configurations.* – The internal field distribution $P(h)$ has been collected across a uniform cubic grid spanning the unit cell of a system with $\mathcal{L} = 4$. The average has been done over 10^4 uncorrelated realisations of disorder for: pure 2in-2out (red line); configurations containing only two maximally separated monopoles, that are evaluated in the unit cell (blue line) or half the way between the pair (purple crosses) and random configurations of Ising spins with local $[111]$ easy axes (green line). In all cases $P(h) \propto h^2$ at small fields, while $P(h) \propto h^{-2}$ at large ones. Cyan and orange lines represents the internal field distribution calculated at the centre of the super tetrahedra and at the centre of the rare earth tetrahedra (low and high fields respectively), while black triangles are the fit of the random distribution using Eq. 4.1.

As is visible from Fig. 4.1 in all cases $P(h) \propto h^2$ at small fields, while $P(h) \propto h^{-2}$ at large fields. The latter property reflects the geometric probability of probing the $1/r^3$ divergence behaviour of h close to a spin. The former is a non trivial result which plays an important role in the interpretation of the recent μSR experiments (see Ref. [65]). In fact it implies that the probability to find magnetic fields of the order of few milli tesla in the bulk of the sample, is very low. The discrepancies of the three curves at low fields are due to the fact that the presence of a monopole

has a strong effect on the nearby environment. Therefore the statistical weight of the distribution is shifted from low to higher fields maintaining at the same time the overall shape.

This is higher counterintuitive, if one considers that spin ice 2in-2out tetrahedra are ferro magnetically ordered. In fact at a single tetrahedron level, the dipolar interactions are minimised by a ferromagnetic arrangement of the spins and the well-known 2in-2out ice rules maximise indeed the magnetic moment of a tetrahedron. Moreover the degeneracy resulting from the frustration leads to longer range correlations where the local moments do not align, like in a usual ferromagnet, and hence do not produce a macroscopic moment.

For a classical ferromagnet, one would expect that the internal fields are larger in the 2in-2out arrangement than they are in the presence of a monopole or otherwise disordered configurations. However, the emergent spin ice gauge structure is one which suppresses the coarse-grained moments locally, and this can be understood if we think about the dipoles aligning head-to-tail to form strings which have a preference for closing back on themselves ("flux loops"). Such strings exhibit zero net mono and dipole moments in a continuum treatment, which in turn leads to an effective suppression of the fields they produce at large distances.

These loops get broken down as monopoles appear since as they introduce endpoints of such loops. Therefore, the rapid decay of the loop field due to the vanishing of the monopole and dipole moments is replaced by the slower decay of the Coulomb field.

There is another reason that explains the non classical ferromagnetic behaviour of spin ice, and it can be described by looking at the detailed structure of the field distribution on the lattice scale. As one can see from Fig. 4.2(a), the internal field distribution for pure 2in-2out configurations exhibits a considerable local structure. Near the spins and at the centres of the rare earth tetrahedra there are large fields, higher than 4 tesla. In the interstitial regions the field average is much lower, and it is the lowest at the centres of super tetrahedra (see Sec. 1.4.2). These positions are the furthest away from the rare earth ions, and the probability of finding a low field site is greatly enhanced (see Fig. 4.1 cyan line), since the fields of nearby spins can cancel locally aided by symmetry, leaving a lower characteristic field scale and hence enhancing low field probability. This characteristic can also be observed in the field distribution, averaged half the way between the monopoles (see Fig. 4.1 purple crosses), which follows the form (see Refs. [67],[68]):

$$P(h) = \frac{h^2}{(h^2 + H_0^2)^2} \tag{4.1}$$

Notice that the value of the parameter H_0 depends on the configurations of the spin, and it can be related to the density of monopoles present in the system. In particular, the higher the density is, the lower the value of H_0 becomes.

Finally the detailed structure for random Ising $[111]$ spins shown in Fig. 4.2(b) directly demonstrates that, along with the breaking of ice rules, the spontaneous spatial organisation of fields strengths into high and low field locations within the

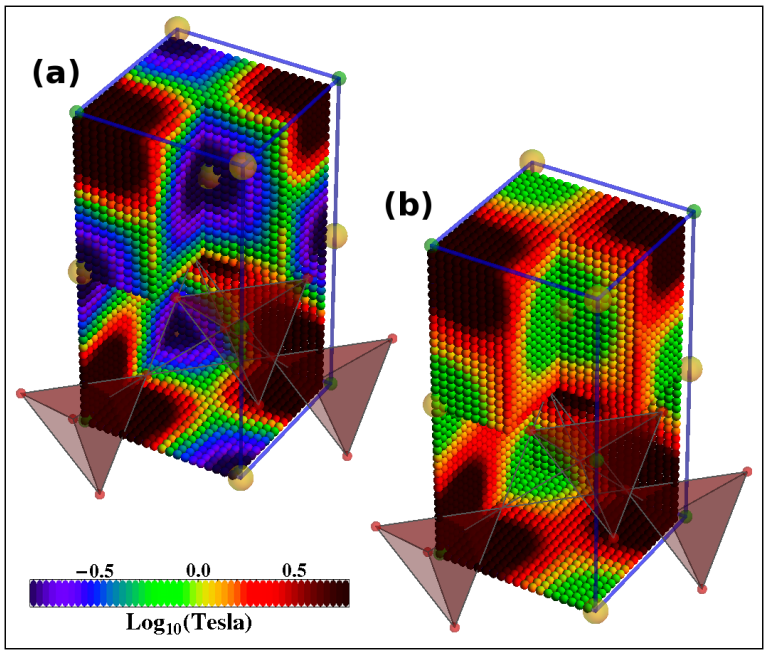

Figure 4.2: *Detailed structure of the field distribution on the lattice scale calculated in a quarter of the unit cell.* – **(a)** The internal fields distribution for pure 2in-2out configurations exhibit a considerable local structure with fields larger than 4 tesla near the spins and at the centres of tetrahedra, but much lower in the interstitial regions. The lowest field is felt at the centres of super tetrahedra (see Sec. 1.4.2). **(b)** Distribution of the internal field for random Ising $[111]$ spins. The comparison of the strength of the fields at the same location for these two cases (especially at the centre of the super tetrahedra) demonstrates that, along with the breaking of ice rules, the spontaneous spatial organisation of field strengths into high and low field locations within the unit cell is suppressed.

unit cell is suppressed. In summary the comparison of the field strengths at the same positions with pure 2in-2out configurations, especially at the centre of the super tetrahedra, show an increase of the strength of the magnetic field due to the presence of a higher degree of disorder in the system (i.e. monopoles).

4.1.1 An exciting challenge: measure the magnetic field set up by a monopole

Having analysed the spatial distribution of fields inside the unit cell, we next turn to visualising the field set up by a monopole.

Magnetic monopoles experience a relative force of Coulombic nature, therefore our question is: how is it possible to measure the corresponding magnetic field of Eq. 1.9 ? This goal is ambitious and quite difficult since internal fields vary

tremendously between different configurations, and the "Dirac string" emanating from the monopole carries a magnetisation M that cancels out the field H to preserve Gauss' law (see Eq. 1.6). In principle one can take care of these two issues averaging over many thousands of different configurations and measuring the field at points as far away as possible from any lattice sites, like at the centre of the super tetrahedra. The latter condition also minimises the strong field felt nearby the spins.

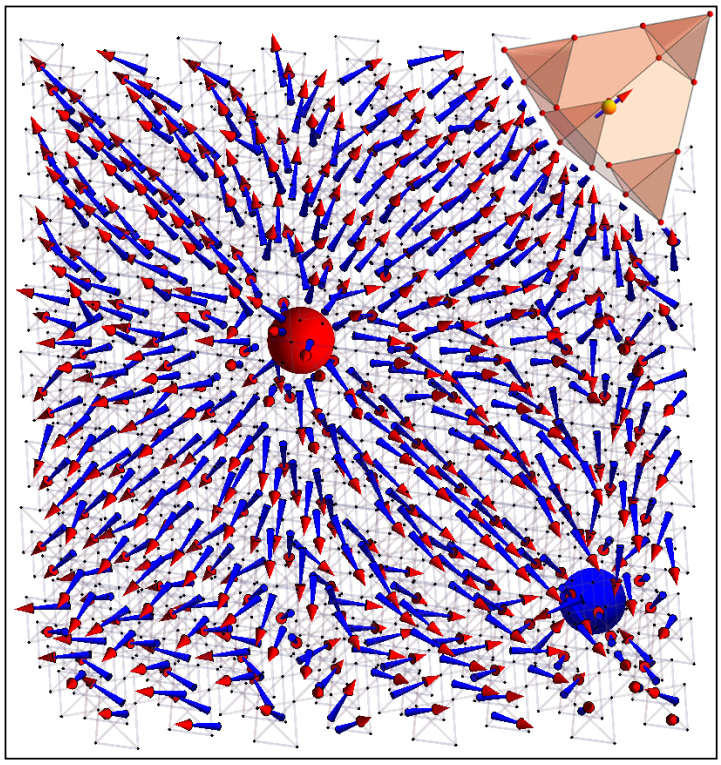

Figure 4.3: *Magnetic field set up by a pair of static monopoles.* – Averaged field set up by two stationary monopoles (blue and red spheres) calculated at the centres of the super tetrahedra (see inset), which visually reproduces the hedgehog like pattern expected from Eq. 1.9.

In Fig. 4.3 we show the direction of the average field calculated only at the centres of the super tetrahedra set up by two stationary monopoles (blue and red spheres), which visually reproduce the expected hedgehog like monopolar field pattern of Eq. 1.9. In particular we can easily see the force lines going from one monopole to the other. An analysis of this field is shown in Fig. 4.4.

The calculated field, averaged over 10^6 configurations (connected blue dots), has been evaluated along a line joining the two monopoles halfway along the $[001]$ direction in a supercell with $\mathcal{L} = 20$. The comparison with the Coulomb field set up by two magnetic charges with $q_M \approx 4.6\mu_B/\text{Å}$ located at the the positions

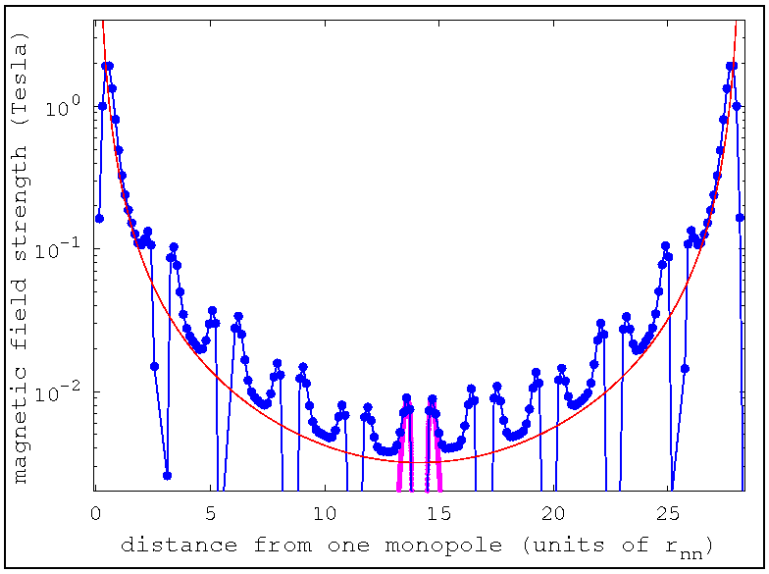

Figure 4.4: *Behaviour of the magnetic field of the monopoles.* – The average field calculated along the $[001]$ line joining two monopoles (connected blue dots) captures the leading behaviour of two magnetic charges ($q_M \approx 4.6\mu_B/\text{Å}$) located at the the positions of the monopoles to within 20% error (red line). The periodic deviations from the Coulomb field form are due to spins sitting very close to the line. This contribution is highlighted in magenta for the spin at the midpoints between the monopoles.

of the monopoles (red line), shows that our predictions are borne out but they are masked in part by the line passing very close to spins which contribute to a strong and periodic deviation from the theoretical curve at positions $2\sqrt{2}n$ with n integer and in units of r_{nn}.

4.2 Comparison with NMR and μSR experiment

We now show how it is possible to measure experimentally the internal field distribution using NMR or muons as probes.

4.2.1 Zero Field NMR experiment at the O(1) site

O-NMR experiments require ^{17}O isotope, which is the only one with a non zero magnetic moment. These measurements have been performed for the first time by Kitagawa and Takigawa from University of Tokyo, and we show their results in Fig. 4.6 (see Ref. [69]).

They have enriched the ^{17}O content in a crystal of $Dy_2Ti_2O_7$ grown by a floating zone image furnace, from the natural abundance of 0.01% to approximately

50% by annealing the crystal under 65% $^{17}O_2$ gas at 1000°C for several days.

According to our MC simulations, only the O(1) sites experience large internal fields higher than 3 tesla (see Fig. 4.1 orange line). By contrast the internal fields at the O(2) sites are much smaller and do not contribute to the observed signal (see Fig. 4.5). Moreover the electric field gradient is zero at the O(1) sites. Therefore, the NMR spectrum at these locations represents the distribution of the local fields directly obtained by dividing the frequency by 5.77185 tesla/MHz, which is the gyromagnetic ratio of ^{17}O nuclei.

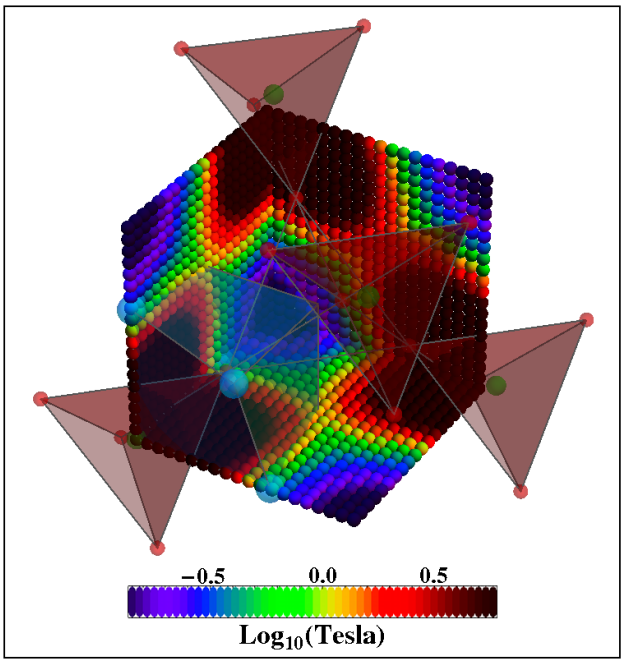

Figure 4.5: *Field strength at the O(2) sites.* – According to our MC simulations, only the O(1) sites (ghost green spheres) experience large internal fields higher than 3 tesla, by contrast the internal fields at the O(2) sites (ghost cyan spheres) are much smaller and do not contribute to the NMR signal.

Low-temperature experiments have been carried out by putting the sample into liquid ^{3}He mixing chamber.

Notice that the experimental data in Fig. 4.6 have been shifted and normalised to the intensity of the strongest peak in order to overlap the maxima of the distributions. The lower scale in Fig. 4.6 is for the experiment while the upper scale for our MC calculations.

As one can see the comparison with our MC simulations using a supercell with $\mathcal{L} = 6$ averaging over configurations at the equilibrium at $T = 0.6$ K (green line) or over an equally weighted ensemble of pure 2in-2out configurations (red line), is remarkably good. The experimental spectrum at $T = 0.1, 0.4$ K (blue and cyan lines respectively) is actually peaked at 4.5 tesla, i.e. about 25% above

the calculated peak. This shift is most likely due to spatial distribution of Dy-4f electrons causing deviations from a point dipole approximation (multipolar effects) or effects of Dy-O chemical bonding.

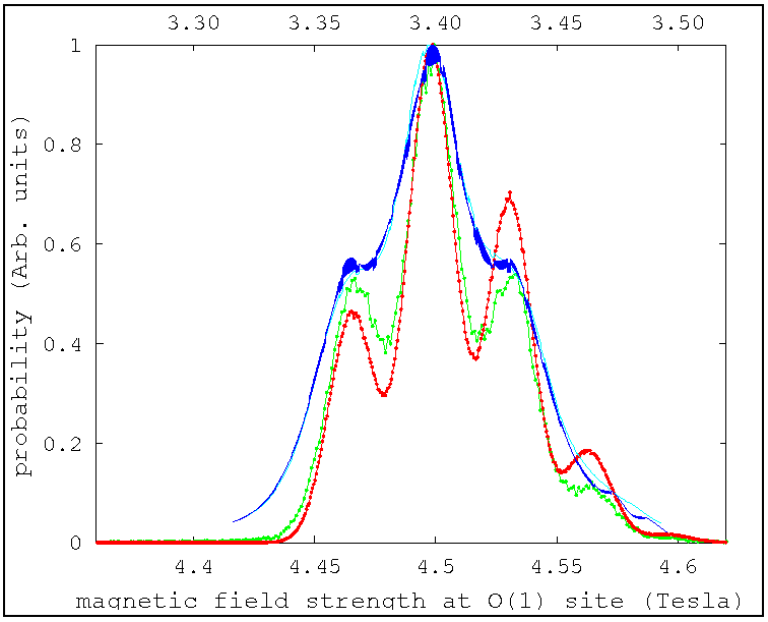

Figure 4.6: *Field distribution at the O(1) sites for $Dy_2Ti_2O_7$.* – Comparison of the histograms of the magnetic field strength at the O(1) site from: experimental NMR at $T = 0.1$ K (blue line) and $T = 0.4$ K (cyan line almost overlapped with the blue line), MC simulations for spin configurations in equilibrium at $T = 0.6$ K (green line) and an equally weighted ensemble of pure 2in-2out configurations (red line). The agreement of the simulations with the data is remarkably good. Notice that the experimental results have been shifted and normalised in order to overlap the maxima of the distributions. The lower scale is for the experimental data while the upper scale for our MC simulations (see Ref. [69] for details).

A promising aspect of these NMR measurements lies in the possibility of direct detection of monopoles. Indeed, when a tetrahedron hosts a monopole, the field at its O(1) site drops by approximately 13%. This effect is 3 times larger than the line width due to variations in the field at the O(1) site because of neighbouring monopoles or more distant spins. Therefore, the relative intensity of the NMR signal at this pair of field values could provide a quantitative measure of the density of monopoles.

In practice small densities may be hard to detect above the background, and monopoles must not move over the time scale of NMR spin-echo experiments (a few tens of microseconds) in order to be detected as a distinct resonance line. Given the insights from modelling AC susceptibility results, which suggest a hopping rate in the range of milliseconds (Ref. [70]), this condition seems comfortably

achievable.

4.2.2 The Muon Spin Rotation technique (μSR)

A muon is a spin $1/2$ lepton, that belongs to the same family as the electron. From a naive point of view it can be considered a heavy electron since its mass at rest is 105.7 MeV, i.e. 200 times the mass of an electron. The electronic charge is -1 for the elementary particle and $+1$ for the antiparticle, which is familiarly called the positive muon. The gyromagnetic ratio is 851.615 MHz/tesla and there are no quadrupolar effects. The muon is an unstable subatomic particle with a relatively long lifetime of 2.2μs, due to the weak interaction force. Since their mass is very large, they are never produced by radioactive decay, but in high energy interactions with normal matter (e.g. particle accelerators or cosmic rays).

When implanted in a solid, the positive muon behaves like a microscopic magnetometer, since its spin can Larmor precess in the local magnetic fields of the crystal. The sensitivity of this probe is quite high $10^{-3} - 10^{-4}\mu_B$. In an experiment we usually detect the decay products (positrons) that are emitted along the direction where the muon was pointing at the moment of death. This technique is called μSR (Muon Spin Rotation) and it provides direct information about local magnetic fields inside the crystal.

Notice that this technique can also be used to obtain dynamical information through the anisotropy of the electron-nuclear hyperfine interaction. In fact dynamical effects, if sufficiently rapid, lead to an averaging of this anisotropy. For example, if the rotation is fast about a single axis, the hyperfine interaction possesses axial symmetry. Therefore the nature of the dynamics (and hence the symmetry of the hyperfine tensor) determine the position and shape of the observed level-crossing resonances.

According to our MC simulations, the probability to find an internal field ≤ 10 mtesla where a positive muon can sit is very small (see Fig. 4.1). However it is reasonable to believe that the most probable positions are the interstitial regions between the ions. The intensity, measured at these sites, can be very useful in order to capture the dynamics of the entire system.

Notice that muons can also be implanted close to the crystal surface, in this case one has to pay attention to the stray field on the surface of the crystal since it can affect the measurement in a non trivial way.

4.2.3 Surface experiments

Ideally, we would like to measure the monopole field by placing probes at the centres of the super tetrahedra which, as we showed in Sec. 1.4.2, correspond also to the centre of Ti tetrahedra in the pyrochlore lattice. Placing an NMR-active ion here would in principle allow access to the Coulomb form of the internal fields. However, even if this remains a tough experiment for the time being, it is clear that a promising strategy is to suppress short-distance fluctuations by moving away

from spin locations even on the scale of a lattice constant. The obvious way to do this is to probe the fields close to the surface of a sample, in this way one can hope to see the farther-ranging monopole magnetic field undisturbed. Indeed, it is such a set-up that was proposed by Qi X-L et al. (see Ref. [71]) to measure the image magnetic monopole induced by an electric charge near the surface of a strong topological insulator.

4.2.4 Magnetic avalanches

Our work also sheds light on a range of non-equilibrium phenomena recently measured in spin ice (Ref. [72]), and their prominent analogues in artificial spin ice (Ref. [73]). While the field strength throughout the unit cell fluctuates wildly, the field projected onto the spin direction on a lattice site is known to be near constant for an "ideal" interaction. Using the conventional dipolar Hamiltonian (Eq. 1.1), we found a broadening of 0.80 ± 0.03 tesla (see Ref. [17]). This field sets the energy scale for creating bound monopole pairs at low temperatures. This quantity, as well as the Coulomb interaction between two monopoles as they separate, is important for triggering the avalanches which have received much attention of late.

4.3 Discussion

A recent article by S. Bramwell et al. (see Ref. [65]) has reported the possibility to use μSR experiments to measure the monopole charge, via an analogy to the Wien effect familiar from electrolytes. The common Wien effect, first explained by Lars Onsager in 1934 (see Ref. [74]), describes the non linear and non equilibrium response of a weak electrolyte from moderate to high electric fields. It is remarkable that this theory can be applied also to a lattice system as shown in Ref. [75].

However, from the perspective of our calculations, we would like to make some comments on that work:

1. We note that one important feature of the data presented in Ref. [65] is that the signal was extracted from sites where positive muons experience very low fields, of the order of a few milli tesla. This follows from the observation that doubling a transverse field of strength 1 mtesla doubles the μSR precession frequency. From our calculation it is clear that there is a very low density of such sites, located preferentially near the centres of super tetrahedra. Therefore it seems very unlikely that the substantial muon signal is emanated from these sites in the bulk.

2. The analysis of Bramwell et al. invokes two distinct phenomena: the applied magnetic field induces an increase in the monopole density, and this increase leads to an enhanced depolarisation rate.

The first feature is an expected phenomenon for the steady state of electrolytes in a field but, for spin ice, it can only occur as a transient. Since monopole motion magnetises the sample, there can be no steady state with a nonzero monopole

current. Moreover, in thermal equilibrium, the density of monopoles is believed to decrease in an applied field.

Regarding the second assumption, our results indicate that a field induced regime with heightened monopole density would be accompanied by a depletion of low-field sites. This aspect is qualitatively in agreement with the results in Ref. [65], where they claim that the rate of decay of the μSR asymmetry gets larger in the Wien setting as the applied field is increased.

Combining the above observations leads us to consider the interesting possibility that the signal arises from the action of an enhanced monopole density on muons implanted outside the sample. The idea here is that outside the sample the monopole fields would dominate over the much smaller fields present in their absence, since the field of a monopole decays less slowly than that of an isolated spin.

Interestingly, it was very recently suggested in Ref. [66] that the signal from muons inside the sample is lost altogether because of large fields (compared to 1 mtesla) and fast magnetic fluctuations relative to the muon timescale, and that the only measurable signal due to spin ice comes from muons implanted outside, sensitive to stray fields, which are analysed in Ref. [76].

A very rough estimate based on a monopole liquid subject to Debye screening (see Ref. [29]) suggests that in the temperature range $T = 0.2-0.5$ K, the magnetic field set up by a monopole measured at a distance $\approx 100 \pm 50^\circ$ Å from the sample surface, lies in the range relevant for μSR (between 0.1 and 1 mtesla), and it dominates the set up of an individual spin in the sample. Notice that, unlike stray fields set up by the magnetisation induced by a uniform external field, the monopole density grows with temperature, thus providing a qualitative discriminant between the two.

All such considerations point to the need for more detailed studies of what happens near the surface of a sample (e.g. what happens to the surface monopole density as a function of time and field). At present concerning little is known about the surface of spin ice samples, and the description of the equilibration in spin ice samples may be incomplete at low temperatures.

Finally, we would stress the fact that our considerations have entirely to do with spatially fluctuating static fields and their de-phasing of muon precession, whereas Ref. [65] proposes that large dynamical fluctuations are present.

4.4 Conclusion

We have provided a way of visualising the magnetic field of a monopole inside spin ice, yielding the first picture of this fractionalised excitation. Our work attests to the reality of the monopolar magnetic field not only at long length scale but also on the lattice scale.

Our analysis has further allowed us to provide a picture of the magnetic field distribution inside spin ice in considerable detail. This is also supported by the

novel zero-field NMR results which we reported here, and it has important implications regarding the μSR measurements which have been interpreted in terms of magnetolyte physics in spin ice.

Chapter 5

Defect structure of oxygen deficient pyrochlores

Contents

Generally speaking the positions of the atoms in the lattice are determined by a combination of the short range repulsion, and the Coulomb force acting between them. A vacancy can produce an imbalance in the Coulomb field set up by the ions, that move in order to compensate this problem. The system reacts finding new equilibrium positions that minimise the Madelung energy, and the evidence of these displacements can be found studying the structural diffuse scattering at low temperatures.

However, to make predictions on the atomic displacement is non trivial.

In Sec. 1.4 we saw that a defect pyrochlore structure could be created e.g. by removing the O(1) from the centre of the rare earth tetrahedra. The anions at these sites have the aim to dilute the Coulomb repulsion of the four A cations, and they are also responsible for the Ising axes of the spins. However, one can speculate that also the removal of an O(2) can affect the Crystal Electric Field (CEF) of the rare earth ions (as we saw in Sec. 2.1).

Therefore we would like to study which of the two oxygen sites has a higher probability to be removed, how the atoms relax in the presence of a vacancy and what are the consequences on both the CEF and on the magnetic properties of the sample.

5.1 The $Y_2Ti_2O_7$ crystals: the ideal candidates to study the structural diffuse scattering

Dr. D. Prabhakaran grew high quality $Y_2Ti_2O_7$ single crystals using the floating zone technique at the Clarendon laboratory at Oxford University. The common starting chemical purity of the powders is always 99.99% of pure RE_2O_3 (where RE stands for rare earth) and TiO_2 (see Ref. [77] for details). Then a few pieces of single crystal from the same batch as the as-grown sample were annealed in O_2 at $T = 1200°C$, with a flow rate of $50 mil/min$ for 2 days to enhance the content of oxygen ions. By contrast the oxygen depleted samples were grown and annealed in a flowing mixed gas of H_2 and Ar to reduce the content of oxygen.

We will refer to the annealed in O_2 sample as the annealed crystal, and to the annealed in H_2 sample as the depleted crystal ($Y_2Ti_2O_{7-\delta}$).

Notice that these crystals do not belong to the spin ice family, so why are we interested in studying them? The absence of large rare earth moments has two advantages:

1. We are able to focus on the structural diffuse scattering of the sample. These measurements are best performed at low temperatures in order to avoid contamination with thermal diffuse scattering, and for $Y_2Ti_2O_{7-\delta}$ there is also no magnetic diffuse background.

2. We are able to investigate the magnetism on the Ti ions for $Y_2Ti_2O_{7-\delta}$, since the magnetic signal is not overwhelmed by rare earth magnetism.

The $Y_2Ti_2O_7$ crystal has a pyrochlore lattice too, but it is non magnetic and all the elements have real scattering lengths and low absorption cross sections. Therefore it is the perfect candidate to study the diffuse scattering pattern.

According to our X-ray and thermo-gravimetric analysis (TGA), the depleted sample has a $\delta = 0.21$. However we were unable to establish accurately the value of δ for both the as grown and the annealed samples by X-ray diffraction, since X-rays are not sensitive enough to oxygen ions. By contrast neutrons are a better probe, and the analysis of the features of the diffuse scattering allowed us to estimate a $\delta = 0.03$ for the as grown sample, and a $\delta = 0.0$ for the annealed one. Table 5.1 summarises the results of the screening of the three samples. Notice that X-ray measurements have been performed by Dr. D.G. Porter at room temperature, who also refined the average structure of the samples using the software JANA2006, and fixing the occupancy value of the Ti ions.

As one can see the three samples have the same space group but different colours, meaning that the band gap is different. Dr. S. Sturniolo used Density Functional Theory (DFT) to calculate the band structure of the annealed $Y_2Ti_2O_7$ crystal, in this case the band gap is ≈ 3.1eV which is close to the UV region of the spectrum. In fact the sample looks transparent using a normal light and it shines under a UV lamp. Unfortunately DFT is not able to provide accurate results for

	Depleted	**As Grown**	**Annealed**
Colour	Black	Yellow	Transparent
Space Group	$Fd\bar{3}m$	$Fd\bar{3}m$	$Fd\bar{3}m$
Lattice parameter	10.123(3) Å	10.111(3) Å	10.102(2) Å
Y	0.992(9)	1.016(5)	1.01(1)
Ti	1	1	1
O(1)	0.88(2)	1.01(2)	0.97(3)
O(2)	0.96(2)	1.06(2)	1.10(2)
R_W	9.38	6.58	11.71
TGA	$\delta = 0.21$	$\delta = 0.03$	$\delta = 0.0$
Unit Formula	$Y_2Ti_2O_{6.79}$	$Y_2Ti_2O_{6.97}$	$Y_2Ti_2O_{7.00}$

Table 5.1: *X-ray and TGA screening of the $Y_2Ti_2O_7$ samples.*

the depleted environment yet. This limitation is due to the fact that the symmetry of lattice is lower and the calculation takes longer to converge.

However Tab. 5.1 shows another interesting result, i.e. the three crystals have different lattice parameters. This is a direct manifestation of the depletion in these systems. In fact in the defect environment an O(1) vacancy leaves the 4 nearest neighbour cations unshielded, and the Coulomb repulsion between them pushes away the ions one from the other. Therefore, the length of the unit cell increases.

The same analysis of the structural diffuse scattering has been repeated using $Dy_2Ti_2O_7$ samples. Table 5.2 shows the X-ray and thermo-gravimetric analysis (TGA) of these crystals, performed again by Dr. D.G. Porter at room temperature.

	Depleted	**Annealed**
Colour	Black	Yellow-Green
Space Group	$Fd\bar{3}m$	$Fd\bar{3}m$
Lattice parameter	10.102(3) Å	10.083(2) Å
Dy	0.994(6)	1.02(2)
Ti	1	1
O(1)	0.89(2)	0.98(2)
O(2)	0.96(2)	1.09(3)
R_W	7.3	6.4
TGA	$\delta = 0.20$	$\delta = 0.0$
Unit Formula	$Dy_2Ti_2O_{6.80}$	$Dy_2Ti_2O_{7.00}$

Table 5.2: *X-ray and TGA screening of the $Dy_2Ti_2O_7$ samples.*

5.2 Structural diffuse scattering of the defect lattice

The three $Y_2Ti_2O_7$ samples have been studied by diffuse neutron scattering using the single crystal diffractometer (SXD) at the ISIS pulsed neutron source at the

Rutherford Appleton Laboratory. SXD combines the white-beam Laue technique with area detectors covering a solid angle of 2π steradians, allowing comprehensive diffraction and diffuse scattering data sets to be collected. Samples were mounted on aluminium pins and cooled to 5 K using a closed-cycle helium refrigerator in order to suppress the phonon contribution to the diffuse scattering. A typical data set requires at least four orientations to be collected for 4 hours each. Data were first corrected for incident flux using a null scattering V/Nb sphere, then they were combined to a volume of reciprocal space and sliced to obtain single planar and linear cuts.

Figure 5.1 shows the experimental diffuse scattering pattern of the $Y_2Ti_2O_{7-\delta}$ crystal in the (hk7) plane at $T = 5$ K. We can see that there are beautiful exotic features made of a cross at the centre of the plane and four arcs that link the cross branches separated by a gap along the axial directions.

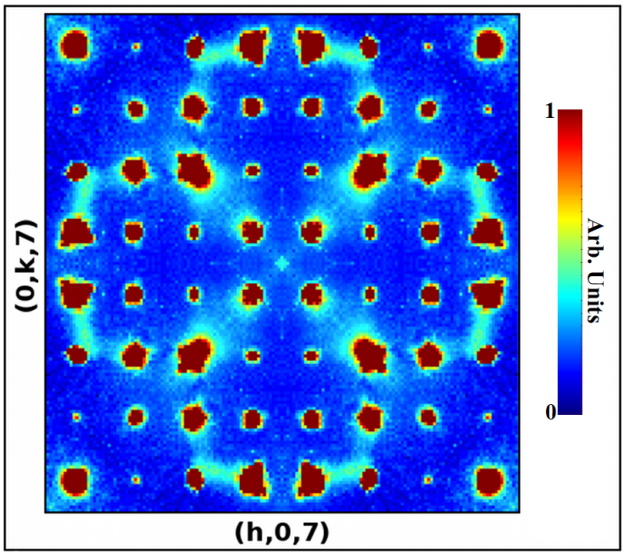

Figure 5.1: *Experimental diffuse scattering pattern of the $Y_2Ti_2O_{7-\delta}$ crystal in the (hk7) plane at $T = 5$ K.* – Notice the exotic features of the pattern made of a cross at the centre of the plane, and four arcs that link its branches separated by a gap along the axial directions.

Figure 5.1 has been created using the SXD2001 software at the SXD facility in ISIS in the following way:

1. The sample, background and Vanadium runs are normalised to the number of μamps of the measurement, notice that Vanadium and background runs are smoothed. Then the software subtracts the background to the sample's runs and it divides the results by the background subtracted Vanadium runs; pixel and time-of-flight are then converted to h,k,l points.

2. The resulting volume for each detector and run is stored separately in binary

files.

3. These files are then loaded into SXD2001 as a volumetric data set and individual planes can be sliced and visualised.

4. For symmetrising the volume one specifies the symmetry operators in reciprocal space in SXD2001, in our case we used $m\bar{3}m$ symmetry. Each symmetry operator is only applied to the part where the data have been measured and the results are collected in a new reciprocal space volume file. In the end this file is normalised by the number of data points contributing to each point of the volume.

5. For slicing line profiles there is again a tool in SXD2001, however a line through a 2D plane can only be drawn by hand and then it can be written to an ASCII file.

We repeated the same measurement on the as grown and annealed sample; the same pattern is present in the former case, but it is completely absent in the latter (see Fig. 5.2 [78]). Moreover the analysis of these features taking cuts in the (hk7) plane, showed a decrease in the intensity of the signal due to the different levels of depletion.

According to our analysis, the main features in Fig. 5.1 can be explained on the basis of short range repulsion and Coulomb interaction between the ions. In particular: the cross at the centre of the plane is originated by the displacements of the 4 Y ions along the local $\langle 111 \rangle$ directions, due to the presence of a nearby vacancy. These are the main displacements, and they produce a chain reaction that forces the surrounding ions to relax to new equilibrium positions whose diffuse scattering signatures are the arcs that links the cross branches. Moreover the removal of an O(1) in the system changes the oxidation state of two Ti^{4+} to Ti^{3+} in order to preserve charge neutrality, forcing the nearest neighbour O(2) to move towards the "more positive" charge (i.e. away from Ti^{3+}). Figure 5.3 shows the main displacements of the ions in the unit cell of the $Y_2Ti_2O_{7-\delta}$ crystal (orange arrows), and the comparison between the SXD data and our MC simulation in the (hk7) plane.

As is clearly visible from Fig. 5.3(b) our model is able to reproduce the main features of the diffuse scattering, that has the form of a beautiful cloverleaf in this plane. The diffuse scattering program that calculates this pattern is based on the "balls and springs" model, that will be discussed in the following section.

Notice that we repeated the same experiment using also a depleted $Dy_2Ti_2O_{7-\delta}$ single crystal. The diffuse scattering pattern in the (hk7) plane, shown in Fig. 5.4, was similar to that of $Y_2Ti_2O_{7-\delta}$ providing a strong link between these compounds. The MC simulations for a similar O(1) vacancy model successfully reproduced the data, but the high neutron absorption made these measurements more challenging, and it was not possible to study as grown samples using this technique.

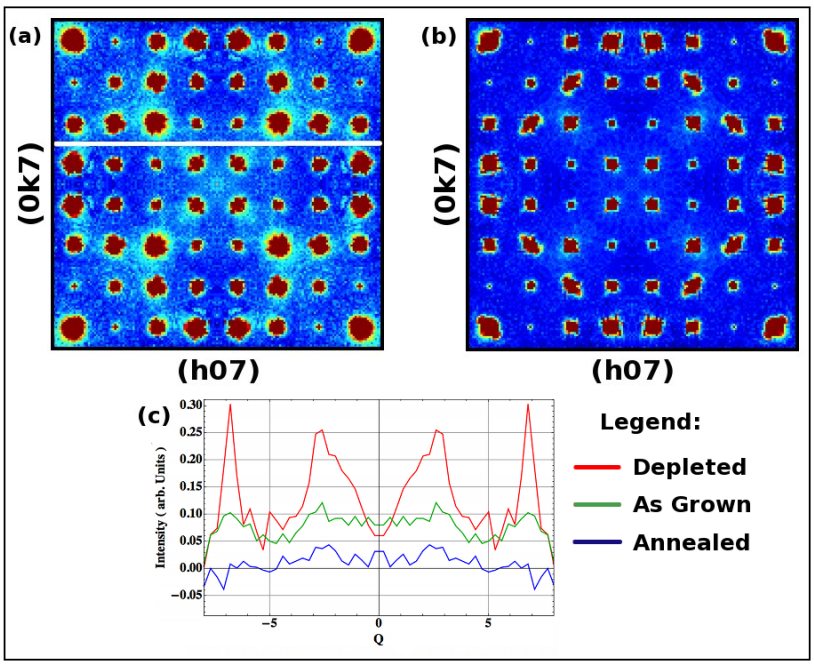

Figure 5.2: *Experimental diffuse scattering pattern of the $Y_2Ti_2O_7$ as grown and annealed crystals in the (hk7) plane at $T = 5$ K.* – The exotic diffuse scattering pattern is still present in the as grown sample **(a)** but it is completely absent in the annealed one **(b)**. **(c)** The cuts through the white line shows that the intensity of the diffuse scattering is higher in the depleted system and it tends to decrease in the others [78].

5.2.1 The "Balls and Springs" model

The diffuse scattering program models the ions as point like particles connected by springs in order to simulate the lattice dynamics and mimic the Coulomb interaction at low temperatures. This model is commonly called "balls and springs".

All the atoms in the system are identified by the three crystallographic coordinates, by the occupancy values (0 for vacancies or 1 in the other case) and by the charge. These ions are then connected only to their closest neighbours using springs of constant F_α, where the index α identifies the bond type between atom pairs. As a first approximation one can choose the springs by looking at the structure of the system (Refs. [79], [80]), and then by comparing the calculated diffuse scattering with the experimental data. The equilibrium length of each spring is chosen to match the stoichiometric lattice parameters.

At the beginning we put springs between every atom in the lattice, but the calculated structural diffuse scattering was completely different from the experimental one due the fact that springs were acting against each other. Therefore we tried to find the minimum number of springs in order to have the best agreement with the

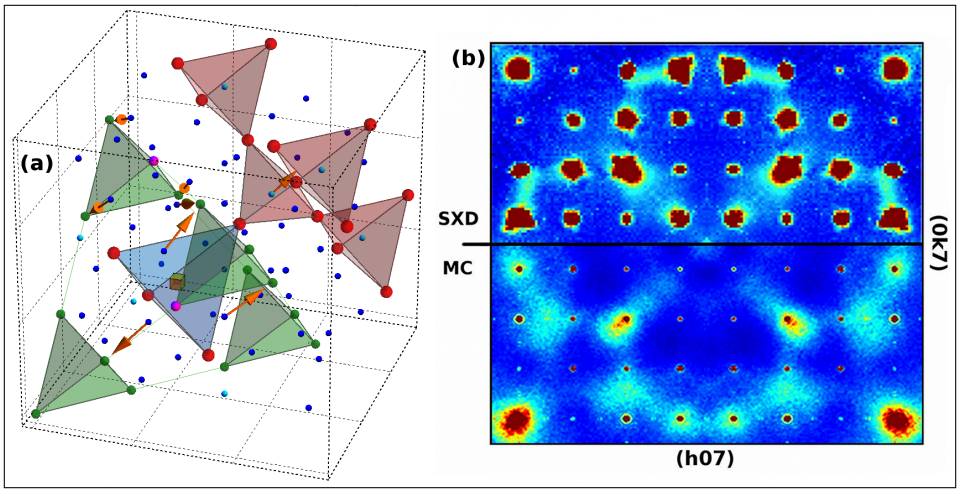

Figure 5.3: *Main displacements in the unit cell of $Y_2Ti_2O_{7-\delta}$ crystal.* – **(a)** The main features in Fig. 5.2 can be explained on the basis of the Coulombic interaction between the ions and the short range repulsion between neighbouring ions. The cross at the centre of the plane is originated by the displacements of the 4 Y ions (red spheres) along the local $\langle 111 \rangle$ directions due to the presence of a nearby vacancy (yellow cube). The removal of an O(1) in the system changes the oxidation state of two Ti^{4+} (green spheres) to Ti^{3+} (magenta spheres) in order to preserve charge neutrality. The closest O(2) (blue spheres) move towards the "more positive" charge (i.e. away from Ti^{3+}) as highlighted with orange arrows. The defect tetrahedron, highlighted in cyan, becomes bigger and it forces the ions to relax in new equilibrium positions (e.g. the O(1) (cyan sphere) moves along the $\langle 111 \rangle$ directions). The arcs are a signature of these displacements. **(b)** The comparison between the SXD data and our MC simulation at $T = 5$ K shows that our simple model is able to capture the main features of the diffuse scattering pattern, where we can clearly distinguish the cloverleaf shape of the pattern in the (hk7) plane.

data by looking at the symmetry of the lattice. After some trial and error we decided to use a total of 5 springs that connect: Y-O(2), Y-O(1), Ti-O(2), O(2)-O(2) along the longest octahedroid side and O(2)-O(1) along the longest cuboid side as shown in Fig. 5.5.

In the first stage of the program a model crystal comprising of $64 \times 64 \times 64$ unit cells is generated from the average structure obtained by the refinement of the SXD data with periodic boundary conditions. For each atom the program creates an array containing the coordinates of its nearest neighbours, labelled with the appropriate bond index α. Then a Marsaglia random generator code (see Ref. [53]) is used to remove randomly some O(1) ions according to the depletion value δ, and to create a pair of Ti^{3+} to preserve charge neutrality. Specifically, for every single O(1) removed the program selects randomly two Ti^{4+} among the 12 neighbours of the vacancy, and it changes their charges. This choice is motivated by the fact that

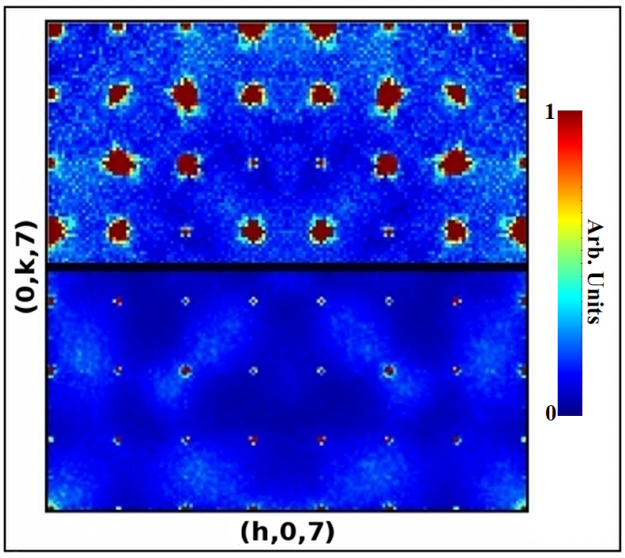

Figure 5.4: *Experimental diffuse scattering pattern of the $Dy_2Ti_2O_{7-\delta}$ crystal in the (hk7) plane at $T = 5$ K.* – The diffuse scattering pattern in the (hk7) plane looks similar to that of $Y_2Ti_2O_{7-\delta}$. The MC simulations for a similar O(1) vacancy model successfully reproduced the data, however, the high neutron absorption made these measurements more challenging, and it was not possible to study as grown samples using this technique.

the Coulomb energy favours the two Ti^{3+} ions to sit near the oppositely charged vacancy. Other choices (e.g. adding correlations between Ti^{3+} ions) are possible but the differences are minimal and discriminating between them is beyond the scope of the present thesis. Therefore we decided to use the most general case where the Ti^{3+} are generated randomly but close to the vacancy in the lattice.

The program assigns to the vacancy a null form factor, so that it does not contribute either to the crystallographic structure factor or to the intensity of the Bragg peaks when the diffuse scattering is calculated. The possibility of introducing correlations between the positions of the vacancies will be discussed later.

In order to account for the presence of vacancies in the spring model, we adjust some of the equilibrium spring lengths according to where we expect the effect to be largest on the grounds of energy considerations. Notice that the removal of the springs connecting to a vacancy would be a rather uncontrolled approximation and may lead to lattice instabilities. These adjustments are commonly called "size effects" (Refs. [79],[80]). Here we consider size effects on Yttrium ions when there is only one vacancy nearby and size effects on O(2) ions close to a Ti^{3+}. Note that Y ions between two occasionally close-by vacancies are not expected to displace significantly from their stoichiometric positions because they occupy a symmetric position; therefore, we displace exclusively Y ions close to only one vacancy. The Y ions are moved along the local $\langle 111 \rangle$ directions according to the symmetry

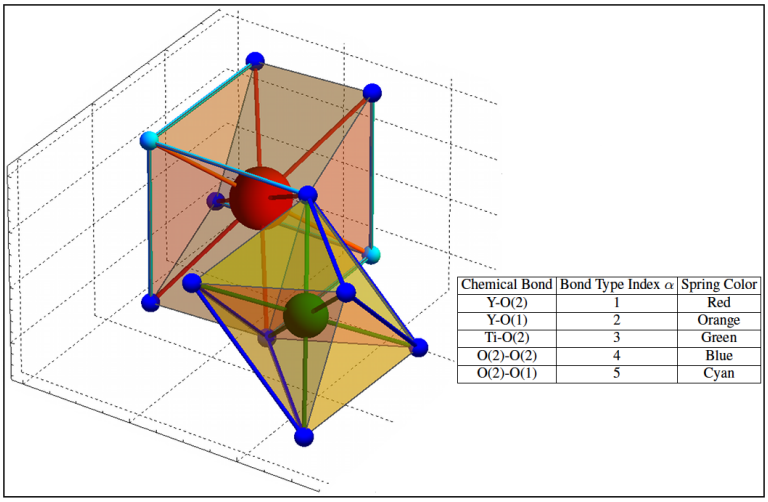

Chemical Bond	Bond Type Index α	Spring Color
Y-O(2)	1	Red
Y-O(1)	2	Orange
Ti-O(2)	3	Green
O(2)-O(2)	4	Blue
O(2)-O(1)	5	Cyan

Figure 5.5: *Different springs used in the simulation.* – Ions are connected to their closest neighbouring ions using springs, in order to mimic the Coulomb interaction in the lattice. There are a total of 5 types of springs in the system: Y-O(2), Y-O(1), Ti-O(2), O(2)-O(2) along the longest octahedroid side and O(2)-O(1) along the longest cuboid side. Each colour of the tubes corresponds to a specific spring as identified in the table. Black lines show the cubic and octahedral cages surrounding Y and Ti ions respectively.

of the system, away from a vacancy as expected from Coulomb interactions (in accord with Refs. [81],[82],[83]), and the value of the shift is set by preliminary comparison with the experimental data. The O(2) anions are moved away from Ti^{3+} towards Ti^{4+} again as expected from Coulomb interactions; the shift is set in order to obtain an average bond length between Ti^{3+}-O(2) $\simeq$ 2.03Å as measured in Ref. [84], preserving at the same time the average structure of the system (see Fig. 5.6(c)).

The program attempts then to relax the lattice in response to the size effects, and accounts for thermal fluctuations using a Monte Carlo algorithm. Each ion in the lattice is moved by a random vector drawn from a Gaussian distribution with zero average and standard deviation given by the refinement of the data. Then the Hook energy of the system is computed and the displacements are accepted or rejected according to the usual Metropolis algorithm.

After each MC cycle the force constants of the springs are adjusted to obtain the target isotropic thermal parameter (B_{iso} value) of the Titanium ions, which is chosen as reference since the Ti displacements are negligible compared to the other ions. The ratios between the springs are not known a priori, however to a first approximation one can set them by preliminary comparison with the experimental data averaged over the disorder. Monte Carlo cycles are repeated until a sufficiently good convergence is found in the values of the spring constants. Once this

is achieved, the spring constants are then fixed and the Monte Carlo simulations are used to compute average quantities of interest, such as the average positions of the ions and the diffuse scattering pattern in Fig. 5.3(b).

We conclude this section explaining the physical origin of the exotic features in the experimental diffuse scattering pattern. We find that the displacement of the Y ions next to a single vacancy is responsible alone for the cross-like pattern at the centre of the (hk7) plane. The four arcs around it are instead due to the relaxation of the other ions. In particular, the size effect introduced on the O(2) ions sitting between Ti^{4+} and Ti^{3+} ions is needed to reproduce the gap in the arcs visible along the axial directions of the plane. Electron density maps were calculated from the x-ray diffraction data using the charge-flipping algorithm in the JANA2006 refinement package [85]. The results presented in Fig. 5.6(e) show that the Y ions are displaced along $\langle 111 \rangle$ directions, providing independent confirmation of the defect structure proposed in Fig. 5.3(a).

The diffuse scattering pattern has been calculated also in other planes for further comparison. Figure 5.7 shows the experimental (upper half) and calculated (bottom half) diffuse scattering in the (hk8) and (hk11) planes. In all of them we find good agreement between the data and the simulation. Notice that all these patterns have been calculated using exactly the same values of the parameters and spring constants obtained for the (hk7) plane, without additional fitting or adjustments.

Finally in order to complete our analysis, we calculated the diffuse scattering pattern in the (hk7) plane using other models:

1. We removed O(2) ions randomly from the lattice according to the depletion value, and we added a size effect on Ti ions, that move away from the vacancy.

2. We randomly removed O(1) ions assuming stuffed Y ions on Ti sites to preserve charge neutrality, adding the previous size effects on both Y ions close to the vacancy and on the O(2) close to a stuffed Y^{3+}.

Figure 5.8 shows the experimental (upper half) and calculated (bottom half) diffuse scattering for these models. The interested reader should refer to App. C.1 for more details. For O(2) vacancies it is not possible to reproduce the cross at the centre of the plane. If it is assumed that the stuffed compound has O(1) vacancies, the model is essentially the same as Fig. 5.3(a), but with Ti^{3+} ions replaced by Y^{3+} ions, and the diffuse scattering is rather similar. However, the very different scattering lengths of Y to Ti gives some scattering features that are not observed in the data.

5.2.2 Correlations between Vacancies

The analysis of the diffuse scattering also provides information about how vacancies are distributed in the system. In order to decide which model we had to use in

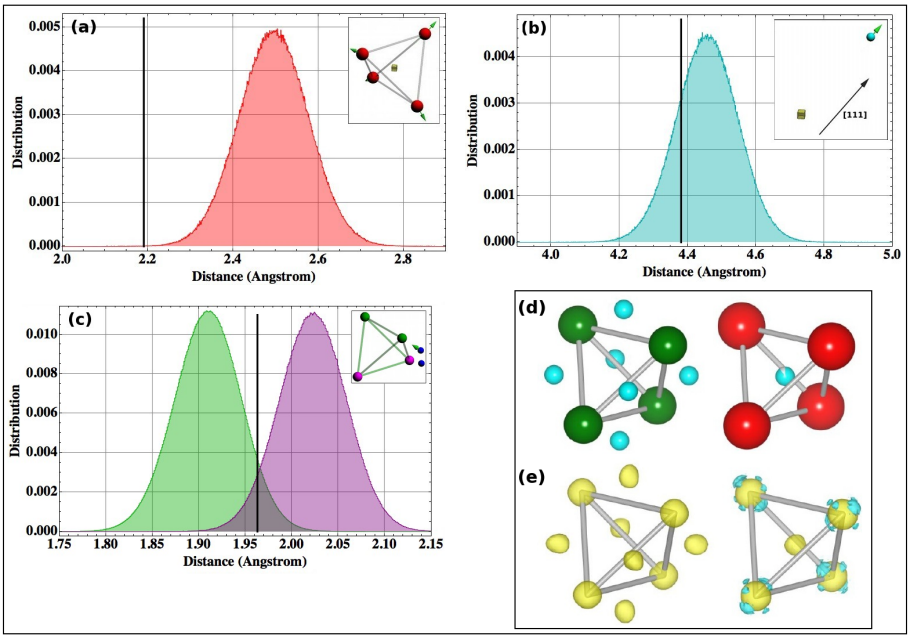

Figure 5.6: *Normalised distribution of the distances between the ions.* – **(a)** Yttrium-vacancy distance. Yttrium ions are moved away from the vacancy along the local $\langle 111 \rangle$ direction due to the Coulomb repulsion between the cations. **(b)** O(1)-vacancy distance. The O(1) moves away from the vacancy pushed by the shift of the Yttrium. **(c)** $Ti^{4+} - O(2)$ (green) and $Ti^{3+} - O(2)$ (purple) distance. The charge difference of these ions changes the bond lengths with the O(2) ions that move towards the Ti^{4+}. The black line in each panel shows the equilibrium distance in an ideal stoichiometric sample. **(d)** Titanium tetrahedron (left) with Ti in green and O(2) in blue, and Yttrium tetrahedron (right) with Y in red and O(1) in blue. **(e)** Electron density map, clearly showing Y displacements along $\langle 111 \rangle$ directions.

the Monte Carlo simulations, we ran some preliminary tests to understand whether the vacancies are distributed at random or their positions appear to be correlated (see Fig. 5.9). For this stage of the analysis, we used the "balls and springs" model with only Y size effects. As a result, the gaps in the arcs are not present in the scattering patterns, cf. Fig. 5.7(a) with Fig. 5.9(a), right panel.

We compared the case of uniformly distributed vacancies both to the case of positive correlations (favouring clustering of vacancies) and negative correlations (keeping the vacancies apart from one another). The corresponding probability distributions were obtained with a pre-existing algorithm [86],[87] that rearranges the positions of the vacancies starting from a uniform distribution (thus keeping the density constant), until the target degree of correlation is achieved.

We can see in Fig. 5.9 that the random distribution of vacancies gives the best agreement with the experimental diffuse scattering pattern. Positive corre-

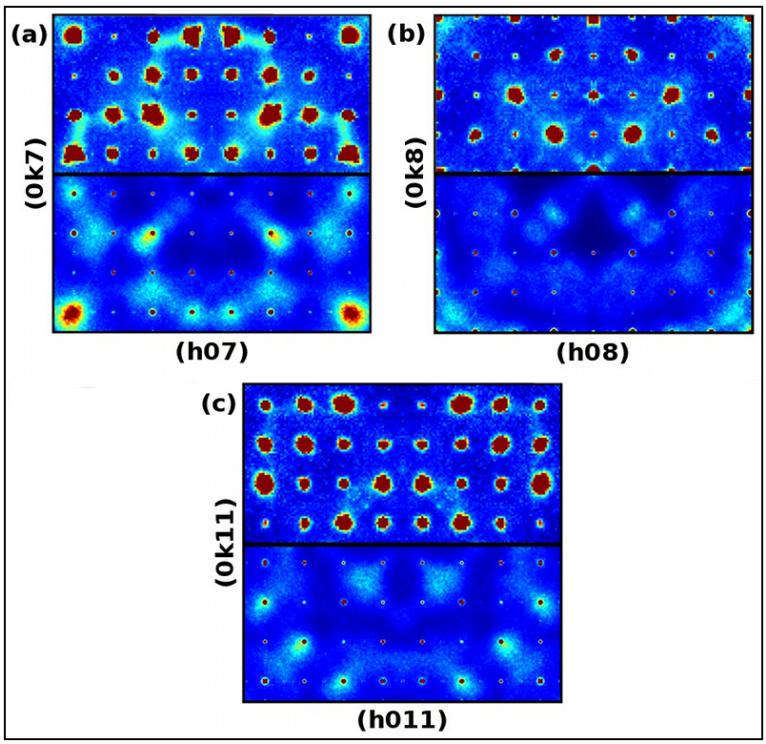

Figure 5.7: *Comparison of the experimental diffuse scattering with the MC calculation.* – The experimental diffuse scattering pattern (upper half quadrant) and the MC calculation (bottom half) for **(a)** the (hk7), **(b)** the (hk8) and **(c)** the (hk11) plane. All the exotic features of these planes are very well captured by our MC calculation. Notice that all these patterns are calculated using exactly the same values of the parameters we used for the (hk7) plane that was taken as our reference.

lations are unable to reproduce the cross-like pattern at the centre of the plane, whereas negative correlations introduce diffuse scattering intensity features that are not present in the experimental data. For this reason, in our simulations, we considered only the case of uniformly distributed oxygen vacancies.

5.3 Discussion

Our analysis of the structural diffuse scattering has pointed out some interesting results that we want to stress here, since they could be useful also to understand the physical properties of other pyrochlore crystals.

1. oxygen vacancies are predominantly located on the O(1) sites of the pyrochlore lattice, and this is due to the fact that the O(2) are more strongly bound with the Ti ions (see Refs. [36], [88]).

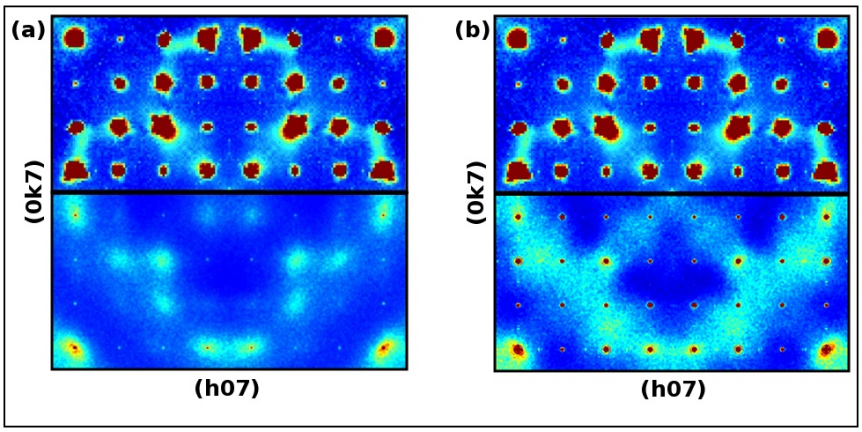

Figure 5.8: *Diffuse scattering calculation in the (hk7) plane.* – **(a)** O(2) vacancy model, **(b)** O(1) vacancy model plus stuffed Y ions on Ti sites. The first model does not reproduce the cross at the centre of the plane, while the second model shows additional diffuse scattering contributions that are not present in the experimental pattern.

2. We found that oxygen vacancies are the dominant defects in as grown crystals of $Y_2Ti_2O_7$. According to the TGA measurement, the oxygen depleted sample has a $\delta = 0.21$. If this sample is simply oxygen depleted, its chemical formula is $Y_2Ti_2O_{6.79}$. For comparison, if the depletion of oxygen was accompanied by substitution of Y^{3+} for Ti^{4+} for charge compensation to yield stuffed $Y_2Ti_2O_7$, the correct formula would be $Y_{2.42}Ti_{1.58}O_{6.79}$.

   Now, the fit to the X-ray diffraction data yields a ratio of occupation numbers for Y and Ti of $0.992(9)$. This value rules out significant stuffing for the oxygen depleted sample. The diffuse neutron scattering shows, even without the need to model the data, that the as grown sample has the same defect structure as the oxygen depleted one. Furthermore, annealing the crystal in an oxygen atmosphere gives a transparent crystal with no detectable diffuse neutron scattering. Hence, oxygen vacancies are firmly established as the leading structural defects in the as grown samples.

   We note that measurements of several samples from the same boule suggest that we can only tie down occupation numbers to within about 2% in our single crystal diffraction experiments. Hence we were unable to settle this issue by single crystal diffraction from as grown samples alone. We can, however, obtain a reasonably accurate estimate of $\delta = 21\%$ at the 10% accuracy level for the oxygen depleted sample by TGA analysis. Scaling the diffuse scattering signal from the as grown sample indicates a concentration of $\delta = 3\%$. The difference in signals in Fig. 5.2 where no signal is seen in a 2D plot for the annealed sample, places an upper limit on defects at about 0.3%.

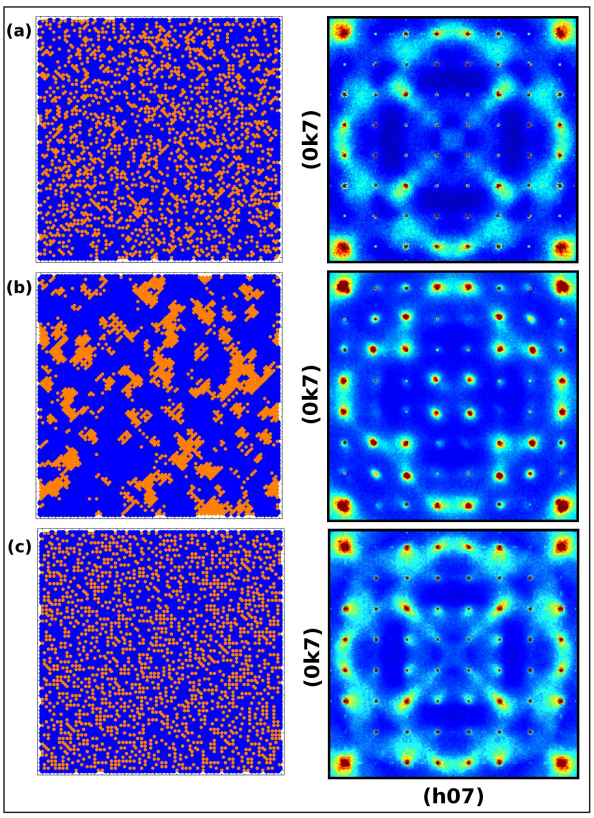

Figure 5.9: *Diffuse scattering calculation due to different correlations between vacancies in the system.* – **(a)** Randomly distributed, **(b)** positively correlated and **(c)** negatively correlated vacancies. The left panels show a 2D projection of the 3D system (blue) highlighting the positions of the missing oxygens (orange). For each case we calculated the diffuse scattering pattern (right panels), to be compared with the experimental data in Fig. 5.1. The best agreement is clearly given by the choice of a uniformly random distribution.

3. Ross et al. (see Ref. [89]) have performed careful powder neutron diffraction studies of $Yb_2Ti_2O_7$ to compare starting materials with crushed single crystals grown using the floating zone technique. They identify light stuffing of Ti sites by Yb at the percent level. They do not find much change upon annealing in oxygen and, therefore, oxygen deficiency does not seem to be significant in that case. However, it seems quite reasonable that other defects may be important for the other pyrochlores and with different growth conditions. In this specific case Yb has a smaller ionic radius than Y or Dy and, therefore, it will much more easily substitute for Ti.

   We stress that, in order to preserve charge neutrality, stuffing of Y^{3+} or Dy^{3+} on Ti^{4+} sites must be accompanied by a corresponding depletion of oxygen

ions in the system. The chemical formula is $\mathrm{R_{2+x}Ti_{2-x}O_{7-x/2}}$ where R is a rare earth or Y. Therefore, even in an ideally stuffed sample one has that for every two stuffed $\mathrm{Y^{3+}/Dy^{3+}}$ ions there must be a missing O(1), and we shall see in the next chapter that this affects the CEF of 4 neighbouring Y/Dy ions. Moreover, the fact that a change is observed in the sample upon annealing, strongly suggests that the oxygen depletion level in the as grown samples is higher than the level required to compensate any possible stuffing. This is all in keeping with the claim that oxygen depletion is the leading cause of magnetic impurities.

4. In the case of $\mathrm{Tb_{2+x}Ti_{2-x}O_{7-x/2}}$, Taniguchi et al. (see Ref. [90]) deliberately introduced stuffing, adjusting x by changing the mass ratio of the starting materials. It is clear from this interesting paper that stuffing can also affect low temperatures physical properties. The authors of this study do not appear to have explicitly considered the oxygen stoichiometry, simply stating that it depends on "oxidising conditions". Although they quote the formula $\mathrm{Tb_{2+x}Ti_{2-x}O_{7+y}}$, considerations of charge neutrality would seem to make it unlikely that y is positive and, as described above for stuffed pyrochlores, oxygen vacancies are again likely to play an important role.

5. The interesting analysis conducted by Blundred et al. on $\mathrm{Lu_2Ti_2O_{6.43}}$ (see Ref. [91]) showed that this compound has an anti site disorder between the two cation sub lattices (i.e. stuffing), oxygen vacancies both on O(1) and O(2) sites and the possibility of having a split vacancy consisting of two O(2) oriented along $\langle 110 \rangle$. As we said before our refinement rules out the presence of stuffed ions on both the cation sites, and we clearly demonstrated that oxygen vacancies are predominantly on the O(1) sites of the lattice. The probability of having a split vacancy in $\mathrm{Y_2Ti_2O_7}$ crystals is quite small; according to Ref. [92] the difference in energy between a split vacancy and a single O(2) vacancy is positive, thus a single symmetric vacancy is more stable. If this is the case, the simulations in Ref. [92] showed that the lowest energy configuration for a single vacancy system is a symmetric relaxation of neighbouring ions: towards the vacancy for anions and away from it for cations, which is excellent agreement with our model.

   A comparison between the structural diffuse scattering of $\mathrm{Lu_2Ti_2O_{6.43}}$ using neutrons and Fig. 5.1 could give us further informations on this mechanism.

6. Finally we would make a comment on the relative sensitivity of the diffuse neutron scattering. This was the only probe that allowed us to estimate the concentration of oxygen vacancies in the as grown and annealed samples, since it is much more sensitive to light elements (like oxygen) than diffuse X-ray scattering, neutron or X-ray diffraction.

5.4 Conclusion

We showed how it is possible to study the structural diffuse scattering of a compound by means of neutron scattering, which is also the best probe to investigate oxygen vacancies in the lattice. In our case, the different content of oxygen vacancies produced a pattern in the (hk7) plane made of a cross at the centre of the plane and four arcs that link the cross branches. This "cloverleaf" pattern has been studied with the "balls and springs" model, which mimics the Coulomb interactions of the ions in the crystal.

This analysis showed that vacancies are randomly distributed in the crystal, mainly on the O(1) sites of the pyrochlore lattice since they are not strongly bound with the cations (Refs. [36], [88]). The best agreement with the data was obtained using an oxygen vacancy model where we randomly removed O(1) ions and we moved Y and O(2) ions according to the Coulomb force. Finally we noticed that the gap in the four arcs can be related to the presence of Ti^{3+} in the system. These ions are created for charge compensation in presence of the vacancy.

It would be interesting to analyse the structural diffuse neutron scattering from other pyrochlore systems, in this way one can study the role played by oxygen vacancies, stuffing etc. in all these series of compounds and benchmark the results of the analysis with Ref. [92].

Chapter 6

Magnetism of oxygen deficient pyrochlores

Contents

Recent experiments conducted at sub-Kelvin temperatures show that magnetisation dynamics in spin ice samples occurs on far longer time scales than one could explain using straightforward monopole hydrodynamics, even accounting for Coulomb interactions (Refs. [93]-[95]). In an attempt to explain this discrepancy, magnetic impurities were shown to be capable of dramatically reducing the flow of magnetic monopoles, similarly to electrical conductors in which local impurities can decrease the electrical conductivity (see Ref. [96]). To date, magnetic impurities in spin ice have been modelled based on the assumption that they resemble "stuffed spin ice" (Ref. [97]). The determination of the nature of the defects in as-grown samples, whether they comprise substitutions or vacancies, the extent of the distortion of the surrounding lattice, and the effects on the magnetic properties, has become a pressing issue. Understanding these defects is crucial for experiments directed at single monopole detection, the observation of monopole currents, and the design of potential spin-ice devices.

In this chapter we study how O(1) vacancies affect the CEF and the magnetism of the sample, then we will discuss the role of these vacancies in the study of the dynamics of magnetic monopoles.

6.1 CEF analysis of the oxygen deficient spin ice crystals

The analysis of the Crystal Electric Field (CEF) set up by the defect oxygen environment surrounding a rare earth ion has been performed using the Point Charge Model (PCM) approximation developed in Sec. 2.1.

In order to proceed with the calculations, we used the "balls and springs" model to obtain the average positions of the oxygen ions surrounding a Dy next to a vacancy (averaged over all of the isolated vacancies in the system and over all the realisations of disorder).

The reference system for the CEF calculation was chosen following Prather's convention, i.e. we put the local $[111]$ easy axis along $\hat{z}$ and one of the C_2 axes along $\hat{y}$ (Ref. [40]). Tables 6.1, 6.2 show the crystallographic positions of the ions according to our "balls and springs" model averaged over 10000 realisations of disorder, for Dy next to only one or in between two vacancies respectively. The reference frame used in the tables is that of the crystallographic unit cell (the specific choice of origin is immaterial since only relative positions are relevant).

Ion Type	**x**	**y**	**z**
Dy	0.6236 ± 0.0167	0.6237 ± 0.0174	0.6241 ± 0.0166
O(1)	0.4950 ± 0.0066	0.4949 ± 0.0073	0.4950 ± 0.0070
O(2)	0.4985 ± 0.0075	0.8016 ± 0.0057	0.4997 ± 0.0079
O(2)	0.7500 ± 0.0073	0.7479 ± 0.0077	0.4501 ± 0.0057
O(2)	0.8014 ± 0.0061	0.4979 ± 0.0076	0.4985 ± 0.0071
O(2)	0.4493 ± 0.0055	0.7491 ± 0.0076	0.7493 ± 0.0070
O(2)	0.4981 ± 0.0070	0.4980 ± 0.0073	0.8020 ± 0.0053
O(2)	0.7496 ± 0.0070	0.4493 ± 0.0055	0.7496 ± 0.0072

Table 6.1: *Crystallographic positions according to the "balls and springs" model in the presence of one vacancy.*

Ion Type	**x**	**y**	**z**
Dy	0.6254 ± 0.0080	0.6238 ± 0.0071	0.6256 ± 0.0083
O(2)	0.4975 ± 0.0072	0.7995 ± 0.0052	0.4992 ± 0.0075
O(2)	0.7519 ± 0.0063	0.7512 ± 0.0082	0.4507 ± 0.0060
O(2)	0.8002 ± 0.0050	0.4973 ± 0.0067	0.4978 ± 0.0075
O(2)	0.4513 ± 0.0053	0.7539 ± 0.0076	0.7506 ± 0.0067
O(2)	0.4977 ± 0.0069	0.4966 ± 0.0075	0.7995 ± 0.0057
O(2)	0.7523 ± 0.0073	0.4493 ± 0.0053	0.7529 ± 0.0081

Table 6.2: *Crystallographic positions according to the "balls and springs" model in the presence of two vacancies.*

The coordinates of the ions give information on the symmetry of the environment and on the number of Stevens operators needed to describe it. In the case

of one vacancy it is still possible to recognise a scalenohedra, even if one of its corners is missing. By contrast when we remove two O(1) we are no longer able to recognise the cage, and the environment has a hexagonal symmetry where the O(2) are alternatingly located above and below the plane of the rare earth ion (see Fig. 6.2(b)).

In the PCM CEF calculation, the Coulomb potential is approximated by a spherical harmonic expansion. The number of spherical harmonics is directly related to the symmetry of the environment. For the ideal stoichiometric system the point group is D_{3d}, and according to Ref. [44] one needs only six Steven's operators in the expansion: $B_{20}, B_{40}, B_{43}, B_{60}, B_{63}$, and B_{66}. The depleted environment where we remove (at least) an O(1) and we relax all the ions in the lattice is far less symmetric. The system has no inversion centre and we are forced to use all 27 Stevens operators. Nevertheless our calculation shows that the six terms in the stoichiometric case are still the dominant ones in the expansion.

Indeed the difference in the CEF levels calculated with the full expansion or with an ad hoc expansion truncated to those six terms is negligible, as illustrated in Tabs. 6.3, 6.4.

Dy^{3+} Level	**Full one vacancy (meV)**	**Reduced one vacancy (meV)**
GS	0.0 (d)	0.0 (d)
1	14.22 (d)	14.12 (d)
2	41.35 (d)	41.28 (d)
3	79.91 (d)	79.85 (d)
4	126.58 (d)	126.52 (d)
5	178.48 (d)	178.41 (d)
6	232.19 (d)	232.12 (d)
7	285.36 (d)	285.3 (d)

Table 6.3: *CEF levels for* Dy^{3+} *in the presence of one vacancy.*

Dy^{3+} Level	**Full two vacancies (meV)**	**Reduced two vacancies (meV)**
GS	0.0 (d)	0.0 (d)
1	22.11 (d)	21.99 (d)
2	65.82 (d)	65.73 (d)
3	131.04 (d)	130.96 (d)
4	216.57 (d)	216.48 (d)
5	321.13 (d)	321.05 (d)
6	442.45 (d)	442.37 (d)
7	577.44 (d)	577.36 (d)

Table 6.4: *CEF levels for* Dy^{3+} *in the presence of two vacancies.*

Figure 6.1 shows the shape of the anisotropy of the magnetisation calculated in the PCM approximation for a Dy^{3+} ion, applying an external field of 1 tesla and

in the presence of one O(1) vacancy. The large blue spheres are a guide to the eye showing the defective oxygen environment surrounding the rare earth ion, namely one O(1) (cyan) and six O(2) (blue). The shape of the ellipsoid suggests that the typical strong easy-axis behaviour has been dramatically altered by the vacancy, which produces instead a strong easy plane behaviour perpendicular to the local [111] direction, as is clearly visible in Fig. 6.1.

Figure 6.2 shows the shape of the anisotropy of the magnetisation for a Dy^{3+} ion between two vacancies. Again, we observe a strong easy plane behaviour. In both cases we find that the magnitude of the in-plane magnetic moment is approximately $5.7\mu_B$, reduced with respect to the stoichiometric (easy axis) value $10\mu_B$.

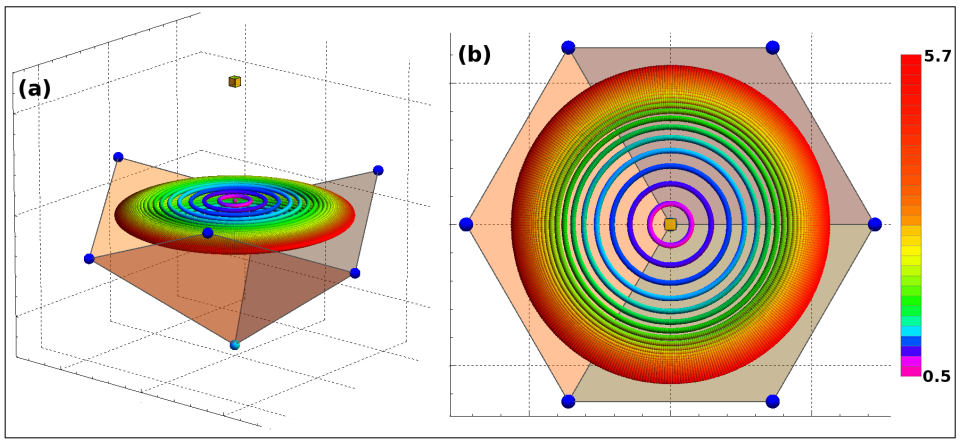

Figure 6.1: *CEF calculation of the shape of the anisotropy of the magnetisation in the presence of one vacancy for* Dy^{3+}. – **(a)** Each small coloured dot represents the tip of the magnetisation vector centred at the Dy^{3+} ion in response to a given applied external field of 1 tesla, calculated in the PCM approximation. Many values of the magnetisation are shown simultaneously for applied fields uniformly distributed on the unit sphere. The large spheres show the depleted environment surrounding the rare earth ion: one O(1) (cyan) and and six O(2) (blue). The positions of the atoms were averaged over 1000 realisations of disorder. The ellipsoid shape suggests an easy plane behaviour of the Dy^{3+} in the depleted environment, perpendicular to the local [111] direction. **(b)** Top view of the ellipsoid down the [111] axis. The colour bar indicates the magnitude of the magnetic moment of the rare earth ion in units of Bohr magnetons.

Notice that we only considered the surrounding oxygen ions in constructing the CEF Hamiltonians for the central rare-earth ion, and we ignored the six surrounding Ti ions. The latter are expected to account only for a small correction. In the specific case of oxygen-depleted samples, some of the surrounding Ti ions are likely Ti^{3+} instead of Ti^{4+}, which could introduce a further (minor) anisotropy in the easy-plane behaviour of a Dy ion close to a vacancy.

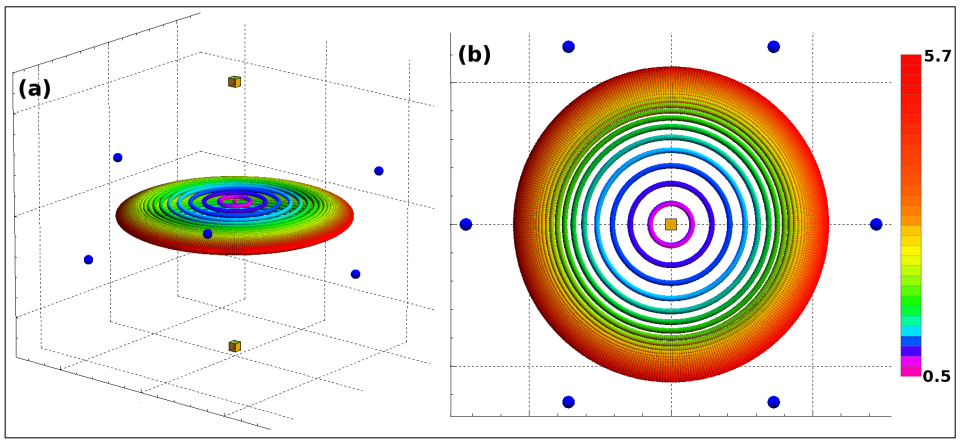

Figure 6.2: *CEF calculation of the shape of the anisotropy of the magnetisation in the presence of two vacancies for* Dy^{3+}. – **(a)** Same as in Fig. 6.1, for the case where the Dy ion lies between two vacancies. Again, we find evidence of strong easy-plane behaviour. **(b)** Top view down the [111] axis. The colour bar indicates the magnitude of the magnetic moment in units of Bohr magnetons.

6.2 Experimental evidence of the anomalous behaviour in the presence of vacancies

A change in the magnetic properties of the sample can be easily verified measuring the magnetisation of the system e.g. with a 7 tesla SQUID magnetometer. The analysis of the data using the theory developed in Chap. 2 provides useful information on the behaviour of the magnetic ions in the sample.

6.2.1 DC magnetisation analysis of $Y_2Ti_2O_7$ crystals

The annealed $Y_2Ti_2O_7$ crystal is non magnetic, since both Y^{3+} and Ti^{4+} have no electrons in the outer shell ($4d^0$ and $3d^0$ respectively). However the presence of Ti^{3+} in the lattice to preserve charge neutrality, makes the depleted $Y_2Ti_2O_7$ magnetic. Figure 6.3 shows the comparison of the magnetisation for the three $Y_2Ti_2O_7$ crystals collected with a 7 tesla SQUID magnetometer at $T = 2$ K.

As it is clearly visible the magnetisation of the annealed and as grown crystals is substantially reduced, but we found that in the latter sample the magnetic moment is a little bit higher than in the annealed one. This is consistent with the TGA measurement that showed tiny oxygen vacancies in the as grown system.

By contrast the depleted $Y_2Ti_2O_7$ shows a non zero magnetic moment, that has been fitted using the Brillouin function. Note that the external configuration of Ti^{3+} is $3d^1$ therefore, according to Hund's rules, we should have $J = 3/2$. However we also considered the possibility that the angular momentum is quenched, as often occurs for transition metal ions, and in this case we assumed $J = S = 1/2$.

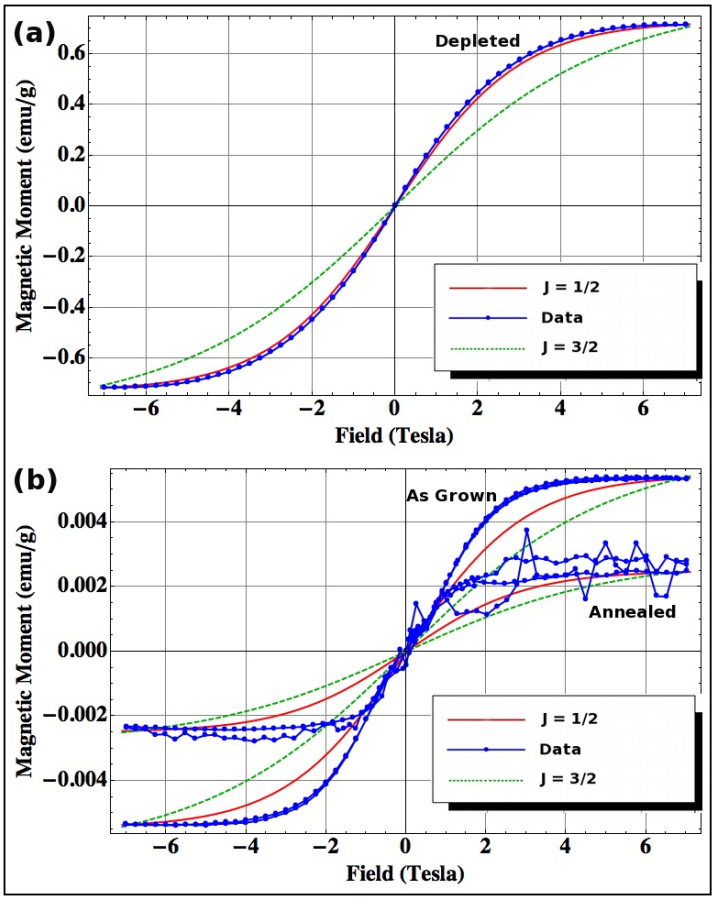

Figure 6.3: *Comparison of the magnetisation data for $Y_2Ti_2O_7$ crystals.* – The magnetisation measured with a 7 tesla SQUID magnetometer at $T = 2$ K, shows that the magnetic moment of the annealed and as grown crystals is substantially reduced. By contrast the depleted $Y_2Ti_2O_{7-\delta}$ shows a non zero magnetic moment.

The comparison of the two Brillouin functions for $J = 1/2$ (red line) and $J = 3/2$ (green dotted line) are shown in Fig. 6.3, the excellent agreement with the former fit confirms the presence of quenched Ti^{3+} ions in this compound.

We have to note here three important aspects:

1. The experimental data have been fit also using a classical Langevin function for an Ising, Heisenberg and easy plane system (see Chap. 2). However we obtained a poor agreement with the data because, unlike Dy^{3+}, Ti^{3+} is not a high spin classical system.

2. The only fitting parameter in the Brillouin function is the number of Ti^{3+} ions present in the compound. In principle one can calculate this number from the unit formula provided the knowledge of δ. However in all our

attempts we found that the number of Ti^{3+} in the compound was always an order of magnitude lower than the estimated one.

3. The discrepancies between the $J = 1/2$ model and the data of the as grown and annealed samples, suggest the presence of additional magnetic impurities.

4. At present we do not know why the annealed measurement looks so noisy. It seems unlikely that the oscillations and spikes are due to the physics of the system, rather than the sensitivity and accuracy of the instrument (according to the manual this should be $\geq 10^{-6}$ emu, a value much smaller than the saturation of the sample $\approx 10^{-4}$ emu).

The second aspect is not trivial, it implies that the magnetism in this compound is not simply due to a charge compensating number of isolated Ti^{3+} present in the system. One possible explanation is that the majority of neighbouring Ti^{3+} form strong antiferromagnetic bonds, and the observed signal arises from the remaining isolated Ti^{3+} ions. Another possibility is that a proportion of the Ti ions form Ti^{2+}, which is expected to have a non magnetic singlet ground state. It is even possible that partial charge compensation may be achieved through trapped electrons on vacancies, via the so-called F-centres often responsible for colour in this class of material. Incidentally, the presence of almost-free Ti^{3+} ions may be the rapidly fluctuating magnetic impurities required to understand the NMR relaxation at low temperatures (Ref. [98]).

6.2.2 DC magnetisation analysis of $Dy_2Ti_2O_7$ crystals

Figure 6.4 shows the comparison of the magnetisation for two $Dy_2Ti_2O_7$ crystals: annealed and as grown. In this case the data have been collected with a 7 tesla magnetometer at $T = 2$ K.

We have to stress here an important fact, regarding how we did the measurement on the the as grown and annealed crystals. In order to obtain a perfect comparison between the magnetisation of these two samples, we used this technique: first we measured a sharp needle taken from the as grown crystal, then we took out the needle and we annealed it in O_2 to create the annealed crystal. The advantage of this technique is that we have a great control on the orientation of the system when we apply the external field.

Finally the sample was remounted in exactly the same orientation of the previous one and, in this way, we were able to resolve this subtle difference in saturation magnetisation.

The as grown sample has a magnetisation lower than the annealed one, which is consistent with our CEF calculation that shows a decrease in the magnetic moment of Dy^{3+} ions.

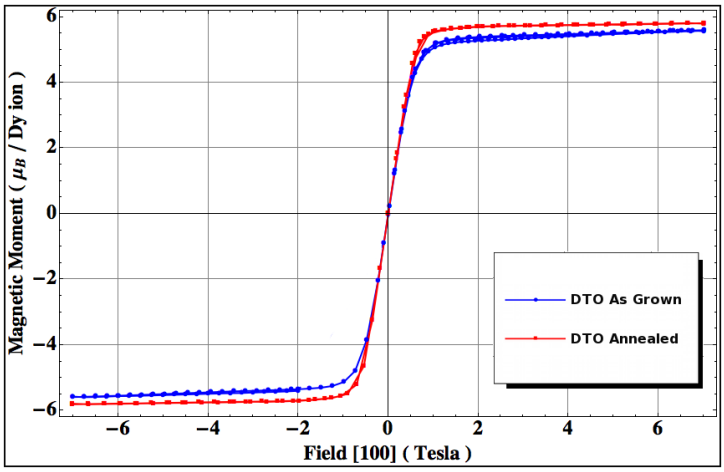

Figure 6.4: *Comparison of the magnetisation for the $Dy_2Ti_2O_7$ annealed and as grown crystals.* – The magnetisation measured with a 7 tesla magnetometer at $T = 2$ K, shows that the magnetic moment in the as grown system is lower than in the annealed case. This is expected to be due to tiny oxygen vacancies in the as grown system.

6.2.3 AC magnetisation analysis of $Dy_2Ti_2O_7$ crystals

J. Kycia and his team, conducted AC susceptibility measurements using a magnetometer in a dilution refrigerator at the University of Waterloo. For this experiment they used an as grown $Dy_2Ti_2O_7$ crystal with dimensions 1.0x1.0x4.0 mm^3, and an annealed $Dy_2Ti_2O_7$ crystal with dimensions 1.0x0.32x4.0 mm^3. The long axis was directed along the direction of the magnetic field. The data from Revell et al. (see Ref. [96]) were obtained on a different, non-annealed $Dy_2Ti_2O_7$ sample with dimensions 1.0x1.0x3.9 mm^3.

These samples are both needle-shaped to reduce the demagnetisation correction, they have the same crystallographic orientation, and the results were obtained at the same temperature $T = 800$ mK. The measured imaginary portion of the AC susceptibility, $\chi(\omega)$", was transformed to the dynamic correlation function $C(t) = \langle M(0)M(t)\rangle$, where $M(t)$ is the time-dependent magnetisation of the sample (Ref. [99]). The dynamic correlation function results are presented in Fig. 6.5, where they are compared with previous results on a different, non-annealed sample of $Dy_2Ti_2O_7$, at $T = 800$ mK (see Ref. [96]).

The very slow long-time tail in $C(t)$ associated with magnetic defects is observed for the as-grown sample, but it is entirely suppressed for the annealed sample. The as grown sample characteristics match closely with the previous results. Revell et al. attributed the long time tail as being a result of interactions of monopoles with magnetic impurities from a slight level of stuffed sites (substitution of Dy for Ti). The fact that annealing in oxygen eliminates the long-time tale suggests that the magnetic impurity sites in the as-grown sample results from

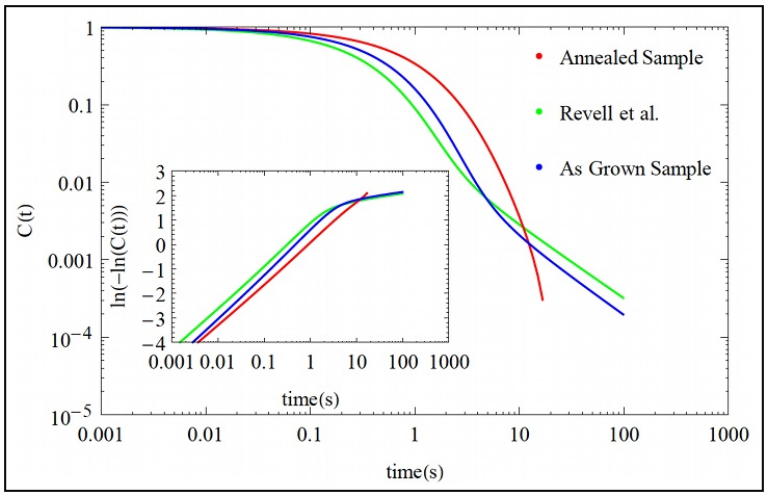

Figure 6.5: *The dynamic correlation functions from AC susceptibility measurements at* $T = 0.8$ *K.* – The as grown sample exhibits the long time tail seen previously and attributed to magnetic defects (Ref [96]), but this tail is entirely suppressed by annealing in oxygen. The inset shows $\ln[C(t)]$ versus time on a log-log scale, where a linear regime identifies stretched exponential behaviour.

oxygen vacancies. The stretched exponentials seen in the correlation function at early times for all samples were very similar.

Notice that the rather unused choice of axes has been made to obtain a straight line for the stretched exponential behaviour, the departure from straight line behaviour is one way of emphasising where the long-time tail occurs.

6.3 Experimental Results

The difference in the magnetism of these samples has also been investigated using polarised neutrons to study the magnetic diffuse scattering collected at $T = 0.6$ K at the DNS facility in Munich. One of the most challenging aspects of measuring the magnetic diffuse scattering in $Dy_2Ti_2O_7$ spin ice crystals, is that Dy^{3+} is a huge neutron absorber, since its scattering length is complex. In this case a possible solution to study the system is to grow a $Dy_2Ti_2O_7$ crystal using an isotope of Dy^{3+} that has a real scattering length, or measure the common compound for a long period of time (according to our experience ≥ 30 hours per orientation). The last technique can also be improved if we measure the common $Dy_2Ti_2O_7$ at two different temperatures (e.g. 0.6 K and 10 K); the mutual subtraction of the two orientations at these temperatures will show only the magnetic signal coming from the sample, since all the background noise will cancel.

This choice has been successfully applied to study the magnetic diffuse scattering of both $Dy_2Ti_2O_7$ annealed and $Dy_2Ti_2O_7$ depleted crystal at the DNS facility

in Munich. Two cylindrical samples of $Dy_2Ti_2O_7$ (5x4 mm) have been oriented using the Laue camera at the DNS facility in order to have the (hhl) parallel to the scattering plane. The screening measurements using X-rays and TGA, shown in Tab. 5.2, gave us a $\delta = 0.0, 0.20$ for the annealed and depleted samples respectively. Neutrons have been polarised applying an external field of 10 mtesla, and the polarisation direction was chosen along $[1, -1, 0]/\sqrt{2}$.

MC simulations have been performed using the classical spin ice Hamiltonian (Eq. 1.1) and a supercell with $\mathcal{L} = 8$, averaging over 10000 realisations of disorder. Figure 6.6 shows the comparison between the calculated magnetic diffuse scattering in the (hhl) plane using Eqs. 3.18, 3.24, and the measured SF ad NSF channels at $T = 0.6$ K for the $Dy_2Ti_2O_7$ annealed sample.

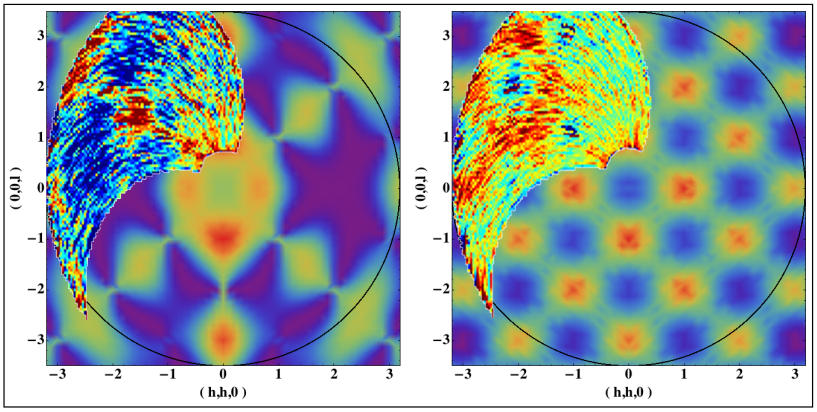

Figure 6.6: *SF and NSF channels of annealed $Dy_2Ti_2O_7$.* – The comparison between the experimental data (insets) and our MC simulations, shows a remarkable agreement between the two. The snowflake shape of the SF channel as well as the chessboard motif in the NSF are present, and these patterns are also in perfect agreement with previous measurements collected using $Ho_2Ti_2O_7$ samples (see Ref. [61]).

Despite the great difficulties of this experiment, there is a remarkable agreement between the data and our simulations. The snowflake shape of the SF channel as well as the chessboard motif in the NSF are present, and these patterns are in perfect agreement with previous measurements collected using $Ho_2Ti_2O_7$ samples (see Ref. [61]).

All the previous MC simulations have been realised using the common spin ice Hamiltonian (Eq. 1.1) in order to minimise the energy of the system, however it can be interesting to study what is the contribution to the SF and NSF channels of the exchange and the dipolar interactions alone. Figure 6.7 shows the comparison of the calculated SF and NSF channels at $T = 1.0$ K, assuming the two following Hamiltonians:

$$H = J_{eff} \sum_{<ij>} \mathbf{S}_i \cdot \mathbf{S}_j \tag{6.1}$$

where $J_{eff} = 1.11$ K.

$$H = D \sum_{i<j} \left[\frac{\mathbf{S}_i \cdot \mathbf{S}_j}{|\mathbf{r}_{ij}|^3} - \frac{3(\mathbf{S}_i \cdot \mathbf{r}_{ij})(\mathbf{S}_j \cdot \mathbf{r}_{ij})}{|\mathbf{r}_{ij}|^5} \right] \tag{6.2}$$

where $D = 1.41$ K.

The calculations used a supercell with $\mathcal{L} = 8$, and they are averaged over 10000 realisations of spin configurations. As is clearly visible from Fig. 6.7, the two SF channels calculated using Eqs. 6.1-6.2 look quite similar; the snowflake shape is present but the intensity of the peaks in the nearest neighbour model is different compared to the experimental pattern. By contrast the NSF channel calculated truncating the Hamiltonian to only nearest neighbour interactions is in complete disagreement with the data. The chessboard pattern is completely absent and what is visible is only the magnetic form factor of Dy^{3+}.

Therefore we can conclude that the dipolar interaction contributes to both the SF and NSF intensity, while the exchange only to the SF channel. Notice that this statement is not trivial, it confirms that both these contributions are essential in order to model spin ice crystals, since the nearest neighbour interaction alone is insufficient to describe the system in the correct way.

We repeated the same experiment (i.e. same experimental set up and same exposure time) using the depleted $Dy_2Ti_2O_{7-\delta}$ sample. The SF and NSF channels in the (hhl) plane at $T = 0.6$ K are shown in Fig. 6.8. In this case the intensity of the previous features are barely distinguishable from the background, and this is consistent with a suppression of the magnetic moment of Dy^{3+} close to a vacancy.

Naively one could set up a MC simulation to calculate the magnetic diffuse scattering in depleted samples, assuming easy plane like spins; in this case the dipolar and exchange interaction constants between easy plane-easy axis and easy plane-easy plane would be our free parameters to tune according to the experimental data. However the poor statistics of our data due to the high neutron absorption of Dy, makes it impossible to obtain useful information for a good MC comparison. A better study could be done by increasing the measurement time or possibly using depleted $Ho_2Ti_2O_7$ crystals.

6.4 A light on the future: exploring the dynamics of magnetic monopoles

A recent comparison between low-temperature magnetic relaxation measurements on spin ice materials and numerical simulations suggests that magnetic impurities acting as monopole pinning centres may be the origin of the surprisingly long time scales observed (see Ref. [96]). It is therefore interesting to see how the magnetic distortion introduced by an O(1) vacancy can act as a pinning centre for the monopoles.

According to our CEF calculation for $Dy_2Ti_2O_7$ (see Sec. 6.1), an isolated O(1) vacancy should introduce a tetrahedron with 4 easy plane spins surrounded

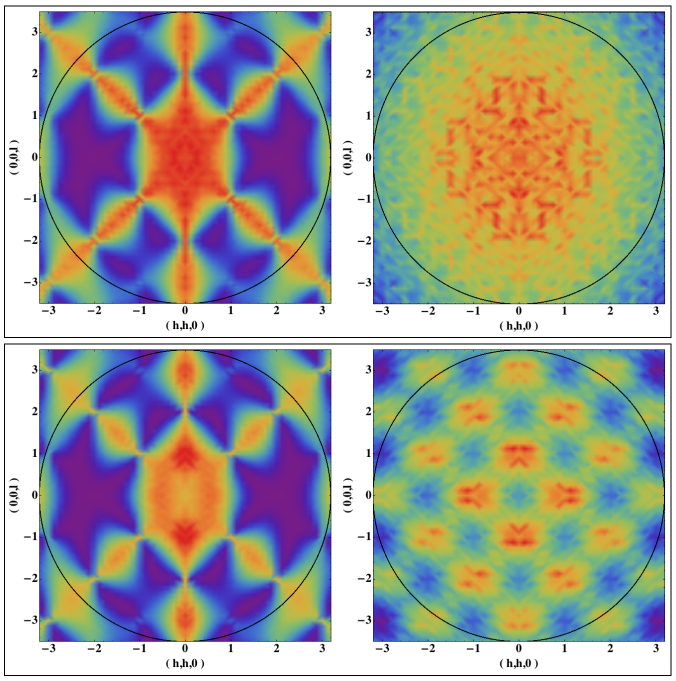

Figure 6.7: *SF (left) and NSF (right) channels calculated with only nearest neighbour interactions (top) and only dipolar interaction (bottom).* – The SF channels look quite similar; the snowflake shape is present but the intensity of the peaks in the nearest neighbour model is a little bit different compared to the experimental pattern. By contrast the NSF channel calculated truncating the Hamiltonian to only nearest neighbour interactions is in complete disagreement with the data. The chessboard pattern is completely absent and what is visible is only the magnetic form factor of Dy^{3+}. This analysis is clear evidence that the nearest neighbour model is insufficient to describe spin ice crystals, we can not neglect long range interactions in the system because the energy will not be minimised in the correct way leading to the wrong spin configuration in the lattice.

by 4 neighbouring tetrahedra with 3 easy axis and 1 easy plane spin each. We shall refer to this ensemble of spins as a 16-spin cluster (see Fig.6.9). Notice that tetrahedra adjacent to the 16-spin cluster or farther away include a priori only easy axis spins.

The removal of an O(1) is also likely to affect the super exchange interactions between neighbouring rare-earth ions. These are difficult to estimate from first principles and we shall consider them as free parameters in our qualitative calculations below.

For either $Dy_2Ti_2O_7$ or $Ho_2Ti_2O_7$, the ice rules are no longer well-defined in the 5 tetrahedra close to a vacancy. When a monopole (say a 3out-1in topological defect as shown in Fig. 6.9) approaches the cluster, it can hop onto it and seemingly disappear. Of course there is no violation of either gauge or magnetic

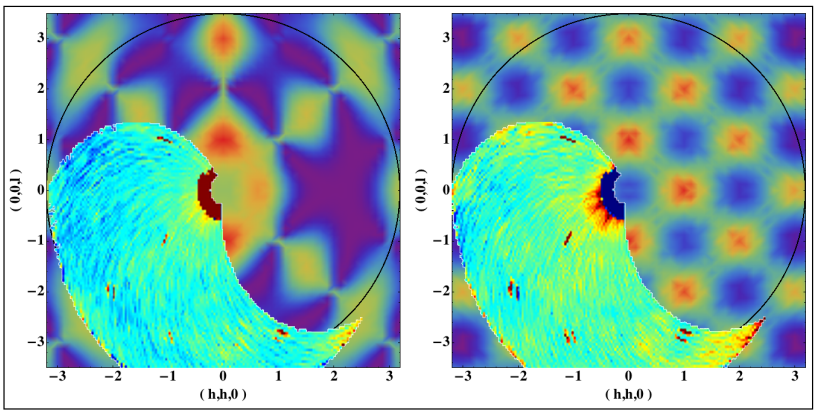

Figure 6.8: *SF and NSF channels of* $Dy_2Ti_2O_{7-\delta}$. – The intensity of the previous features are barely distinguishable from the background, and this is consistent with a suppression of the magnetic moment of Dy^{3+} close to a vacancy like shown in our CEF calculation. However the poor statistic, due to the high neutron absorption of Dy, makes impossible to obtain useful information for a good MC comparison.

charge conservation in this process; an appropriate measurement of the magnetic flux through a surface surrounding the 16-spin cluster must show that its charge (gauge or magnetic) changes by the appropriate amount. Pictorially, the incoming monopole charge has "delocalised" over 5 tetrahedra and one can no longer identify a specific tetrahedron where it resides.

Whereas at a coarse grained level this may seem immaterial, the process can have measurable consequences on the energy of the system. A significant fraction of the bare cost of a monopole derives from the nearest neighbour part of the interaction between spins (i.e. the energy difference between e.g. 3in-1out and 2in-2out on a single tetrahedron), and this part of the energy is different for a monopole delocalised over the 5 tetrahedra compared to the case where the monopole sits on a given stoichiometric tetrahedron.

Dr. C. Castelnovo explicitly computed the energy difference using Eq. 1.1 by comparing spin configurations such as those illustrated in Fig. 6.9, i.e. he computed the change in energy caused by a spin flip process that hops a monopole from a stoichiometric tetrahedron onto one of the 5 tetrahedra affected by the vacancy. Here, we limit our considerations to exchange and dipolar interactions truncated at nearest-neighbour distance. Farther range contributions to the energy require large scale Monte Carlo simulations which are beyond the scope of our discussion. Moreover, at intermediate temperatures, the Coulomb interaction between monopoles is screened and the long-range contribution to their bare cost is reduced. Therefore the nearest neighbour contribution calculated here becomes more and more accurate.

Firstly, he fixed the (yellow) spin connecting the outlying (easy-axis) tetrahedron to point in a given direction (immaterial by symmetry), and he imposed that

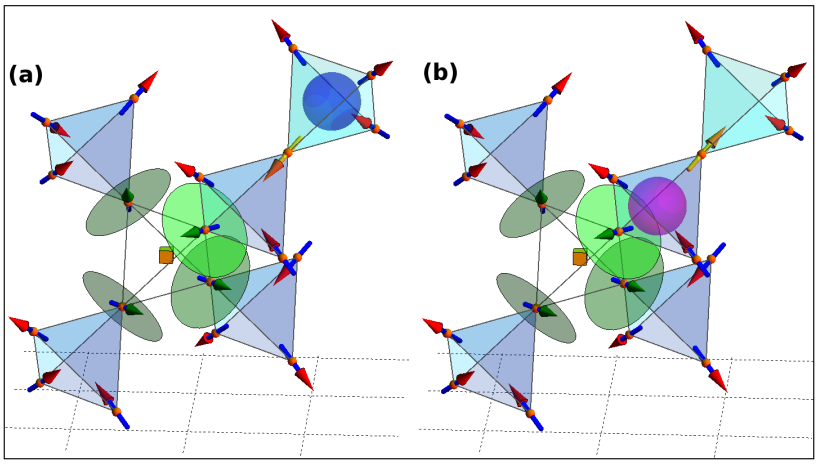

Figure 6.9: *Monopole trapping by oxygen vacancies.* – **(a)** An isolated O(1) vacancy (yellow cube) directly affects the 4 nearest neighbour Dy ions that become easy plane spins (green-tip arrows). An additional tetrahedron is shown adjacent to the cluster, hosting a 3out-1in monopole (blue sphere); the connecting spin is coloured in yellow. Easy-plane spins are free to rotate in the plane perpendicular to the local $\langle 111 \rangle$ directions (represented by the corresponding green semi-transparent disc); easy-axis spins (red-tip arrows) can only point directly into or out-of a tetrahedron. **(b)** Given this spin configuration and upon flipping the yellow easy-axis spin, the monopole hops onto one of the defected tetrahedra and it "delocalises", i.e. one can no longer identify a specific tetrahedron where it resides (magenta sphere).

the outlying tetrahedron is in a 3out-1in excited state. He then considered all the possible configurations of the remaining 11 easy-axis spins in the 16-spin cluster. For each configuration he computed the energy of the system after allowing the easy plane spins to relax to their ground state. In these calculations we have interactions between easy axis spins, between easy-plane spins, as well as interactions between easy axis and easy plane spins. Since the strengths of the latter two types of interaction are not not known a priori, he considered separately the 4 following working assumptions:

1. We naively assume that all the exchange and dipolar coupling constants are the same as in the stoichiometric case.

2. We change the dipolar couplings involving easy-plane spins to account for their reduced magnetic moment of approximately $5.7\mu_B$.

3. We further switch off exchange interactions between easy-plane spins (but not between easy-plane and easy-axis spins). This is the extreme scenario where the removal of an O(1) suppresses the super exchange interaction between Dy spins connected by the missing O(1).

4. Finally, we remove all interactions that involve any of the easy-plane spins. This corresponds to the Ho case where the O(1) vacancy suppresses altogether the magnetic moment of the 4 spins in the central tetrahedron.

In all of the above cases he used the Dy value of the exchange interaction $J/3 = -1.24$ K, with the exception of the last case where he used the Ho value $J/3 = -0.52$ K (see Refs. [10],[11],[50]).

Out of all these 2^{11} configurations, he selected a low energy ensemble defined as those configurations whose energy falls within 1 Kelvin of the lowest energy configuration. These are expected to be the relevant configurations at low temperatures. For each of them, he flipped the yellow spin connecting the 16-spin cluster to the outlying tetrahedron and he computed the corresponding energy difference (after allowing the easy-plane spins to relax to their lowest energy state). This spin flip corresponds to the absorption of a monopole by the 16-spin cluster, and the spin flip energy he computed is the corresponding change in energy of the system. Histograms of the resulting energies from all configurations in the low energy ensemble are shown in Fig. 6.10, separately for each of the four working assumptions discussed above.

For all four choices of coupling strengths, we can observe a broad distribution of energies down to large negative values. These are large enough to be comparable to the bare energy cost of an isolated monopole (approximately 2.2 K and 3.7 K for Dy and Ho parameters with interactions truncated at the nearest-neighbour level). This means that a monopole coming into contact with a vacancy cluster can become strongly pinned to it. Notice that, given a spin configuration (of the 11 easy-axis spins that we vary), the energy depends on the direction of approach of the monopole.

It is remarkable to notice the similarity in the way that monopoles interact with these oxygen vacancies compared to the static stuffed moments discussed by Revell et al. Depending on the direction of approach, a static magnetic moment can either attract or repel a monopole [96]. Vacancy clusters appear to do just the same, with nearby monopoles being either attracted or repelled depending on the configuration of the 16-spin cluster surrounding a vacancy. Since the static magnetic moments introduced in the simulations by Revell et al. were able to explain the long-time tail in the magnetic relaxation of the system [96], one can reasonably expect that local magnetic distortions introduced by oxygen vacancies can lead to similar long-time tails. This is indeed what we see in our experimental results, where the long time tails in the decay of the magnetisation are present in the as-grown sample but disappear upon annealing (see Fig. 6.5).

Of course, any distribution of magnetic defects capable of trapping monopoles, and whose pinning energies can be less than the creation of a bare monopole, also alter the thermodynamics of the system. In thermal equilibrium, these magnetic defects act as nucleation centres for monopole defects; in fact it is cheaper to change the configuration of one such magnetic defect and emit a monopole than flipping spins in (locally) stoichiometric spin ice and creating plus separating a

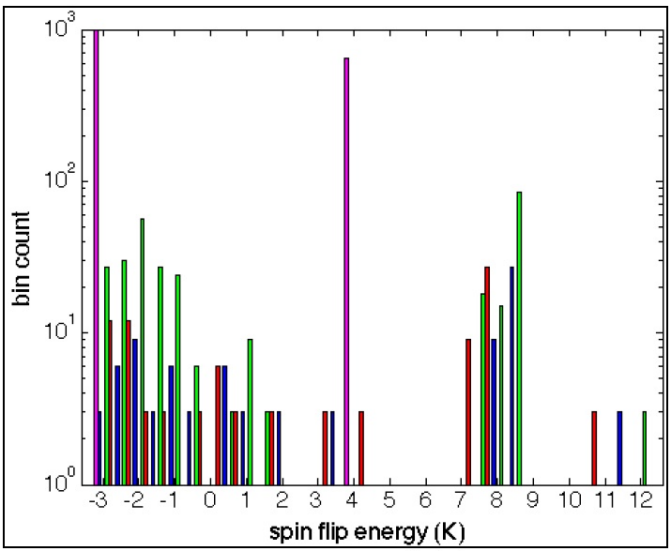

Figure 6.10: *Histogram of the energy change for the spin flip process in Fig. 6.9.* – The different colours correspond to three different choices of the exchange and dipolar interactions between the spins (truncated at nearest-neighbour distance): in the red histogram the exchange and dipolar coupling constants are the same as in the stoichiometric case; in the blue histogram we changed the dipolar couplings involving easy-plane spins to account for their reduced magnetic moment while in the green histogram we further switched off the exchange interactions between easy-plane spins (but not between easy-plane and easy-axis spins). Finally in the magenta histogram we removed all interactions that involve any of the easy-plane spins, this corresponds to the Ho case where the O(1) vacancy suppresses the magnetic moment of the 4 surrounding spins. Notice that the four distinct histograms have been shifted along the horizontal axis by up to 0.3 K to enhance visibility.

pair of monopoles. Therefore, magnetic defects can raise the monopole density in thermal equilibrium, and correspondingly make the magnetic relaxation dynamics faster [27],[100].

Studying the competition of these two effects, namely the thermodynamic speedup due to increased monopole concentration and the out-of-equilibrium trapping by the very same magnetic defects, is a tall order. A proper understanding of the effect of the trapping energy distribution on the thermodynamic and out-of-equilibrium properties of spin ice requires an extensive study of a many body system that goes well beyond our simple few-body description. Notwithstanding, it is tempting to speculate that the speedup is more likely to dominate at intermediate time scales, when the system is close to its thermodynamic equilibrium, whereas the slowing down due to pinning should become important in the far from equilibrium motion of monopoles. This picture is in fact consistent with our experimental data (see Fig. 6.5), which shows an initial slowing down of magnetic relaxation in

the annealed sample with respect to the as-grown one.

6.5 Discussion

On the basis of these important results on the dynamic of magnetic monopoles in presence of oxygen vacancies, we would like to stress a couple of points of our analysis on the physical properties of depleted systems.

1. The presence of oxygen vacancies dramatically changes the single ion anisotropy of neighbouring Dy ions from easy axis to easy plane spins. In this case ice rules do not apply to the neighbouring tetrahedra and the physical properties of the system changes in a non trivial way.

2. We are able to detect empirically changes to the uniform susceptibility and to the dynamical susceptibility.

3. We found that oxygen vacancy defects, identified in the previous chapter, have a direct effect on the monopole dynamic at low temperatures.

The magnetic residual resistance was previously attributed to the stuffing of random Dy ions on Ti sites, however:

1. Dy ions in this specific CEF environment (i.e. the trigonal anti prism of Ti ions) would not have Ising anisotropy, but again an easy plane behaviour with an average moment $\mu = 5.4\mu_B$ as shown in Fig. 6.11.

2. Depending on the direction of approach, a static magnetic moment can either attract or repel a monopole. Vacancy clusters do the same, and one can reasonably expect that they too will result in the long time tails.

The reason for the suppressed magnetic response from the Ti ions in $Y_2Ti_2O_7$ is still an unresolved question. However, since the saturated moment in the as grown sample is only a few thousandth of a percent of $Dy_2Ti_2O_7$, the Ti magnetism is unlikely to affect the monopole dynamics in spin ice.

The calculation of the magnetic diffuse scattering relies only on the knowledge of how spins are oriented in the lattice. Spin orientations are given by the MC loop that tries to minimise the energy of the system, therefore they strongly depend on the Hamiltonian we are using. If we neglect the dipolar interaction truncating the expansion to only nearest neighbour terms, we lose a fundamental contribution in the energy of the system. The MC does not minimise the energy in the correct way and the resulting spin configurations give wrong results.

There are already extensive experimental polarised neutron data sets for the $Ho_2Ti_2O_7$ crystals (Ref. [61]) and, for comparison, we calculated the magnetic diffuse scattering of $Ho_2Ti_2O_7$ in the (hhl) plane for both the nearest neighbour model and the nearest neighbour plus dipolar model (see Fig. 6.12). The MC calculations clearly show that the nearest neighbour model is insufficient to obtain the correct pattern in both the SF and NSF.

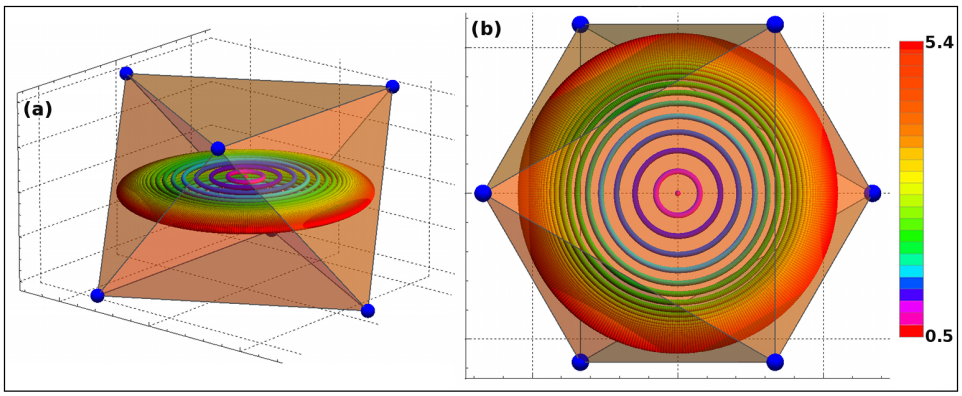

Figure 6.11: *Dy ion in the trigonal anti prism environment.* – The CEF field calculation assuming stuffing of Dy ions on Ti sites, shows that the the rare earths would not have Ising anisotropy, but again an easy plane behaviour with a calculated average moment $\mu = 5.4\mu_B$.

Another quantity of interest that can be related with the presence of magnetic monopoles in the system is the shape of the pinch points (Ref. [101]). If we take a cut through the pinch point (002) we can see that its shape is greatly affected by the interactions we are using in our Hamiltonian (see Fig. 6.13) and, again, the use of the truncated neighbour model could lead to uncontrolled approximation.

6.6 Conclusion

We have clearly demonstrated the important role of oxygen vacancies in the physics of monopoles at low temperatures, however further studies are required in order to understand how the magnetic response of the rare earth ions is suppressed.

The magnetism on the rare-earth sites makes a substantial contribution to the monopole dynamics, but it would be of great interest to explore further the effects on the system. Our results make it apparent that the density of oxygen vacancies in spin ice samples is of key importance in the interpretation and understanding of relaxation and response properties, and far from equilibrium behaviour in general.

Many experimental results in this direction are already available and, in some cases, it may be that further work is needed to distinguish the effects of oxygen vacancies from the stoichiometric behaviour. Moreover, theoretical work to date has largely focused on stoichiometric models, and it will be interesting to see which new phenomena may emerge when a tuneable density of impurities is introduced via oxygen depletion.

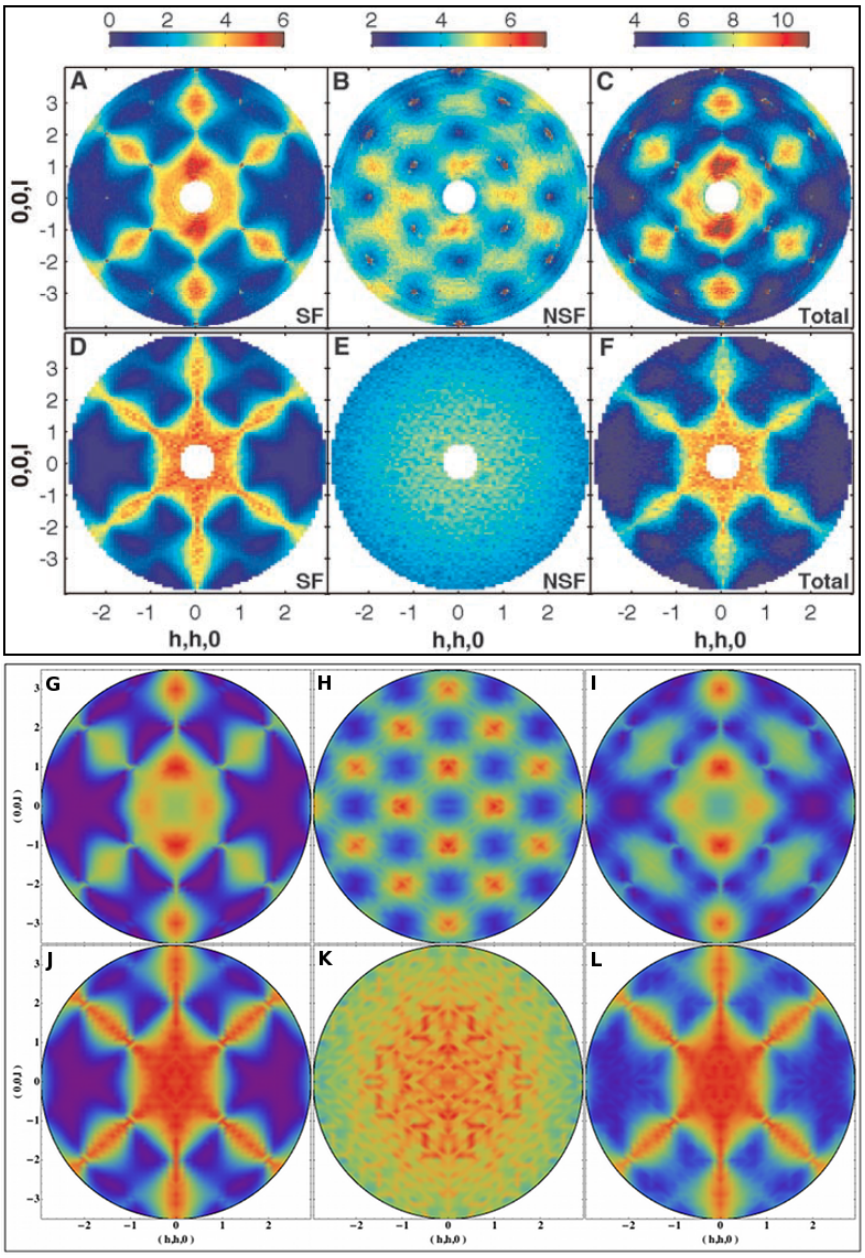

Figure 6.12: *Comparison between the results in Ref. [61] (A-F panels) and our MC simulation for $Ho_2Ti_2O_7$ using the classical spin ice Hamiltonian (G-I panels) and the nearest neighbour model (J-L panels).* – The MC calculations clearly show that the nearest neighbour model is insufficient to describe the correct pattern in both the SF and NSF.

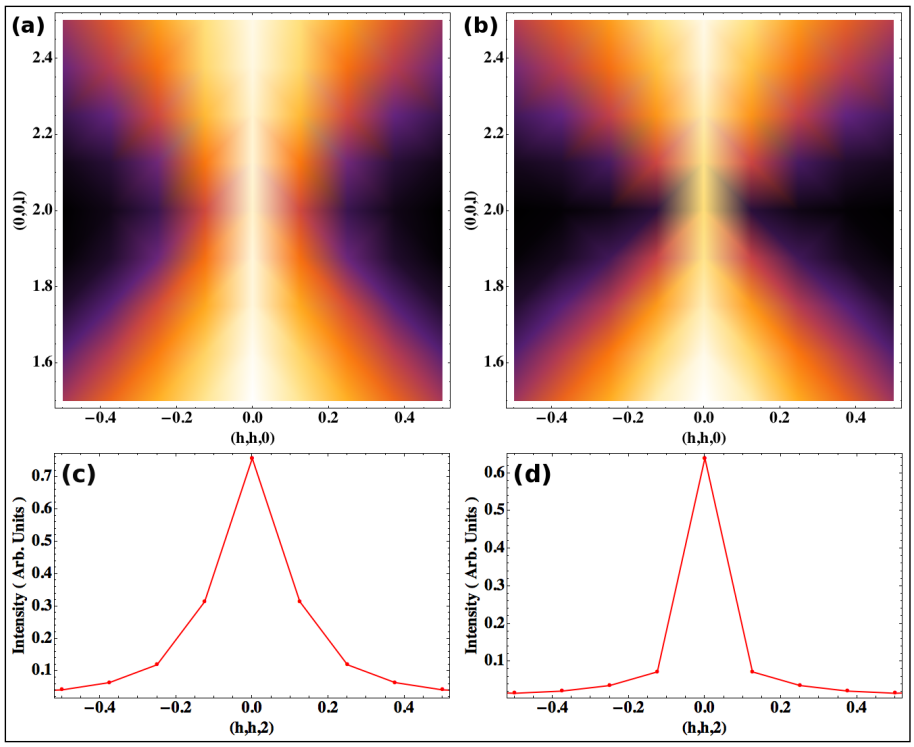

Figure 6.13: *Comparison of the pinch point (002) calculated with only nearest neighbour interactions (a) and only dipolar interaction (b) at T = 0.7 K.* – The shape of the pinch point can be related to the density of magnetic monopoles present in the system (see Ref. [101]), therefore the correct calculation of these quantities is of fundamental importance in simulation in order to bench mark the theory. As is clearly visible the HWHM calculated using the truncated neighbour model **(a)** is larger than for the dipolar model in **(b)**. Finally panels **(c),(d)** show a comparison of the intensities of the pinch point (hh2) for the truncated neighbour model and the dipolar model respectively. Note that the pinch points depend on the temperature and on whether the spins are Ising, Heisenberg or easy planar. Hence these features need to be taken into account when deriving monopole densities.

Chapter 7

The doped system: An analysis on $Dy_{2-x}Y_xTi_2O_7$

Contents

In the previous two chapters we have discussed the role played by oxygen vacancies in spin ice crystals. We have seen that a different environment around the magnetic ion modifies the nature of the compound and its physical properties in a non trivial way, and we studied how it is possible to model this new system.

However, there is another type of defect that we would bring to attention: doping the crystal with non magnetic impurities. In our specific case the crystal is grown mixing Dy/Ho powders with a non magnetic ion (e.g. Y) that substitutes Dy/Ho in the pyrochlore lattice, effectively doping the crystal. This system has been studied previously by polarised neutron scattering (Ref. [102]), heat capacity (Ref. [103]) and recently by muons (Ref. [104]).

In this chapter we will focus our attention on the magnetic and thermodynamic properties developed by these systems, and we will see how the frustration and the ice rules are affected by the doping.

7.1 The $Dy_{2-x}Y_xTi_2O_7$ pyrochlore lattice

The structure of $Dy_{2-x}Y_xTi_2O_7$ crystals is identical to $Dy_2Ti_2O_7$. There is a negligible distortion in the lattice due to the substitution of Dy^{3+} with Y^{3+} even at very

high doping levels, since their ionic radii are comparable ($R_{Dy} = 1.027$ Å and $R_Y = 1.019$ Å respectively). Therefore all the internal structures of the lattice (i.e. scalenohedra and trigonal anti prisms) are preserved. This statement has also been confirmed by our neutron scattering data, that show no trace of diffuse scattering in all these systems both at room temperature (RT) and at $T = 5$ K.

Figure 7.1 shows the unit cell of a $Dy_{2-x}Y_xTi_2O_7$ crystal, from now on Y^{3+} will be identified in yellow according to our colour scheme.

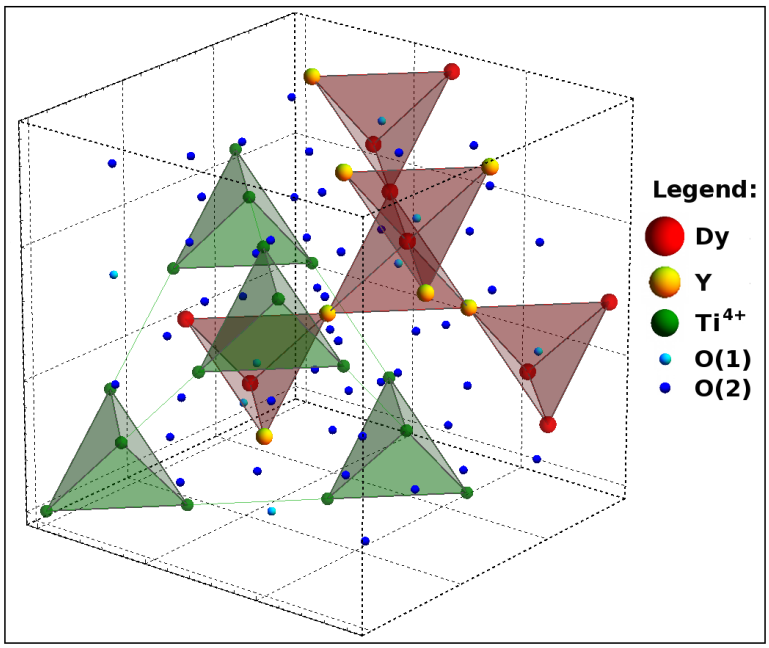

Figure 7.1: *Cubic unit cell of $Dy_{2-x}Y_xTi_2O_7$.* – The pyrochlore lattice is almost identical to the $Dy_2Ti_2O_7$ one, even at very high dilutions, since the ionic radii of Y^{3+} is similar to Dy^{3+}. Therefore there is a negligible distortion in the lattice and all the internal structures (i.e. scalenohedra and trigonal anti prisms) are preserved. According to our colour scheme Y^{3+} will be in yellow.

According to our neutron scattering measurements non magnetic impurities are randomly distributed in the system, since the diffuse scattering pattern at $T = 5$ K does not show any trace of superstructures or clusters inside the system. A priori there is no correlation between the impurities, and we have to take care of this characteristic in our MC simulations. Moreover, since the CEF environment surrounding the remaining rare earth ions is preserved, it seems natural to describe this system using the classical spin ice Hamiltonian written in Eq. 1.1.

7.2 Experimental Procedure

Dr. D. Prabhakaran grew five $Dy_{2-x}Y_xTi_2O_7$ single crystals with $x = 0.5, 1.0, 1.5, 1.75$ and 1.9 using the floating zone technique at the Clarendon Laboratory in Oxford. All the crystals have been annealed in O_2 to eliminate any trace of oxygen vacancies and they were screened at room temperature by Dr. D. Porter using X-ray at Royal Holloway University of London. Table 7.1 shows the result of the X-rays refinement, fixing the occupation value of Ti ions.

$\mathbf{Dy_{2-x}Y_xTi_2O_7}$	**x=0.5**	**x=1.0**	**x=1.5**	**x=1.75**	**x=1.9**
Colour	Brown	Yellow	Yellow	Yellow	White
Space Group	$Fd\bar{3}m$	$Fd\bar{3}m$	$Fd\bar{3}m$	$Fd\bar{3}m$	$Fd\bar{3}m$
Lattice par. (Å)	$10.121(2)$	$10.123(2)$	$10.118(3)$	$10.109(3)$	$10.102(3)$
Dy	$0.77(2)$	$0.49(2)$	$0.28(3)$	$0.13(4)$	$0.07(3)$
Y	$0.23(4)$	$0.51(2)$	$0.72(2)$	$0.87(2)$	$0.93(2)$
Ti	1	1	1	1	1
O(1)	$1.01(2)$	$1.02(2)$	$0.97(3)$	$1.01(1)$	$0.98(2)$
O(2)	$1.03(3)$	$0.98(2)$	$1.02(2)$	$0.95(3)$	$0.97(3)$
R_W	6.9	7.8	7.1	7.3	6.7

Table 7.1: *X-ray screening of the $Dy_{2-x}Y_xTi_2O_7$ samples.*

These samples have been measured using a 7 tesla magnetometer at the Clarendon laboratory in Oxford by Dr. D. Prabhakaran to study the magnetisation. The sweep scan has been done applying an external field from $-7 \leq H \leq 7$ tesla at $T = 2$ K, along the $[100]$ direction.

After that we checked the samples for defect clusters arising from distortions next to dopant Y ions, oxygen vacancies etc. more rigorously, studying their structural diffuse scattering with unpolarised neutrons at $T = 5$ K. The experiment has been performed at the SXD facility in ISIS. All the crystals showed no trace of diffuse scattering in all the 3D volume of the reciprocal space measured, confirming the absence of vacancies and any possible distortion in the lattice due to the substitution of Dy with Y. These measurements also ruled out the possibility of Y ions forming superstructures.

7.3 DC Magnetic susceptibility in doped systems

Figure 7.2 shows the comparison of the magnetisation of the five $Dy_{2-x}Y_xTi_2O_7$ annealed crystals measured using a 7 tesla magnetometer, with our MC simulations. In particular, the MC simulation has been performed in a supercell with $\mathcal{L} = 4$, assuming a random distribution of Y ions in the lattice, and using the same parameters as the experimental set up (i.e. field direction, nominal doping levels and temperature). The average has been performed over 10000 realisations of disorder.

As expected, the comparison of the magnetisation M with the stoichiometric

annealed $Dy_2Ti_2O_7$ sample (red line), shows that it decreases due to the introduction of non magnetic ions in the system. The overall shape of the curves is maintained, and there is no trace of a structural phase transition between different doping levels, which is consistent with the fact that the introduction of Y ions does not affect the lattice.

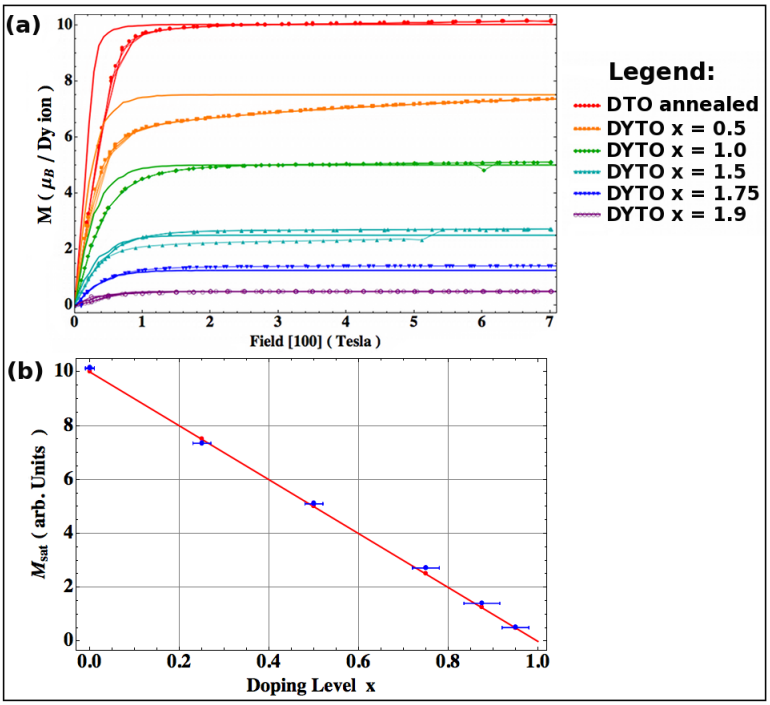

Figure 7.2: *Magnetisation of $Dy_{2-x}Y_xTi_2O_7$ crystals.* – **(a)** The magnetisation M decreases due to the introduction of non magnetic impurities. Our MC calculations for a system with $\mathcal{L} = 4$ (solid lines), shows that the saturation values are in good agreement with the experimental data. However the simulation is not able to capture the correct behaviour at low fields, probably because our MC calculation is neglecting spin correlations that are relevant at low temperatures. **(b)** Comparison between M_{sat} obtained from magnetisation data (blue dots) and MC simulations (red dots) at 7 tesla versus the doping level $0 \leq x \leq 1$. The magnetisation decreases linearly with the dilution, following a law $\propto \mu(1-x)$ (red line). Notice that the error bars of the $Dy_{2-x}Y_xTi_2O_7$ samples have been calculated from the X-ray refinement.

If we plot the saturation value of M at 7 tesla for every single sample (blue dots) versus the doping level x, we can see in Fig. 7.2(b) that M_{sat} decreases linearly with x, in particular:

$$M_{sat} \propto \mu(1-x) \tag{7.1}$$

where $0 \leq x \leq 1$ and $\mu = 10\mu_B$.

Notice that our MC calculation is able to predict the correct value of M_{sat} for every single sample, and it also confirms the linear decrease of M with the doping level (see Fig. 7.2(b) red dots). However, at present, we are not able to explain the discrepancies in the knee at low fields. We can speculate that our MC calculation is neglecting spin correlations that are relevant at low temperatures. Therefore, in order to improve it, we could calculate a high temperature expansion of the magnetisation. In this way the lowest non-trivial order of the expansion should be equivalent to our MC calculation, and the inclusion of higher orders terms should give a better agreement with the data.

7.4 Polarised neutron scattering

Chang et al. (see Ref. [102]) have measured the spin flip (SF) and non spin flip (NSF) channels of an analogous compound: $\mathrm{Ho_{2-x}Y_xTi_2O_7}$ for $x = 0.0, 0.3$ and 1. At $T = 2$ K, their results show that the SF scattering patterns are consistent with a nearest neighbour spin ice model and the effects of Y doping are seen in the widths of the pinch points. By contrast, at low temperatures the SF patterns are characteristic of a dipolar spin ice and are unaffected by Y doping. Moreover, in the NSF channel, they observed the signature of strong antiferromagnetic correlations at the same temperature as the dipolar spin ice correlations appear in the SF channel.

Just for comparison, we used our MC program to calculate the SF and NSF channels at $T = 2,\ 10$ K using the classical spin ice Hamiltonian (Eq. 1.1). Figure 7.3 shows the comparison of our calculation with the experimental results in Ref. [102].

As is clearly visible there is an excellent agreement between our calculation and the experimental data, however, we should notice that the shape of the pinch points in the data is a little bit larger compared to the calculated one.

7.5 Internal field analysis in doped systems

We can now use our MC program to calculate the internal field distributions of $\mathrm{Dy_{2-x}Y_xTi_2O_7}$ for $x = 0.5, 1.0$ and $x = 1.5$, as we have successfully done for the annealed $\mathrm{Dy_2Ti_2O_7}$ sample (see Chap. 4). In order to be consistent with the previous analysis, we should have calculated the internal fields for two specific types of spin configurations: pure 2in-2out and random Ising $[111]$ configurations. However, since we are dealing with doped systems where we actually remove spins from a tetrahedron, the terms 2in-2out and random Ising $[111]$ configurations can be misleading. Therefore, from now on, we will refer to these spin configurations as the low and high temperature configurations.

In particular, we decided to perform the calculation in the following way:

1. The program removes randomly spins in the system according to the doping level x.

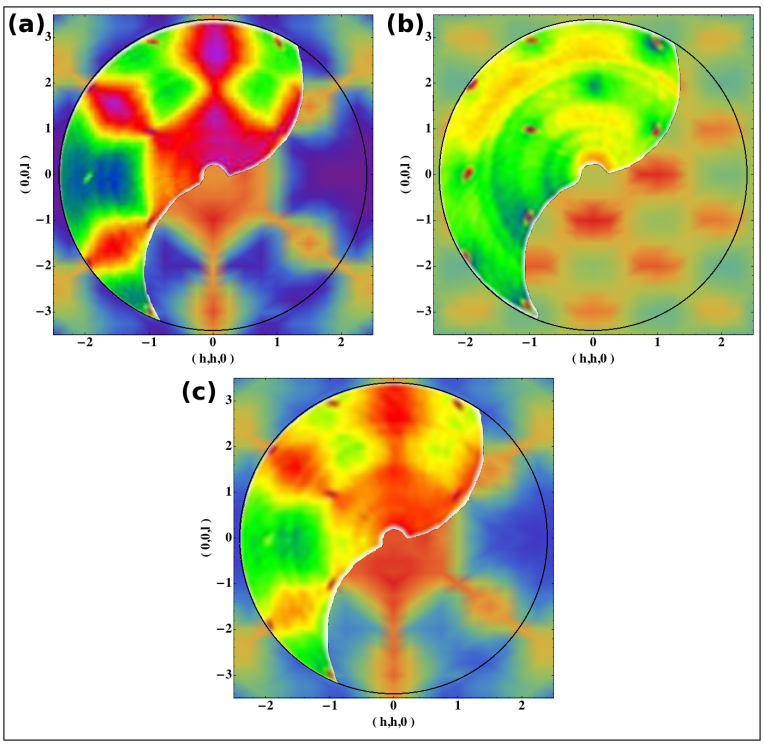

Figure 7.3: *SF and NSF channels for* $Ho_{2-x}Y_xTi_2O_7$ *with* $x = 0.3$. – The comparison with the experimental data in Ref. [102] for: **(a)** the SF channel at $T = 2$ K, **(b)** the NSF channel at $T = 2$ K and **(c)** the SF channel at $T = 10$ K, shows a remarkable agreement between our MC calculations and the data.

2. The Monte Carlo algorithm minimises the energy of this particular configuration using the classical spin ice Hamiltonian (Eq. 1.1) with the standard constants $D = 1.41$ K and $J_{ex} = -1.24$ K. Notice that we decided to use a temperature of $T = 0.6$ K for the low temperature (LT) configurations and $T = 10$K for high temperature (HT).

3. The final spin configuration is saved and used to calculate the internal field distribution in a quarter of the unit cell of the pyrochlore lattice (see Sec. 1.4.2), on a grid of 16000 points.

4. The process is iterated averaging over the disorder of the impurities and over different spin configurations.

Figure 7.4 shows the comparison of the histograms of the internal field distribution of $Dy_{2-x}Y_xTi_2O_7$ for $x = 0.5, 1.0$ and $x = 1.5$, calculated across the grid of 16000 points spanning a quarter of the unit cell. As we could expect the overall shape is maintained and the weight of the distribution is shifted towards low fields due to the reduced number of spins. An interesting result is that the histograms

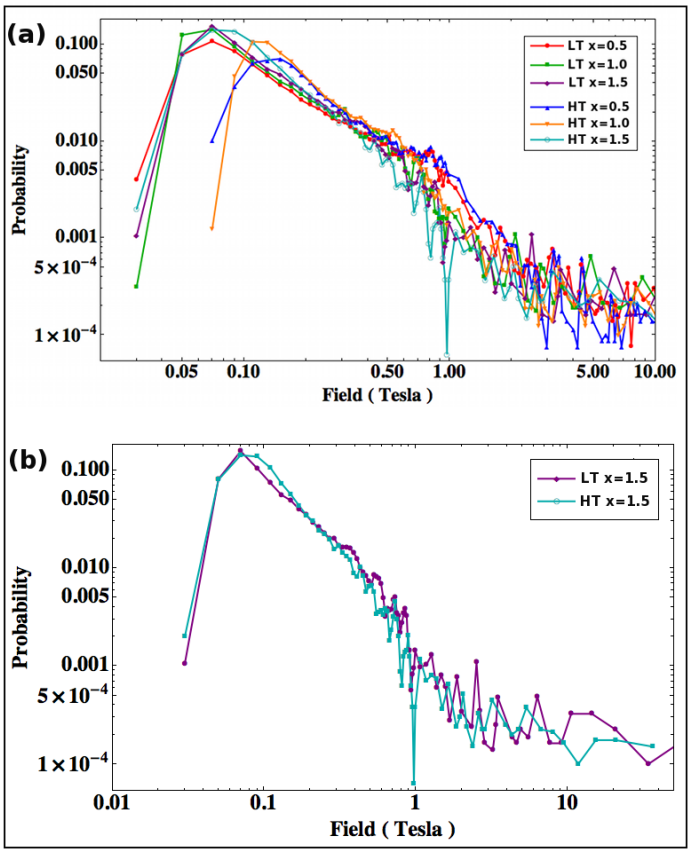

Figure 7.4: *Histograms of the internal field distribution of* $Dy_{2-x}Y_xTi_2O_7$ *for* $x = 0.5, 1.0$ *and* $x = 1.5$*, calculated in a quarter of the unit cell.* – **(a)** The overall shape of the distribution is similar to the annealed case, but its weight is shifted towards low fields due to the reduced number of spins. **(b)** The histograms for LT and HT spin configurations look quite similar for $x \geq 1.5$, due to the fact that at large Y concentrations the average interaction between the spins drops.

for LT and HT spin configurations look quite similar for $x \geq 1.5$ (see Fig. 7.4(b)). In the un-doped $Dy_2Ti_2O_7$ crystal the difference between the average over pure 2in-2out and random Ising $[111]$ configurations, was mainly due to the fact that the presence of monopoles was altering the symmetry of the system breaking the "flux loops" between spins, and thus increasing the strength of the field (especially at the centres of the super tetrahedra). Monopoles were acting as defects, and their final effect was to suppress the local order between high and low fields.

In the doped environment the strength of the average interaction between the spins drops, and at large Y concentrations the decrease can be very sizeable. Therefore, the spins will remain poorly correlated (essentially randomly oriented) down to substantially lower temperatures than classical spin ice. To give an example: if 2in-2out correlations become important in $Dy_2Ti_2O_7$ below approximately $T = 2$

K, when we dope the crystal with e.g. 75% Y ions, low temperature correlations are suppressed and are likely to play a role only for temperatures much smaller than $T = 2$ K.

Now, let us examine the field distribution on the lattice scale in a quarter of the unit cell. Figures 7.5, 7.6, 7.7 show the comparison of our MC simulation for low and high temperature spin configurations, averaged both over the defects and the disorder of the system.

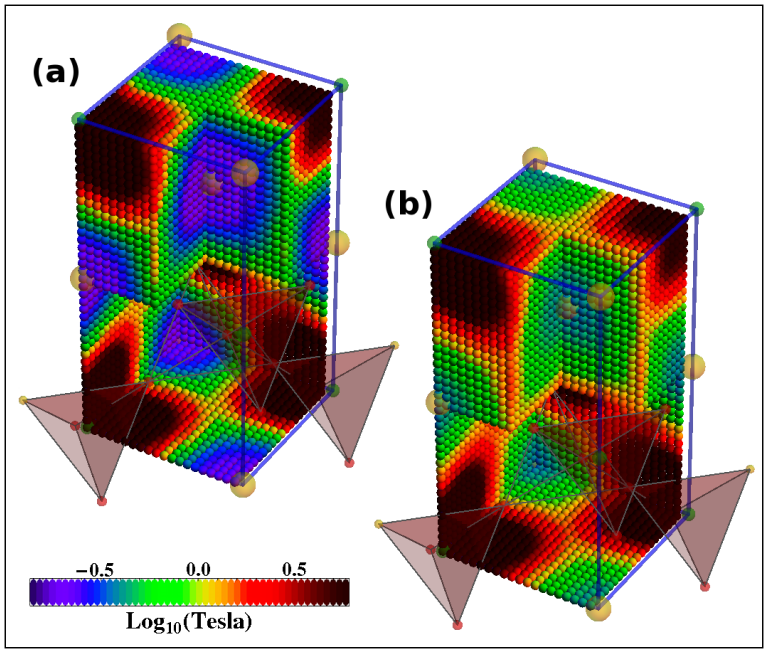

Figure 7.5: *Detailed structure of the field distribution of* $Dy_{2-x}Y_xTi_2O_7$ *for* $x = 0.5$ *on the lattice scale, calculated in a quarter of the unit cell.* – **(a)** The internal fields distribution for LT spin configurations shows even in this case a local structure, with the highest fields at the centres of the rare earth tetrahedra (green ghost spheres) and the lowest at the centres of the super tetrahedra (big yellow ghost spheres). The comparison of these positions for HT spin configurations in **(b)** shows that the spatial local organisation into low and high field is still valid in this case, but the intensity of the field is higher due to the presence of defects (magnetic monopoles) in the system. Notice that we show Y^{3+} and the remaining Dy^{3+} in the pyrochlore lattice with ghost spheres, according to our colour scheme.

In all cases for LT spin configurations, we can see that the field has its highest strength at the centre of the rare earth tetrahedra (i.e. close to the spins) and its lowest strength at the centres of the super tetrahedra. This is in good agreement with the $Dy_2Ti_2O_7$ annealed crystal, but we can notice that the intensity of the field in the latter positions is a little bit higher than in the stoichiometric case. This is a direct manifestation of the presence of magnetic impurities that breaks the

symmetry of the "flux loops" of the spins (see Chap. 4).

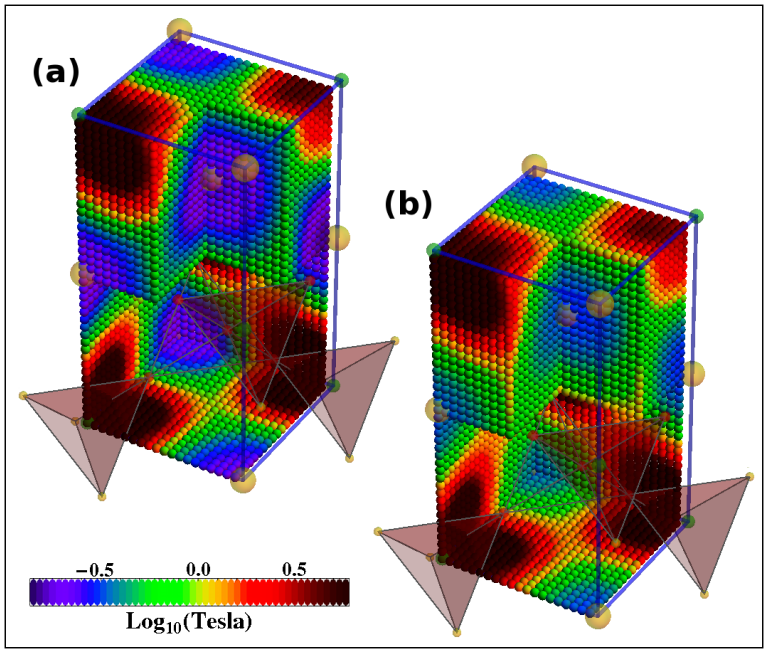

Figure 7.6: *Detailed structure of the field distribution of* $Dy_{2-x}Y_xTi_2O_7$ *for* $x = 1.0$ *on the lattice scale, calculated in a quarter of the unit cell.* – **(a)** Internal fields distribution for LT spin configurations and **(b)** for HT.

The high temperature spin configurations looks very different from the stoichiometric $Dy_2Ti_2O_7$ system. As we said before, the doping destroys the correlations between spins. This phenomenon preserves the local structure of the fields inside the crystal and, at very high doping levels, the difference between LT and HT spin configurations vanishes (see Figs. 7.4,7.7). We can still recognise that the intensity of the field at the centre of the super tetrahedra is a little bit higher for HT configurations, but definitely the global local structure is now preserved.

7.6 Discussion

On the basis of the previous results, we would like to make a couple of comments on the analysis of the internal field distribution. All the previous calculations rely on the fact that Eq. 1.1 is also able to model the doped systems in the correct way.

Notice that this statement is not trivial since, in order to calculate the internal fields of the sample we need to know the correct spin configurations at a certain value of temperature. In principle this problem does not affect the HT configurations, since they correspond to infinite temperature states of the system, and we checked that the difference between HT and random [111] Ising spin configurations is negligible. However we have to be careful about the LT spin configurations,

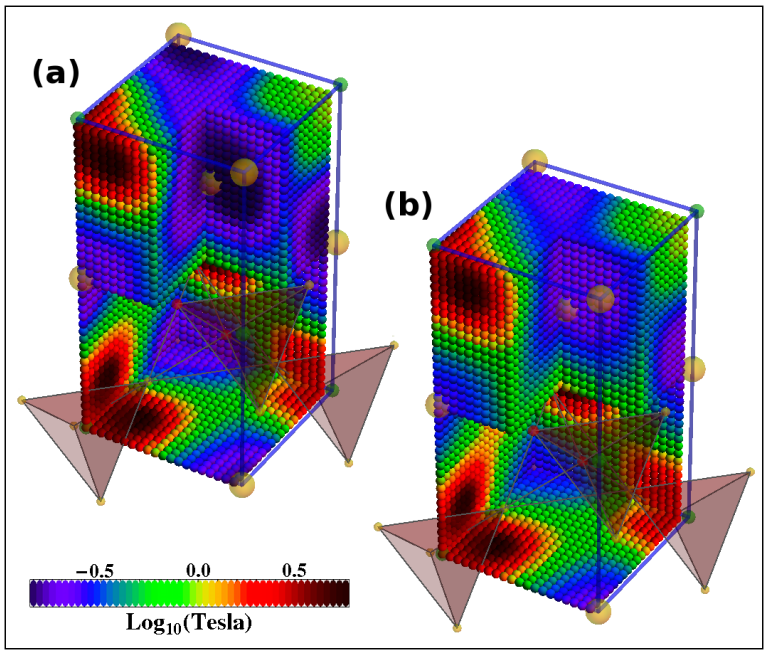

Figure 7.7: *Detailed structure of the field distribution of* $Dy_{2-x}Y_xTi_2O_7$ *for* $x = 1.5$ *on the lattice scale, calculated in a quarter of the unit cell.* – **(a)** Internal fields distribution for LT spin configurations and **(b)** for HT. As it is visible, at very high doping levels, the difference between LT and HT spin configurations vanishes.

since they are generated at the end of the MC loop that minimise the energy of the system, and this calculation is strongly related to the Hamiltonian we are using.

We could investigate this phenomenon, e.g. by comparing the heat capacity of the doped systems with the one calculated with our MC using the classical spin ice Hamiltonian (Eq. 1.1) or the truncated expansion at the nearest neighbour level. In principle we can speculate that the removal of spins should suppress the dipolar interaction in Eq. 1.1, especially at very high doping levels, leaving the nearest neighbour interaction as the leading contribution in the energy of the system.

Figure 7.8 shows the comparison between our MC simulations using Eq. 1.1 with $D = 1.41$ K and $J_{ex} = -1.24$ K (solid lines) or the truncated nearest neighbour expansion with $J_{ex} = 1.11$ K (dashed lines), and the heat capacity data taken from Ref. [103] (dotted lines).

As is clearly visible from Fig. 7.8(a), the classical spin ice Hamiltonian is able to reproduce the heat capacity of the system even at a dilution of $x = 1.4$. Once again the nearest neighbour model alone is insufficient to describe the physics of the system, and the lack of a long range interaction does not allow us to minimise the energy (and obtain the spin configurations) in the correct way, at least until $x = 1.4$.

We have to notice that after this "threshold" it seems that the agreement of our

MC simulation using Eq. 1.1 fails, and the model that is able to fit the heat capacity data (at least at low temperatures) is the nearest neighbour one.

The failure of the dipolar model at high dilution may reflect a need to use a larger system for MC simulations in this case. However, we would like to stress two points:

1. According to Ref. [103], the blue dotted line in Fig. 7.8(c) should represent the heat capacity of a $\mathrm{Dy}_{0.2}\mathrm{Y}_{1.8}\mathrm{Ti}_2\mathrm{O}_7$ crystal. In order to have a better agreement with the data, we found that the correct value of x should be 1.75. This may indicate uncertainty about the uniformity and absolute value of the stoichiometry of the sample.

2. Our simulation is not able to reproduce the relative noisy behaviour of the highly doped compound after $T = 3$ K, which would seen to be an indication of a high background level.

7.7 Conclusion

We analysed in great detail the physical properties of several $\mathrm{Dy}_{2-x}\mathrm{Y}_x\mathrm{Ti}_2\mathrm{O}_7$ annealed crystals. The magnetisation data, benchmarked with our X-ray, neutron scattering analysis and our MC simulations, showed a linear decrease of the magnetisation in the samples according to the doping level, and no trace of a structural phase transition since the similar atomic radius of Dy and Y ions does not affect the lattice.

The comparison of the internal field analysis averaged over LT spin configurations showed that there is still a considerable local order between high and low fields, localised at the centres of the rare earth tetrahedra and at the centres of the super tetrahedra respectively. This is consistent with what we found for the stoichiometric $\mathrm{Dy}_2\mathrm{Ti}_2\mathrm{O}_7$ sample (see Chap. 4) however, unlike the latter, this order seems to be preserved even for HT configurations, since non magnetic impurities are decreasing the correlations between spins.

The heat capacity data showed that the classical spin ice Hamiltonian is able to model the physics of the doped system until $x = 1.4$, after this "threshold" the nearest neighbour model seems to predict the correct behaviour at low temperatures.

We hope that this analysis can be taken as a basis towards a more detailed study of the dynamics of magnetic monopoles in doped systems. In particular it could be very interesting to study how the monopoles can be trapped by non magnetic impurities, in analogy with what we have done for oxygen vacancies.

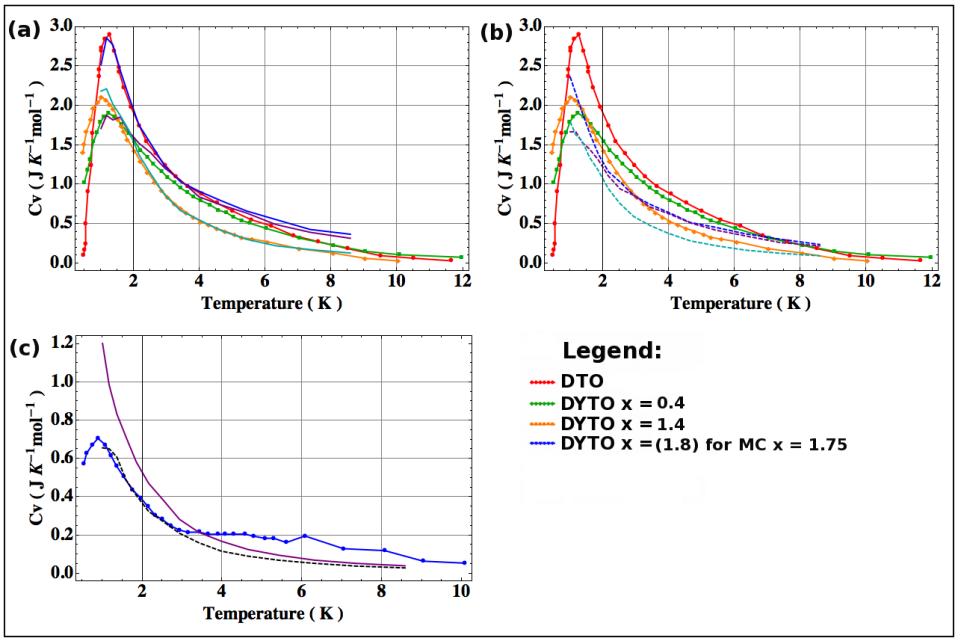

Figure 7.8: *Comparison between the heat capacity data of* $Dy_{2-x}Y_xTi_2O_7$ *for* $x = 0.0, 0.4, 1.4$ *and* 1.8 *according to Ref. [103], and our MC simulations.* – **(a)** Heat capacity calculation using Eq. 1.1 with $D = 1.41$ K and $J_{ex} = -1.24$ K (solid lines). **(b)** Heat capacity calculation using Eq. 1.1 truncated at the nearest neighbour level with $J_{ex} = 1.11$ K (dashed lines). The nearest neighbour model alone is insufficient to describe the physics of the system, and the lacking of a long range interaction does not allow us to minimise the energy (and obtain the spin configurations) in the correct way, at least until $x = 1.4$. **(c)** Comparison of the heat capacity calculation using Eq. 1.1 with $D = 1.41$ K and $J_{ex} = -1.24$ K (solid lines) or the truncated nearest neighbour expansion with $J_{ex} = 1.11$ K (dashed lines) for the highly diluted $Dy_{2-x}Y_xTi_2O_7$ sample. At high doping levels it seems that the agreement of our MC simulation using Eq. 1.1 fails presumably because the size of the MC simulation is too small, and the model that is able to fit the heat capacity data (at least at low temperatures) is the nearest neighbour one. Nevertheless we have to notice that this good agreement has been reached in our simulation using $x = 1.75$ and, at present, we do not know the origin of the discrepancy between data and theoretical predictions after $T = 3$ K.

Chapter 8

Conclusion and Future Outlook

Contents

I was mainly concerned in the study of defects in spin ice crystals. They may rise as topological defects (magnetic monopoles) in the pure compound, or as structural defects from the presence of vacancies and dopant ions.

In particular: the analysis of the internal fields showed that there is a considerable local order between high and low fields due to the symmetry of the pyrochlore lattice. The highest field is felt at the centre of the rare earth tetrahedra, while the lowest field is felt at the centre of the super tetrahedra of the rare earth ions. In principle μSR and NMR techniques can access to these regions of the crystal, providing further information on the internal field distribution in spin ice and quantifying the density of magnetic monopoles present in the system. Notice that the distinction between low and high fields gets broken down as monopoles appear, since their strong fields interact with the other spins in the crystal and break the symmetry. This is indeed a clear evidence of the fact that they act as topological defects of the lattice.

We also studied the effect of oxygen depletion in the crystal. The introduction of oxygen vacancies alters the nature of the compound and, in extreme cases, the system undergoes a structural phase transition from the pyrochlore to the perovskite lattice, loosing the distinctive spin ice features. The analysis of the structural diffuse scattering at low temperatures showed that the 4 rare earth ions close to the vacancy move away along the local $\langle 111 \rangle$ directions, due to the Coulomb repulsion.

This phenomenon creates a chain reaction in the system, forcing the surrounding ions to find new equilibrium positions in order to minimise the Madelung energy. Vacancies affect the Crystal Electric Field (CEF) of the compound changing

the energy of the levels and suppressing the magnetic moment of the spins. Indeed magnetisation measurements on the depleted compounds showed that the magnetisation decreases in the presence of oxygen vacancies.

The structural diffuse scattering also showed that we can get rid of oxygen vacancies (always present even in the common as grown compound), by annealing in O_2 the crystal at $T = 1200°$C. This technique is able to change the oxygen stoichiometry of the compound, which becomes much closer to the ideal one.

According to our CEF calculation the easy axis of the 4 rare earth spins surrounding the vacancy is broken down, and the magnetic moment acquires an easy plane behaviour. This new characteristic is likely to affect also the exchange interaction between spins, and the dynamics of magnetic monopoles. Indeed in the nearest neighbour approximation a simple cluster model of 16 spins showed that, when a monopoles hops into one of the defect tetrahedra, it delocalises and it is not possible to identify where it resides anymore.

This argument can be used to explain the anomalous behaviour of the magnetic monopoles at low temperatures. AC susceptibility measurements confirmed an initial slowing down of magnetic relaxation in the annealed sample with respect to the as-grown one. The presence of vacancies initially speeds up the dynamic due to the increased number of monopoles, the long time dynamics is slowed due to the trapping of diffusing monopoles by the defective clusters. However, a full understanding would require knowledge of all of the exchange constants in the system.

Finally we studied how doping affects spin ice crystals. We saw that there is a linear decrease of the magnetisation of the compound proportional to the doping level, but ice rules are still preserved at low temperatures. Moreover, the impurities affect the spin correlations suppressing the local order between high and low fields. In fact we observed that the internal field distribution at high and low temperatures look very similar for high doping levels.

The possibility of creating magnetic circuits in analogy to electrical circuits, the so called magnetricity, opens up huge potential for practical applications. Here we have identified oxygen vacancies as a source of magnetic residual resistance. The magnetic equivalent of electrical resistance is of great importance in developing magnetic devices. Recently magnetic currents have been created and measured by S.R. Giblin et al. (Ref. [105]), and it would be of great interest to see how these are affected by the controlled introduction of oxygen vacancies, doping etc.

One way to get closer to practical applications is to grow artificial nano structures. L. Bovo et al. (Ref. [106]) have succeeded in growing thin films of spin ice materials, and the properties differ from the bulk at low temperatures. This may be due to epitaxial strain or, alternatively, defects may play a role. It is difficult to grow high quality single crystals for large oxygen deficiencies. However, it may be possible to stabilise much larger departures from stoichiometric compositions in epitaxial single crystal films and, in this way, enable the study of new strongly correlated phenomena.

The magneto thermal avalanche quench has been identified as a mechanism to

study far from equilibrium monopole dynamics in spin ice (Ref. [107]). Here we showed that oxygen vacancies strongly affect the long time out of the equilibrium behaviour. Hence studies of the type described in Refs. [107]-[111] on samples with controlled concentration of oxygen vacancies and other defects would be a promising approach to the study of non equilibrium phases.

We hope that the characterisation contained in this thesis can be used as a starting point for future researches in the spin ice field; in particular towards a proper understanding of the dynamics of the topological defects at low temperatures, which represent a challenging out of the equilibrium system.

Appendix A

Contents

A.1 Ewald 3D Calculation for a spin along the easy axis

Now we show the calculation of the three components of the magnetic field for a spin with magnetic moment along $[1,1,1]/\sqrt{3}$. Notice that this calculation has been done with the conventions expressed in Chap. 2.

$$
\begin{aligned}
B_{x1} = \sum_{n_x,n_y,n_z=-\infty}^{\infty} & +\frac{6(n_x+x)^2\alpha e^{-[(n_x+x)^2+(n_y+y)^2+(n_z+z)^2]\alpha^2}}{\sqrt{\pi}[(n_x+x)^2+(n_y+y)^2+(n_z+z)^2]^2} \quad + \\
& \frac{4\alpha^3(n_x+x)^2 e^{-[(n_x+x)^2+(n_y+y)^2+(n_z+z)^2]\alpha^2}}{\sqrt{\pi}[(n_x+x)^2+(n_y+y)^2+(n_z+z)^2]} \quad + \\
& \frac{3(n_x+x)^2 \mathrm{erfc}[\sqrt{(\mathrm{n_x+x})^2+(\mathrm{n_y+y})^2+(\mathrm{n_z+z})^2}\alpha]}{[(n_x+x)^2+(n_j+y)^2+(n_z+z)^2]^{5/2}} \quad + \\
& \frac{6(n_x+x)(n_y+y)\alpha e^{-[(n_x+x)^2+(n_y+y)^2+(n_z+z)^2]\alpha^2}}{\sqrt{\pi}[(n_x+x)^2+(n_y+y)^2+(n_z+z)^2]^2} \quad + \\
& \frac{4\alpha^3(n_x+x)(n_y+y) e^{-[(n_x+x)^2+(n_y+y)^2+(n_z+z)^2]\alpha^2}}{\sqrt{\pi}[(n_x+x)^2+(n_y+y)^2+(n_z+z)^2]} \quad + \\
& \frac{3(n_x+x)(n_y+y)\mathrm{erfc}[\sqrt{(\mathrm{n_x+x})^2+(\mathrm{n_y+y})^2+(\mathrm{n_z+z})^2}\alpha]}{[(n_x+x)^2+(n_j+y)^2+(n_z+z)^2]^{5/2}} \quad + \\
& \frac{6(n_x+x)(n_z+z)\alpha e^{-[(n_x+x)^2+(n_y+y)^2+(n_z+z)^2]\alpha^2}}{\sqrt{\pi}[(n_x+x)^2+(n_y+y)^2+(n_z+z)^2]^2} \quad +
\end{aligned}
$$

$$\frac{4\alpha^3(n_x+x)(n_z+z)e^{-[(n_x+x)^2+(n_y+y)^2+(n_z+z)^2]\alpha^2}}{\sqrt{\pi}[(n_x+x)^2+(n_y+y)^2+(n_z+z)^2]} +$$
$$\frac{3(n_x+x)(n_z+z)\mathrm{erfc}[\sqrt{(\mathrm{n_x+x})^2+(\mathrm{n_y+y})^2+(\mathrm{n_z+z})^2}\alpha]}{[(n_x+x)^2+(n_j+y)^2+(n_z+z)^2]^{5/2}} -$$
$$\frac{2\alpha e^{-[(n_x+x)^2+(n_y+y)^2+(n_z+z)^2]\alpha^2}}{\sqrt{\pi}[(n_x+x)^2+(n_y+y)^2+(n_z+z)^2]} -$$
$$\frac{\mathrm{erfc}[\sqrt{(\mathrm{n_x+x})^2+(\mathrm{n_y+y})^2+(\mathrm{n_z+z})^2}\alpha]}{[(n_x+x)^2+(n_j+y)^2+(n_z+z)^2]^{3/2}}\hat{x} \qquad \text{(A.1)}$$

$$B_{y1}=\sum_{n_x,n_y,n_z=-\infty}^{\infty} +\frac{6(n_x+x)(n_y+y)\alpha e^{-[(n_x+x)^2+(n_y+y)^2+(n_z+z)^2]\alpha^2}}{\sqrt{\pi}[(n_x+x)^2+(n_y+y)^2+(n_z+z)^2]^2} +$$
$$\frac{4\alpha^3(n_x+x)(n_y+y)e^{-[(n_x+x)^2+(n_y+y)^2+(n_z+z)^2]\alpha^2}}{\sqrt{\pi}[(n_x+x)^2+(n_y+y)^2+(n_z+z)^2]} +$$
$$\frac{3(n_x+x)(n_y+y)\mathrm{erfc}[\sqrt{(\mathrm{n_x+x})^2+(\mathrm{n_y+y})^2+(\mathrm{n_z+z})^2}\alpha]}{[(n_x+x)^2+(n_j+y)^2+(n_z+z)^2]^{5/2}} +$$
$$\frac{6(n_y+y)^2\alpha e^{-[(n_x+x)^2+(n_y+y)^2+(n_z+z)^2]\alpha^2}}{\sqrt{\pi}[(n_x+x)^2+(n_y+y)^2+(n_z+z)^2]^2} +$$
$$\frac{4\alpha^3(n_y+y)^2e^{-[(n_x+x)^2+(n_y+y)^2+(n_z+z)^2]\alpha^2}}{\sqrt{\pi}[(n_x+x)^2+(n_y+y)^2+(n_z+z)^2]} +$$
$$\frac{3(n_y+y)^2\mathrm{erfc}[\sqrt{(\mathrm{n_x+x})^2+(\mathrm{n_y+y})^2+(\mathrm{n_z+z})^2}\alpha]}{[(n_x+x)^2+(n_j+y)^2+(n_z+z)^2]^{5/2}} +$$
$$\frac{6(n_y+y)(n_z+z)\alpha e^{-[(n_x+x)^2+(n_y+y)^2+(n_z+z)^2]\alpha^2}}{\sqrt{\pi}[(n_x+x)^2+(n_y+y)^2+(n_z+z)^2]^2} +$$
$$\frac{4\alpha^3(n_y+y)(n_z+z)e^{-[(n_x+x)^2+(n_y+y)^2+(n_z+z)^2]\alpha^2}}{\sqrt{\pi}[(n_x+x)^2+(n_y+y)^2+(n_z+z)^2]} +$$
$$\frac{3(n_y+y)(n_z+z)\mathrm{erfc}[\sqrt{(\mathrm{n_x+x})^2+(\mathrm{n_y+y})^2+(\mathrm{n_z+z})^2}\alpha]}{[(n_x+x)^2+(n_j+y)^2+(n_z+z)^2]^{5/2}} -$$
$$\frac{2\alpha e^{-[(n_x+x)^2+(n_y+y)^2+(n_z+z)^2]\alpha^2}}{\sqrt{\pi}[(n_x+x)^2+(n_y+y)^2+(n_z+z)^2]} -$$
$$\frac{\mathrm{erfc}[\sqrt{(\mathrm{n_x+x})^2+(\mathrm{n_y+y})^2+(\mathrm{n_z+z})^2}\alpha]}{[(n_x+x)^2+(n_j+y)^2+(n_z+z)^2]^{3/2}}\hat{y} \qquad \text{(A.2)}$$

$$B_{z1}=\sum_{n_x,n_y,n_z=-\infty}^{\infty} +\frac{6(n_x+x)(n_z+z)\alpha e^{-[(n_x+x)^2+(n_y+y)^2+(n_z+z)^2]\alpha^2}}{\sqrt{\pi}[(n_x+x)^2+(n_y+y)^2+(n_z+z)^2]^2} +$$
$$\frac{4\alpha^3(n_x+x)(n_z+z)e^{-[(n_x+x)^2+(n_y+y)^2+(n_z+z)^2]\alpha^2}}{\sqrt{\pi}[(n_x+x)^2+(n_y+y)^2+(n_z+z)^2]} +$$

$$\frac{3(n_x+x)(n_z+z)\mathrm{erfc}[\sqrt{(\mathrm{n_x+x})^2+(\mathrm{n_y+y})^2+(\mathrm{n_z+z})^2}\alpha]}{[(n_x+x)^2+(n_j+y)^2+(n_z+z)^2]^{5/2}} +$$
$$\frac{6(n_y+y)(n_z+z)\alpha e^{-[(n_x+x)^2+(n_y+y)^2+(n_z+z)^2]\alpha^2}}{\sqrt{\pi}[(n_x+x)^2+(n_y+y)^2+(n_z+z)^2]^2} +$$
$$\frac{4\alpha^3(n_y+y)(n_z+z)e^{-[(n_x+x)^2+(n_y+y)^2+(n_z+z)^2]\alpha^2}}{\sqrt{\pi}[(n_x+x)^2+(n_y+y)^2+(n_z+z)^2]} +$$
$$\frac{3(n_y+y)(n_z+z)\mathrm{erfc}[\sqrt{(\mathrm{n_x+x})^2+(\mathrm{n_y+y})^2+(\mathrm{n_z+z})^2}\alpha]}{[(n_x+x)^2+(n_j+y)^2+(n_z+z)^2]^{5/2}} +$$
$$\frac{6(n_z+z)^2\alpha e^{-[(n_x+x)^2+(n_y+y)^2+(n_z+z)^2]\alpha^2}}{\sqrt{\pi}[(n_x+x)^2+(n_y+y)^2+(n_z+z)^2]^2} +$$
$$\frac{4\alpha^3(n_z+z)^2e^{-[(n_x+x)^2+(n_y+y)^2+(n_z+z)^2]\alpha^2}}{\sqrt{\pi}[(n_x+x)^2+(n_y+y)^2+(n_z+z)^2]} +$$
$$\frac{3(n_z+z)^2\mathrm{erfc}[\sqrt{(\mathrm{n_x+x})^2+(\mathrm{n_y+y})^2+(\mathrm{n_z+z})^2}\alpha]}{[(n_x+x)^2+(n_j+y)^2+(n_z+z)^2]^{5/2}} -$$
$$\frac{2\alpha e^{-[(n_x+x)^2+(n_y+y)^2+(n_z+z)^2]\alpha^2}}{\sqrt{\pi}[(n_x+x)^2+(n_y+y)^2+(n_z+z)^2]} -$$
$$\frac{\mathrm{erfc}[\sqrt{(\mathrm{n_x+x})^2+(\mathrm{n_y+y})^2+(\mathrm{n_z+z})^2}\alpha]}{[(n_x+x)^2+(n_j+y)^2+(n_z+z)^2]^{3/2}}\hat{z} \quad \text{(A.3)}$$

and for the second part:

$$B_{x2} = \sum_{n_x=+1}^{\infty} -8\pi\cos(2\pi n_x x)e^{-\frac{\pi^2 n_x^2}{\alpha^2}} +$$
$$\sum_{n_x,n_y,n_z=+1}^{\infty} \frac{-32\pi n_x^2 e^{-\frac{\pi^2(n_x^2+n_y^2+n_z^2)}{\alpha^2}}}{n_x^2+n_y^2+n_z^2}\cos(2\pi n_x x)\cos(2\pi n_y y)\cos(2\pi n_z z) +$$
$$\frac{+32\pi n_x n_y e^{-\frac{\pi^2(n_x^2+n_y^2+n_z^2)}{\alpha^2}}}{n_x^2+n_y^2+n_z^2}\sin(2\pi n_x x)\sin(2\pi n_y y)\cos(2\pi n_z z) +$$
$$\frac{+32\pi n_x n_z e^{-\frac{\pi^2(n_x^2+n_y^2+n_z^2)}{\alpha^2}}}{n_x^2+n_y^2+n_z^2}\sin(2\pi n_x x)\cos(2\pi n_y y)\sin(2\pi n_z z) +$$
$$\sum_{n_x,n_y=+1}^{\infty} \frac{-16\pi n_x^2 e^{-\frac{\pi^2(n_x^2+n_y^2)}{\alpha^2}}}{n_x^2+n_y^2}\cos(2\pi n_x x)\cos(2\pi n_y y) +$$
$$\frac{+16\pi n_x n_y e^{-\frac{\pi^2(n_x^2+n_y^2)}{\alpha^2}}}{n_x^2+n_y^2}\sin(2\pi n_x x)\sin(2\pi n_y y) +$$

$$\sum_{n_x,n_z=+1}^{\infty} \frac{-16\pi n_x^2 e^{-\frac{\pi^2(n_x^2+n_z^2)}{\alpha^2}}}{n_x^2+n_z^2}\cos(2\pi n_x x)\cos(2\pi n_z z) \quad +$$

$$\frac{+16\pi n_x n_z e^{-\frac{\pi^2(n_x^2+n_z^2)}{\alpha^2}}}{n_x^2+n_z^2}\sin(2\pi n_x x)\sin(2\pi n_z z)\hat{x} \quad \text{(A.4)}$$

$$B_{y2} = \sum_{n_y=+1}^{\infty} -8\pi\cos(2\pi n_y y)e^{-\frac{\pi^2 n_y^2}{\alpha^2}} \quad +$$

$$\sum_{n_x,n_y,n_z=+1}^{\infty} \frac{-32\pi n_y^2 e^{-\frac{\pi^2(n_x^2+n_y^2+n_z^2)}{\alpha^2}}}{n_x^2+n_y^2+n_z^2}\cos(2\pi n_x x)\cos(2\pi n_y y)\cos(2\pi n_z z) \quad +$$

$$\frac{+32\pi n_x n_y e^{-\frac{\pi^2(n_x^2+n_y^2+n_z^2)}{\alpha^2}}}{n_x^2+n_y^2+n_z^2}\sin(2\pi n_x x)\sin(2\pi n_y y)\cos(2\pi n_z z) \quad +$$

$$\frac{+32\pi n_y n_z e^{-\frac{\pi^2(n_x^2+n_y^2+n_z^2)}{\alpha^2}}}{n_x^2+n_y^2+n_z^2}\cos(2\pi n_x x)\sin(2\pi n_y y)\sin(2\pi n_z z) \quad +$$

$$\sum_{n_x,n_y=+1}^{\infty} \frac{-16\pi n_y^2 e^{-\frac{\pi^2(n_x^2+n_y^2)}{\alpha^2}}}{n_x^2+n_y^2}\cos(2\pi n_x x)\cos(2\pi n_y y) \quad +$$

$$\frac{+16\pi n_x n_y e^{-\frac{\pi^2(n_x^2+n_y^2)}{\alpha^2}}}{n_x^2+n_y^2}\sin(2\pi n_x x)\sin(2\pi n_y y) \quad +$$

$$\sum_{n_y,n_z=+1}^{\infty} \frac{-16\pi n_y^2 e^{-\frac{\pi^2(n_y^2+n_z^2)}{\alpha^2}}}{n_y^2+n_z^2}\cos(2\pi n_y y)\cos(2\pi n_z z) \quad +$$

$$\frac{+16\pi n_y n_z e^{-\frac{\pi^2(n_y^2+n_z^2)}{\alpha^2}}}{n_y^2+n_z^2}\sin(2\pi n_y y)\sin(2\pi n_z z)\hat{y} \quad \text{(A.5)}$$

$$B_{z2} = \sum_{n_z=+1}^{\infty} -8\pi\cos(2\pi n_z z)e^{-\frac{\pi^2 n_z^2}{\alpha^2}} \quad +$$

$$\sum_{n_x,n_y,n_z=+1}^{\infty} \frac{-32\pi n_z^2 e^{-\frac{\pi^2(n_x^2+n_y^2+n_z^2)}{\alpha^2}}}{n_x^2+n_y^2+n_z^2}\cos(2\pi n_x x)\cos(2\pi n_y y)\cos(2\pi n_z z) \quad +$$

$$\frac{+32\pi n_x n_z e^{-\frac{\pi^2(n_x^2+n_y^2+n_z^2)}{\alpha^2}}}{n_x^2+n_y^2+n_z^2}\sin(2\pi n_x x)\cos(2\pi n_y y)\sin(2\pi n_z z) \quad +$$

$$\frac{+32\pi n_y n_z e^{-\frac{\pi^2(n_x^2+n_y^2+n_z^2)}{\alpha^2}}}{n_x^2+n_y^2+n_z^2}\cos(2\pi n_x x)\sin(2\pi n_y y)\sin(2\pi n_z z) \quad +$$

$$\sum_{n_x,n_z=+1}^{\infty} \frac{-16\pi n_z^2 e^{-\frac{\pi^2(n_x^2+n_z^2)}{\alpha^2}}}{n_x^2+n_z^2} \cos(2\pi n_x x)\cos(2\pi n_z z) \quad + \\ \frac{+16\pi n_x n_z e^{-\frac{\pi^2(n_x^2+n_z^2)}{\alpha^2}}}{n_x^2+n_z^2} \sin(2\pi n_x x)\sin(2\pi n_z z) \quad + \\ \sum_{n_y,n_z=+1}^{\infty} \frac{-16\pi n_z^2 e^{-\frac{\pi^2(n_y^2+n_z^2)}{\alpha^2}}}{n_y^2+n_z^2} \cos(2\pi n_y y)\cos(2\pi n_z z) \quad + \\ \frac{+16\pi n_y n_z e^{-\frac{\pi^2(n_y^2+n_z^2)}{\alpha^2}}}{n_y^2+n_z^2} \sin(2\pi n_y y)\sin(2\pi n_z z)\hat{z} \quad \text{(A.6)}$$

Finally the magnetic field is:

$$\|\vec{B}\| = \frac{\mu_0\mu}{4\pi\sqrt{3}}\frac{1}{\mathcal{L}^3}\sqrt{(B_{x1}+B_{x2})^2+(B_{y1}+B_{y2})^2+(B_{z1}+B_{z2})^2} \quad \text{(A.7)}$$

where

$$\begin{cases} x = (r_i^x - r_j^x)/\mathcal{L} = r_i^x/\mathcal{L} \\ y = (r_i^y - r_j^y)/\mathcal{L} = r_i^y/\mathcal{L} \\ z = (r_i^z - r_j^z)/\mathcal{L} = r_i^z/\mathcal{L} \end{cases} \quad \text{(A.8)}$$

and again $\mathcal{L}$ is the dimensional size of the total simulation cell (i.e. $\mathcal{L} = 2\sqrt{2}Lr_{nn}$).

Appendix B

Contents

B.1 The Ewald 2D calculation of the magnetic field

We present here the Ewald calculation of the magnetic field for a 2D lattice, the comparison with the 3D case can be very useful to understand the physical properties of these systems.

According to Ref. [112], the total Coulomb energy for a system periodic in two dimensions and finite in the third one is:

$$U = \frac{1}{2}\sum_{i,j=1}^{N}\left\{\sum_{|\vec{n}|=0}^{\infty'} q_i q_j \frac{\mathrm{erfc}(\alpha|\vec{r}_{ij}+\vec{n}|)}{|\vec{r}_{ij}+\vec{n}|} + \frac{\pi}{A}\sum_{\vec{h}\neq 0} q_i q_j \frac{\cos(\vec{h}\cdot\vec{r}_{ij})}{|\vec{h}|}\right.$$
$$\left.\left[e^{|\vec{h}|z_{ij}}\mathrm{erfc}\left(\alpha z_{ij}+\frac{|\vec{h}|}{2\alpha}\right) + e^{-|\vec{h}|z_{ij}}\mathrm{erfc}\left(-\alpha z_{ij}+\frac{|\vec{h}|}{2\alpha}\right)\right]\right\} -$$
$$\frac{\pi}{A}\sum_{i,j=1}^{N} q_i q_j \left\{z_{ij}\mathrm{erf}(\alpha \mathrm{z_{ij}}) + \frac{1}{\alpha\sqrt{\pi}}\mathrm{e}^{-\alpha^2 \mathrm{z_{ij}^2}}\right\} \qquad \text{(B.1)}$$

Here $\vec{h} = 2\pi(n_x/\mathcal{L}, n_y/\mathcal{L}, 0)$ is a reciprocal vector, $A = \mathcal{L}\times\mathcal{L}$ is the area of the simulation cell and the term erfc(z) represents the complementary error function of the system:

$$\mathrm{erfc(z)} = 1 - \mathrm{erf(z)} = \frac{2}{\sqrt{\pi}}\int_z^\infty e^{-t^2}dt = \frac{e^{-z^2}}{z\sqrt{\pi}}\sum_{n=0}^{\infty}(-1)^n\frac{(2n-1)!!}{(2z^2)^n} \qquad \text{(B.2)}$$

Notice that the last term in Eq. B.2 represents the boundary condition on the $\hat{z}$ axis, this term is of fundamental importance in order to calculate the low field along it.

Now if we use again the three assumptions we made for the 3D calculation, in perfect analogy we can observe that:

$$\phi(\vec{r}_{ij})_{d.d} = -\frac{1}{q_i q_j}(\mu_i \cdot \nabla)(\mu_j \cdot \nabla)\phi(\vec{r}_{ij})_{c.c} \tag{B.3}$$

and the Hamiltonian can be explicitly rewritten the summation over i, j as:

$$H = \sum_{ij} \frac{1}{\mathcal{L}} q_i q_j U + const. \tag{B.4}$$

where again the term $const.$ takes care of all the terms regarding the chemical potential. Adding the dipole-dipole interaction, we obtain the following Hamiltonian:

$$H = \sum_{ij} -\frac{1}{q_i q_j}(\mu_i \cdot \nabla)(\mu_j \cdot \nabla)\left[\frac{1}{\mathcal{L}} q_i q_j U + const\right] \tag{B.5}$$

$$H = -\frac{1}{2}\sum_{i \neq j} \frac{1}{\mathcal{L}}(\mu_i \cdot \nabla)(\mu_j \cdot \nabla) U \tag{B.6}$$

where we put $1/2$ to avoid the double counting, and we split the two summations because we only need the terms where $i \neq j$.

This equation can be compared with the classical Hamiltonian:

$$H = -\frac{1}{2}\sum_{i \neq j} \vec{\mu_j} \cdot \vec{B}_i(r_{ij}) + \sum_i v_i \tag{B.7}$$

Again the terms $\sum_i v_i$ takes care of the terms where $i = j$, but we do not need them.

We can therefore identify:

$$H = -\vec{\mu_j} \cdot \vec{B}_i(r_{ij}) = -\frac{1}{\mathcal{L}}(\vec{\mu_j} \cdot \nabla)(\vec{\mu_i} \cdot \nabla) U \tag{B.8}$$

And

$$\vec{B}_i(r_{ij}) = \frac{1}{\mathcal{L}} \nabla \left[\vec{\mu_i} \cdot \nabla U\right] \tag{B.9}$$

Note that the gradients are taken with respect to $\vec{r}_{ij}$. Expressing B in S.I. units and re-writing the gradients with respect to $\vec{x} = \vec{r}_{ij}/\mathcal{L} = (x,\ y,\ z)$ we obtain:

$$\vec{B}_i(\vec{r}_{ij}) = \frac{\mu_0 \mu}{4\pi} \frac{1}{\mathcal{L}^3} \nabla_x \left[\hat{\mu_i} \cdot \nabla_x U(\vec{x})\right] \tag{B.10}$$

Therefore the only problem left is to calculate the gradient of the function U but, thanks to assumptions we made, we obtain for the first part:

$$B_{x1} = \sum_{n_x,n_y=-\infty}^{+\infty} + \frac{6\alpha(n_x+x)(z)e^{-[(n_x+x)^2+(n_y+y)^2+(z)^2]\alpha^2}}{\sqrt{\pi}[(n_x+x)^2+(n_y+y)^2+(z)^2]^2} + \frac{4\alpha^3(n_x+x)(z)e^{-[(n_x+x)^2+(n_y+y)^2+(z)^2]\alpha^2}}{\sqrt{\pi}[(n_x+x)^2+(n_y+y)^2+(z)^2]} + \frac{3(n_x+x)(z)\mathrm{erfc}[\alpha\sqrt{(\mathrm{n_x+x})^2+(\mathrm{n_y+y})^2+(\mathrm{z})^2}]}{[(n_x+x)^2+(n_y+y)^2+(z)^2]^{5/2}} \quad \text{(B.11)}$$

$$B_{y1} = \sum_{n_x,n_y=-\infty}^{+\infty} + \frac{6\alpha(n_y+y)(z)e^{-[(n_x+x)^2+(n_y+y)^2+(z)^2]\alpha^2}}{\sqrt{\pi}[(n_x+x)^2+(n_y+y)^2+(z)^2]^2} + \frac{4\alpha^3(n_y+y)(n_y+z)e^{-[(n_x+x)^2+(n_y+y)^2+(z)^2]\alpha^2}}{\sqrt{\pi}[(n_x+x)^2+(n_y+y)^2+(z)^2]} + \frac{3(n_y+y)(z)\mathrm{erfc}[\alpha\sqrt{(\mathrm{n_x+x})^2+(\mathrm{n_y+y})^2+(\mathrm{z})^2}]}{[(n_x+x)^2+(n_y+y)^2+(z)^2]^{5/2}} \quad \text{(B.12)}$$

$$B_{z1} = \sum_{n_x,n_y=-\infty}^{+\infty} - \frac{2\alpha e^{-[(n_x+x)^2+(n_y+y)^2+(z)^2]\alpha^2}}{\sqrt{\pi}[(n_x+x)^2+(n_y+y)^2+(z)^2]} + \frac{6\alpha(z)^2e^{-[(n_x+x)^2+(n_y+y)^2+(z)^2]\alpha^2}}{\sqrt{\pi}[(n_x+x)^2+(n_y+y)^2+(z)^2]^2} + \frac{4(z)^2\alpha^3e^{-[(n_x+x)^2+(n_y+y)^2+(z)^2]\alpha^2}}{\sqrt{\pi}[(n_x+x)^2+(n_y+y)^2+(z)^2]} - \frac{\mathrm{erfc}[\alpha\sqrt{(\mathrm{n_x+x})^2+(\mathrm{n_y+y})^2+(\mathrm{z})^2}]}{[(n_x+x)^2+(n_y+y)^2+(z)^2]^{3/2}} + \frac{3(z)^2\mathrm{erfc}[\alpha\sqrt{(\mathrm{n_x+x})^2+(\mathrm{n_y+y})^2+(\mathrm{z})^2}]}{[(n_x+x)^2+(n_y+y)^2+(z)^2]^{5/2}} \quad \text{(B.13)}$$

and for the second part:

$$B_{x2} = \sum_{n_x,n_y=-\infty,\neq 0}^{+\infty} \frac{2n_x\pi^2}{A}\left[e^{-z\sqrt{4n_x^2\pi^2+4n_y^2\pi^2}}\mathrm{erfc}\left(\frac{\sqrt{4\mathrm{n_x^2}\pi^2+4\mathrm{n_y^2}\pi^2}}{2\alpha}-\mathrm{z}\alpha\right) - e^{z\sqrt{4n_x^2\pi^2+4n_y^2\pi^2}}\mathrm{erfc}\left(\frac{\sqrt{4\mathrm{n_x^2}\pi^2+4\mathrm{n_y^2}\pi^2}}{2\alpha}+\mathrm{z}\alpha\right)\right]\sin(2\pi n_x x+2\pi n_y y) \quad \text{(B.14)}$$

$$B_{y2} = \sum_{n_x,n_y=-\infty,\neq 0}^{+\infty} \frac{2n_y\pi^2}{A}\left[e^{-z\sqrt{4n_x^2\pi^2+4n_y^2\pi^2}}\mathrm{erfc}\left(\frac{\sqrt{4\mathrm{n_x^2}\pi^2+4\mathrm{n_y^2}\pi^2}}{2\alpha}-\mathrm{z}\alpha\right) -$$

$$e^{z\sqrt{4n_x^2\pi^2+4n_y^2\pi^2}}\mathrm{erfc}\left(\frac{\sqrt{4\mathrm{n_x^2}\pi^2+4\mathrm{n_y^2}\pi^2}}{2\alpha}+\mathrm{z}\alpha\right)\Bigg]\sin(2\pi n_x x+2\pi n_y y) \quad \text{(B.15)}$$

$$\begin{aligned} B_{z2} = \sum_{n_x,n_y=-\infty,\neq 0}^{+\infty} \frac{\pi\cos(2\pi n_x x+2\pi n_y y)}{A}\Big[& e^{-z\sqrt{4n_x^2\pi^2+4n_y^2\pi^2}} \\ & \mathrm{erfc}\left(\frac{\sqrt{4\mathrm{n_x^2}\pi^2+4\mathrm{n_y^2}\pi^2}}{2\alpha}-\mathrm{z}\alpha\right)\sqrt{4\mathrm{n_x^2}\pi^2+4\mathrm{n_y^2}\pi^2} \quad + \\ e^{z\sqrt{4n_x^2\pi^2+4n_y^2\pi^2}}\mathrm{erfc}\left(\frac{\sqrt{4\mathrm{n_x^2}\pi^2+4\mathrm{n_y^2}\pi^2}}{2\alpha}+\mathrm{z}\alpha\right)\sqrt{4\mathrm{n_x^2}\pi^2+4\mathrm{n_y^2}\pi^2} & - \\ & \frac{4\alpha e^{-\frac{4n_x^2\pi^2+4n_y^2\pi^2}{4\alpha^2}-z^2\alpha^2}}{\sqrt{\pi}}\Big] \end{aligned} \quad \text{(B.16)}$$

$$B_{z3} = -\frac{4\alpha\sqrt{\pi}}{A}e^{-z^2\alpha^2} \quad \text{(B.17)}$$

Finally the magnetic field is:

$$\|\vec{B}\| = \frac{\mu_0\mu}{4\pi}\frac{1}{\mathcal{L}^3}\sqrt{(B_{x1}+B_{x2})^2+(B_{y1}+B_{y2})^2+(B_{z1}+B_{z2}+B_{z3})^2} \quad \text{(B.18)}$$

where

$$\begin{cases} x = (r_i^x - r_j^x)/\mathcal{L} = r_i^x/\mathcal{L} \\ y = (r_i^y - r_j^y)/\mathcal{L} = r_i^y/\mathcal{L} \\ z = (r_i^z - r_j^z)/\mathcal{L} = r_i^z/\mathcal{L} \end{cases} \quad \text{(B.19)}$$

and $\mathcal{L}$ is the dimensional size of the total simulation cell (i.e. $\mathcal{L} = 2\sqrt{2}Lr_{nn}$).

B.1.1 A comparison between the Ewald 3D and 2D

Now we can analyse the differences between these equations and the ones obtained with the Ewald 3D method. This is very important in order to better understand their behaviour and their physically meaning.

Our method is known as the Hayes, Barber and Clarke method (HBC) and it uses a Fourier integral representation of the sum of Dirac delta functions that stand for the point charges of the system (see Ref. [113]). This approach was originally developed by Bertaut and derived by Parry for the 2D case, in order to compute deviations of the potential near the surface of ionic crystals. The HBC method uses the Gaussian integral to rewrite the inverse particle distance as:

$$\frac{1}{r} = \frac{1}{\sqrt{\pi}}\int_0^\infty \frac{e^{-tr^2}}{\sqrt{t}}dt \quad \text{(B.20)}$$

The integral is separated at $1/\alpha^2$ and gives a short-range part for the integral from $1/\alpha^2$ to ∞, which corresponds to the complementary error function, and a long-range part (for the integral from 0 to $1/\alpha^2$) as in the classical Ewald method to give:

$$\frac{1}{|r_{i,j,\nu}|} = \frac{\mathrm{erfc}(\alpha|\mathrm{r_{i,j,\nu}}|)}{|r_{i,j,\nu}|} + \frac{1}{\sqrt{\pi}} \int_0^{1/\alpha^2} \frac{e^{-t(s_{i,j,\nu}^2 + z_{i,j,\nu}^2)}}{\sqrt{t}} dt \tag{B.21}$$

Here α, whose unit is an inverse length, is the screening parameter for the Gaussian "charge cloud" and should be chosen so that only few real-space vectors ν have to be considered for the short-range summation. With the correct Fourier transformation one ends up with Eq. B.1, correct with the periodic boundary condition on the $\hat{z}$ axis.

Now, if we check the two methods, we can see that the first three terms of the magnetic field (B_{x1}, B_{y1}, B_{z1}) are the same, except for the fact that the summation over n_z is not applied in the 2D case. These functions are the second derivative of the complementary error function and they are computed in the real space. As we said before these equations give the magnetic field strength near the dipole, for a reasonable choice of the α parameter.

The second terms (B_{x2}, B_{y2}, B_{z2}) are computed in the reciprocal space, and they are very different from the Ewald 3D ones. For the 2D case we do not need imaginary terms in the summation, so we can approximate the exponential with a cosine multiplied by two oscillatory functions needed to preserve the 2D structure. These functions are used to calculate the fields very far from the origin, and their approximation is of vital importance in order to obtain a good agreement with the data.

Finally the last term (B_{z3}) appears only in the 2D method, and it expresses the boundary condition over the $\hat{z}$ axis in order to suppress the oscillatory behaviour of the functions very far from the origin.

B.1.2 A comparison between simulations and the analytic formula

In order to benchmark the calculations given by the simulation with the Ewald 2D method, it is possible to compare the results of the simulations with the analytic formula. We can consider a system made up of an infinite array of dipoles pointing along $\hat{z}$, at the same distance and with no thickness (see Fig B.1). This plane will be identified with the X-Y plane of our simulation, then we can measure the strength of the magnetic field in the $\hat{z}$ direction (i.e. in the direction perpendicular to the plane).

In literature, the magnetic field of a dipole is calculated as:

$$\vec{B} = const. \left[\frac{\vec{m}}{r^3} - \frac{3(\vec{m} \cdot \hat{r})\hat{r}}{r^5} \right] \tag{B.22}$$

Where $\vec{m}$ is the magnetic dipole moment and $\hat{r}$ is the verso of the direction.

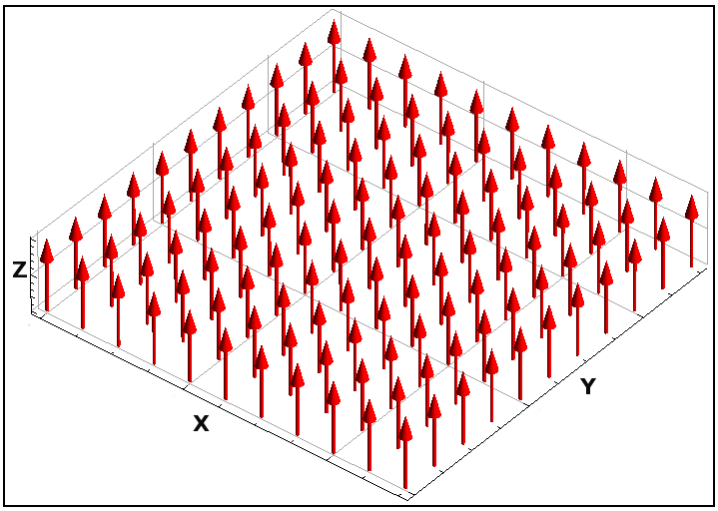

Figure B.1: *Ewald 2D simulation system X-Y plane.* – Red arrows represent spin arrangement in the system.

Taking the module of Eq. B.22 and inserting the characteristic of our system, we can find that the magnetic field strength along $\hat{z}$ is:

$$|\vec{B}| = B_z = const. \sum_{l,m=-N_{\max}}^{N_{\max}} \left[\frac{3z^2}{(z^2+l^2+m^2)^{5/2}} - \frac{1}{(z^2+l^2+m^2)^{3/2}} \right] \quad \text{(B.23)}$$

Where l and m is the replicator vector in the X-Y plane, $N_{\max}$ is the number of spins and $const. = \mu_0\mu/4\pi\mathcal{L}^3$.

Obviously in order to have a good agreement with the simulation the parameter $N_{\max}$ must tend to infinity, but this case is very time consuming so we chose to consider only the case with $N_{\max} = 16, 32, 64$ and 128. Figure B.2 compares $|\vec{B}|$ in function of distance (in unit of $\mathcal{L}$), for the Ewald 2D method (blue dots) and for the analytic formula (solid lines).

As one can see there is a perfect agreement between our simulation and the analytic formula, in particular the agreement gets better and better as soon as $N_{\max}$ gets higher. The plateu is due to the fact that the analytic formula represent a finite system, in fact this plateau tends to decrease as $N_{\max}$ is increased, and then it disappears when $N_{\max} = \infty$. We can check this assumption with a simple calculation; first of all we have to integrate Eq. B.23 over a circle of radius R, and then take the limit to infinity.

In particular:

$$const. \int_0^R 2\pi r \left[\frac{3z^2}{(z^2+r^2)^{5/2}} - \frac{1}{(z^2+r^2)^{3/2}} \right] dr = const. \frac{2\pi R^2}{(R^2+z^2)^{3/2}} \quad \text{(B.24)}$$

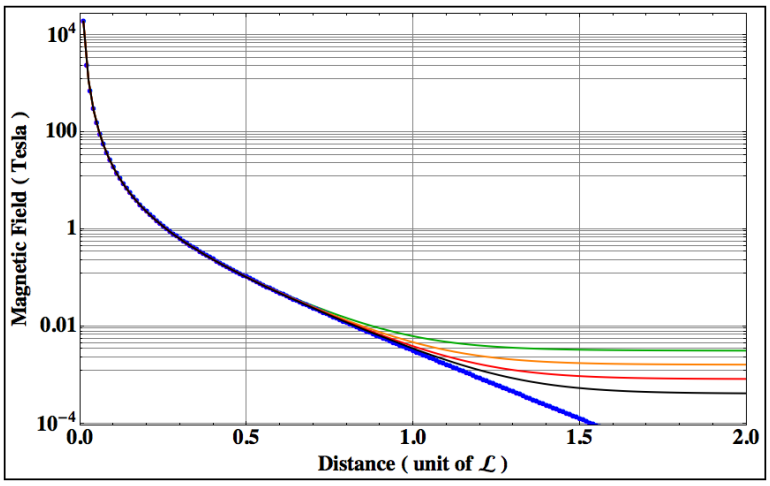

Figure B.2: *Comparison between the Ewald 2D simulation and the analytic formula.* – The solid curve represents the analytic formula (Eq. B.23) for $N_{\max} = 16$ (green), $N_{\max} = 32$ (orange), $N_{\max} = 64$ (red) and $N_{\max} = 128$ (black); blue dots are the simulation data. The initial field decay is power law as $1/z^3$ when the dominant contribution is that of the closest spin. Then it crosses over to an exponential decay in z at large distances, when the system tends asymptotically to the behaviour of a continuum parallel-plate capacitor.

Now taking the limit, we obtain that:

$$\lim_{R\to\infty} const. \frac{2\pi R^2}{(R^2+z^2)^{3/2}} \approx \frac{1}{R} = 0 \tag{B.25}$$

Notice that if we measure the field very far from the surface, the system behaves as a parallel-plate capacitor. We can calculate the magnetic field strength also along $\hat{x}$ and $\hat{y}$, in this case the periodic system will create a series of parabola with the periodicity of the cell (see Fig. B.3).

As we can see the Ewald 2D method replies the dipole in the X-Y plane, the agreement with the analytic result is very good and again it gets better and better as $N_{\max}$ is raised. Notice that we decided to truncate the simulation to the first 2 cells in order to highlight the differences with the analytic formula.

B.1.3 Ewald 2D Calculation for large value of z

Watching closely at Fig. B.2 we can see that when the distance increases, the behaviour of the curve is $\propto e^{-Cz}$ (where C is a constant) and not to $\propto e^{-Cz^2}$. This characteristic is very peculiar and its origin is due to the function f(z) $\propto \mathrm{e}^{-\mathrm{z}}\mathrm{erfc}(-\mathrm{z})$ located in the B_{z2} component; in fact if we expand this term around infinity we find that:

$$f(z\to\infty) \propto \mathrm{e}^{-\mathrm{z}}\mathrm{erfc}(-\mathrm{z}) \approx$$

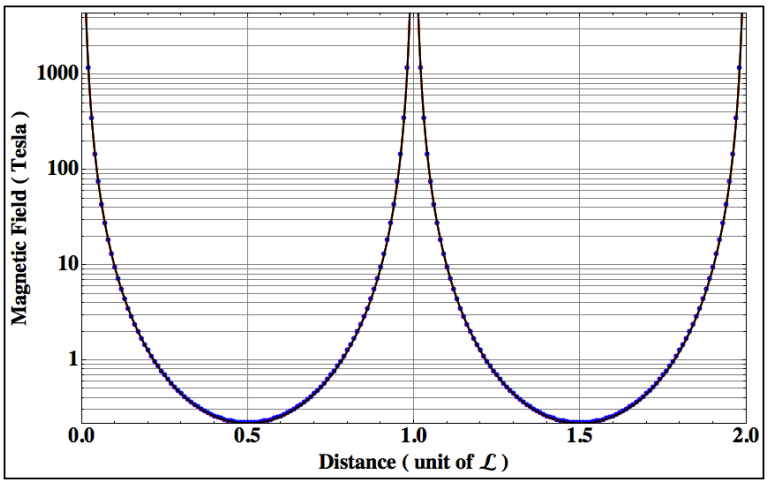

Figure B.3: *Ewald 2D simulation check with the analytic formula along $\hat{x}$ and $\hat{y}$.* – The solid curve represents the magnitude of the field via the analytic formula (Eq. B.23) for $N_{\max} = 16$ (green), $N_{\max} = 32$ (orange), $N_{\max} = 64$ (red) and $N_{\max} = 128$ (black); blue dots are the simulation data.

$$e^{-z-z^2}\left(2e^{z^2}+\left(-\frac{1}{z\sqrt{\pi}}+\frac{1}{2z^3\sqrt{\pi}}-\frac{3}{4z^5\sqrt{\pi}}+O\left[\frac{1}{z^6}\right]\right)\right)\approx 2e^{-z} \quad \text{(B.26)}$$

Figure B.4 shows the behaviour of the three curves $\mathrm{e}^{-\mathrm{z}}\mathrm{erfc}(-\mathrm{z})$ (red line), its Taylor expansion (black line) and $2e^{-z}$ (blue line), for large values of z. As one can see their agreement is indeed remarkable.

Lets try to analyse every single term in Eqs.1.120-1.126, assuming for simplicity that $x = y = 0$:

$$\sum_{n_x,n_y=-\infty}^{+\infty} -\frac{2\alpha e^{-[n_x^2+n_y^2+z^2]\alpha^2}}{\sqrt{\pi}[n_x^2+n_y^2+z^2]} =$$

$$2\alpha e^{-\alpha^2 z^2}\sum_{n_x,n_y=-\infty}^{+\infty} -\frac{e^{-[n_x^2+n_y^2]\alpha^2}}{\sqrt{\pi}[n_x^2+n_y^2+z^2]} \quad \text{(B.27)}$$

If we call $n_x^2 + n_y^2 = r^2$, the above term becomes:

$$2\alpha e^{-\alpha^2 z^2}\sum_{r=0}^{\infty} -\frac{e^{-r^2\alpha^2}}{\sqrt{\pi}[r^2+z^2]} \quad \text{(B.28)}$$

This function satisfies the equality:

$$\frac{2\alpha e^{-\alpha^2 z^2}}{z^2\sqrt{\pi}} \leq 2\alpha e^{-\alpha^2 z^2}\sum_{r=0}^{\infty}\frac{e^{-r^2\alpha^2}}{\sqrt{\pi}[r^2+z^2]}$$

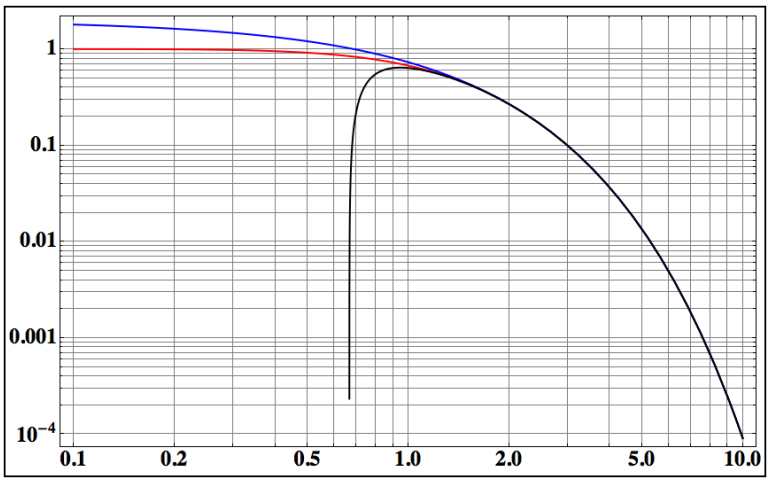

Figure B.4: *Study of the behaviour of the tail for large values of z.* – The red curve represents $\mathrm{e}^{-\mathrm{z}}\mathrm{erfc}(-\mathrm{z})$, the black one is its Taylor expansion while the blue one is the asymptotic expression $2e^{-z}$.

$$\leq 2\alpha e^{-\alpha^2 z^2}\left(\frac{1}{\sqrt{\pi}z^2}+\sum_{r=1}^{\infty}\frac{e^{-r^2\alpha^2}}{\sqrt{\pi}r^2}\right) \tag{B.29}$$

The lower bound was found taking the minimum value of r; the upper bound was found extracting z from the summation and observing that the denominator is the sum of two square quantities that go to infinity. Therefore we can neglect z. The last term in brackets is a constant, so if we now take the limit for $z \to \infty$ due to the Squeeze Theorem, this term is $\propto \mathrm{e}^{-\alpha^2\mathrm{z}^2}$. All the other terms are analogue to this one, except for:

$$\sum_{n_x,n_y=-\infty}^{+\infty} -\frac{\mathrm{erfc}[\alpha\sqrt{\mathrm{n_x^2}+\mathrm{n_y^2}+\mathrm{z^2}}]}{[n_x^2+n_y^2+z^2]^{3/2}} \tag{B.30}$$

In this case the term is composed of a sum of square terms. We can call $r^2 = n_x^2 + n_y^2$ and, since we are looking for the large z behaviour, we can make a Taylor expansion of the complementary error function for z$\to\infty$:

$$\sum_{r=0}^{+\infty} -\frac{\mathrm{erfc}[\alpha\sqrt{\mathrm{r^2}+\mathrm{z^2}}]}{[r^2+z^2]^{3/2}} \approx e^{-\alpha^2 z^2}\sum_{r=0}^{+\infty} -\frac{1}{\alpha\sqrt{\pi}}\frac{e^{-\alpha^2 r^2}}{(r^2+z^2)^2} \tag{B.31}$$

Now this term is analogous to the previous one thus, taking the limit for large z, it is $\propto \mathrm{e}^{-\alpha^2\mathrm{z}^2}$. All the other terms can be analysed in the same way.

The last two functions we are going to analyse are located in the component

B_{z2}. The first one is:

$$\sum_{n_x,n_y=-\infty,\neq 0}^{+\infty} e^{z\sqrt{4n_x^2\pi^2+4n_y^2\pi^2}}\mathrm{erfc}\left(\frac{\sqrt{4\mathrm{n_x^2}\pi^2+4\mathrm{n_y^2}\pi^2}}{2\alpha}+\mathrm{z}\alpha\right)\frac{}{\sqrt{4n_x^2\pi^2+4n_y^2\pi^2}} \tag{B.32}$$

Even for this case we can call $r=\sqrt{n_x^2+n_y^2}$ and then make a Taylor expansion of the complementary error function for large z:

$$\sum_{r=1}^{+\infty} 2\pi r e^{2\pi z r}\mathrm{erfc}\left(\frac{\pi \mathrm{r}}{\alpha}+\mathrm{z}\alpha\right)\approx \mathrm{e}^{-\alpha^2\mathrm{z}^2}\sum_{\mathrm{r}=1}^{+\infty}\frac{2\pi\mathrm{r}}{\sqrt{\pi}(\frac{\pi\mathrm{r}}{\alpha}+\mathrm{z}\alpha)}\mathrm{e}^{-\frac{\pi^2\mathrm{r}^2}{\alpha^2}} \tag{B.33}$$

Now the analysis is similar to the previous cases.

Finally we analyse the term $\propto \mathrm{e}^{-\mathrm{z}}\mathrm{erfc}(-\mathrm{z})$. This term is a bit different from the previous ones and it needs an accurate analysis in order to check the behaviour for large z:

$$\sum_{n_x,n_y=-\infty,\neq 0}^{+\infty} e^{-z\sqrt{4n_x^2\pi^2+4n_y^2\pi^2}}\mathrm{erfc}\left(\frac{\sqrt{4\mathrm{n_x^2}\pi^2+4\mathrm{n_y^2}\pi^2}}{2\alpha}-\mathrm{z}\alpha\right)\frac{}{\sqrt{4n_x^2\pi^2+4n_y^2\pi^2}} \tag{B.34}$$

First of all we can express this summation using a Kronecker delta, in order to express the condition that n_x and n_y can not be zero at the same time:

$$\sum_{n_x=-\infty}^{+\infty}\sum_{n_y=-\infty}^{+\infty}[1-\delta(n_x)\delta(n_y)]e^{-z\sqrt{4n_x^2\pi^2+4n_y^2\pi^2}}$$
$$\mathrm{erfc}\left(\frac{\sqrt{4\mathrm{n_x^2}\pi^2+4\mathrm{n_y^2}\pi^2}}{2\alpha}-\mathrm{z}\alpha\right)\sqrt{4\mathrm{n_x^2}\pi^2+4\mathrm{n_y^2}\pi^2} \tag{B.35}$$

The coefficient n_x and n_y are the component of the reciprocal vector $2\pi(n_x,n_y,0)$ and $\sqrt{4\pi^2n_x^2+4\pi^2n_y^2}$ is its modulo. So, if we fix this value to $\sqrt{n_x^2+n_y^2}=r$, the previous summation can be split in the sum over all the possible value of r:

$$\sum_{r=1}^{\infty}\sum_{n_x=-\infty}^{+\infty}\sum_{n_y=-\infty}^{+\infty}\delta(r^2-n_x^2-n_y^2)2\pi r e^{-2\pi r z}\mathrm{erfc}\left(\frac{\pi\mathrm{r}}{\alpha}-\mathrm{z}\alpha\right) \tag{B.36}$$

The summation over n_x and n_y gives $\approx 2\pi r$, as we can see calculating the integral in polar coordinate:

$$\sum_{n_x=-\infty}^{+\infty}\sum_{n_y=-\infty}^{+\infty}\delta(r^2-n_x^2-n_y^2)\approx 2\pi r \tag{B.37}$$

Therefore the expression can be re-written as:

$$\sum_{r=1}^{\infty} 4\pi^2 r^2 e^{-2\pi r z}\mathrm{erfc}\left(\frac{\pi \mathrm{r}}{\alpha} - \mathrm{z}\alpha\right) \tag{B.38}$$

and this function satisfies the equality:

$$\begin{aligned} 4\pi^2 e^{-2\pi z}\mathrm{erfc}\left(\frac{\pi}{\alpha} - \mathrm{z}\alpha\right) &\leq \sum_{\mathrm{r}=1}^{\infty} 4\pi^2 \mathrm{r}^2 \mathrm{e}^{-2\pi \mathrm{r z}}\mathrm{erfc}\left(\frac{\pi \mathrm{r}}{\alpha} - \mathrm{z}\alpha\right) \\ &\leq 8\pi^2 \sum_{r=1}^{\infty} r^2 e^{-2\pi r z} = \frac{8\pi^2 e^{2\pi z}(1+e^{2\pi z})}{(e^{2\pi z}-1)^3} \end{aligned} \tag{B.39}$$

The lower bound was found taking the minimum value of r, the upper bound was found noting that the complementary error function for large z tends to 2. Now the summation can be explicitly calculated and, using again the Squeeze Theorem, we can check that this term is $\propto \mathrm{e}^{-\mathrm{z}}$ as we wanted to show.

Notice that it is very important to look for the exact coefficients in order to find the function that correctly fits the data. A possible method is to extrapolate from Eq. B.36 all the terms that go as $e^{-2\pi z}$, checking that the remaining parts are negligible and finally multiply the function times π. Thus:

$$\sum_{r=1}^{\infty}\sum_{n_x=-\infty}^{+\infty}\sum_{n_y=-\infty}^{+\infty} \delta(r^2 - n_x^2 - n_y^2) 2\pi r e^{-2\pi r z}\mathrm{erfc}\left(\frac{\pi \mathrm{r}}{\alpha} - \mathrm{z}\alpha\right) =$$

$$\begin{aligned} &\sum_{n_x=-\infty}^{+\infty}\sum_{n_y=-\infty}^{+\infty} \delta(1 - n_x^2 - n_y^2) 4\pi e^{-2\pi z} + \sum_{r=2}^{\infty}\sum_{n_x=-\infty}^{+\infty} \\ &\qquad \sum_{n_y=-\infty}^{+\infty} \delta(r^2 - n_x^2 - n_y^2) 4\pi r e^{-2\pi r z} \end{aligned} \tag{B.40}$$

Where we already used the fact that the complementary error function as $z \to \infty$ tends to 2. The first term can be exactly calculated, and we obtain:

$$16\pi e^{-2\pi z} + \sum_{r=2}^{\infty}\sum_{n_x=-\infty}^{+\infty}\sum_{n_y=-\infty}^{+\infty} \delta(r^2 - n_x^2 - n_y^2) 4\pi r e^{-2\pi r z} \tag{B.41}$$

The second term is negligible because it goes to zero faster than the first one:

$$\begin{aligned} \sum_{r=2}^{\infty} 8\pi^2 r^2 e^{-2\pi r z} = -4\pi \frac{d}{dz}\sum_{r=2}^{\infty} r e^{-2\pi r z} &= -4\pi \frac{d}{dz}\left(\frac{e^{-2\pi z}(2e^{2\pi z}-1)}{(e^{2\pi z}-1)^2}\right) \\ &= \frac{8\pi^2[-3 + 5\cosh(2\pi z) + 3\sinh(2\pi z)]}{(e^{2\pi z}-1)^3} \end{aligned} \tag{B.42}$$

Clearly this term goes to zero faster than the previous one, so the function that approximates our data is only the first term in Eq. B.41 multiplied per π, i.e. $f(z) = 16\pi^2 e^{-2\pi z}$. Figure B.5 shows the comparison between the Ewald 2D data (blue balls) and the previous function (red line) for large values of z.

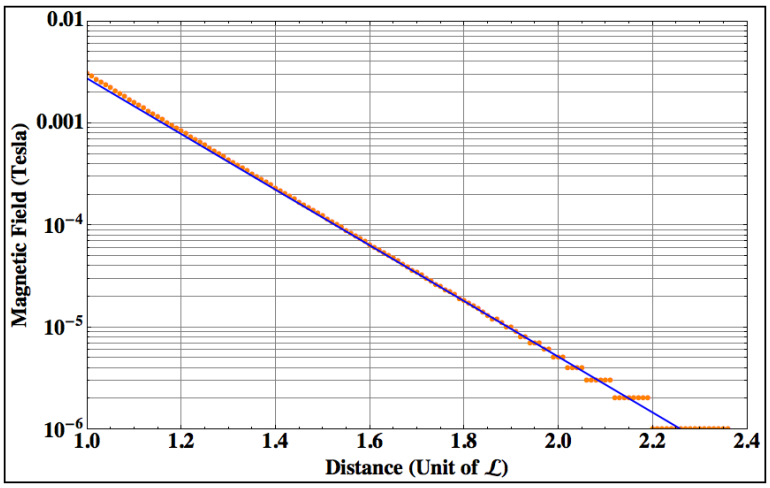

Figure B.5: *Comparison between Ewald 2D simulation data (orange dots) and the analytic function* $f(z) = 16\pi^2 e^{-2\pi z}$ *(blue line) for very large values of z.* – There is a perfect agreement between the simulation data and the analytic formula but the behaviour at large z is crucially dominated by the distance of the spins inside the system.

As we can see there is a perfect agreement between our analytical calculation and the data, nevertheless we must notice that the behaviour at large z is crucially dominated by the distance of the spins inside the system, i.e. from the value we give to n_x and n_y in order to replicate the spins. In fact if we multiply n_x and n_y times a constant A, and we repeat all the previous calculations, we find that the correct function that fits the large z behaviour is:

$$f(z) = 16\pi^2 A e^{-2\pi A z} \tag{B.43}$$

Where the constant $A = a/\mathcal{L}$ with $a \, \epsilon \, R$.

B.1.4 Magnetic field components along the three axes

We conclude this study with a short analysis regarding the sign of the field along the three axes, this is of fundamental importance in order to study the direction of the magnetic field inside a system as in Fig B.1. For this reason we show the three components of the magnetic field calculated along $\hat{x}, \hat{y}$ in Fig B.6, and along $\hat{z}$ in Fig B.7, compared to the analytic formula with $N_{\max} = 16, 32, 64$ and 128.

Simulation data are in good agreement with the analytic formula, as it is clearly visible from Fig B.6; on the X-Y plane the field is periodic nevertheless the sign of

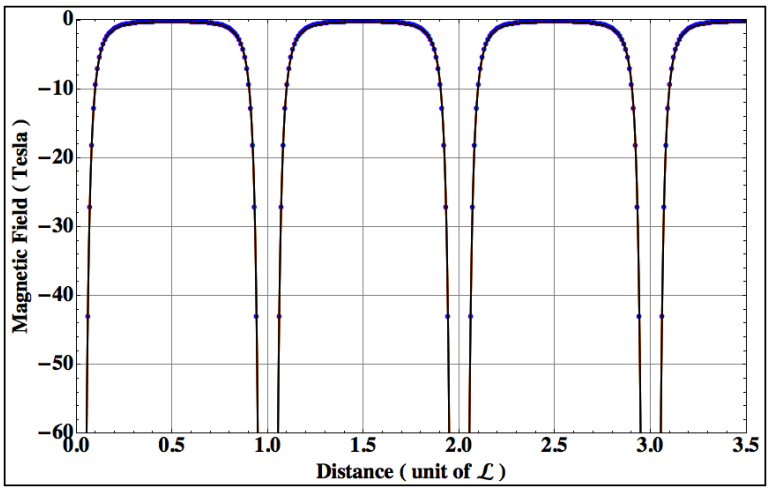

Figure B.6: *Magnetic field component B_z along $\hat{x}$ and $\hat{y}$ axes.* – The solid curve represents the magnitude of the field via the analytic formula (Eq. B.23) for $N_{\max} = 16$ (green), $N_{\max} = 32$ (orange), $N_{\max} = 64$ (red) and $N_{\max} = 128$ (black); blue dots are the simulation data. As one can see the data replies exactly the periodicity of the system.

the component is negative and only B_z is present. These statements are physically correct and they are both due to the spin direction inside the system.

In particular: all the spins are pointing in the $\hat{z}$ direction, so the field is entering in the X-Y plane and the scalar product in Eq. B.22 is zero. The new equation is now:

$$\vec{B} = -const.\frac{\vec{m}}{r^3} \Rightarrow B_z = -const \sum_{l,m=-N_{\max}}^{N_{\max}} \frac{1}{((x+l)^2+m^2)^{3/2}} \qquad \text{(B.44)}$$

This equation takes care of all the assumptions made before since $\vec{m}$, the magnetic dipole moment, points only in the $\hat{z}$ direction.

Fig B.7 shows the three magnetic field components calculated along the $\hat{z}$ direction. Even in this case only B_z is present but the system has no periodicity, we also verified that the component B_x and B_y are perfectly zero in the data.

For all these cases there is a good agreement between the Ewald 2D simulation and the analytic formula.

Now we can analyse the B_x and B_y components of the field along $\hat{x}$ and $\hat{y}$ axes with $z = \mathcal{L}/100$, Fig. B.8 shows the result of the simulation (magenta dots) compared with the analytic formula (Eq. B.22) for $N_{\max} = 16$ (green), $N_{\max} = 32$ (orange), $N_{\max} = 64$ (red) and $N_{\max} = 128$ (black). In this case the components B_x and B_y are not zero, and we have a remarkable agreement with the simulation.

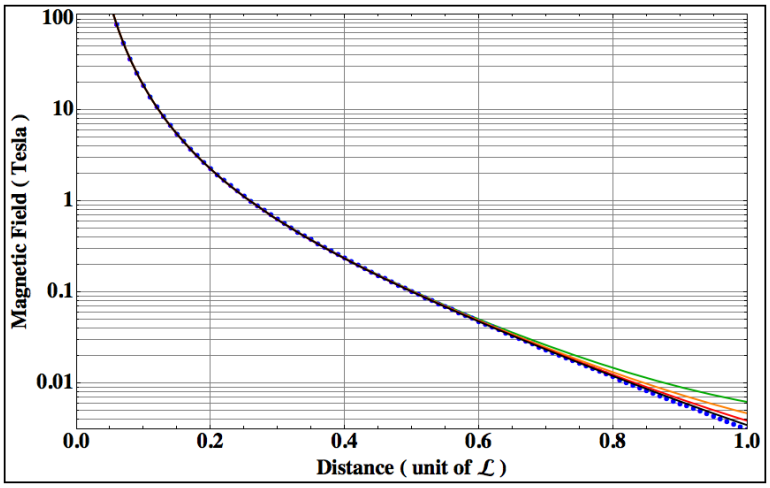

Figure B.7: *Magnetic field component B_z along $\hat{z}$ axis.* – The solid curve represents the magnitude of the field via the analytic formula (Eq. B.22) for $N_{\max} = 16$ (green), $N_{\max} = 32$ (orange), $N_{\max} = 64$ (red) and $N_{\max} = 128$ (black); the blue dots are the simulation data. In this case there is no periodicity along the direction (which is clearly visible) and even in this case only the z component survives due to the spin direction. We verified that the component in x and y are perfectly zero in the data. The sign of the component must be positive, because all the spins are pointing along the $\hat{z}$ direction.

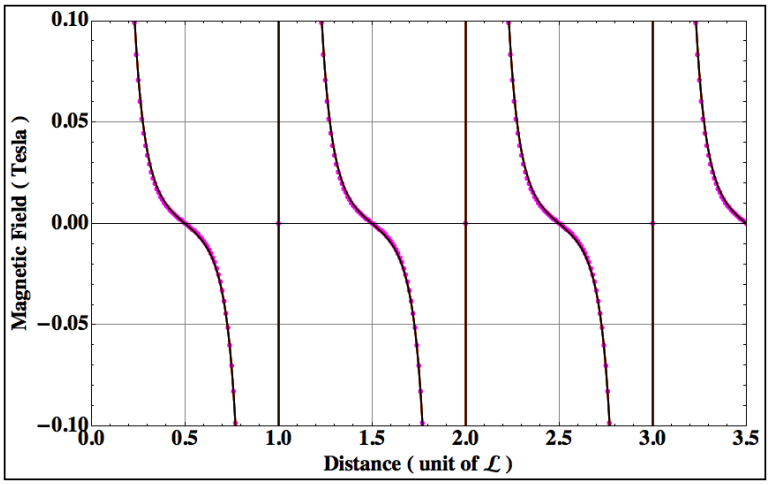

Figure B.8: *Magnetic field components B_x and B_y along $\hat{x}$ and $\hat{y}$ axes with $z = \mathcal{L}/100$.* – The solid curve represents the magnitude of the field via the analytic formula (Eq. B.22) for $N_{\max} = 16$ (green), $N_{\max} = 32$ (orange), $N_{\max} = 64$ (red) and $N_{\max} = 128$ (black); magenta dots are the simulation data. In this case the components B_x and B_y are not zero, and the agreement with the simulation is indeed very good.

Appendix C

Contents

C.1 Studies of the Size Effect without the "balls and springs" model

We present here a detailed study about all the possible size effects we can introduce in our model to calculate the diffuse scattering pattern in the (hk7) plane of the $Y_2Ti_2O_{7-\delta}$ crystal. All these calculations have been performed with and without the use of the "balls and springs model", because our aim is to reproduce qualitatively the main features of the diffuse scattering (arcs, cross and gaps as shown in Fig 5.1) even with the absence of this stage.

Notice that a size effect corresponds to a particular distortion in the lattice of the system, where one or more ions can move along particular symmetrical directions due to the Coulomb force they experience in presence of a vacancy.

C.1.1 Size Effects due to oxygen Vacancies

In this section we study which type of size effects we can take into account by removing only O(1) or O(2) in the lattice. Vacancies are randomly distributed in the system according to the nominal depletion value $\delta = 0.21$, and the parameters of the size effects have been found by trial and error, comparing the calculated diffuse scattering with the experimental one in Fig. 5.1. Notice that all of the following figures show the calculated diffuse scattering pattern using the best values of the size effect parameters we found in our study.

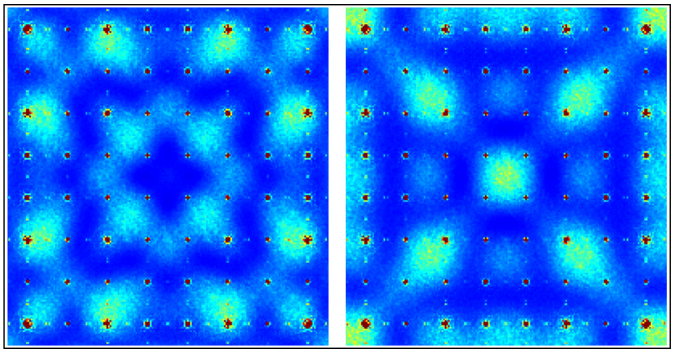

Figure C.1: *Calculated Diffuse Scattering of $Y_2Ti_2O_{7-\delta}$ in the (hk7) plane.* – Left: We impose only O(1) vacancies and the size effect on the Y atoms that are moved away from the vacancy along the local $\langle 111 \rangle$ directions without the application of the "balls and springs". Right: We impose only O(1) vacancies and the size effect on the Y atoms that are moved towards the vacancy along the local $\langle 111 \rangle$ directions without the application of the "balls and springs".

Figure C.1 shows the calculated diffuse scattering pattern in the (hk7) plane due to the presence of O(1) vacancies randomly distributed in the system. In this case the size effect has been imposed only on the Y ions that are the first nearest neighbours of the vacancies. Naively one would expect that, in presence of a vacancy, the four Y cations would tend to move away one from the other due to the fact that they are no more shielded from the Coulomb repulsion. Moreover since they are located on the pyrochlore lattice that has a high degree of symmetry, the most probable directions of the displacements should be the local $\langle 111 \rangle$. As one can see from the left panel in Fig. C.1 when the four Y ions are moved away from the vacancy we obtain a cross-like pattern at centre of the (hk7) plane overlapped by a square. By contrast if we move the Y ions towards the vacancies we can still see a cross shape at the centre but the intensity of the diffuse scattering is in wrong areas compared to the experimental one (see Fig 5.1).

Figure C.2 shows the calculated diffuse scattering pattern in the (hk7) plane due to the presence of only O(2) vacancies randomly distributed in the system. In this case the size effect has been imposed only on Ti ions that are the first nearest neighbours of the vacancies. We show the calculated diffuse scattering pattern when the Ti ions are moved away from the vacancy in the left panel of Fig. C.2, and vice versa in the right one. The two patterns are complementary, and the size effect was chosen on the base of the fact that the absence of an O(2) changes the charge of the two nearest neighbour Ti ions from $4+$ to $3+$ to preserve charge neutrality. Thus, due to the Coulomb repulsion, the two cations should move away one from the other. The calculation of the diffuse scattering showed in the left panel of Fig. C.2 is in better agreement with the experimental pattern, we can see a sort of arcs in the (hk7) plane, but it is not possible to obtain the cross and the gap. Another possible size effect that takes into account the charge difference between

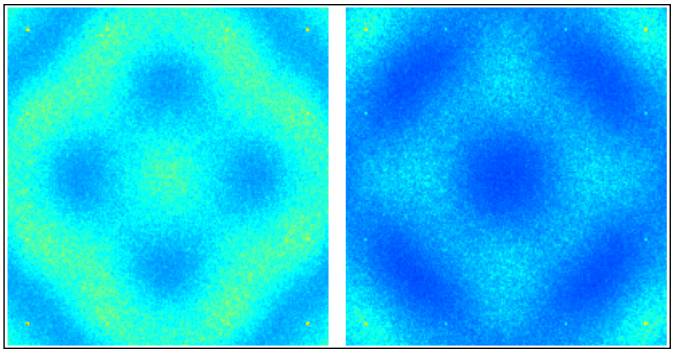

Figure C.2: *Calculated Diffuse Scattering of $Y_2Ti_2O_{7-\delta}$ in the (hk7) plane.* – Left: We impose O(2) vacancies and the size effect on the Ti atoms that are moved away from the vacancy without the application of the "balls and springs". Right: We impose only O(2) vacancies and the size effect on the Ti atoms that are moved towards the vacancy without the application of the "balls and springs".

Ti^{4+} and Ti^{3+} is shown in Fig C.3.

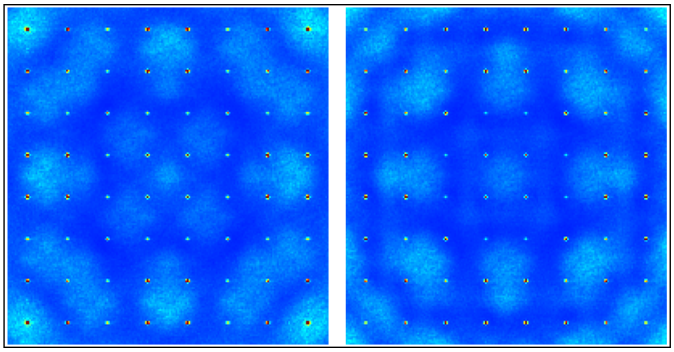

Figure C.3: *Calculated Diffuse Scattering of $Y_2Ti_2O_{7-\delta}$ in the (hk7) plane.* – Left: We impose only O(1) vacancies and the size effect on the O(2) atoms that are moved away from the Ti^{3+} ions without the application of the "balls and springs". Right: We impose only O(1) vacancies and the size effect on the O(2) atoms that are moved towards the Ti^{3+} ions without the application of the "balls and springs".

In this case we calculated the diffuse scattering pattern in the (hk7) plane due to the presence of only O(1) vacancies randomly distributed in the system that create a couple of Ti^{3+} ions to preserve charge neutrality. The size effect has been imposed only on the O(2) ions that are moved towards the Ti^{4+}, taking care of the fact that the bond length between Ti^{3+}-O(2) is longer than Ti^{4+}-O(2). We show the calculated diffuse scattering pattern moving the O(2) away from Ti^{3+} in Fig C.3 left panel and towards them in the right one. Even in this case we can notice that there is a sort of cross at the centre of the plane when we are moving the O(2) away from the Ti^{3+}, and no particular features in the other case.

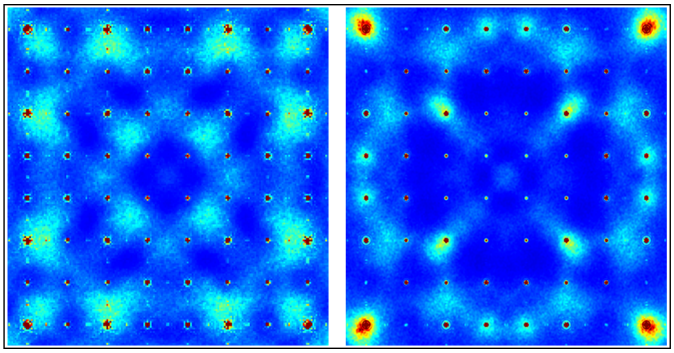

Figure C.4: *Calculated Diffuse Scattering of $Y_2Ti_2O_{7-\delta}$ in the (hk7) plane.* – We impose only O(1) vacancies and two size effects: the first one on the Y atoms that are moved away from the vacancy, and the second one on the O(2) atoms that are moved away from Ti^{3+} ions without and with the application of the "balls and springs" (left and right panel respectively).

Finally the left panel of Fig C.4 shows the calculated diffuse scattering pattern imposing only O(1) vacancies and two size effects: the first one on the Y atoms that are moved away from the vacancy due to the Coulomb repulsion of the cations, and the second one on the O(2) atoms that are moved away from Ti^{3+} ions to increase the bond length. The calculated diffuse scattering pattern shows a cross at the centre of the plane but it is still very difficult to see the four arcs. Now we can try to couple those size effects with the "balls and springs" model, that tries to minimise the unbalance in the Coulomb force relaxing all the other ions in the lattice. As one can see from the right panel in Fig C.4 our calculation improves a lot, all the exotic features (arcs, cross and gaps) are present and we have a remarkable agreement with the experimental data.

C.1.2 Size Effects due to Stuffing

Another possibility to explain the diffuse scattering pattern is the stuffing. In this case one of the ion (Y or Ti) can occupy a site reserved for another ion, and the charge difference between them can create and unbalance in the Coulomb energy forcing a displacement of the involved ions. Notice that the following figures show the calculated diffuse scattering pattern in the (hk7) plane in presence of isolated stuffed ions randomly distributed in the lattice. We distinguished the case where the stuffing is only on the Y sites or only on the Ti sites.

Figure C.5 shows the calculated diffuse scattering pattern in the (hk7) plane when we impose only Y stuffing on Ti sites. In this case the Ti tetrahedron has three Ti^{4+} and one Y^{3+} ion, thus the nearest neighbour O(2) is shifted towards the Ti ions that are "more positive" than the other one. The calculated diffuse scattering pattern moving the O(2) towards the Ti is shown in the left panel of Fig. C.5, vice versa in the right one. Notice that in the former case we can see a barely cross at

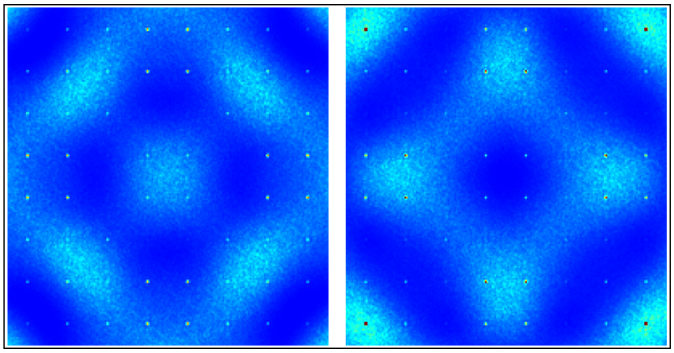

Figure C.5: *Calculated Diffuse Scattering of $Y_2Ti_2O_7$ in the (hk7) plane.* – Left: We impose only Y stuffing on Ti sites and the size effect on the O(2) that are moved away from the Y and towards the Ti^{4+} without the application of the "balls and springs". Right: We impose only Y stuffing on Ti sites and the size effect on the O(2) that are moved towards the Y and away from Ti^{4+} without the application of the "balls and springs".

the centre of the plane and something similar to four arcs that link the branches of the cross, however the gap in the arcs is not present even in this case.

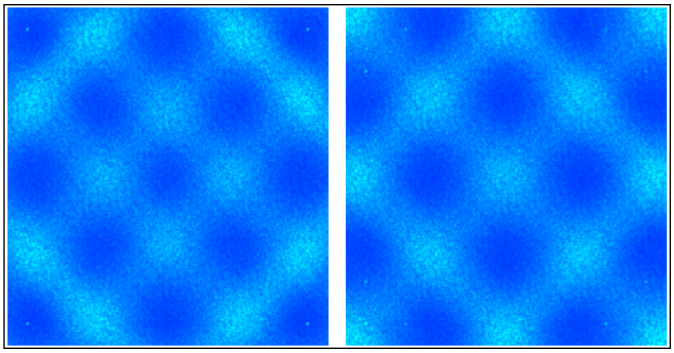

Figure C.6: *Calculated Diffuse Scattering of $Y_2Ti_2O_7$ in the (hk7) plane.* – Left: We impose only Ti stuffing on Y sites and the size effect on the O(1) that are moved away from the Ti ion along without the application of the "balls and springs". Right: We impose only Ti stuffing on Y sites and the size effect on the O(1) that are moved towards the Ti ion without the application of the "balls and springs".

Now we can reverse the stuffing and put isolated Ti ions on Y sites (see Fig. C.6). In this case the tetrahedron hosts three Y^{3+} and one Ti^{4+} ion, thus the O(1) at the centre should move towards the Ti ion. The calculated diffuse scattering pattern moving the O(1) towards the Ti is shown in the right panel of Fig. C.6, vice versa in the left one. Once again the movement of the O(1) towards the Ti ions gives the best agreement with the experimental diffuse scattering pattern, showing the presence of a cross at the centre of the plane inside a big square. Finally we can

conclude this analysis coupling the previous two size effects.

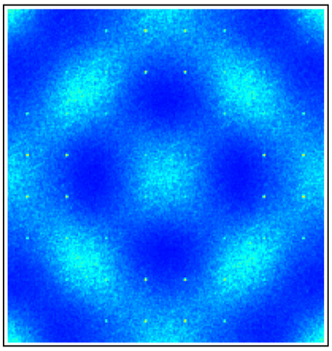

Figure C.7: *Calculated Diffuse Scattering of $Y_2Ti_2O_7$ in the (hk7) plane.* – We imposed the stuffing on both Y and Ti sites in order to preserve charge neutrality, and we moved the O(1) and O(2) towards the Ti ions according to the Coulomb force.

Figure C.7 shows the calculated diffuse scattering pattern in a stuffed $Y_2Ti_2O_7$ system where we put isolated Y ions on Ti sites and vice versa in order to preserve charge neutrality, and we moved the O(1) and O(2) towards the Ti ions according to the Coulomb force. The calculated diffuse scattering pattern looks pretty similar to the experimental one, we can notice the cross at the centre of the plane overlapped by a square. Nevertheless it is still not possible to get the gap in the arcs.

C.1.3 Conclusion

We presented a detailed analysis about possible size effects that can be used to simulate the diffuse scattering pattern of the $Y_2Ti_2O_{7-\delta}$ crystal shown in Fig. 5.1. The analysis has been carried out without the introduction of the "balls and springs" model and all the size effects have been motivated on the base of the Coulomb force acting on the ions. We saw that it is possible to explain the origin of the cross at the centre of the plane using a displacement along the local $\langle 111 \rangle$ directions, however no one of the previous size effects alone gave us the arcs present in the experimental pattern. The best agreement with the data can only be reached coupling the size effect with the "balls and springs" model, that takes into account the relaxation of distant neighbours from the vacancies too. It is also possible to get a good agreement with the data using isolated stuffed ions, in this case the size effect is able to reproduce the cross at the centre of the plane but the arcs are in some way distorted into a square superimposed to the cross.

C.2 Size Effects due to oxygen Vacancies with the "balls and springs"

We reproduced all the previous calculations of the diffuse scattering in the (hk7) plane using the best set of parameters for the size effects, and applying the "balls and springs" model to the simulation. We first calculated the diffuse scattering pattern in presence of only oxygen vacancies on O(1) or O(2) sites, with no stuffing on the other sites.

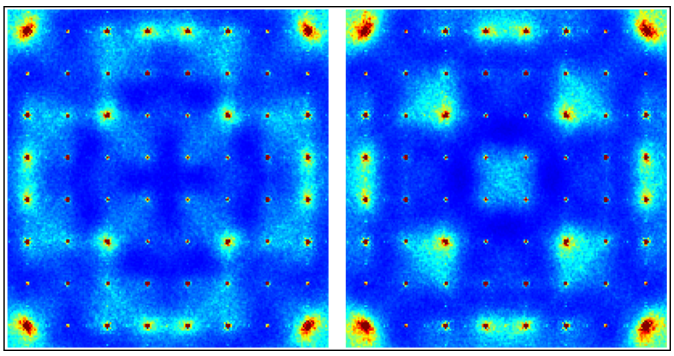

Figure C.8: *Calculated Diffuse Scattering of $Y_2Ti_2O_{7-\delta}$ in the (hk7) plane.* – We imposed only O(1) vacancies in the system and we added the "balls and springs" model to the size effect moving Y ions away from a vacancy (left panel), or towards it (right panel).

Figure C.8 shows the calculated diffuse scattering pattern in the (hk7) plane in presence of only O(1) vacancies. In particular we show the calculation of the diffuse scattering moving Y ions away from the vacancies in the (a) panel, and opposite in the (b) panel. As one can see there is a remarkable agreement between Fig. C.8(a) and the experimental data in Fig. 5.1. All the main features of the diffuse scattering are present even if we can not see the gap in the arcs. By contrast the pattern looks completely different in the (b) panel, since there is no sign of both arcs and cross.

Figure C.9 shows the calculated diffuse scattering pattern in the $(hk7)$ plane in presence of only O(2) vacancies. In this case the (a) panel shows the calculation of the diffuse scattering moving Ti ions away from the vacancies, while the (b) panel shows the opposite. We can see that it is not possible to reproduce the cross at the centre of the plane using this type of size effect, but we can notice one important aspects arising from this calculation: we have the best agreement with the experimental data when Ti ions are moved away from the O(2) vacancies, since in the other case we obtained diffuse scattering also at the centre of the plane.

Finally we can also consider the charge difference between Ti^{4+} and Ti^{3+} in presence of only O(1) vacancies. Figure C.10 shows the calculated diffuse scattering pattern in the $(hk7)$ plane moving the O(2) away or towards Ti^{3+} ions adding

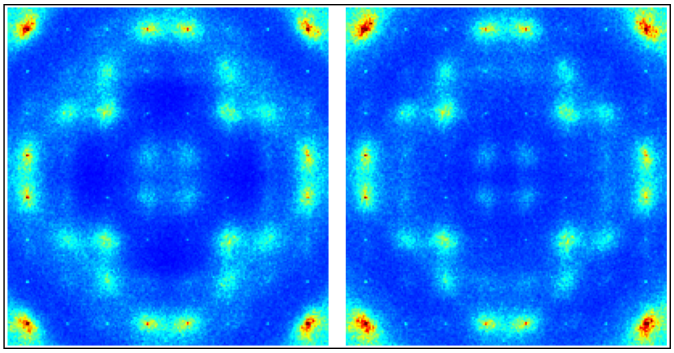

Figure C.9: *Calculated Diffuse Scattering of $Y_2Ti_2O_{7-\delta}$ in the (hk7) plane.* – We imposed only O(2) vacancies in the system and we added the "balls and springs" model to the size effect moving Ti ions away from a vacancy (left panel), or towards it (right panel).

the "balls and springs" model. Notice that the arcs are barely visible in this case and there is no cross at all, but the gap is clearly appearing along the axial directions of the plane. The fact that we are able to reproduce the gaps in the arcs with this size effect is not trivial, and it could be used to prove the existence of Ti^{3+} in the system.

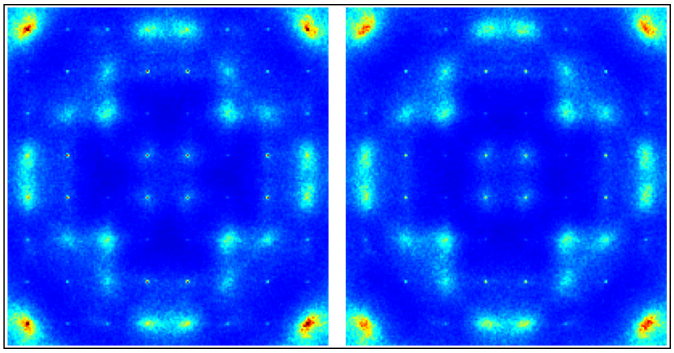

Figure C.10: *Calculated Diffuse Scattering of $Y_2Ti_2O_{7-\delta}$ in the (hk7) plane.* – We imposed only O(1) vacancies in the system and we added the "balls and springs" model to the size effect moving O(2) ions away from a Ti^{3+} (left panel), or towards it (right panel).

C.2.1 Size Effects due to Stuffing

We can now study the effect due to stuffed ions, considered as isolated defects in the lattice. The aim of this analysis is to study how the relaxation of the other ions can affect the diffuse scattering pattern in these systems.

Figure C.11 shows the calculated diffuse scattering pattern in the $(hk7)$ plane

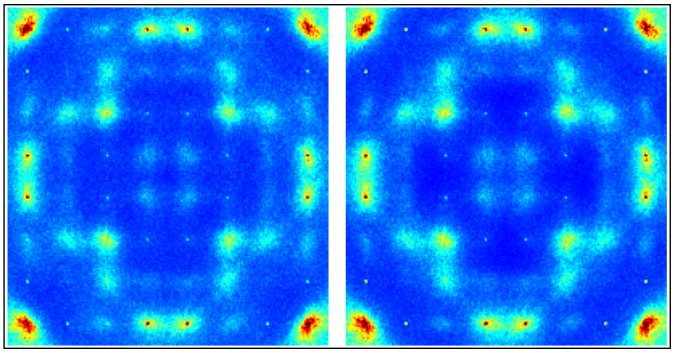

Figure C.11: *Calculated Diffuse Scattering of $Y_2Ti_2O_7$ in the (hk7) plane.* – We imposed stuffed Ti ions on Y sites, and we added the "balls and springs" model to the size effect moving the O(1) away from Ti^{4+}, or towards it.

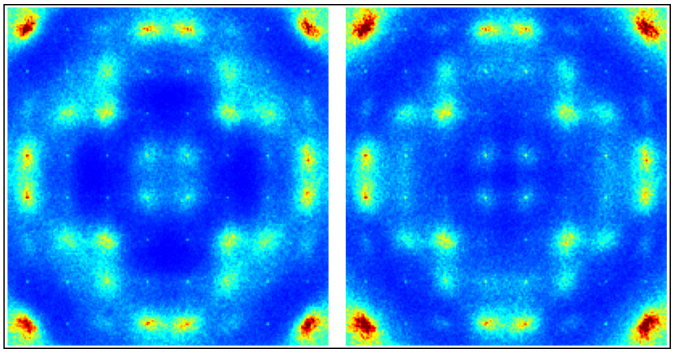

Figure C.12: *Calculated Diffuse Scattering of $Y_2Ti_2O_7$ in the (hk7) plane.* – We imposed stuffed Y ions on Ti sites, and we added the "balls and springs" model to the size effect moving the O(2) away from Y ions and towards Ti^{4+}, or only towards Y ions.

for a Ti stuffed system (i.e. Ti ions are on Y sites), in particular we calculated the diffuse scattering pattern moving the O(1) away from Ti^{4+} in (a) panel and the opposite in the (b) one. By contrast Fig. C.12 shows the calculated diffuse scattering pattern in the $(hk7)$ plane in a Y stuffed system (i.e. Y ions are on Ti sites) where we moved the O(2) away from Y ions in the (a) panel or towards them in the (b) one. As it is clearly visible the cross at the centre of the plane is completely absent in all these calculations, and the best agreement with the experimental pattern is observed only when oxygen ions are moved towards Ti^{4+}, as we explained previously. The fact that it is not possible to reproduce the cross using a stuffed model is not trivial, since it implies that only oxygen vacancies can create that particular feature. Moreover we were able to simulate it only when we removed the O(1) and we switched on the size effect on Y ions close to the vacancy. This statement could be used to prove that the O(1) have a higher probability to be removed compared

to the O(2) as stated in literature (see Ref. [36]).

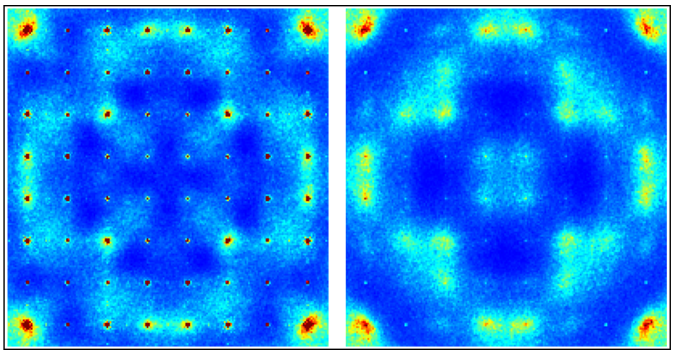

Figure C.13: *Calculated Diffuse Scattering of $Y_2Ti_2O_{7-\delta}$ and $Y_2Ti_2O_7$ in the (hk7) plane.* – Comparison between the oxygen vacancy model (left panel) and the stuffed one (right panel). Notice the good agreement of the former model with the experimental pattern shown in Fig. 5.1, where we can see that all the main features (arcs, cross and gaps) are present.

Finally Fig. C.13 shows the comparison between the oxygen vacancy model (a) and the stuffed one (b). In the former calculation we removed randomly only the O(1) and we applied the size effect on Y ions (moved away from the vacancy) and on the O(2) that are moved away from Ti^{3+} and towards Ti^{4+}. In the latter calculation we put stuffed ions on both Y and Ti sites to preserve charge neutrality and we moved O(1) and O(2) towards Ti^{4+} according to the Coulomb force.

Once again the oxygen vacancy model has the best agreement with the experimental data. All the main features are present, and we can notice that there is a trace of the gap arising in the arcs too.

C.3 $\mathrm{Y_2(Ti_{2-x}Y_x)O_{7-x/2}}$ crystal: Combination of stuffing and vacancies

In order to investigate all the possible diffuse scattering models, we calculated the diffuse scattering pattern in the (hk7) plane for a $\mathrm{Y_2(Ti_{2-x}Y_x)O_{7-x/2}}$ crystal. In this system we merged stuffing and oxygen vacancies in order to preserve charge neutrality, in particular we put Y ions on Ti sites that remain in the highest oxidation state and we introduced only O(1) vacancies. The pattern was calculated for $x = 0.1, 0.2, 0.5$ adding the "balls and springs" model to the size effects on Y ions that are moved away from a vacancy, and on O(2) ions that are moved towards Ti ions in presence of stuffing. Figure C.14 shows the comparison of the diffuse scattering patterns.

As it is clearly visible from Fig. C.14 the cross at the centre of the plane becomes visible from $x = 0.2$, below that threshold its intensity is barely visible since the number of O(1) vacancies is too low. The "balls and springs" model re-

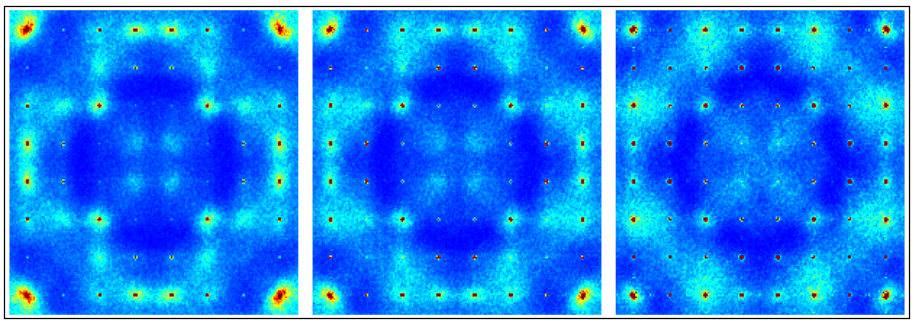

Figure C.14: *Calculated Diffuse Scattering of* $Y_2(Ti_{2-x}Y_x)O_{7-x/2}$ *in the (hk7) plane for* $x = 0.1, 0.2, 0.5$ *respectively.* – The cross at the centre of the plane becomes visible from $x = 0.2$, below that threshold its intensity is barely visible since the number of O(1) vacancies is too low. Arcs and gaps are present but in this case their intensity is much more diffuse than in the previous cases, the boundaries are not clear and their shape tend to become a circle at very high stuffing levels.

produces both the arcs and the gaps but in this case their intensity is much more diffuse than in the previous cases, the boundaries are not clear and their shape tend to become a circle at very high stuffing levels. We can now add a correlation between O(1) vacancies and the stuffed Y ions, in particular we can distribute these ions randomly but close to one vacancy. The calculated diffuse scattering pattern in the (hk7) plane is shown in Fig. C.15. Even in this case the cross becomes visible from $x = 0.2$ due to the low number of vacancies in the system, but the shape of the arcs looks much more similar to the experimental pattern of Fig. 5.1 especially at very low stuffing levels. Notice that the depletion value of our crystal should correspond to $x = 0.5$ in these calculations, thus the fact that the calculated diffuse scattering has a poor agreement with the data indicates a very low stuffing level in our compound.

In conclusion we can state again that the oxygen vacancy model has the best agreement with the experimental diffuse scattering patten shown in Fig. 5.1, all the features in the (hk7) plane are the result of a particular displacement of the ions due to the presence of vacancies and they can be understood on the base of Coulomb force. The combination of stuffing and vacancies did not produce any significant improvement to our calculation, unless we are assuming a possible correlation between vacancies and stuffed ions. In this case the cross at the centre of the plane becomes visible above a particular threshold and the rings tend to become a circle at high stuffing levels. Notice that the presence of the gap is connected to the movement of the O(2) towards Ti^{4+}, due to the presence of stuffed Y^{3+} on Ti sites. This size effect is qualitatively equal to the movement of the O(2) in presence of Ti^{3+}, and it can give us an evidence of the presence of these ions in the lattice. However we can exclude the possibility to have a very high stuffing level of Y ions in the system, since the calculated diffuse scattering presents features that are not

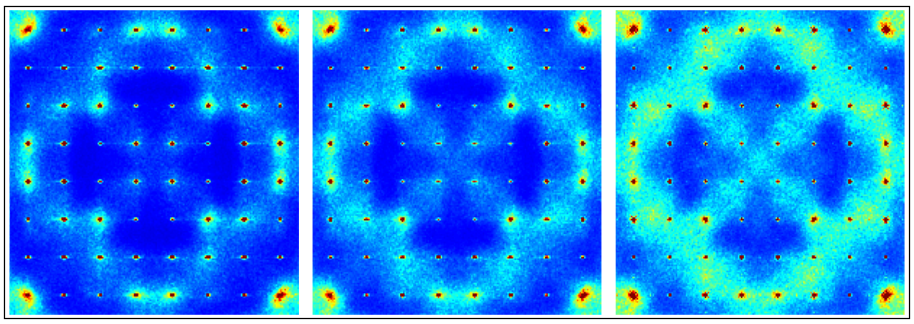

Figure C.15: *Calculated Diffuse Scattering of* $\mathrm{Y_2(Ti_{2-x}Y_x)O_{7-x/2}}$ *in the (hk7) plane for* $x = 0.1, 0.2, 0.5$ *respectively.* – We added a possible correlation between the O(1) vacancies and the stuffed Y ions, that are created randomly in the system but close to the vacancy. Even in this case the cross becomes visible from $x = 0.2$, and the shape of the arcs looks more similar to the experimental pattern.

consistent with the data.

Bibliography

Contents

[1] Rajaraman R., "In Quantum (Un)speakables." (2002) ed Bertlemann RA, Zeilinaer A., 389-399 Berlin: Springer-Verlag

[2] Laughlin R. B., "Nobel Lecture: Fractional Quantisation." Rev. Mod. Phys. **71**, 863-874 (1999)

[3] Goldmann VJ and Su B., "Resonant Tunnelling in the Quantum Hall Regime: Measurement of Fractional Charge." Science **267**, 1010-1012 (1995)

[4] Wen X-G. and Int. J., "Topological Orders in rigid states." Mod. Phys. B **4**, 239-271 (1990)

[5] Anderson P. W., "Resonating valence bonds: a new kind of insulator ?" Mater. Res. Bull. **8**, 153-160 (1973)

[6] Wegner F. J., "Duality in Generalized Ising Models and Phase Transitions without Local Order Parameter." Math. Phys. **12**, 2259-2272 (1971)

[7] Kogut J. B., "An introduction to lattice gauge theory and spin systems." Rev. Mod. Phys. **51**, 659-713 (1979)

[8] Wen X. G., "Vacuum degeneracy of chiral spin states in compactified space." Phys. Rev. B **40**, 7387-7390 (1989)

[9] Dirac P. A. M., "Quantised singularities in the electromagnetic field." Proc. R. Soc. A **133**, 60-72 (1931)

[10] Harris M. J., Bramwell, S. T., McMorrow, D. F., Zeiske, T. Godfrey, K. W., "Geometrical Frustration in the Ferromagnetic Pyrochlore $\mathrm{Ho_2Ti_2O_7}$." Phys. Rev. Lett. **79**, 2554-2557 (1997)

[11] Bramwell S. T. and Gingras M. J. P., "Spin Ice State in Frustrated Magnetic Pyrochlore Materials." Science **294**, 1495-1501 (2001)

[12] Bramwell S. T. and Gingras M. J. P., Holdsworth P. C. W., "Frustrated Spin Systems, Ch. 7." (H. T. Diep,World Scientific, Singapore, 2004)

[13] Fennell T. et al., "Neutron scattering investigation of the spin ice state in $Dy_2Ti_2O_7$." Phys. Rev. B **70**, 134408 (2004)

[14] Yavors'kii T. et al., "$Dy_2Ti_2O_7$ Spin ice: A test case for the Emergent Clusters in a Frustrated Magnet." Phys. Rev. Lett. **101**, 037204 (2008)

[15] Ehlers G. et al., "Dynamical crossover in hot spin ice." J. Phys. Condens. Matter **15**, L9-L15 (2003)

[16] den Hertog B. C., Gingras M. J. P., "Dipolar Interactions and Origin of Spin Ice in Ising Pyrochlore Magnets." Phys. Rev. Lett. **84**, 3430-3433 (2000)

[17] Isakov, S. V., Moessner, R. Sondhi, S., "Why spin ice obeys the ice rules." Phys. Rev. Lett. **95**, 217201 (2005)

[18] Anderson P. W., "Ordering and antiferromagnetism in ferrites." Phys. Rev. **102**, 1008-1013 (1956)

[19] Ramirez A. P., Hayashi, A., Cava, R. J., Siddharthan, R. Shastry, B. S., "Zero-point entropy in spin ice." Nature **399**, 333-335 (1999)

[20] Pauling L., "The Structure and Entropy of Ice and of Other Crystals with Some Randomness of Atomic Arrangement." J. Am. Chem. Soc. **57**, 2680-2684 (1935)

[21] Giauque W. F. Stout, J. W., "The entropy of water and the third law of thermodynamics. The heat capacity of ice from 15 to 273K." J. Am. Chem. Soc. **58**, 1144-1150 (1936)

[22] Bernal J. D., Fowler R. H., "A theory of water and ionic solution, with particular reference to hydrogen and hydroxyl ions." J. Chem. Phys. **1**, 515-548 (1933)

[23] Castelnovo C., Moessner, R. Sondhi S., "Magnetic monopoles in spin ice." Nature **451**, 742-45 (2008)

[24] Nagle J. F., "Theory of the dielectric constant of ice." Chem. Phys. **43**, 317-328 (1979)

[25] Wang R. F. et al., "Artificial spin ice in a geometrically frustrated lattice of nanoscale ferromagnetic islands." Nature **439**, 303-306 (2006)

[26] Jackson J. D., "Classical Electrodynamics." Ch. 6.11-6.12 (Wiley, New-York, 1999)

[27] Ryzhkin I. A., "Magnetic relaxation in rare-earth oxide pyrochlores." J. Exp. Theor. Phys. **101**, 481-486 (2005)

[28] Sakurai J. J., "Meccanica quantistica moderna." Zanichelli (2003)

[29] Castelnovo C. et al., "Debye-Hückel theory for spin ice at low temperature." Phys. Rev. B **84**, 144435 (2011)

[30] Liu B. et al., "Theoretical elastic stiffness, structure stability and thermal conductivity of $La_2Zr_2O_7$ pyrochlore." Acta Materialia **55**, 2949-2957 (2007)

[31] "https://chemistry.osu.edu/woodward/ch754/lect2003/solid_electro_lect27.pdf"

[32] Goodwin A. L. et al., "Real-space refinement of single-crystal electron diffuse scattering and its application to $Bi_2Ru_2O_{7-\delta}$." J. Phys. Condens. Matter **19**, 335216 (2007)

[33] Reimers J. N. et al., "The crystal structure of the spin glass pyrochlore, $Y_2Mo_2O_7$." J. Solid State Chem. **72**, 390-394 (1988)

[34] Mori D. et al., "Single crystal growth of $Tl_2Ru_2O_7$ pyrochlore using high pressure and flux method." J. Solid State Chem. **179**, 935-940 (2006)

[35] Jin R. et al., "Superconductivity in the correlated pyrochlore $Cd_2Re_2O_7$." Phys. Rev. B **64**, 180503(R) (2001)

[36] Subramanian M. A., Aravamudan, G., Rao, G. V. S. "Oxide pyrochlores a review." Prog. Solid State Chem. **15**, 55-143 (1983)

[37] Pena M. A. and Fierro J. L. G., "Chemical Structures and performance of perovskite oxides." Chem. Rev. **101**, 1981-2017 (2001)

[38] Hines R. I., "Atomistic simulation and ab-initio studies of polar solids." PhD Thesis Bristol, (1997)

[39] Raghavender A.T. et al., "Nano ilmenite $FeTiO_3$: Synthesis and characterisation." J. Magnetism and Mag. Mater. **331**, 129-132 (2013)

[40] Hutchings M. T., "Point-Charge Calculations of Energy Levels of Magnetic Ions in Crystalline Electric Fields." Solid State Physics **16**, 27273 (1964)

[41] Abragam A. and Bleaney B., "Electron Paramagnetic Resonance of Transition Ions." Clarendon Press Oxford (1970)

[42] Griffith J. S., "The Theory of Transition-Metal Ions." Cambridge University press (1961)

[43] Prather J. L., "Atomic Energy Levels in Crystals." NBS monograph **19**, (1961)

[44] Walter U., "Treating Crystal Field Parameters in lower than cubic symmetries." J. Phys. Chem. Solids **45**, No. 4, 40-408, (1984)

[45] Freeman A. J. and Watson R. E., "Theoretical Investigation of some magnetic and spectroscopic properties of rare earth ions." Phys. Rev. **127**, 2058 (1962)

[46] Martin J. K., "On a Degeneracy Theorem of Kramers." American Journal of Physics **20**, Issue 2, 65-71 (1952)

[47] Wigner E. P., "Group Theory and Its Application to the Quantum Mechanics of Atomic Spectra." Academic Press Inc. New York (1959)

[48] Rosenkrantz et al., "Crystal-field Interaction in the pyrochlore magnet $Ho_2Ti_2O_7$." J. Appl. Phys. **87**, 5914 (2000)

[49] Ewald P. P., "Die Berechnung optischer und elektrostatischer Gitterpotentiale." Ann. Phys. **369**, 253287 (1921)

[50] Melko R. G. and Gingras J. P., "Monte Carlo studies of the dipolar spin ice model." J. Phys. Condens. Matter **16**, R1277-R1319 (2004)

[51] De Leeuw, S.W., "Simulation on electrostatic systems in periodic boundary conditions." Proc. R. Soc. Lond. A **373**, 27-56 (1980)

[52] Binder K., "The Monte Carlo Method in Condensed Matter Physics." Springer New York (1995)

[53] Marsaglia G. and Zaman A., "Toward a Universal Random Number Generator." Florida State University Report: FSU-SCRI-87-50 (1987)

[54] Squires G.L., "Introduction to the theory of thermal neutron scattering." Cambridge university press (1978)

[55] "http://www.isis.stfc.ac.uk/instruments/sxd/"

[56] "http://www.mlz-garching.de/dns"

[57] Wang R. F. et al., "Artificial spin ice in a geometrically frustrated lattice of nanoscale ferromagnetic islands." Nature **439**, 303 (2006)

[58] Moller G. and Moessner R., "Magnetic multipole analysis of kagome and artificial spin-ice dipolar arrays." Phys. Rev. B **80**, 140409(R) (2009)

[59] Ladak S., Read D. E., Perkins G. K., Cohen L. F., and Branford W.R., "Direct observation of magnetic monopole defects in an artificial spin-ice system." Nature Phys. **6**, 359 (2010)

[60] Mengotti E., "Real-space observation of emergent magnetic monopoles and associated Dirac strings in artificial kagome spin ice." Nature Phys. **7**, 68 (2011)

[61] Fennell T. et al., "Magnetic Coulomb phase in the spin ice $Ho_2Ti_2O_7$." Science **326**, 415-417 (2009)

[62] Kadowaki H. et al., "Observation of Magnetic Monopoles in Spin Ice." J. Phys. Soc. Japan **78**, 103706 (2009)

[63] Morris D. J. P. et al., "Dirac Strings and Magnetic Monopoles in the Spin Ice $Dy_2Ti_2O_7$." Science **326**, 411 (2009)

[64] Lago J., Blundell S. J., and Baines C., "μSR investigation of spin dynamics in the spin-ice material $Dy_2Ti_2O_7$." J. Phys. Condens. Matter **19**, 326210 (2007)

[65] Bramwell S. T. et al., "Measurement of the charge and current of magnetic monopoles in spin ice." Nature **461**, 956-959 (2009)

[66] Dunsiger S. R. et al., "Spin Ice: Magnetic Excitations without Monopole Signatures Using Muon Spin Rotation." Phys. Rev. Lett. **107**, 207207 (2011)

[67] Margenau H., "Theory of pressure effects of foreign gases on spectral line." Phys. Rev. **48**, 755-765 (August 1935)

[68] Rivier N. and Adkins K., "Amorphous Magnetism." edited by H.O. Hooper and A.M. de Graaf (Plenum, New York, 1973), p. 215

[69] Sala G. et al., "Magnetic Coulomb Fields of Monopoles in Spin Ice and Their Signatures in the Internal Field Distribution" Phys. Rev. Lett. **108**, 217203 (2012)

[70] Snyder J. et al., "Low-temperature spin freezing in the $Dy_2Ti_2O_7$ spin ice." Phys. Rev. B **69**, 064414 (2004)

[71] Qi X-L., Li R., Zang J., and Zhang S-C., "Inducing a Magnetic Monopole with Topological Surface States." Science **323**, 1184 (2009)

[72] Slobinsky D. et al., "Unconventional Magnetization Processes and Thermal Runaway in Spin-Ice $Dy_2Ti_2O_7$." Phys. Rev. Lett. **105**, 267205 (2010)

[73] Mellado P., Petrova O., Shen Y., and Tchernyshyov O., "Dynamics of Magnetic Charges in Artificial Spin Ice." Phys. Rev. Lett. **105**, 187206 (2010)

[74] Onsager L., "Deviations from Ohms law in weak electrolytes." J. Chem. Phys. **2**, 599-615 (1934)

[75] Kaiser V. et al., "Onsager's Wien effect on a lattice." Nature Mat. **12**, 1033-1037 (2013)

[76] Blundell S. J., "Monopoles, Magnetricity, and the Stray Field from Spin Ice." Phys. Rev. Lett. **108**, 147601 (2012)

[77] Prabhakaran D. and Boothroyd A. T., "Crystal growth of spin-ice pyrochlores by the floating-zone method." Journal of Crystal Growth **318**, 1053-1056 (2011)

[78] Notice that we corrected the symmetry of the cuts in Fig. 5.2(c). In the previous version of the figure the cuts have been drawn by hand using the SXD2001 software at the ISIS facility. However, we noticed that the line was not perfectly straight since the symmetry of the features was not respected. We resolved the mistake exporting the entire (hk7) plane in an ASCII file, and making the cuts using Mathematica.

[79] Welberry T. R. et al., "The interpretation and analysis of diffuse scattering using Monte Carlo simulation methods." Acta Cryst. **A64**, 23-32 (2007)

[80] Goossens D. J. et al., "Monte Carlo modelling of diffuse scattering from single crystals: The program ZMC." Metallurgical and materials transactions **42A**, (2011)

[81] Welberry T. R., "Diffuse x-ray scattering and models of disorder." IUCr Monographs on Crystallography **16** (OUP, Oxford, 2004)

[82] Welberry T. R., "Single crystal neutron diffuse scattering and Monte Carlo study of the relax or ferroelectric $\mathrm{PbZn_{1/3}Nb_{2/3}O_3}$ (PZN)." J. Appl. Cryst **38**, 639-647 (2005)

[83] Gutmann M. J., "Accelerated computation of diffuse scattering patterns and application to magnetic neutron scattering." J. Appl. Cryst. **43**, 250-255 (2010)

[84] Abrahams S. C., "Magnetic and crystal structure of titanium sesquioxide." Phys. Rev. **130**, (1963)

[85] Oszlányi G. and Süto, A., "Ab initio structure solution by charge flipping." Acta Cryst. **A60**, 134-141 (2004)

[86] Welberry T. R., "Diffuse x-ray scattering and models of disorder." Rep. Prog. Phys. **48**, 1543-1593 (1985)

[87] Proffen T. and Neder R., "DISCUS 3.4 users guide", www.pa.msu.edu/cmp/billingegroup/discus/dis_man.pdf

[88] Longo J. M., Raccah P. M., Goodenough J. B., "$\mathrm{Pb_2M_2O_{7-x}}$ (M = Ru, Ir, Re) preparation and properties of oxygen deficient pyrochlores." Mat. Res. Bull. **4**, 191-202 (1969)

[89] Ross K. A. et al., "Lightly stuffed pyrochlore structure of single-crystalline $\mathrm{Yb_2Ti_2O_7}$ grown by the optical floating technique." Phys. Rev. B **86**, 174424 (2012)

[90] Taniguchi T. et. al., "Long-range order and spin-liquid states of polycrystalline $\mathrm{Tb_{2+x}Ti_{2-x}O_{7+y}}$." Phys. Rev. B **87**, 060408 (2013)

[91] Blundred G. D. et al., "New Oxidation States and defect chemistry in the pyrochlore structure." Angew. Chem. Int. Ed. **43**, 3562-3565 (2004)

[92] Pirzada M. et al., "Oxygen migration in $\mathrm{A_2B_2O_7}$ pyrochlores." Solid State Ionics **140**, 201-208 (2001)

[93] Quilliam J. A., Yaraskavitch, I. R., Dabkowska, H. A., Gaulin, B. D., Kycia, J. B., "Dynamics of the magnetic susceptibility deep in the coulomb phase of the dipolar spin ice material $\mathrm{Ho_2Ti_2O_7}$." Phys. Rev. B **83**, 094424 (2011)

[94] Matsuhira K. et al., "Spin dynamics at very low temperature in spin ice $\mathrm{Dy_2Ti_2O_7}$." J. Phys. Soc. Jpn. **80**, 123711 (2011)

[95] Yaraskavitch L. R. et al., "Spin dynamics in the frozen state of the dipolar spin ice material $\mathrm{Dy_2Ti_2O_7}$." Phys. Rev. B **85**, 020410 (2012)

[96] Revell H. M. et al., "Evidence of impurity and boundary effects on magnetic monopole dynamics in spin ice." Nature Physics **9**, 34-37 (2013)

[97] Lau G. C., et al., "Zero-point entropy in stuffed spin ice." Nature Phys. **2**, 249-253 (2006)

[98] Henley C. L., "NMR relaxation in spin ice due to diffusing emergent monopoles I." arXiv:1210.8137 (2012).

[99] Biltmo A. and Henelius P., "Unreachable glass transition in dilute dipolar magnet." Nature Comm. **3**, 857 (2012)

[100] Jaubert L. D. C. and Holdsworth P. C. W., "Signature of magnetic monopole and Dirac string dynamics in spin ice." Nature Physics **5**, 258-261 (2009)

[101] Arnab S. et. al., "Coulomb phase diagnostics as a function of temperature, interaction range and disorder." Phys. Rev. Lett. **110**, 107202 (2013)

[102] Chang L. J. et al., "Magnetic correlations in the spin ice $\mathrm{Ho_{2-x}Y_xTi_2O_7}$ as revealed by neutron polarisation analysis." Phys. Rev. B **82**, 172403 (2010)

[103] X Ke et al., "Nonmonotonic Zero-Point Entropy in Diluted Spin Ice." Phys. Rev. Lett. **99**, 137203 (2007)

[104] Chang L. J. et al., "Low-temperature muon spin rotation studies of the monopole charges and currents in Y doped $\mathrm{Ho_2Ti_2O_7}$." Scientific Reports **3**, 1881 (2013)

[105] Giblin S. R. et al., "Creation and measurement of long-lived magnetic monopole currents in spin ice." Nature Physics **7**, 252-258 (2011)

[106] Bovo L. et al., "Brownian motion and quantum dynamics of magnetic monopoles in spin ice." Nature Comm. **4**, 1535 (2013)

[107] Paulsen C. et al., "Far-from-equilibrium monopole dynamics in spin ice." Nature Physics **10**, 135-139 (2014)

[108] Jaubert L. D. C. et al., "Topological-Sector Fluctuations and Curie-Law Crossover in Spin Ice." Phys. Rev. X **3**, 011014 (2013)

[109] Pomaranski D. et al., "Absence of Paulings residual entropy in thermally equilibrated $Dy_2Ti_2O_7$." Nature Physics **9**, 353-356 (2013)

[110] Khomskii D.I., "Electric dipoles on magnetic monopoles in spin ice." Nature Comm. **3**, 904 (2012)

[111] Kolland G. et al., "Thermal conductivity and specific heat of the spin-ice compound $Dy_2Ti_2O_7$: Experimental evidence for monopole heat transport." Phys. Rev. B **86**, 060402 (2012)

[112] In-Chul Yeh and Berkowitz M. L., "Ewald summation for system with slab geometry." J. Chem. Phys. **111**, 3155 (May 1999)

[113] Widmann A. H. and Adolf D. B., "A comparison of Ewald summation techniques for planar surfaces." Computer Phys. Comm. **107**, 167-186 (1997)